Spot evolution and differential rotation of the ultrafast rotator Speedy Mic

Dissertation
zur Erlangung des Doktorgrades
des Fachbereichs Physik
der Universität Hamburg

vorgelegt von
Uwe Wolter

aus Rendsburg

Hamburg
2004

Gutachter der Dissertation:	Prof. J.H.M.M. Schmitt Prof. A.P. Hatzes
Gutachter der Disputation:	Prof. J.H.M.M. Schmitt Prof. P.H. Hauschildt
Datum der Disputation:	7. 5. 2004
Vorsitzender des Prüfungsausschusses:	Dr. F.-J. Zickgraf
Vorsitzender des Promotionsausschusses:	Prof. R. Wiesendanger
Dekan des Fachbereichs Physik:	Prof. G. Huber

Zusammenfassung

Eine Vielzahl von Erscheinungen der Sonnenatmosphäre wird unter dem Begriff Sonnenaktivität zusammengefasst. Auch auf anderen Sternen werden Aktivitätsphänomene beobachtet, die anscheinend eine Ähnlichkeit zu denen der Sonne aufweisen. Stellare Aktivität steht in engem Zusammenhang zu magnetohydrodynamischen Prozessen in stellaren Konvektionszonen. Vermutlich führen komplexe Strömungen des konvektierenden Plasmas im Zusammenspiel mit der Rotation des Sterns zu einem selbsterregenden Dynamo. Die Beobachtung differentieller (d.h. nicht starrer) Oberlächenrotation ist ein wichtiger Beitrag zum Verständnis der Dynamik äusserer stellarer Konvektionszonen.

Ein auffälliges Zeichen solarer Aktivität sind Sonnenflecken; auch die Oberflächen anderer Sterne als der Sonne zeigen dunkle Flecken. In welchem Maße diese Sternflecken analog zu Sonnenflecken sind, ist gegenwärtig weitgehend unbekannt; das gilt ebenso für die Prozesse, die ihre Eigenschaften bestimmen.

Doppler-Tomographie überwindet die Beugungsbegrenzung der Auflösung direkter und interferometrischer Abbildungsverfahren, indem sie die rotationsmodulierte Information in Sternspektren ausnutzt. Derzeit ist Doppler-Tomographie die einzige Methode zur Erzeugung aufgelöster Oberflächenbilder sonnenartiger Sterne.

Nach einer Darstellung von Beobachtungsergebnissen und theoretischer Grundlagen beschreibt der erste Teil dieser Arbeit das Doppler-tomographische Verfahren CLDI (CLEAN-like Doppler imaging = CLEAN-artige Doppler-Tomographie). CLDI wurde als Teil dieser Arbeit entwickelt, aufbauend auf den Arbeiten von Kürster (1991). CLDI wurde weiterentwickelt und in die Lage versetzt, Doppler-Bilder hoher Auflösung zu erzeugen. Umfangreiche Tests zeigen, dass die Leistungsfähigkeit von CLDI verbessert worden ist. Im Gegensatz zu Maximum-Entropie-Methoden ist CLDI kein explizites Optimierungsverfahren; die daraus resultierenden grundlegenden Beschränkungen wurden für CLDI systematisch untersucht. Es wird vorgeschlagen, CLDI zu verwenden, um die Zuverlässigkeit von Doppler-Bildern anderer Verfahren zu prüfen. Seine teilweise methodische Unabhängigkeit von anderen Verfahren macht CLDI für ein solches Verfahren geeignet.

Der zweite Teil dieser Arbeit enthält eine Darstellung des Verfahrens sLSD (selective least-squares deconvolution = selektive Quadratmittel-minimierende Entfaltung). sLSD dient der Entfaltung von Spektren schnellrotierender Sterne und baut auf dem Verfahren LSD auf, das von Donati et al. eingeführt wurde. Als eine Weiterentwicklung von LSD ist sLSD auf eine Anwendung auf relativ schmalen Wellenlängenbereichen ausgerichtet; dadurch können indivduelle Eigenschaften der zu entfaltenden Spektrallinien berücksichtigt werden. sLSD verwendet eine Tichonov-Regularisierung, um sein Funktionieren auf schmalen Spektralbereichen zu unterstützen. Die Konsistenz der Ergebnisse von sLSD wurde durch seine Anwendung auf verschiedene Spektralbereiche und Musterspektren überprüft.

Der dritte Teil beschreibt die Resultate dieser Arbeit über den ultraschnell rotierenden, hochaktiven sonnenartigen Vorhauptreihenstern "Speedy Mic" (= HD197890, K2 V, $P_{\rm rot} = 0.380$ days). Im Rahmen dieser Arbeit wurde mit dem Spektrographen UVES am "Very Large Telescope" (VLT) eine spektrale Zeitserie von Speedy Mic aufgenommen, die eine homogene Qualität und eine dichte Abdeckung der Rotationsphasen zweier stellarer Umdrehungen aufweist. Diese Zeitserie wurde für die Konstruktion zweier Doppler-Bilder mit Hilfe von CLDI verwendet. Die Auflösung dieser Doppler-Bilder wurde zu etwa zehn Grad auf der Oberfläche Speedy Mics bestimmt, indem Rekonstruktionen von verschiedenen Untermengen der spektralen Daten verglichen wurden.

Die Doppler-Bilder Speedy Mics weisen im Gegensatz zu den meisten anderen ultraschnell rotierender K-Zwergsternen keinen polaren Fleck auf. Sie zeigen, dass Großteile der Flecken auf Speedy Mic im Zeitraum zwischen den Doppler-Bildern, etwa 13 stellare Umdrehungen, auf allen aufgelösten Skalen stabil sind. Allerdings treten auch Veränderungen der Fleckenverteilung auf Skalen von bis zu etwa 30 Grad in stellarer Länge und Breite auf.

Diese Veränderungen führen zu einer aperiodischen Lichtkurve; dieses Verhalten wurde durch photometrische Beobachtungen zwischen den beiden Dopplerbildern bestätigt. Eine Analyse aller für Speedy Mic verfügbaren photometrischen Daten deutet darauf hin, dass Speedy Mic sowohl Zeiträume stabiler Fleckenverteilungen während einiger Wochen aufweist als auch Epochen wesentlicher Fleckenveränderungen während weniger Tage.

Die Stärke der differentiellen Rotation wurde aus einer Kreuzkorrelation der Doppler-Bilder mit $|\alpha| = \Delta\Omega/\Omega < 0.004 \pm 0.002$ nach oben abgeschätzt, er liegt also unterhalb von fünf Hundertsteln des solaren Wertes. Lediglich die Entwicklung der größten rekonstruierten Fleckengruppe liefert Hinweise auf eine mögliche anti-solare differentielle Rotation. Anti-solar bedeutet hier, dass der Äquator mit höherer Winkelgeschwindigkeit rotiert als die polaren Regionen. Anti-solare differentielle Rotation sonnenartiger Sterne ist nicht durch grundlegende Argumente auszuschliessen, sie widerspricht jedoch gegenwärtigen theoretischen Modellen.

Eine teilweise Untersuchung der zeitabhängigen Emission im Kern der Ca II K Linie liefert Anzeichen von örtlich begrenzten Regionen chromosphärischer Aktivität auf Speedy Mic. Einige dieser Regionen scheinen langlebig zu sein, während andere nur kurz beobachtbar sind. Eine weitergehende Untersuchung auf der Grundlage der vorhandenen Daten wird vorgeschlagen, um eine weitergehende Lokalisierung dieser Regionen zu ermöglichen.

Abstract

The Sun shows a variety of transient surface features which are summarized as solar activity. Activity phenomena, apparently similar to the solar case, are also observed on stars other than the Sun. Stellar activity is closely related to magneto-hydrodynamic processes in a star's convection zone. A dynamo is believed to operate in the outer convection zone of solar-like stars, generating magnetic fields by complex motions of the convecting plasma under the influence of rotation. Differential (i.e. non-rigid) rotation of the stellar surface is an important indicator of the overall dynamics of a star's outer convection zone.

Sunspots are a conspicuous token of solar activity; dark spots can also be observed on the surface of stars other than the Sun. To which degree "starspots" are analogues of sunspots is presently only poorly known; the processes governing their lifetime and structure are largely unexplored.

Doppler imaging overcomes the diffraction-limitations of direct and interferometric imaging techniques by making use of information that is modulated into a star's spectrum due to its rotation. Doppler imaging is currently the only method to produce well-resolved images of solar-like stars.

After a selective review of the observational and theoretical foundation, the first part of this thesis describes a method for Doppler imaging called CLDI (CLEAN-like Doppler imaging). CLDI has been developed during this thesis, continuing the work of Kürster (1991). CLDI has been adapted to reconstructions at high surface resolution; its performance has been improved, as verified by extensive tests. Unlike maximum entropy Doppler imaging methods, CLDI is not an explicit optimization procedure; the resulting fundamental limitations of CLDI have been systematically studied. Due to the partial independence of CLDI's approach from other Doppler imaging methods, it is proposed as a means of checking the reliability of Doppler images reconstructed by other methods.

The second part presents the method sLSD (selective least-squares deconvolution), developed for the deconvolution of spectra of fast rotating stars; it is based on the method LSD introduced by Donati et al. (1997b). As an improvement compared to LSD, sLSD is well-suited for operating on relatively narrow wavelength ranges, allowing to account for individual characteristics of the deconvolved spectral lines. An important feature of sLSD is a Tikhonov-regularization which enables it to work on narrow spectral ranges. The consistency of the line profile extraction by sLSD has been verified by applying it to different spectral ranges and template spectra.

The third part of this thesis describes results concerning the ultrafast rotating, highly active, pre-main-sequence "solar-like" star "Speedy Mic" (= HD197890, K2 V, $P_{\rm rot} = 0.380$ days). CLDI was applied to a densely phase sampled spectral time series of homogeneous quality covering two complete rotations of Speedy Mic. These spectra have been observed as a part of this thesis using the spectrograph UVES mounted on the "Very Large Telescope" (VLT). The reconstructed Doppler images were verified to have a resolution of about ten degrees on the stellar surface by systematically comparing reconstructions based on different wavelength regions and data subsets. In contrast to many ultrafast rotating K-dwarf stars, the Doppler images of Speedy Mic do not show a polar spot.

The Doppler images of Speedy Mic show that many features of the spot pattern have been stable on large, intermediate and even small scales during the about thirteen rotations between them. However, a few spot reconfigurations have taken place on scales up to about 30° in stellar longitude and latitude.

These reconfigurations lead to an aperiodic behaviour of the lightcurve which has been confirmed by V-band photometry observed between the two Doppler images. An analysis of all photometric time series available for Speedy Mic was performed; its results indicate that Speedy Mic shows epochs of stable spot patterns for weeks as well as epochs of significant spot reconfigurations during a few days.

The differential rotation deduced from a cross-correlation of the Doppler images is weak compared to the Sun ($|\alpha| = \Delta\Omega/\Omega < 0.004 \pm 0.002$), i.e. less than five hundredth of the solar value. Only the evolution of the largest reconstructed spot group can be interpreted as caused by anti-solar differential rotation of the given strength. In this context, anti-solar means that the pole rotates faster than the equator in terms of the angular velocity Ω; anti-solar differential rotation of solar-like stars is not ruled out by fundamental arguments, but it contradics current theoretical predictions.

A study of the time-dependant core emission of the Ca II K line has been carried out for Speedy Mic. It has yielded indications of localized regions of chromospheric activity; there appear to be both stable and transient chromospherically active regions on Speedy Mic. A further study on the basis of the available data is suggested to allow a precise localization of these regions.

Contents

The influence of this eminent body,
on the globe we inhabit,
is so great and so widely diffused,
that it becomes almost a duty for us
to study the operations
which are carried on upon the solar surface.

W. Herschel,
Observations tending to investigate
the nature of the Sun (1801)

Lo duca e io per quel cammino ascoso
intrammo a ritornar nel chiaro mondo
e sanza cura aver d'alcun riposo

salimmo sù, el primo e io secondo,
tanto ch'i' vidi de le cose belle
che porta 'l ciel, per un pertugio tondo.

E quindi uscimmo a riveder le stelle.

Dante, Divina Commedia
(Inferno XXXIV)
In memoriam patris.

Introduction

Motivation and a little history

The basic global properties of stars can be understood by modeling them as radially stratified but otherwise homogeneous "plasma balls" (or "gas balls" as in the title of Emden's pioneering work of 1907). However, already a pinhole projection of the Sun can render spots on its surface which indicate that the Sun is not at all homogeneous on all scales.

Regular systematic observations of sunspots (as carried out by Galilei and others in the seventeenth century) readily reveal that the Sun rotates; performed carefully, they also show that it rotates markedly *non-rigidly*, as apparently first noted by Carrington (1859): The equatorial solar regions perform a complete rotation during about 25 days, higher latitude regions need more than 30 days for that. This phenomenon is called *differential rotation*.

Observations of the Sun at increasingly higher resolution and in a wide range of the electromagnetic spectrum have shown that sunspots are merely one among a variety of transient features on the solar surface; these features are nowadays summarized as *activity phenomena*. Starting out with observations of a Zeeman-splitting of lines in the spectrum of sunspot umbrae (Hale, 1908), the relation of activity phenomena to magnetic fields became clear during the following decades. The idea of dynamo processes operating in the Sun gradually emerged (Larmor, 1919; Parker, 1955; Cowling, 1958; Babcock, 1961); the most conspicuous feature of these dynamo processes is the solar activity cycle with a period of about 22 years. The presumed dynamo processes relate the activity phenomena directly to the "thick" convection zone occupying the outer 30% of the Sun. It appears that only convection under the influence of rotation can supply complex plasma motions required for such a self-sustained stellar dynamo.

Observations of stars other than the Sun have revealed signatures of phenomena apparently similar to solar activity, although in many cases of much greater vigour than on the Sun. However, these phenomena are found to be apparently restricted to stars which are expected, based on models of stellar structure and on observational signatures, to have outer convection zones. This fact considerably substantiates the idea of a magnetic dynamo operating in *solar-like* stars.

Observing surface differential rotation for the Sun as well as other stars is the most direct way to learn about the overall dynamics of their convection zone. In addition, differential rotation appears to be a vital ingredient for the dynamo processes in stars as active or more active than the Sun.

As mentioned above, the Sun is at most a moderately active star. The precise way in which stellar parameters control the "level" of activity is presently not known. However, the rotation period of a star and the depth of its convection zone play a key role in this respect. This is an important motivation for studying fast rotating stars of otherwise similar parameters as the Sun. The study of fast-rotating, but otherwise "solar-like" stars is also related to exploring the Sun's past, because these stars are believed to undergo a substantial rotational slowdown during their early evolution.

A pronounced token of the activity of solar-like stars are cool (and resultingly dark) surface spots. On the Sun, these sunspots are caused by concentrations of magnetic fields inhibiting the convection and hence the energy transport below the solar photosphere. While the behaviour of sunspots is observationally well studied, although at present only

partly understood theoretically, the behaviour, the lifetimes and the structure of non-solar starspots are still poorly known.

Doppler imaging is currently the only method for creating surface images of solar-like stars other than the Sun. Such images allow the study of starspots and, to the (unknown) degree these spots follow the surrounding plasma motions, the observation of differential rotation. The basic idea of Doppler imaging (dating back to the work of Deutsch, 1958) is straightforward: It overcomes the diffraction limitation of direct or interferometric observation methods by making use of information that is modulated into a star's spectrum due to its rotation.

The algorithm described and developed in this work, based on the work of Kürster (1991), is named CLDI (CLEAN-like Doppler imaging). CLDI realizes a framework for Doppler imaging using a rather direct approach and concentrating on the geometric aspects of the Doppler imaging problem.

Working on very fast rotating stars is a well-suited context for such an approach; it makes rotation by far the dominating agent shaping the spectral line profiles through the Doppler effect. In this way the influence of characteristics of individual spectral lines is reduced.

Obtaining undistorted spectral line profiles is a non-trivial task for fast rotating stars: The rotational Doppler broadening makes the lines shallower and tends to introduce overlaps between adjacent lines, called blends. There are two ways to tackle that problem: Either by synthesizing a wide spectral range including (as far as possible) all significant blending lines, or by deconvolving such a spectral range. The latter procedure has been adopted in this work; it has the potential advantage of increasing the signal-to-noise ratio of the resulting profiles due to the averaging involved. The aim of such a deconvolution is to extract a common function (line profile) describing the rotational broadening and spot-induced deformations of the spectral lines.

The algorithm used for spectrum deconvolution in this work is called sLSD (*selective* least-squares deconvolution); it is based on the method LSD introduced into Doppler imaging by Donati et al. (1997b). As an improvement compared to LSD, sLSD is adapted to operating on narrow wavelength ranges, allowing to account for individual characteristics of the averaged spectral lines.

Finally, the main star studied in the context of this thesis, HD197890 (nicknamed "Speedy Mic"), is a highly active, very fast rotating, presumably young solar-like star. Its properties, as well as the high quality of the spectra that could be observed in August 2002 have made it an ideal candidate for this work.

Remarks on the structure of this work

This work is embedded in several thematic contexts; the *prerequisites* (Chapter 1) highlight central aspects of these contexts concerning Doppler imaging. The subsequent chapters appear to require no particular comment for orientation; they describe the observational and theoretical fundament of this work, its methods and its results in about the order just given. A comparison to the results of M. Kürster's work is carried out in Section 5.6.2.

Somewhat unusually, the construction and analysis of the Doppler images of Speedy Mic have been slightly obstructed by the photometric observations which were carried out nearly in parallel with the spectral observations. The reason for this obstruction was a veiling of Speedy Mic's (apparently) true rotation period. This has led to adopting an (apparently) wrong rotation period during a significant time span of the analysis. However, the resolution estimations of Doppler imaging carried out adopting the (apparently) wrong rotation period remain valid (Section 7.5), as a consequence these estimations have only been carried out for one rotation period.

Finally, the *appendix* comprises issues that have not been fully comprehensively treated (Sections 8.3 and 8.4), as well as material that is largely technical in nature (Sections 8.1 and 8.5).

This work is not a tutorial or "cookbook" for Doppler imaging; however, many fundamental aspects are discussed, including a number of practical issues. So it should to some degree be suited as a starting point for working on Doppler imaging; it is explicitly designed to form the basis for potential future work along the lines of CLDI. To make this work a useful companion in practice, rather extensive cross-references and often detailed references to other works have been included.

In order not to disturb the train of thought of the main text, extensively commented references, numerical examples, derivations not of central importance for the main topic and occasional practical aspects have been put into footnotes.

Chapter 1

Prerequisites

This chapter sketches subjects fundamental for the following material. The selection of topics and their treatment is not exhaustive. It is intended to highlight ideas that motivated and guided the work of this thesis.

1.1 Inverse problems

Doppler imaging, like many problems of observational science, is a so-called "inverse problem" (Lucy, 1994). An instructive example of an inverse problem is three-dimensional vision: While it is straightforward to draw a two-dimensional picture of a three-dimensional situation, completely reconstructing the original situation from the picture is in general impossible. The reconstruction requires *a priori information* or assumptions about the situation, e.g. about the relative size of the depicted objects or the illuminating light sources. Several suitable pictures of the same situation may supply this information.

The need of additional information for interpreting the picture is due to the substantial *information loss* during the projection of the original scene onto the the picture. As nicely demonstrated by some optical illusions (e.g. Figure 1.1)[1] the interpretation of a picture depends crucially on the a priori information used. Solution algorithms for inverse problems have to take the named information loss carefully into account.

Inverse problems are often described by an integral equation (cf. e.g. Press et al., 1992), a *Fredholm equation of the first kind*:

$$D(y) = \int_M K(y,x)\, I(x)\, dx \tag{1.1}$$

Solving the equation means determining the function I, given the observed data D and the kernel function K. The integral in Equation 1.1, i.e. the transformation $I \to D$, describes the so-called *forward problem*.

Well-known examples of such equations are deconvolution problems. The "data" results from the convolution of an (unknown) function I with a kernel function $K(y,x) = K(y-x)$. Deconvolution means reconstructing the function I, given the kernel function K.

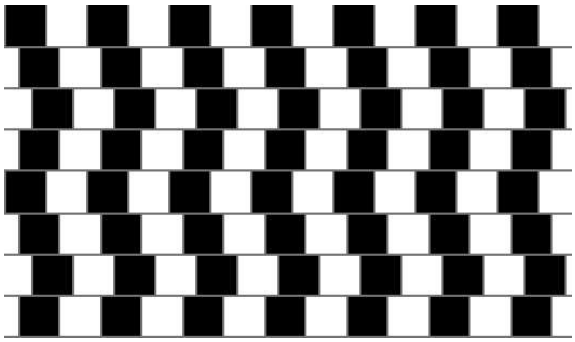

Figure 1.1: Image perception and a priori information: The "Café Wall illusion" (Gregory, 1979). The gray horizontal lines are straight and parallel. Due to a in this case inadequate "algorithm" of the human visual system we do not see them that way.

Many inverse problems are *ill-posed*, and *ill-conditioned*. Ill-posed means that the solution is non-unique. A problem is called ill-conditioned, if its solution sensitively depends on insignificant, small variations of the input data. In physical applications such variations are dominated by measurement noise. For numerical applications they may be introduced by the limited floating-point accuracy of the computations.

The above mentioned information loss of the forward problem makes the inverse problem ill-posed: D does not contain enough information to fully constrain the solution I. Ill-posedness provokes ill-conditioning if the solution algorithm tries to extract this missing information

[1] According to Gregory (1979) the wrong perception of the figure is due to the shape detection "algorithm" (*border locking*) of the human visual system, concentrating on strong luminance contrast edges. The figure is primarily perceived as a set of shapes, the black and white squares. The gray lines fall out of that scheme and are inconsistently attached to the squares. In a way, the figure is wrongly interpreted by the human visual system, due to an incorrect a priori information or assumption. The incorrect assumption is that the small structures of intermediate luminance carry no relevant information.

It is interesting to note that Gregory describes *border locking* as a potential means of getting human image perception more robust in everyday situations.

from irrelevant small-scale variations.

Already the form of Equation 1.1 illustrates, why inverse problems tend to be ill-posed (Lucy, 1994): It usually incorporates a convolution of the function I, modelling the resolution of the observation (e.g. the point spread function). This convolution *dampens* small-scale structures during the transformation $I \rightarrow D$. The reverse transformation $D \rightarrow I$ can be expected to *amplify* small-scale structures (as introduced by noise) of D. Naturally, this ill-posedness worsens, if the forward problem additionally comprises a projection to lower dimension, as in the above example of three-dimensional vision and in the case of Doppler imaging.

After this outline of the mathematical context of Doppler imaging, the following sections present some physical basics of the stellar phenomena which are observable by Doppler imaging.

1.2 Trapped magnetic fields

Dark starspots (in analogy to sunspots) are presumably structures of stellar convection zones induced by concentrations of magnetic fields. The behaviour of magnetic fields in stars is often completely different from everyday experience. Bulk matter motions and magnetic fields are partially tied to one another in a sense described below. The magnetic field lines are said to be "frozen" in the plasma. This behaviour of magnetic fields is crucial for the presumed generation of magnetic fields by dynamo processes in the outer layers of solar-like stars.

Frozen field lines

Given the assumptions of magnetohydrodynamics (MHD) the Maxwell equations and Ohm's law, can be combined into the "MHD induction equation" (Schrijver & Zwaan, 2000; Mestel, 1999)

$$\begin{aligned} \frac{\partial \mathbf{B}}{\partial t} &= \nabla \times (\mathbf{v} \times \mathbf{B}) + \eta \nabla^2 \mathbf{B} \qquad (1.2) \\ \mathcal{O}\left(\frac{\Delta \mathbf{B}}{\tau}\right) &\sim \mathcal{O}\left(\frac{v\mathbf{B}}{\ell}\right) + \mathcal{O}\left(\frac{\eta \mathbf{B}}{\ell^2}\right) \end{aligned}$$

Here $\mathbf{B}$ is the magnetic field strength, $\mathbf{v}$ is the plasma velocity and $\eta = c^2/4\pi\sigma$ is the magnetic diffusivity, determined by the electric conductivity σ. In the second equation, τ and ℓ designate "characteristic" length and time scales of the system considered.

On the right hand side of Equation 1.2 the local rate of change of B is expressed as the sum of magnetic field strength advected by the plasma motion and that lost by diffusion due to the conductivity of the medium. Analogous to the Reynolds number measuring the diffusion of momentum relative to advection terms in fluid motion (Acheson, 1990), the magnetic Reynolds number can be defined:

$$\mathcal{R}_\mathrm{m} \equiv \frac{v\ell}{\eta} = \frac{\frac{v}{\ell}}{\frac{\eta}{\ell^2}}$$

For $\mathcal{R}_\mathrm{m} \gg 1$ the diffusion term can be neglected in Equation 1.2 and the magnetic field lines are "frozen" in the plasma motions.

This freezing of magnetic fields is typical for stellar interiors and atmospheres: The large scales usually involved, in conjunction with the relatively high electrical conductivity of the stellar plasma make $\mathcal{R}_\mathrm{m} \gg 1$ mostly a good approximation there.

Magnetic flux tubes

The interaction of plasma motions and magnetic fields presumably leads to the formation of magnetic flux tubes in convective flows. The flux tube model explains the highly localized and organized structure of magnetic fields observed in the solar upper convection zone and the photosphere. It also explains much of the observed behaviour of sunspots. Flux tubes are further discussed in Section 2.1.2

1.3 Convecting shells in rotation

In a rotating sphere of highly viscous material, all points have the same angular velocity Ω around the rotation axis. Such *rigid rotation* is not "enforced" a in gaseous or fluid sphere of low viscosity. In this case, rigid rotation is usually not an equilibrium situation. *Differential rotation* is the result, i.e. Ω is not constant, but a function of latitude and depth.

As L. Biermann (1951) demonstrated, *rigid rotation in a gaseous sphere occurs if and only if the motions inside the sphere are isotropic* (as inside an isothermal sphere). Any deviations from this isotropy, e.g. by convective motions, result in meridional flows (Biermann, 1948)[2] and differential rotation.

An example of meridional flows and differential rotation is close at hand: The large scale circulations and wind belts on the Earth. For slow rotation and without surface inhomogeneities (like oceans and continents), the atmosphere of each terrestrial hemisphere would presumably contain one large cell of meridional circulation (currents directed north-south). Due to the different solar irra-

[2] The manuscript was actually submitted 1944, but due to the historic circumstances not directly published. This took place 1948, after the manuscript had been revised by Biermann at the Hamburger Sternwarte.

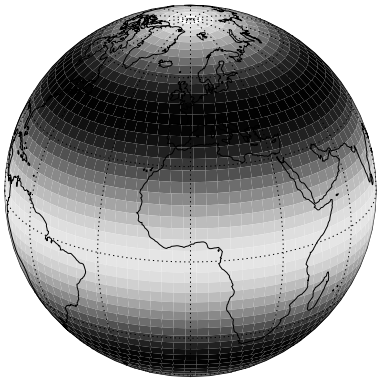

Figure 1.2: Schematic illustration of global wind direction belts of the Earth's atmosphere. Bright and dark regions indicate preferred east and west wind zones respectively. They correspond roughly to the large atmospheric circulation cells, named Hadley (near equator, responsible for the trade-winds), Ferrel (mid-latitudes, causing the "Westerlies") and polar cells.

diance, these cells would be driven by warm air rising up at the equator and sinking down at the poles.

In the presence of rotation (and oceans), the circulation on each hemisphere, much simplified, is split up into three convective cells (Weischet, 1977). Due to the Earth's rotation these circulations are subjected to Coriolis forces. This causes the latitude belts of alternating east-west preferred wind directions observed on the Earth (Figure 1.2).

Fortunately, conditions on the Earth are in nearly every respect very different from those on stars. However, as the complex circulation patterns of the Earth's atmosphere and oceans control the terrestrial climate, the equally complex circulation patterns in stellar convection zones profoundly influence the physical conditions encountered there. Differential rotation as part of these circulations, in conjunction with smaller scale turbulence, is presumably vital for the operation of the solar dynamo (Section 2.1.1).[3]

For stars of several solar masses, strong rotation is believed to significantly influence their evolution (Maeder & Meynet, 2000). Since the convection zone in solar-like stars is located far from the core (in about the outer $0.3\,R_\odot$ in the Sun) and contains only a small fraction of their total mass (about 1.5% for the Sun; Foukal, 1990, Ch. 6.4), a less pronounced influence of rotation on their evolution may be expected. However, this question is presently not settled (Pinsonneault, 1997). As outlined in the introduction of Chapter 2 the influence of rotation during star formation and early evolution is undoubtedly large (cf. Gray, 1988, p. 5-13, for a cartoon on this).

[3] Citing Gilman (1979, p. 20): "Differential rotation is from a fluid dynamical point of view a very important quantity to know about a star. It is possibly the key to guessing its overall global dynamics."
This citation must be seen in context: Here "dynamics" focusses on the star's *hydro*dynamics. In addition, it is important to keep in mind that the *surface* differential rotation is only a "surface projection" of the three-dimensional rotation law (which is currently only known for the Sun). However, this surface projection yields (albeit only indirect) information about the interior hydrodynamics of a star which is otherwise largely hidden below the surface convection for late-type stars.

1.4 The solar-stellar connection

The term "solar-stellar connection" appears occasionally in publications related to stellar astrophysics. It is related to the rather peculiar observational situation of stellar astrophysics, similarly encountered in other astrophysical fields. Stellar astrophysicists, aiming at understanding and modelling the physical nature of stars, have an extended observational basis of one individual case, the Sun, and a much coarser observational knowledge of a large amount of other stars, at least a factor of 10^5 farther away from the Earth.

On the one hand, the Sun is possibly not a bad starting point for understanding other stars. In the words of Christensen-Dalsgaard (2003), p. 288:

> *"In many ways, it is difficult to imagine a star simpler than the Sun; it is relatively unevolved, it has no convective core complicating the modelling of the evolution of the abundance profile, it rotates comparatively slowly, and the physical conditions, as far as microphysics is concerned, are rather benign ..."*

On the other hand this obviously means that solar observations do not directly yield information about the influence of the wide range of stellar parameters observed in other stars. Citing Giampapa (1990),

> *"Quantities such as rotation rate, depth of the convection zone, surface gravity, effective temperature and evolutionary status can take a wide range of non-solar values, stretching models far beyond any familiar territory".*

Following the often apparently successful general procedure of physics, models of solar physics are used as a "seed" for models of other stars. As Figure 1.3 nicely reminds us, this and other simplifying assumptions should be kept in mind.
Two issues of this context are of special interest for this work:

- "Starspots"
  A critical discussion of sunspots as prototypes for starspots is given by (Schrijver, 2002); see also Section 2.1.2.

- Models of non-solar rotation
  See e.g. Rüdiger et al. (1998) and Stix (2002a); see also Section 2.2.2.

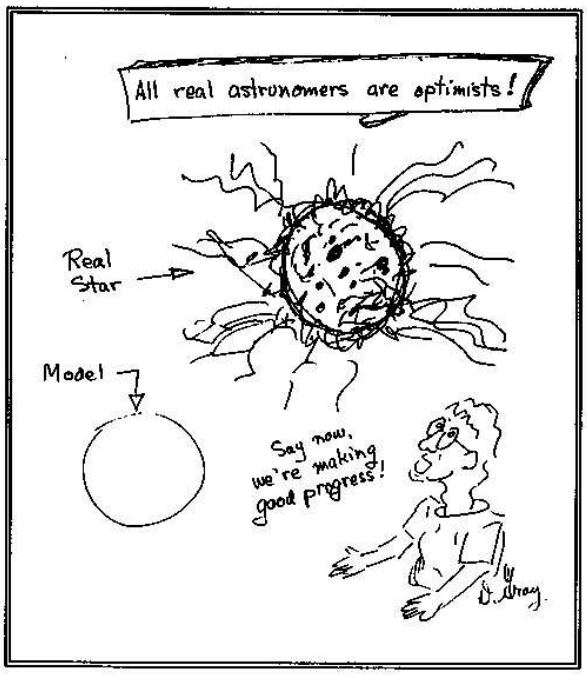

Figure 1.3: David Gray on the complexity of stellar activity phenomena, reproduced from Gray (1988, p. 1-34). See Strassmeier (1997, Fig. 9.20) for another cautioning cartoon. After all, most of our knowledge about stars is indirect.

Chapter 2

Solar-like stars

This work is concerned with "ultrafast rotating solar-like" stars. This is partly a paradox, because the Sun is a comparatively slowly rotating star. However, its rotation suffices to markedly influence the dynamics of its convection zone (Section 2.2); in that sense the solar rotation is fast (e.g. Durney & Spruit, 1979, Sec. Ib) .[1]

Since the angular velocity of the Sun is about two orders of magnitude lower compared to some other objects of similar spectral type, another term is needed. Probably that is how the term *ultrafast rotator* found its way into the literature (e.g. Soderblom et al., 1993b). Since there is no generally accepted definition of "ultrafast", in the context of this work it could be replaced by "a late-type star whose spectral line broadening is by far dominated by rotation" (see Section 5.4 and Reiners, 2002). As outlined below, this is presumably connected to qualitative changes in the physics of the star. For a star of similar spectral type as the Sun this means objects whose projected rotational velocity satisfies $v \sin i \gtrsim 50 \,\mathrm{km\,s^{-1}}$. Naturally, this is just a rule of thumb, the $v \sin i$ of the objects studied in the context of this work even exceed $100 \,\mathrm{km\,s^{-1}}$ (requiring a rotation period below 0.5 days for a star of solar radius).

"Ultrafast" rotation

Such fast rotation for stars close to solar spectral type is expected for objects much younger than the Sun (e.g. Tassoul, 2000, Chs. 1&7). Solar-like stars appear to undergo rapid braking (during time scales of several 10 Myr, Keppens et al., 1995) before and during their early main sequence evolution. This braking is presumably caused by the magnetic field of the star coupling to surrounding material (of an accretion disk and/or self-ejected, Schatzmann, 1962). The early phase of rapid braking is apparently followed by less vigorous braking during main sequence evolution (at an age $\gtrsim$ 1 Gyr) (Skumanich, 1972; Schrijver, 2002, Ch. 13), caused by the stellar magnetic field coupling to the stellar wind.

[1] Centrifugal forces on the Sun are small compared to gravitation, but its rotation period is of similar order of magnitude as the presumed convective turnover times. In the former sense the Sun is a slow rotator, in the latter sense it is not.

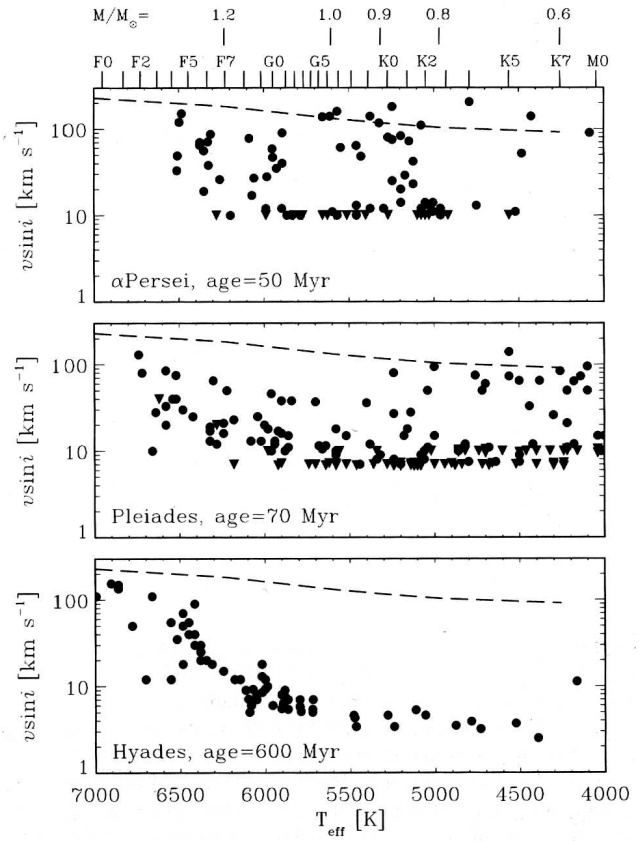

Figure 2.1: Projected equatorial rotational velocities vs. effective temperature, observed in open clusters (reproduced from Schrijver & Zwaan, 2000). Triangles are upper limits. The dashed curve is the extrapolation of a semi-analytical expression for the total stellar angular momentum J as a function of stellar mass M ($J \propto M^{2.02}$), approximately valid for $1.5\,\mathrm{M}_\odot \lesssim \mathrm{M} \lesssim 20\,\mathrm{M}_\odot$ (Kawaler, 1987, Sec. IV).

As suggested by observations of stellar clusters, only a small fraction of stars (about 20% for the Plejades, according to Soderblom et al., 1993a) go through the state of ultrafast rotation. This trend is visible in Figure 2.1; reasons for it are presently not well understood. According to Tassoul (2000, p. 204), there is "compelling evidence that saturated magnetized stellar winds, structural evolution, and core-envelope decoupling are the main agents determining the rotational history of a low-mass star [...] how-

ever, the effects of disc regulation [due to magnetic coupling] during the PMS (pre main sequence) phase should also be taken into account". Possibly, much of the later rotational evolution of a solar-like star is already determined during its T Tauri phase (i.e. at an age $\lesssim 10\,\mathrm{Myr}$), by the presence and details of its circumstellar disc (Edwards et al., 1993; Eaton et al., 1995; Choi & Herbst, 1996).

As already mentioned, ultrafast rotation presumably leads to qualitative changes in behaviour, compared to moderate rotation. Possible changes are dynamo saturation (e.g. Baliunas et al., 1995; Patten & Simon, 1996; Schrijver & Zwaan, 2000), saturation of (near) surface magnetic fluxes (e.g. Saar, 1996) and a potentially different regime of turbulence in the convection zone (S. Brun, priv. comm.). This must be kept in mind for comparisons with solar results.

In summary, the term "solar-like star" in the context of this work is used for dwarf stars of spectral type G and K; other terms found in this context are "low-mass" or "early-type" stars. So a star is considered solar-like irrespective of its rotation and age (but not including relevantly evolved stars). These stars have convective envelopes associated with a dynamo, the generated magnetic fields are presumed to be the main reason for their observed activity phenomena.

2.1 Magnetic activity

2.1.1 The dynamo problem

As discussed in Section 1.2, any magnetic field in a plasma of finite conductivity and/or in turbulent motion will vanish sooner or later due to diffusion and local reconnection. The timescale of field dissipation τ due to diffusion can be estimated from the rightmost term in the sum of Equation 1.2 as $\tau \approx \frac{\ell^2}{\eta}$. For the conditions encountered in sunspots close to the surface, it would be of the order of a few years (e.g. Kippenhahn & Möllenhoff, 1975 § 11). This estimated dissipation time, valid for diffusion alone, is reduced by the presence of turbulence.

The mean solar magnetic diffusivity is a few orders of magnitudes lower than at the surface of sunspots. However, if the linear dimensions of sunspots are taken as roughly comparable to magnetic flux concentrations deeper in the solar convection zone (SCZ), the resulting lifetimes of magnetic fields in the SCZ are much shorter than evolutionary timescales of solar-like stars of the order of 10^9 years. Consequently, mechanisms regenerating the magnetic fields on the Sun and other magnetically active stars are needed. Formulating a consistent model for this magnetic field generation is called the dynamo problem.

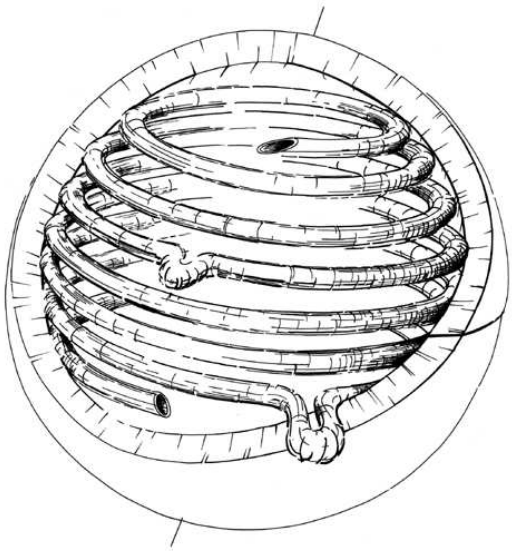

Figure 2.2: Schematic illustration of the nowadays presumed behaviour of magnetic flux tubes in the Sun: Storage in the overshoot layer below the SCZ proper, shearing by differential rotation and instabilities caused by convection and buoyant bulging after entering the SCZ.

It turns out, that a rather complex geometry of currents is needed to sustain a stellar dynamo. The main mechanism generally accepted to be active in the Sun is called the $\alpha\Omega$-dynamo (Parker, 1955). Figures like 2.2 are sometimes used to illustrate this type of dynamo; it sketches the emergence of flux tubes to the photosphere as well as their stretching and winding up by the differential rotation (Babcock, 1961). Such an illustration has its merits, but also conceals some relevant aspects. Far from a comprehensive discussion (found e.g. in Mestel, 1999), the following sections aim at showing up the basics of the mechanisms presumed to underlie the solar dynamo and their relation to differential rotation.

The presumed fundamental pattern of a solar-like dy-

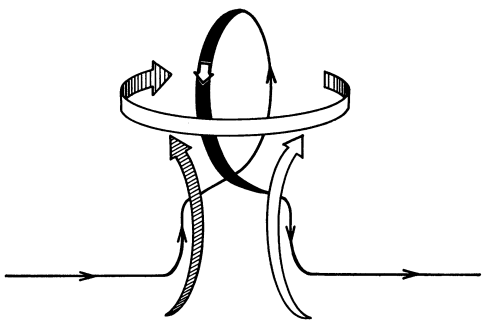

Figure 2.3: Illustrating the plasma motions responsible for the α-effect (Parker, 1970): Upward bulging, expansion perpendicular to the upward motion and twisting due to Coriolis forces caused by the expanding motions.

namo is the transformation of a poloidal field, i.e. a dipole field with field lines roughly in meridional planes, into a toroidal field and vice versa. These transformations are performed by the so-called $\alpha-$ and $\Omega-$ mechanisms.

The Ω mechanism

In the presence of differential rotation, a poloidal field locked to the plasma motions will be sheared as sketched in Figure 2.2; this shearing results in the required toroidal component of the field. This is called the Ω mechanism. Present models of the solar dynamo locate it (mainly) in the boundary layer between the solar core and the convection zone, the so-called tachocline (e.g. Schrijver & Zwaan, 2000, Ch. 7&15). Here the strong *radial* gradients of the radial velocity supply the shear needed for the Ω mechanism (in contrast to the latitudinal shear visible in Figure 2.2).

The α mechanism

While the Ω mechanism requires *differential* rotation, the α mechanism is independent of it. It is caused by the interplay of convection and rotation, rigid or not.

The fundamental geometry of the α mechanism is shown in Figure 2.3: An initially "locally straight" magnetic field is shown at the bottom of the figure. A blob of matter rising radially outward expands due to the pressure gradient. The lateral motions (i.e. perpendicular to the radius) caused by this expansion are deflected into a "twirling" motion by the Coriolis force. If the field lines are locked to the described plasma motions, the depicted field loop is formed from the initial field. Associated with this field loop is a current antiparallel to the initial field. This current can be used for generating a field parallel to the initial field, i.e. to amplify it (for the basic idea, cf. Fig. 14.2 of Kippenhahn & Möllenhoff, 1975).

The generation of this current is slightly subtle. It is caused by an additional term in the MHD form of Ohm's law for mean fields. In the mean field approximation, all quantities are expressed as the sum of a time-independent component and a varying component $j = \bar{j} + j'$, the bar indicating the mean, the prime indicating the varying component respectively. The mean of the variable component is vanishing. $\overline{j'} = 0$.

Taking the mean of Ohm's law,

$$\mathbf{j} = \sigma \left(\mathbf{E} + \frac{1}{c} \mathbf{v} \times \mathbf{B} \right) \tag{2.1}$$

one gets

$$\begin{aligned} \overline{\bar{\mathbf{j}} + \mathbf{j}'} &= \sigma \overline{\left[\bar{\mathbf{E}} + \mathbf{E}' + \frac{1}{c} (\bar{\mathbf{v}} + \mathbf{v}') \times (\bar{\mathbf{B}} + \mathbf{B}') \right]} \\ \bar{\mathbf{j}} &= \sigma \left[\bar{\mathbf{E}} + \frac{1}{c} (\bar{\mathbf{v}} \times \bar{\mathbf{B}}) + \frac{1}{c} (\overline{\mathbf{v}' \times \mathbf{B}'}) \right] \end{aligned} \tag{2.2}$$

For an explanation of the symbols see Equation 1.2. If $\mathbf{v}'$ and $\mathbf{B}'$ were uncorrelated, one could write $\overline{\mathbf{v}' \times \mathbf{B}'} = \overline{\mathbf{v}'} \times \overline{\mathbf{B}'} = 0$. But that is in general not the case, since the changes of $\mathbf{B}$ and $\mathbf{v}$ are correlated via the MHD-equations (e.g. Equation 1.2). Consequently, the corresponding term in Equation 2.2 can be non-vanishing. This is the case for anisotropic flows like convection under the influence of Coriolis forces (Mestel, 1999). The resulting mean current can amplify the initial magnetic field - this is the α mechanism.

Dynamo types

The Ω mechanism, fed by differential rotation, can only convert poloidal into toroidal fields, not the reverse. Since the α mechanism can do both, a dynamo operating primarily ($\alpha^2\Omega$-dynamo) or solely (α^2-dynamo) on the α mechanism is conceivable. Beside stellar dynamos driven by large scale motions (of $\alpha^x\Omega$-type), α^2-models of dynamos can be driven by small scale turbulence alone, i.e. independent of differential rotation. However, they are currently not believed to produce the field strengths observed in stars as active or more active than the Sun.

Current models of the solar dynamo, although yet far from a complete modelling, indicate that the strong, large-scale solar magnetic fields are generated by a $\alpha\Omega$-type dynamo, associated with the solar cycle (Schrijver & Zwaan, 2000, Ch. 7).[2] An $\alpha\Omega$ dynamo needs strong gradients of the angular velocity at least in parts of the convection zone; hence it depends on differential rotation.

2.1.2 Sunspots and starspots

Stars other than the Sun exhibit dark surface regions, apparently correlated with localized magnetic features (e.g. Solanki, 2002). In analogy to sunspots, they have been named starspots. Their existence can be inferred from periodic brightness variations caused by rotational modulation (Hall, 1991), possibly from disk integrated measurements of stellar magnetic fields (Saar, 1996), from

[2] Following Durney (1993) and others, Schrijver & Zwaan propose that the (relatively weak) solar small-scale magnetic fields, e.g. the photospheric internetwork field, are partly generated by small-scale "turbulent" dynamo processes.

Table 2.1: Continuum intensities of sunspots, as well as of observed and tentative starspots, relative to the undisturbed photosphere. The temperatures for LQ Hya are taken from Saar et al. (2001). Note that the intensity contrasts are estimates, calculated for black bodies of the given temperatures.

Intensity:	total	specific at 6000Å	7000Å
Sunspot umbra :			
3950 K vs. 5780 K			
	22%	14%	19%
Starspots :			
3640 K vs. 5180 K (LQ Hya)			
	24%	14%	18%
4200 K vs. 5200 K (tentative spot on K0V)			
	43%	33%	39%
4700 K vs. 5200 K (tentative spot on K0V)			
	67%	61%	65%

the presence and analysis of molecular lines (Berdyugina, 2002) as well as optical and magnetic Doppler imaging studies (e.g. Donati et al., 1999). However, in which respects and to what extent starspots are analogous to sunspots is not strictly known at present.

Unsolved key issues of starspot observations and physics are discussed in Hall 1996 (with the suggestive title "What we don't know about starspots") and Schrijver (2002, especially Tab. 1). They include: Energy flow, relation to magnetic features,[3] lifetime, fine structure, relation to spectral type and other stellar parameters. While the knowledge of starspots is characterized by comparatively few observational facts, for sunspots the difficulty is partly selecting from the variety of known attributes those of primary importance for their understanding (Stix, 2002, "Sunspots: What is interesting ?").

In the context of this work, the term "spot" is used for regions of the stellar surface emitting a considerably lower continuum intensity than the surrounding "undisturbed" or "unspotted" photosphere. This is the only assumption about starspots indispensable for interpreting the line profile deformations used for the construction of the presented Doppler images.

Individual sunspots show a considerable homogeneity and similarity of many properties, as outlined below. This homogeneity suggests them to be a kind of "second equilibrium state of the solar mantle" (Zwaan, 1968). However, at present it is largely unknown what parameters of the solar convection zone and dynamo control the properties of this "second state". Also, the values of such parameter candidates (e.g. the size and lifetime of convection cells, properties of subsurface magnetic features) are only partially known.

The motivation of the two-temperature assumption of CLDI (CLEANlike Doppler imaging, see Section 5.1) is the working hypothesis that such a "second state" of starspots with quite well defined properties exists for stars other than the Sun.

The following summary of sunspot features and models is not comprehensive, further material and references can be found in Zwaan (1968), Spruit (1981), Moore & Rabin 1985 (mostly a loose collection of observational facts), Foukal (1990) and Stix (2002).[4] Instead the discussion sketches the currently (mostly) undisputed aspects of the sunspot phenomenon, concentrating on the parameter homogeneity, as well as on formation and decay of sunspots.

Sunspot observational characteristics

A typical sunspot consists of a central dark region (umbra), surrounded by a less dark region (penumbra). The umbral radii range between about 2 and 10 Mm, i.e. up to the order of 1/100 of a solar radius. The penumbra may exceed an outer radius of 25 Mm for very large sunspots, on average the umbra covers 15-20% of the total spot area (Foukal, 1990). Sunspot umbrae and penumbrae are irregularily shaped, spots without a well-developed penumbra occur but are unusual. Spots below the given size are called pores, they do not show a penumbra, they have lifetimes below an hour.

Large sunspots predominantly develop in pairs roughly aligned along solar latitude. These pairs are called bipolar, because they show opposing magnetic polarity. Their orientation depends systematically on the solar hemisphere and on the solar cycle (Hale-Nicholson law).

In spite of the mentioned individual characteristics, umbrae have quite well defined features in common. The magnetic field strength ranges from 2900 ± 400 G $\approx$

[3] It is important to note, that the darkest regions of Doppler images *do not coincide* with the strong magnetic field regions of the corresponding magnetic (Zeeman) Doppler images ("the apparent spatial correlation between brightness and magnetic features is rather weak", Donati et al., 1999, p. 452). This also applies to pronounced dark polar spots.
Whether this is due to the weak polarization signal caused by the low brightness (Solanki, 2002, Sec. 5.1 or Donati et al., 1999, Fig. 16), or reflects a truly different physical nature of the two kinds of regions is presently unclear. Donati et al. (2003, Secs. 3.1 & 3.2) speculate in favour of the latter alternative, based on different differential rotation amplitudes derived for dark spots and magnetic regions, respectively. However, no such difference of differential rotation amplitude between dark and magnetic features is visible in Donati et al. (1999, Fig. 14).

[4] A more recent review by Thomas & Weiss is scheduled to appear in AR&A in September 2004.

0.29 T for large spots down to 2400±200 G for small spots (Brants & Zwaan, 1982), deviations from these values are rare. Near the umbral center, the magnetic field is vertical within 10°, changing gradually to nearly horizontal in the penumbra. The effective temperature of umbrae is 3950±150 K compared to 5780±15 K for the quiet photosphere. The resulting brightness contrasts, together with rough estimates for exemplary tentative starspots, are given in Table 2.1.[5] Within the given limits, the umbral effective temperatures vary systematically during the solar activity cycle (Albregtsen & Maltby, 1978).[6]

Penumbrae emit on average about 75% of the undisturbed photospheric intensity, 60% in the dark and 95% in the bright filaments (Schrijver & Zwaan, 2000). This corresponds to a mean effective temperature of about 5400 K, considerably higher than the umbral temperature. Because of the intricate and dynamical structure of penumbrae, this value is of little physical significance. It is however useful to illustrate that the *average* intensity deduced from an *unresolved* observation of a sunspot would depend on its umbra to penumbra ratio. It would deviate considerably from the quite well defined values of its umbra and penumbra alone.

Sunspot evolution

Large long-lived (a few weeks, up to a few months in rare cases) sunspots develop as part of "*active regions*" comprising different magnetically induced phenomena and containing several spots (Tab. 4.1 of Schrijver & Zwaan, 2000, gives an overview). Apart from spots, the most conspicuous active region phenomena are faculae, plages, prominences and an enhanced magnetic network; only spots and faculae are directly observable in white light.

Parameters and shape vary considerably between individual active regions, their total magnetic flux ranges from about 10^{20} to 10^{22} Mx. The spots of a "typical large" active region cover $6 \cdot 10^{-4}$ of the visible hemisphere, the associated plages about a factor of ten more (Cox, 2000, Tab. 14.27 & Sec. 14.11.2).

The detailed evolution of an active region is complicated (Schrijver & Zwaan, 2000, Sec. 5.1); however, concentrating on the spots, the following general description holds true (Foukal, 1990, Sec. 8.1.2, see also Meyer et al., 1974, Sec. 5, noting that the role of the supergranulation is less clear in more recent discussions):
A small fraction of the pores of an active region grow into spots and develop penumbrae. During typically a few days these small spots coalesce to form larger spots. The spot group thus formed is roughly east-west aligned and mostly show a marked asymmetry between the the spot(s) preceeding in the direction of rotation ("leader", usually mostly one large) and those following ("follower", usually many and small).

Summing up, large sunspots only form as "leaders" in active regions, i.e. as a part of regions where magnetic flux enters the photosphere from below; they are formed by "collecting" small spots.

The decay of spots in the photosphere is less well understood than their formation; although directly related, it is not equivalent to the removal of magnetic flux from the photosphere (Martínez Pillet, 2002).[7] Basically, the magnetic flux of the spots is dispersed over increasingly large areas, reducing the flux density, finally no longer inducing spots. The dispersal process is markedly different for small spots, decaying by subsequent fragmentation, and large "leader" spots, which mostly "shrink" (Martínez Pillet, 2002; Schrijver & Zwaan, 2000, Sec. 4.1.1.4).

The nature of this shrinking process of large sunspots is presently not understood, it is closely related to the (also unsettled) detailed decay law of spot area or flux as a function of time (Martínez Pillet, 2002, Sec. 3.1). A part of the question is what portion of the magnetic flux is removed from the photosphere inside the spot and how much is transported to the outside via the penumbra.

Sunspot models

The magnetic nature of sunspots was suggested by Hale's observations, showing the Zeeman splitting of spectral lines in spots (Hale, 1908).[8] The basic mechanism inhibit-

[5] These values, calculated for black bodies of the given temperatures, are only rough estimates of the actual quasi-continua. As an example, the ratio of the quasi-continuum fluxes at 6000Å for the synthetic spectra shown in Fig. 6.8 (4000 K vs. 5200 K) is about 23%.

[6] The dependence of the umbral effective temperature on the spot size is still a matter of dispute (Walton et al., 2003). The results apparently depend significantly on the observation method used (e.g. scattered light corrections). However, inspecting Fig. 2 of Walton et al., their measure of "spot contrast" only shows a weak dependence on spot size for large spots ($\gtrsim$ 500 μhemispheres), quite in accordance with the results of Albregtsen & Maltby (1981).

[7] The mechanisms of flux removal from the photosphere are not further discussed here (see Schrijver & Zwaan, 2000, Sec. 6.4); citing Martínez Pillet (2002, p. 342): "The exact active region flux removal mechanism is still a mystery".
However, at least for the Sun with its alternating magnetic polarity patterns during the activity cycle, flux needs to be removed from the convection zone. Citing (Schrijver & Zwaan, 2000, p. 170): "We can only picture such an ultimate removal of strong-field magnetic flux through a chain of processes transforming the strong field into a weak field, grinding the weak field by convection to smaller and smaller scales, so that it eventually can be destroyed by ohmic dissipation".

[8] Although Hale proposes an (in retrospect wrong) vortex (or "cyclonic") model for sunspots, his conclusions are still worth reading today. It is interesting, although fully understandable, that he notes the "apparent constancy of the field strength [...] in different spots" as a possible "weak point" of his interpretation of the spectral features as Zeeman-splittings induced by magnetic fields (Hale, 1908, p. 341).

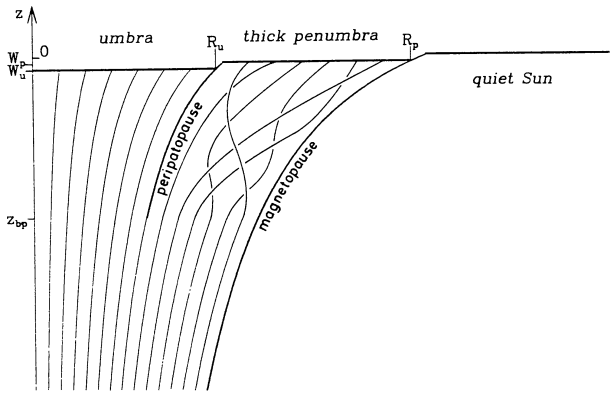

Figure 2.4: Schematic sketch of a sunspot, illustrating the tentative *interchange convection* in the penumbra. The thin lines represent magnetic flux tubes. Figure reproduced from Schüssler (1995), it is due to Jahn & Schmidt who apparently did not publish it in this form.

ing the heat flux below a sunspot has been put forward by Biermann (1941): Due to the coupling of plasma motions and magnetic fields described in Section 1.2, the overturning motions of convection, transporting most of the energy flux, are severely inhibited by the strong magnetic fields in umbrae and penumbrae (Foukal, 1990, p. 262).

At present, no coherent overall model of sunspots is available (e.g. Solanki, 2002, and references therein). Nowadays many observations apparently favour cluster or "spaghetti" models of sunspots proposed by Parker (1979). They conjectures that the magnetic subsurface field of a sunspot is composed of many thin flux tubes instead of a thick monolithic structure. Such a "spaghetti" composition would possibly allow for the remaining convection observed in the umbra (*umbral dots*). However, it is not necessarily required to model this convection (Weiss, 2002).

The penumbra appears as a kind of interface between the umbra and the quiet photosphere. In contrast to the nearly vertical field in umbrae it is characterized by strongly inclined fields. Since freely overturning convection is suppressed by the strong magnetic field, other convection processes take over (Hurlburt et al., 2000). A suggestive mechanism has been proposed by Jahn & Schmitt, called *interchange convection* (Schüssler, 1995), it is illustrated in Figure 2.4. The plasma in magnetic flux tubes in the penumbra is heated at the boundary between the penumbra and the quiet surface (the *magnetopause*). These flux-tubes become buoyant and more vertical, stopping at the umbra/penumbra boundary (the *peripatopause*); see Solanki (2002) and Weiss (2002) for comments and further references.

Meyer et al. (1974, Sec. 5) proposed that long-lived sunspots are stabilized by annular (i.e. toroidal) subsurface convection cells. This idea has been supported by recent helioseismic observations (Zhao et al., 2001, Fig. 3) and (yet rather simplified) MHD model calculations (Hurlburt & Rucklidge, 2000a, Fig. 8).

In Hurlburt & Rucklidge's models such a stable toroidal cell is only formed after a long transient phase, they suggest that only a fraction of large spots reach this phase, thereby forming long-lived spots.

Surfacing flux tubes

In spite of the not yet well understood structure of sunspots, there is a successful model describing the magnetic field configurations generating them: The flux tube model. Interpreting sunspot groups as flux tubes piercing the photosphere (Parker, 1955a) can explain the emergence latitudes of spots, the observed tilt of bipolar groups, the asymmetry of follower and leader spots with respect to rotation and the typical motion of spots after their appearance (Caligari; Moreno-Inertis & Schüssler, 1995). In addition, the flux tube model allows predictions for stars rotating faster than the Sun. The following discussion follows closely that of Schüssler (1995).

A magnetic flux tube is a bundle of magnetic field lines surrounded by a thin surface current sheet, separating it from its nonmagnetic surroundings. Flux tubes can be formed by concentrating the magnetic flux contained in a plasma in eddy-like motion (Cattaneo & Hughes, 1988; Kippenhahn & Möllenhoff, 1975). Once formed, the interaction of a flux tube with its surroundings is mostly hydrodynamic, it behaves much like a buoyant rubber string avoiding the eddies. The dominant forces acting on the flux tube are buoyancy (Parker, 1955a), Coriolis forces and magnetic curvature forces trying to straighten it.

A flux tube in thermal and mechanical equilibrium with its environment is buoyant, because the gas pressure, correspondingly the plasma density, is lower inside than outside. The gas pressure difference arises because the total pressure (including magnetic pressure) is equal inside and outside. In this picture, the flux tubes containing the magnetic flux supplied by the dynamo are stored in the subadiabatically stratified layer below the convection zone proper, where the convective downstreams overshoot into the radiative core. The stored flux tubes are stretched by differential rotation, thereby increasing their inner field strength, until they become unstable and form "bulges" (Schüssler & Solanki, 1992). If such a bulge enters the nearly adiabatically stratified convection zone, it will rise to the surface. If the initial field strength suffices (requiring flux densities of the order of $10^5\,G$ inside the overshoot layer, which complies with the threshold estimated for the "bulge instability" named above), flux tubes are expected to remain stable until they emerge at the photo-

sphere, forming bipolar spot groups.

The emergence latitude of the flux tubes is governed by the balance of buoyancy forces, directed radially outward, and Coriolis forces, directed inward, perpendicular to the axis of rotation (Schüssler, 1995, p.20). The Coriolis force arises, because angular momentum conservation leads to a flow *against* the direction of rotation in a rising flux tube. This model can be extended to faster rotating stars, and appears as a promising step towards modelling some emergence characteristics of starspots (cf. Granzer, 2002, and references therein; note that his models do not incorporate meridional flows which may play a significant role).

Starspot temperatures

Any method measuring starspot temperatures has to deal with the difficulty, that the spot extension (filling factor) and contrast information are "intermingled" for surface integrated observations.

Combining several temperature indicators with significantly different temperature dependencies can in principle separate the filling factor and contrast information e.g. Catalano et al., 2002. Particularly molecular features appearing only (or mostly) in the spectra of the cool spots are promising indicators. Also multicolour photometry time-series can be used (e.g. Vogt, 1981; Olah et al., 2001).

However, such measurements of spot temperatures T_S or temperature contrasts to the quiet photosphere $T_Q - T_S$ require substantial assumptions about the atmospheric conditions of the spots; also a significant contribution of e.g. faculae could influence the results (the correlation of other activity phenomena with spots on stars other than the Sun is still unclear, see references in Schrijver 2002, Sec. 5). In addition, rotation induced Doppler shifts of spectral features of spots may hamper such methods, making simultaneous Doppler imaging necessary for fast rotators (Berdyugina, 2002, Fig. 4) .

Saar et al. (2001) present a concise discussion of their method, using TiO bandheads (7050 Å and 8860 Å) in combination with B-V and R-I_C photometric colours. Saar et al. give their determined T_Q and T_S for 11 stars, with temperature contrasts in the range of 600-1900 K. However, the correlation of their T_S with T_Q (and the Rossby number) appears yet inconclusive (see also O'Neal et al., 1996, Fig. 9). Also, an earlier claim of nonuniform starspot temperatures for the RS CVn star II Peg (O'Neal et al., 1998, Fig. 2) seems not fully conclusive.

Starspot lifetimes

As illustrated by the above discussion, the detailed processes of sunspot formation and decay are presently not well understood; this makes theoretical predictions about the behaviour of non-solar spots difficult.

Only strongly active stars (apart from the Sun) are accessible to current observation methods for spot signatures. To what degree the spot evolution on those stars is characterized by a rather continuous dissipation and new appearance of magnetic flux or by an ongoing reorganisation of flux, possibly supplied by long-lived subsurface magnetic structures, is presently not known.[9]

In contrast to the Sun, for long-lived starspots with large latitude extent, differential rotation enters as a lifetime limiting agent: Large spots are sheared apart in the presence of sufficiently strong surface differential rotation (e.g. Strassmeier et al., 1994, Fig. 5). What role this shearing plays in the above context of reorganisation, dissipation and potentially persistent magnetic subsurface patterns is presently not known.

Observational results on spot lifetimes are yet of rather singular nature, concentrating on a few well-observed objects (Hussain, 2002); reliable short-term studies, only covering a few rotations are very rare. Some representative results are collected in the following.

For the long-period RS CVn binary HR 7275 (K1 IV, P=28.6 days), Strassmeier et al. (1994) photometrically deduce spot lifetimes of several, up to a few dozen rotation periods[10] without an obvious correlation with spot size. From an "upper envelope lifetime" decreasing with spot size, Strassmeier et al. deduce an upper limit for the surface differential rotation of HR 7275. However, simulations studying lightcurves of complex spot patterns with random (statistically defined) lifetimes and sizes, suggest that some caution is in order when interpreting lightcurves alone, strongly depending on the sampling (Eaton et al., 1996). Also the results of Vogt et al. (1999, Sec. 4.2) indicate that in this context the significance of photometric studies alone may be limited.

For the considerably shorter period RS CVn binary HR 1099 (=V711 Tau, K1 IV, P=2.8 days) Vogt et al. (1999) observe a *polar spot* in their Doppler images which persisted over the whole observation timespan of 11 years. Some other spots of HR 1099 appear to have

[9] Such long-lived subsurface structures are suggested by "active longitudes" (or "flip-flop" spot configurations alternately switching between them) apparently observed on some stars. See e.g. Korhonen et al. (2001) for the single giant star FK Com (G4 III, P=2.4 days).

[10] The spot lifetimes of Strassmeier et al. for HR 7275 range roughly between 100 and 1600 days. Using the the convective turnover time values of Gunn et al. (1998, Fig. 3) yields a convective turnover time of the order of 100 days for HR 7275. So the above lifetimes translate into a few, up to of the order of ten convective turnover times.

lifetimes of the order of one year (Vogt et al., 1999, Fig. 86).

For estimating spot lifetimes from the comparison of Doppler images (especially on small- and intermediate scales), the phase coverage and total timespan of the underlying observations must be taken into account (cf. e.g. Hussain, 2002, Figs. 9 & 10 for a problematic example).

For the intensively studied apparently single star AB Dor (K0V, P=0.51 days) only the polar spot appears to survive timespans of years (e.g. Donati et al., 1999, Fig. 15). Other spots, extending several 10° on the surface persist longer than about 5 days (Donati & Collier Cameron, 1997a; Donati et al., 1999, Figs. 8-9 & 4-6, respectively). Spots of approximately 10° size (close to the Doppler imaging resolution) seemingly appear and decay on similar timescales. Summing up, the lifetimes of intermediate-sized spots on AB Dor appear to be bounded by the lower limit of a few days and the upper limit of about a year. Results of starspot lifetimes between those limits are very sparse, for example two images of the apparently single star He699 (G3V, P=0.49 days, Barnes et al., 1998), taken 30 days apart (and showing few well-defined features apart from the polar spot), suggest lifetimes below a month for intermediate size non-polar spots.

Starspots as tracers

As discussed in the next Section, *sun*spots are very close tracers of the near-surface plasma differential rotation. On the other hand, sunspots do not significantly follow the (slow) meridional flows. It appears reasonable to assume that this is due to the balance of "rigidity" of the underlying magnetic structures on the one hand and the surrounding plasma motions on the other. Assuming further that these underlying magnetic structures are flux tube loops, roughly aligned parallel to the (local) direction of rotation, this rigidity is possibly anisotropic.

How this balance of magnetic structure rigidity and plasma flows is altered for magnetic filling factors and total fluxes much larger than solar values, is presently not known. Following the above line of thought, higher magnetic fluxes of individual features presumably lead to increased rigidity. Additionally, larger filling factors should lead to an increased influence of magnetic structures on the global plasma flows. In summary, starspots presumably become increasingly poor tracers of plasma motion (and possibly "disturb" them) for stars with increasing total magnetic fluxes .

For the case of HR 1099, a few prominent recurrent spots show indications of differential rotation and some poleward migration (Vogt et al., 1999, Fig. 86). The deduced corresponding differential rotation is much weaker and of opposite sign compared to the solar case ($\alpha \approx -0.003$ compared to $\alpha \approx +0.2$ for the Sun, see Equation 2.6 for a definition of α).

However, Vogt et al. suggest that the large spots on HR 1099 show a closer resemblance to solar *coronal holes* (cf. e.g. Schrijver & Zwaan, 2000)than to sunspots. Basically, this suggests that their (weak) differential rotation and meridional motion is dominantly influenced by the global stellar magnetic field (Vogt et al., 1999, Secs. 4.5 & 4.7-4.8), instead of the underlying plasma motions. As implied by its persistent polar spot, for HR 1099 this global field may contain a strong dipole component, roughly aligned with the rotation axis.

While for HR 1099 it is unclear whether its spots significantly follow photospheric plasma flows, the spot evolution on AB Dor on timescales of a few days is definitely suggestive of a differential rotation similar to the near-photosphere solar plasma (although much weaker with $\alpha \approx 0.004$, cf. Donati & Collier Cameron, 1997a, Fig. 15; Donati et al., 1999, Fig. 14, and Donati et al., 2003, Fig. 2).

2.2 Stellar rotation

Strictly rigid rotation is not expected in the convection zone of a rotating star (Section 1.3). Instead, large scale flows are superimposed on smaller scale convective motions. The flow components roughly parallel to the equatorial plane are observed as *differential rotation*, they make the angular velocity Ω depend on latitude and depth. Flows in planes containing the axis, less prominent in the solar case, are called *meridional flows*.

These flows, as well as other mechanisms transport angular momentum in the rotating stellar convection zone. All angular momentum flows eventually establish an equilibrium. In the case of negligible viscosity, this equilibrium would tend towards a state of constant specific angular momentum throughout the star (Gilman, 1979, p. 21).

While molecular viscosity is negligible in the Sun, "turbulent viscosity" (and Reynolds stresses), caused by the interaction of turbulent eddies, is not. While isotropic viscosity would tend to equalize angular velocities, the behaviour of the generally anisotropic turbulent viscosity (which is an approximation for the transport processes of the convective turbulence) is more complex. Depending on the relative strength of the competing mechanisms, the resulting equilibrium can take qualitatively different forms.

For the Sun this equilibrium results in a rather complex distribution of angular and linear velocities; the current observational results are described in Section 2.2.1. As described there, the temporal variations of the solar differential rotation have been observed to be below a 1% level on timescales of years. This supports the concept of a (quasi-) equilibrium situation. Since these systematic variations, small in case of the Sun, may be considerably larger for other stars they are discussed in detail below.

In spite of massive progress of helioseismic observation techniques (Christensen-Dalsgaard, 2002), many features of the solar convection zone (SCZ) are still inaccessible to direct observations. Especially details of the convective motions deep in the SCZ are largely unobserved because they are "hidden" from direct observations below the near-surface convection and only limited information seems to be available from seismologic methods (Christensen-Dalsgaard, 2002, Sec.X).

As a result, model calculations incorporating the observational constraints and the presumed physical processes are needed to gain insight into the mechanisms governing the SCZ. While these models of the SCZ do yield some insight, many issues are presently unsettled (Rüdiger, 1989; Gilman, 2000; Miesch, 2000).

Since many parameters are presently not known for the *solar* convection zone, it is unclear which properties of the SCZ can successfully be extrapolated to stars markedly different from the Sun. Consequently, the "solar rotation law", i.e. the latitudinal and radial dependence of solar angular velocity, may turn out to be a special case among many others.

The advent of helioseismic measurements of the solar interior rotation from the mid 1980's has brought about a complete revision of solar rotation models (cf. Gilman et al., 1989; it is historically interesting to compare e.g. Durney & Spruit, 1979 to Durney, 2000). This revision turned "Ω-constant-on-cylinders" models of the SCZ into "Ω-roughly-constant-along-radii" models. Both fitted the observational constraints available at *their* time, which means that the former only matched the (near) surface observations (although discrepancies with the expected "deeper anchoring" of magnetic features existed, cf. e.g. Howard 1984, p. 136).

2.2.1 Observations of Solar convection zone flows

Surface observations of rotation

Carrington's measurements of the solar differential rotation based on 6 years of sunspot observations (Carrington, 1863)[11] were soon confirmed as motions of the solar photospheric plasma by the measurements of blue- and redshifts of Fraunhofer lines (Dunér, 1890, 1905).[12] Basically these methods are still applied to obtain the most precise longterm information on the solar *surface* differential rotation. Results from the observations of several tracers of differential rotation are shown in Fig. 2.5. [13]

The given angular velocities correspond to a rotation period of about 25 days at the solar equator, 31 days at ± 60 degrees latitude and 36 days if extrapolated to the

[11] Carrington (1863, p. 221) presents a quantitative fit to the solar rotation law as a function of latitude l (a "$\sin^{\frac{7}{4}} l$-law", explicitly denying the adequacy of a "$\sin^2 l$-law"). However, different rotation rates of sunspots at different heliographic latitudes had already been noted in Carrington (1859).
Peters (1859) remarks that Carrington's observations are compatible with his data, but he does "not recognise [...] a regular law depending on the distance of the spots from the equator" (Peters, 1859, p. 174).
It appears that Spörer (1861,a) had noted different rotation rates of sunspots at different latitudes independently of Carrington, but was more careful in formulating a general law, taking into account the possibility of transient small-scale motions of the spots (Spörer, 1861a, p. 380).

[12] The effect of the stellar rotation on the spectral lines had been discussed theoretically by Vogel (1877), following a suggestion by Abney (1877). However, no reference could be found in Vogel's publications up to 1890 with respect to solar *observations* concerning that issue.

[13] The term "Doppler measurements", in this context, refers to measurements of Doppler shifts of photospheric lines. Ideally they yield the plasma velocity at the formation depth of the line(s); they are however susceptible to e.g. small scale velocity fields (Beck, 1999, p.50)

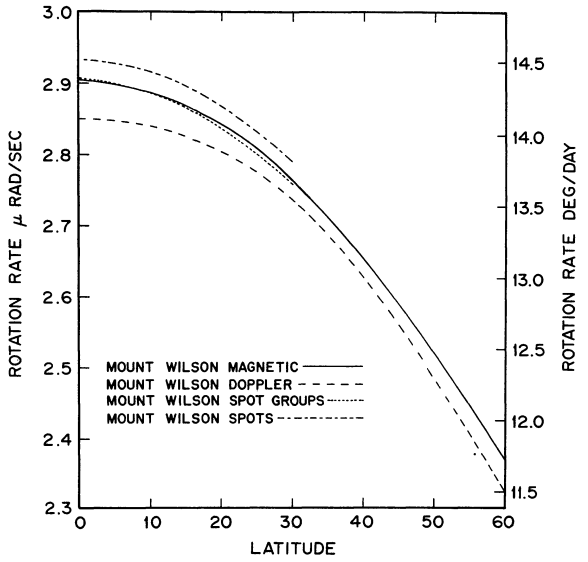

Figure 2.5: Mean solar sidereal rotation rate as a function of latitude (Howard, 1984, Fig.8). The individual graphs show photospheric Doppler measurements (1967-82, dashed), non-spot magnetic features (1967-82, solid), recurrent sunspot groups (1921-82, dotted) and individual sunspots (1921-82, dash-dot). The graphs are smooth fits to longterm observations averaging both hemispheres. Measurement errors (increasing with latitude), spatial and temporal variations are below a 1% level. The equatorial rotation rate is presently measurable with an accuracy of about 0.1%. Extensive plots including more recent measurements, partly extending to about 75° latitude, can be found in Beck (1999).

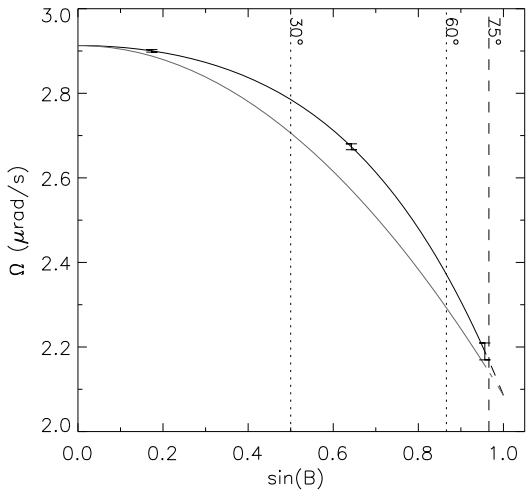

Figure 2.6: Fit to the observed rotation of magnetic surface features (black curve, Eq. 2.3), as a function of the sine of latitude B. Selected latitudes are marked by vertical lines for orientation. The observations extend to about 75° latitude, exemplary measurement errors from Komm et al. (1993) are shown by the error bars. The gray curve shows a $\sin^2$-law with the same pole-equator amplitude for comparison.

poles. Several units are in use (the unit "Carrington rotation" is *defined* as 27.275 days), helpful conversions are

$$0.2020\ \mu\mathrm{rad\,s^{-1}} = 1^\circ\,\mathrm{day}^{-1} = 32.15\ \mathrm{nHz} \quad .$$

At the solar equator, an angular velocity of $1^\circ\ \mathrm{day}^{-1}$ corresponds to a velocity of $0.141\ \mathrm{km\,s^{-1}}$.

Measurements based on sunspot observations are naturally limited to typical latitudes of sunspot occurrence. In spite of discrepancies between different authors (up to about 5% in extreme cases), the following properties of different tracers are significant (Beck, 1999): (a) Supergranules rotate faster than most sunspots. (b) Young sunspots rotate faster than recurrent sunspots, (c) small sunspots rotate faster than large sunspots. (d) Sunspots rotate faster than the surrounding surface plasma, as measured by photospheric Doppler shifts. Apart from (a), these trends can be seen in Figure 2.5.

The increased rotation rate of sunspots compared to the surrounding photospheric plasma, together with helioseismic rotation measurements (see below), suggest a kind of "anchoring" in deeper layers. This anchoring may be complicated in detail due to the precise dynamics of flux tubes in the surrounding plasma; these questions are not settled at present (Beck, 1999). Item (a), namely the "weird" behaviour of supergranules may be due to a (not yet understood) wave phenomenon (Gizon et al., 2003).

The rotation law of surface or transition region magnetic features may be used as an "intermediate" surface rotation law. Note that the rotation law poleward of about 75 degrees latitude is practically unknown at present (e.g. Richokainen et al., 1998, Fig.2). A fit to the *magnetic feature* angular velocity,[14] as a function of latitude B, is given by Komm et al. (1993):

$$\Omega(B) = 2.913 - 0.41\ \sin^2 B - 0.42\ \sin^4 B\ \ \mu\mathrm{rad\,s^{-1}} \tag{2.3}$$

It is plotted in Figure 2.6, illustrating the influence of the $\sin^4$-term.

The expansion in powers of $\sin^4 B$ is commonly used and somewhat "traditional" (Howard, 1984, p.135). Carrington (1863, p. 221) used a $\sin^{\frac{7}{4}}$-law for his poorer constrained fit; see Beck (1999) for a discussion of alternatives. The errors of the coefficients in Equation 2.3 are about 0.1% for the constant term and 5-10% for the higher order terms.

Systematic deviations of the rotation rate from Equation 2.3 appear to be correlated with the solar activity

[14] Sunspot rotation, only observable up to mid-latitudes, shows slightly different Ω gradients and is better approximated by

$$\Omega_{\mathrm{sunspots}}(B) \approx 2.9 - 0.54\ \sin^2 B\ \ \mu\mathrm{rad\,s^{-1}} \quad .$$

The values are taken from Beck (1999, Tab. II). The resulting different latitude gradients of Ω are just about visible in Figure 2.5.

cycle. The most pronounced spatial deviation is a deceleration of about 0.03 $\mu\mathrm{rad\,s}^{-1}$ within 3 degrees of the equator (Howard & LaBonte, 1980). The mean rotation rate apparently performs two oscillations with an amplitude of about 0.04 $\mu\mathrm{rad\,s}^{-1}$ during a 22-year cycle. Torsional oscillations, i.e. alternating bands of faster and slower rotation drifting towards the equator are of roughly the same amplitude (Howard & LaBonte, 1980; Miesch, 2000, p. 62 and references there).

Analysis of the "Greenwich Photoheliographic Results" spanning the years 1879-1957 indicate a 10% difference of the differential rotation amplitude between the first and second half of each 22-year cycle (Javaraiah, 2003). However the significance of these variations is unclear, they are not confirmed by more precise measurements on shorter time scales (Ulrich & Bertello, 1996).

The presently available data indicate no significant asymmetries between the rotation of the two solar hemispheres.

Deep rotation observations

Presently, the only known probe of the solar interior rotation is helioseismology (see Section 3.3), current results are shown in Figure 2.7. Precise details of the reconstructions vary between different observations and inversion techniques (e.g. Schou et al., 1998, Appendix A), but several features can be considered reliable:
In the SCZ, the angular velocity Ω decreases smoothly and monotonically from the equator to high latitudes. Throughout most of the SCZ, there is little variation with depth. At mid latitudes, Ω-contours are close to radial, only close to the equator they are nearly parallel to the rotation axis. At high latitudes, close to the limit of a reliable reconstruction, there are indications of more intricate structures. In the poorly resolved regions below the SCZ a nearly rigid rotation seems to prevail with Ω at intermediate values of the SCZ. A schematic illustration of these features can be found in Gilman (2000, Fig. 1).

At the top and bottom of the SCZ, there are narrow shear layers: A layer of speed-up towards the surface and the so-called *tachocline* at the bottom; the tachocline is located at 0.69 $R_\odot$ with a thickness of about 0.04 $R_\odot$ (these values are valid close to the equatorial plane, they depend weakly on solar latitude, cf. Charbonneau et al., 1999).

Deep convective flows

Supergranulation presently yields the only direct observational manifestation of solar *subsurface* convection patterns. The narrow downflow regions of its cells roughly coincide with the chromospheric and magnetic network

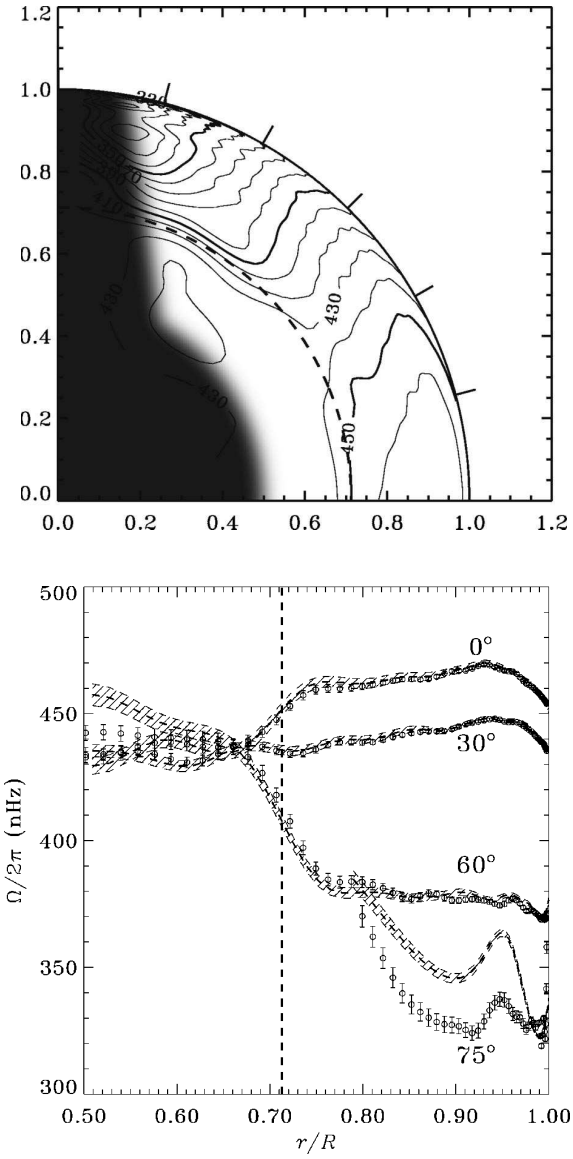

Figure 2.7: Solar interior rotation rate, inferred from helioseismology. *Upper panel:* Contours indicate rotation rates $\Omega/2\pi$, their spacing is 10 nHz. The axes are labelled by fractional radius. The errors in $\Omega/2\pi$ range from 0.5 nHz near the surface and the equator to 4 nHz towards the pole and the interior (Schou et al., 1998, Fig. 4b). The dark region cannot be reliably reconstructed from current observations (Sec. 3.3). *Lower panel:* $\Omega/2\pi$ as a function of radius for the indicated latitudes. Circles and dashes show results from different inversion procedures; they differ significantly only for the 75°-latitude curves. The vertical dashed line marks the base of the SCZ. Reproduced from Christensen-Dalsgaard (2002), showing data of Schou et al. (1998, Fig. 3b).

of the solar surface. The cells have a typical size of 15-30 Mm (compared to 0.6-1.3 Mm for granules). Maximal horizontal flow velocities are 200-400 m/s (about half of the value for granules) and lifetimes of supergranules are of the order of 1 day (about 8 min. for granules); the above values are taken from Schrijver & Zwaan (2000, Tab. 2.4).

Helioseismologic results (Duvall et al., 1997) suggest, that the supergranulation cells extend only a few Mm into the SCZ. This reveals them as a near-surface phenomenon which is not expected to significantly influence the overall dynamics of the SCZ. The only observational indication of much larger convective patterns deeper in the SCZ, predicted by convection theory, are the so-called "giant cells" (Simon & Weiss, 1968). In spite of numerous attempts to detect them (e.g. Beck et al., 1998, report cells of 3.6 m/s rms velocity and several 10° surface extent), their existence has not been reliably confirmed yet.

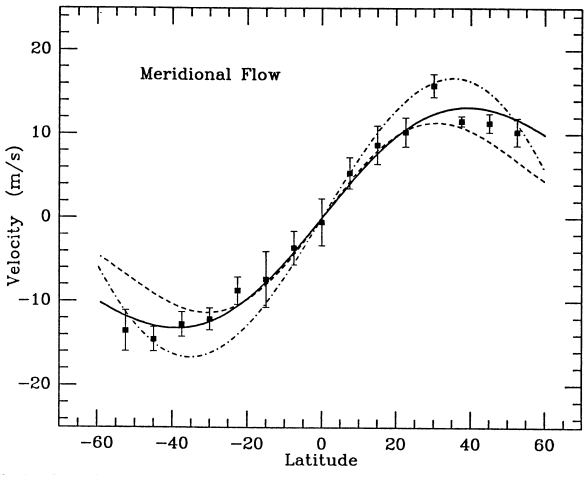

Figure 2.8: Longterm average meridional flow at the solar surface (Komm et al., 1993a). Measured from magnetic features 1978-1990 (the solid curve is a fit to the data points), photospheric Doppler shifts 1968-1990 (dash-dotted) and 1982-1984 (dashed). Positive and negative values indicate northward and southward flows respectively, i.e. the shown flows are poleward on both hemispheres.

Meridional flows

While large scale convective patterns still elude observation, the *presence* of large-scale meridional flows in the SCZ is well established. Long-term observations of magnetic features, as well as Doppler shift measurements of photospheric lines[15] have revealed (near) surface flows *towards the poles* with velocities of the order of up to a few 10 m/s. Some measurements are compared in Figure 2.8. According to helioseismic measurements, these flows extend several Mm deep into the SCZ (Braun & Fan, 1998; Gizon et al., 2003, Fig. 2b).

The meridional motions of active regions and sunspot (groups) are apparently dominated by their local, intrinsic behaviour. On average there is a trend of poleward displacement above about 15° latitude, equatorward below that latitude; both with mean velocities of a few m/s (Howard, 1996, and references there).[16] However, recurrent sunspots do not show a regular meridional motion (Wöhl, 2002).

It should be noted that surface observations of meridional flows are (due to the observational limitations) mostly based on long time series extending over several months or years. Helioseismic observations of meridional flows are usually based on shorter time series (e.g. 40 days in the case of Braun & Fan, 1998, 60 days for Gizon et al. 2003), but their latitude resolution is lower.

As a consequence, the very smooth behaviour, suggested by curves like Figure 2.8, may hide transient spatial variations, potentially related to the solar cycle. Such variations have already been suggested by some surface observations (Snodgrass & Dailey, 1996; Hathaway, 1996, Fig. 3, although Schrijver & Zwaan, 2000 caution that these measurements may be substantially influenced by the intrinsic motions of active regions). They are further substantiated by recent local helioseismic measurements (Haber et al., 2002).

The temperature difference between the equator and the poles, closely related to meridional flows, is an important parameter for restricting SCZ flow models. Kuhn et al. (1998), based on short-term limb measurements, deduce pole temperatures about 1.5 K below the equator temperature.[17] However, the precise value of the solar pole-equator temperature difference (including its sign) is presently not settled by observations. Different measurements agree that it is at most of the order of 10 K.

[15] These Doppler measurements are only partly "direct". They require substantial corrections, e.g. because of the limb angle dependent blueshift of photospheric lines, of the order of 100 m/s, caused mainly by a brightness-velocity correlation of the solar granulation.

[16] Note that at a speed of e.g. 5 m/s, a displacement of e.g. 1 degree along a meridian takes about 28 days, i.e. long compared to sunspot(group) evolutionary timescales.

[17] Actually, the measurements of Kuhn et al. concentrated on measuring the Sun's oblateness (the pole vs. equator difference in radius is of the order of 10^{-5} $R_\odot$). Their results suggest the presence of higher order contributions than only quadrupole terms (corresponding to oblateness) describing the solar shape. If confirmed, these results may become a relevant constraint of solar interior rotation models.

2.2.2 Large scale flow models for rotating stars

As mentioned in the introduction of this chapter, the different processes transporting angular momentum should eventually result in an equilibrium distribution. This is supported by the solar case where the observed pattern of differential rotation is globally stable over the timescales assumed as relevant for the transport processes.[18] While these processes are well understood in principle, their relative magnitude even for the Sun is still a matter of dispute (e.g. Brun & Toomre, 2002, Sec. 4.2).

The first part of this section sums up general aspects of convection in a rotating frame; the second part discusses recent modelling results. Currently, two quite distinct modelling approaches are used (cf. Miesch, 2000, Sec. 3 for a comparative discussion). One approach is associated with the *mean-field approximation* of turbulent hydrodynamics (Rüdiger, 1977, 1989; Durney & Spruit, 1979; Durney, 2000, and references therein). The other is based on a *three-dimensional hydrodynamic simulation* of the turbulent convection on (as many as possible) of the relevant length and time scales (Brun & Toomre, 2002; Miesch, 2000, Ch. 5); following Miesch this approach is termed *spherical-shell simulations* in the following.

The mean-field approach cannot model large-scale coherent structures ("self-organization") of the flow. While such coherent structures play an important role for many convection phenomena (Miesch, 2000, Sec. 4.2), their importance for the SCZ is presently not known.

On the other hand, the spherical-shell simulations fail to yield an appropriate model if the used grid does not resolve all relevant scales (due to computational limitations) and the not explicitly resolved "subgrid-scale processes" are not modelled appropriately (Brun & Toomre, 2002, Sec. 2.). In contrast to mean-field models, spherical-shell simulations do not yield explicit equations for the (mean) large-scale flows, which can reveal information by analysing their structure.

Angular momentum transporters

Gilman (2000) lists four processes transporting angular momentum in the SCZ: (a) Reynolds stresses,[19]

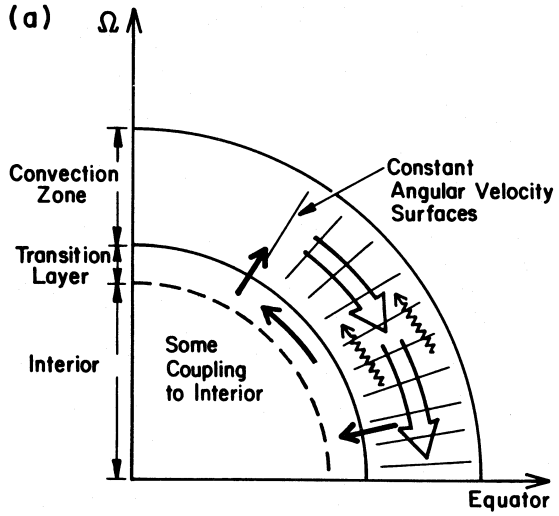

Figure 2.9: Schematic angular momentum flow balance in the solar convection zone (SCZ), from Gilman et al. (1989). Present hydrodynamic models of the SCZ agree that the equatorward net flow is mainly caused by Reynolds stresses (large arrows), while the weaker poleward flow (wiggly arrows) is dominated by meridional circulation. The nature and strength of a possible coupling to the radiative core is presently not known. See text for details.

(b) Maxwell stresses, as "magnetic analogues" of (a), (c) meridional flows and (d) wave motions, e.g. gravity or Alfvén waves. The angular momentum loss due to the solar wind torque is of negligible strength compared to these processes.

In agreement with present models Gilman concludes that the angular momentum transport in the SCZ is dominated by a balance of processes (a) and (c). While present models do agree that far, they disagree on the "main" scales of convection causing the Reynolds stresses. They also disagree on the relative strength of processes responsible for the meridional flows. The mechanisms and the amount of a possible coupling to the solar interior via the tachocline are an open question at present. The situation is schematically illustrated in Figure 2.9.

The influence of magnetic fields on the large-scale convection zone flows is apparently small for the Sun; this may not apply to stars with considerably higher magnetic filling factors inside their convection zones. This aspect is not explicitly treated by any present model; however,

[18] If the presently observed flow speeds are truly characteristic of meridional flows in the SCZ, their "turnover time scales" may well be of the order of a few years. *Convective* turnover times for the Sun are estimated to be of the order of 5-20 days (Noyes et al., 1984; Pizzolato et al., 2001, Fig. 5). Pizzolato et al. discuss the underlying averaging process in their Sec. 2.

[19] Reynolds stresses appear in the *mean-field* description of turbulent hydrodynamics. For illustrations and discussions of the concept see Gilman, 1979, p. 22 and Pedlosky, 1987, Sec. 4.2. Here the variables of the system are split up into average and fluctuating parts (analogous to Equation 2.2). Average correlations between different components of the fluctuating velocities lead to an (angular) momentum transport in the fluid. This momentum transport is in general anisotropic and can be described by the Reynolds stress tensor (cf. also Tassoul, 2000, Chs. 2.4, 3.6 & 5.2).
Basically this can be understood as an analogue to molecular viscosity appearing in the average (large-scale) equations of motion, caused by the interaction of turbulence cells. In contrast to molecular viscosity, it is generally not isotropic and depends on the parameters of the turbulence.
In general, anisotropic Reynolds stresses are associated with an anisotropic heat flux (Durney & Spruit, 1979; Kitchatinov et al., 1994).

it may significantly complicate the extrapolation of solar rotation models to much faster rotating stars.

The Taylor-Proudman state

The nowadays outdated "Ω-constant-on-cylinders" models of the SCZ are a special case of an often useful approximation for rotating fluid motion, the Taylor-Proudman state, sometimes also named in conjunction with the Poincaré-Wavre theorem (Acheson, 1990; Tassoul, 2000; Miesch, 2000, Sec. 2.2).

The Taylor-Proudman theorem is a statement about the steady motion of a rotating fluid: If Coriolis forces dominate (a) inertial forces and (b) viscous forces and if (c) baroclinic forces[20] can be neglected, it follows that the fluid velocity is independent of the coordinate parallel to the rotation axis. This means that the angular velocity is constant on cylinders around the rotation axis.

Conditions (a) and (b) can equivalently be expressed by stating that the flow is characterized by small Rossby and Ekman numbers, respectively.[21] These conditions imply that any rotating fluid approaches a Taylor-Proudman state for sufficiently fast rotation.

As Figure 2.7 shows, the SCZ is distinctly not in a Taylor-Proudman state. Again, present models of the SCZ disagree on the reason why; the relative importance of baroclinic forces is estimated very differently (Kitchatinov & Rüdiger, 1995; Durney, 2000; Brun & Toomre, 2002, Sec. 4.2).

A 3D model of the SCZ

The following paragraphs present results of a recent spherical-shell simulation of the SCZ (Brun & Toomre, 2002). Deemed by Brun & Toomre a "faithful, if highly simplified" model of the SCZ, it offers a detailed view of the modelled dynamics and processes. The resulting "inside view" of the convective flows in the Sun can currently not be verified by direct observations. It is presented in some detail here to convey a rough (tentative) idea of the subsurface convection dynamics.

The model reproduces some key features of the observed rotation law of the SCZ (see Figure 2.11), i.e. a strong (solar-like) Ω-gradient extending to high latitudes and a non-parallel alignment of Ω-contours with respect to the rotation axis. Neither "surface boundary effects" (i.e. (super) granulation) nor the inner boundary (i.e. the tachocline) of the SCZ are included in the simulations. On scales not resolved by the simulation grid, the model falls back on a mean-field formulation.

Apart from the problem of resolving all "relevant scales" of turbulent motions with the simulation grid, the spherical-shell simulation have to tackle the problem that several parameters (of partly poorly known value) control the properties of the turbulence.[22] As a result Brun & Toomre study five models with different settings of these parameters (cf. their Table 1); only the model leading to differential rotation most similar to the Sun (termed "AB") is presented here.

The radial velocities of the convective patterns are shown in Figure 2.13; notice that strong convective downflows extend practically through the whole modelled part of the SCZ. The "organized tilts" of the narrow downflows cause the main portion of Reynolds stresses found in the model of Brun & Toomre (2002, Sec. 4.1).

The average meridional flows in the model are shown in Figure 2.12, the flow speeds are of comparable magnitude as observed on the Sun (Section 2.2.1). The reality of the multi-cellular structure is presently unclear; however,

[20] Baroclinic forces arise if the surfaces of constant density do not coincide with the surfaces of constant pressure (Pedlosky, 1987, Sec. 2.2 and Fig. 2.2.4). Basically this situation leads to regions of different density in the considered fluid being affected by the same pressure gradients (= force per unit mass). The lower density fluid elements "rise" faster than their higher density counterparts in that situation.

[21] Two dimensionless parameters are particularly useful to characterize a fluid flow in a rotating frame of reference (Tassoul, 2000). For a rotation with the angular velocity Ω the Rossby number R_0 is defined as

$$R_0 = \frac{U}{\Omega\, L}$$

where U and L are a "typical" velocity and length of the flow, respectively. A large Rossby number indicates that inertial forces of the fluid flow dominate Coriolis forces. For convective motions, it is usually estimated as the ratio of the rotation period and a typical convective turnover time $R_0 \approx P/\tau_c$.
The Ekman number

$$E = \frac{\nu}{\Omega\, L^2}$$

characterizes the influence of the kinematic viscosity ν (the coefficient of viscosity divided by the density) compared to Coriolis forces.

[22] This considerable bunch of parameters is listed in Brun & Toomre (2002, Tab. 1); some of them are explained below.
The Reynolds number $\mathcal{R}_e$ is defined as

$$\mathcal{R}_e = \frac{U\, L}{\nu}$$

where again U and L are a "typical" velocity and length of the flow, respectively; ν is the kinematic viscosity. $\mathcal{R}_e$ describes the "viscous damping" of turbulence, a sufficiently large value of $\mathcal{R}_e$ leads to the onset of turbulence (Acheson, 1990, Secs. 2.2 & 9).
The "behaviour" of the turbulence is (partly) controlled by the Prandtl number, defined as

$$\mathcal{P}_r = \frac{\nu}{\kappa}$$

with κ representing the thermal diffusivity (thermal conductivity divided by the density and the specific heat). $\mathcal{P}_r$ describes "how much" the heat generated by the turbulence influences the viscosity (which increases with temperature for an ideal gas) and thereby further turbulent instabilities.
The onset and behaviour of thermal convection is controlled by the Rayleigh number $\mathcal{R}_a$ which relates thermal conduction, viscosity and buoyant forces (Acheson, 1990, Sec. 9.3)

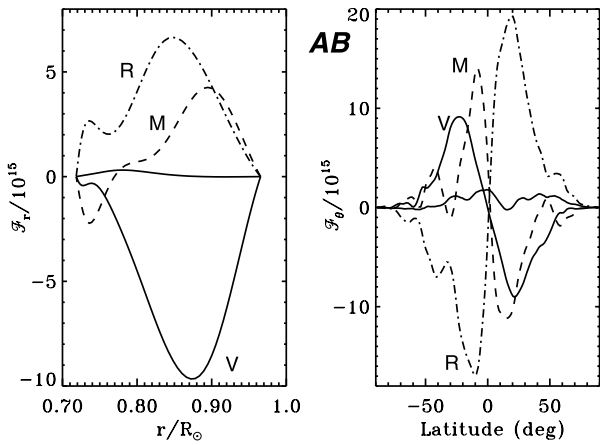

Figure 2.10: Average angular momentum fluxes corresponding to Fig. 2.11. The left panel shows the latitudinal fluxes as a function of radius, positive values are southward. The right panel shows the radial fluxes as a function of latitude, positive values are outward. The flux components are labelled as induced by Reynolds stresses (R), meridional flows (M) and (turbulent) viscosity (V). Note that all three components contribute with roughly comparable amounts to the total angular momentum flux balance. The unlabelled solid curves represent the total flux, i.e. the sum of the three components, indicating to what degree the models have achieved a stationary state. Fig. 11 of Brun & Toomre (2002).

it is to some degree suggested by recent solar observations (Haber et al., 2002).

Finally, Figure 2.10 shows the relative contribution of different angular momentum transport processes to the angular momentum flux; the three shown components contribute with comparable amounts to the total balance of fluxes. Due to the stress-free boundary conditions of the model the total angular momentum is conserved. The small total fluxes in each panel indicate that the simulations have nearly reached an equilibrium state. Concerning latitudinal differential rotation, Brun & Toomre (2002, p. 881) conclude that "Reynolds stresses have the dominant role in achieving the prograde equatorial rotation [i.e. the "fast" equator] seen in the simulations, with its effectiveness limited by the opposing transport of angular momentum by the meridional circulation". This agrees qualitatively with the mean-field models of Kitchatinov & Rüdiger (1999) who do unfortunately not show a similar plot for their models.

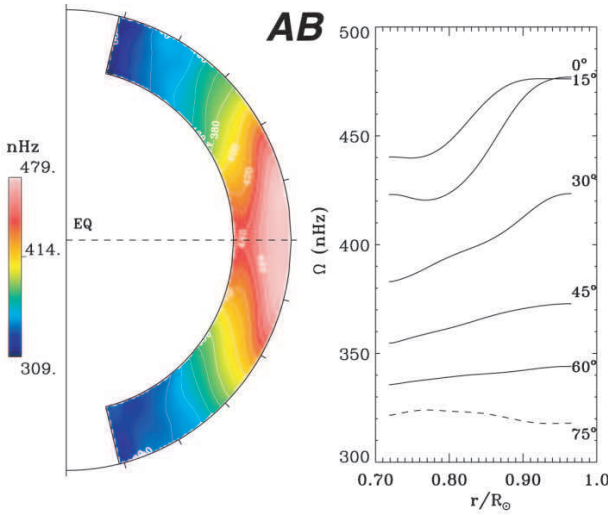

Figure 2.11: Average angular velocity profile of a three-dimensional simulation of the solar convection zone (SCZ) (from Fig. 4 of Brun & Toomre, 2002). "AB" indicates the parameter set of the model, resulting in the "most solar-like" behaviour of the five models discussed by Brun & Toomre. A comparison with solar observations (Fig. 2.7) shows elements of agreement as well as of disagreement, e.g. concerning the radial gradients of the angular velocity.

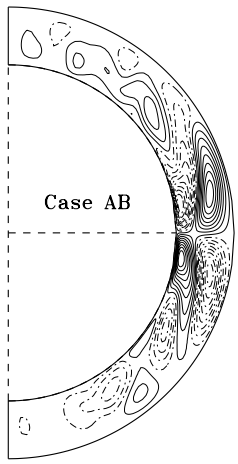

Figure 2.12: Streamlines of (temporally and longitudinally) averaged meridional mass flows in the SCZ belonging to the same model as Fig. 2.11. Solid contours denote counterclockwise circulation; dashed contours indicate the opposite. Typical meridional flow velocities of the model are of the order of 20 m s^{-1}. Fig. 8 of Brun & Toomre (2002).

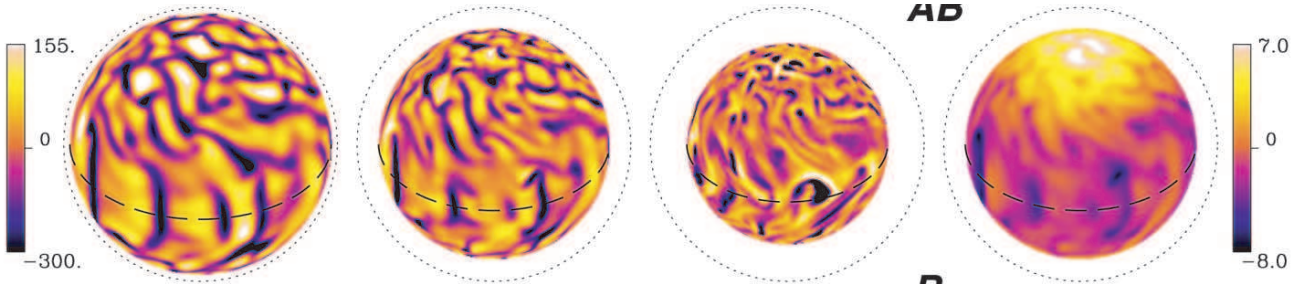

Figure 2.13: Snapshot of convective radial velocities shown at three depths in the SCZ, belonging to the same model as Fig. 2.11. The maps show the velocities near the top, middle and bottom of the SCZ, at 0.95, 0.83 and 0.73 $R_\odot$, respectively. Downflows are shown as dark/purple, upflows as light/orange hues (the scale is annotated in m/s). The rightmost map shows the corresponding temperature differences in Kelvin at the middle layer (0.83 $R_\odot$); a pole-equator temperature gradient is clearly visible. It can be seen that the pronounced narrow downflows visible in the velocity maps are cool. From Fig. 3 of Brun & Toomre (2002).

Mean-field models and non-solar extrapolations

An extensive study of large-scale flows in stellar convection zones based on mean-field hydrodynamics has been carried out by G. Rüdiger, L. Kitchatinov and collaborators.[23]

The following outlines a thread of Kitchatinov & Rüdiger's approach with the aim of illustrating the principles of angular momentum flow in their models. For more comprehensive discussions cf. Pedlosky (1987, Secs. 2.2, 4.2), Foukal (1990, Secs. 7.3.3, 7.3.7), Tassoul (2000, Chs. 2.4, 3.6 & 5.2) and Stix (2002a, Sec. 7.5) As mentioned above, the mean-field formulation builds on attempting a separation of the large-scale flows (differential rotation and meridional flows) from the small scale motions (turbulent or "eddy-like" motions). The aim is to derive equations describing *stationary axisymmetric* average large-scale flows.

However, the turbulence (*assumed* to be appropriately uniform for the performed averaging) significantly influences the large-scale motions in stellar convection zones. The anisotropy of the turbulence arises because of the density stratification of the convection zone and because of the rotation of the star; These influences lead to anisotropic turbulent viscosity,[24] Reynolds stresses and anisotropic heat transport by the convection.

The coefficients describing the turbulent viscosity (Kitchatinov et al., 1993) and the turbulent heat transport (Kitchatinov et al., 1994) need to be calculated, partly based on ad-hoc assumptions (the nature and validity of them is beyond the scope of this discussion, cf. Tassoul, 2000, pp. 89 and 142 for some related remarks).[25] The treatment of Kitchatinov et al. makes use of the mixing-length theory of convection (Foukal, 1990, Sec. 7.3.3 and Stix, 2002a, Sec. 6.2) and leaves the mixing-length parameter $\alpha_{\rm MLT}$ as the only free parameter for calculating the turbulent viscosity and heat transport coefficients; fortunately the results depend only weakly on $\alpha_{\rm MLT}$ (Kitchatinov & Rüdiger, 1995, Sec. 2.3).

The equation governing the steady mean flow $\overline{\mathbf{u}}$ (Kitchatinov & Rüdiger, 1999, Eq. 2) can be turned into a continuity equation for the angular momentum flux (Kitchatinov & Rüdiger, 1999, Eq. 11) which can equivalently be expressed as (using spherical polar coordinates r, θ and ϕ)

$$\mathrm{div}\Big(\rho r\ \sin\theta\ \overline{u_\phi \mathbf{u}}\ +\ \rho r^2\ \sin^2\theta\ \Omega\, \mathbf{V}^m\Big) = 0 \quad (2.4)$$

where ρ and Ω denote the density and the angular velocity, respectively; $\overline{u_\phi \mathbf{u}}$ indicates the average indicated product of fluctuating velocities, $\mathbf{V}^m$ represents the meridional flow velocity. The interesting point about Equation 2.4 is that it clearly shows the two agents that control the angular momentum distribution (and hence the differential rotation): Reynolds stresses (represented by the fluctuating velocity term) and meridional flows.

Using the symbol $z = r\cos\theta$ for the distance to the equatorial plane, the equation for the meridional flow velocity reads (Kitchatinov & Rüdiger, 1999, Eq. 17)

$$\mathcal{D}(\mathbf{V}^m) \ =\ r\ \sin\theta\ \frac{\partial \Omega^2}{\partial z}\ -\ \frac{g}{c_{\rm p} r}\ \frac{\partial S}{\partial \theta} \qquad (2.5)$$

where $\mathcal{D}(\mathbf{V}^m)$ represents the viscous damping of the flow (Kitchatinov & Rüdiger, 1999, Eq. 14); g, $c_{\rm p}$ and S are the gravitational acceleration, the heat capacity at constant pressure and the specific entropy, respectively.

Equation 2.5 is interesting, because it highlights the two "drivers" of meridional flows in the model: (a) Gradients of the angular velocity parallel to the rotation axis[26] and (b) latitudinal gradients of specific entropy (which

[23] This study is documented in a voluminous genealogy of publications, ranging from e.g. Rüdiger (1977) to Rüdiger & Küker (2002). No comprehensive presentation of this study exists to date; Rüdiger (1989) contains an outline of the fundamental concepts of the approach, Rüdiger et al. (1998) present some selected issues. No comprehensive discussion is attempted here, instead an overview of the key concepts and results of the approach is given, without claiming to be authoritative.
Some milestones of Kitchatinov & Rüdiger's approach are listed below; they are useful as an orientation among the related publications (for earlier milestones cf. Rüdiger, 1989):
Küker et al. (1993) present a model qualitatively reproducing the solar interior differential rotation, somewhat perplexingly based on neglected meridional flows. Kitchatinov et al. (1994) model the anisotropic heat transport by convection. Kitchatinov & Rüdiger (1995) combine these results, yielding a consistent integration of meridional flows into the model. Kitchatinov & Rüdiger (1999) present analogous models for fast rotating stars of different spectral type, as well as for evolved stars.

[24] The "viscous" influence of the turbulent motions on the large-scale flows is formulated in analogy to the treatment of molecular viscosity (apart from the anisotropy); this formulation is historically due to Bussinesq. It leads to a horizontal and a vertical coefficient of turbulent viscosity, μ_H and μ_V used to build up the components of the Reynolds stress tensor (Tassoul, 2000, Eqs. 3.127-3.132).
μ_H and μ_V only parametrize the anisotropy of the turbulence due to the radial stratification, to additionally incorporate the anisotropy caused by rotation, two more parameters are introduced, termed λ_H and λ_V (Tassoul, 2000, Eqs. 3.131-3.132, 5.4-5.5).
The above train of thought can also be followed in Rüdiger (1989); λ_H and λ_V appear as Λ_H and Λ_V in his Eq. 20 (again in Eq. 52 where $\Lambda_H \approx 0$ has been adopted for slow rotation). A non-vanishing λ_V gives rise to differential rotation in a rotating convection zone, called the "Λ-effect" by Rüdiger (1989), cf. also Tassoul (2000, Sec. 3.3.2).

[25] Citing Tassoul (2000, p.142): "[...] it thus seems highly probable that anisotropy plays a key role in the solar rotation problem, since calculations involving isotropic transport coefficients always yield angular velocities that are constant on cylinders in the models."

[26] These Ω-gradients can be associated with the "non-conservative" part of the centrifugal acceleration: If Ω does *not* depend on z, the effective gravity can be derived from an "effective potential" (Tassoul, 2000, Eqs. 2.28 and 3.18-3.22).

translate into temperature gradients at constant pressure and are hence related to baroclinicity).[27]

Agent (a) causes a meridional flow from the equator to the pole (in the upper layers of the convection zone), driven by centrifugal acceleration. Irrespective of the detailed dynamics the system would tend to develop into (close to) a Taylor-Proudman state in the absence of agent (b), thereby making $\frac{\partial\Omega}{\partial z}$ (nearly) vanish. However, in the models of Kitchatinov & Rüdiger agent (b) prevents the system from thus turning into "Ω-constant-on-cylinder" rotation: The anisotropic heat transport of the convection results in a pole-equator temperature difference of a few Kelvin (with a "warmer" pole). This is currently near the uncertainty limit of solar observations, however it agrees qualitatively with the results of spherical-shell simulations by Brun & Toomre (2002). This temperature difference leads to a slow down of the poleward upper-layer meridional flow. (Kitchatinov & Rüdiger, 1995, abstract and Sec. 3.1).[28]

The following list sums up the key features of Kitchatinov & Rüdigers' models:

(0) The mass flow due to the meridional flow is poleward in the bulk of the convection zone, independent of the rotation period.[29] This meridional flow is driven by the "nonconservative centrifugal" term ($\propto \partial\Omega^2/\partial z$) in Equation 2.5 and counteracted by the baroclinic term ($\propto \partial S/\partial\theta$).

(1) Reynolds stresses "speed up" the equator relative to the poles in terms of Ω, leading to a positive value of α (Equation 2.6).

(2) The poleward meridional flow in the bulk of the convection zone reduces the equator-pole Ω gradient, i.e. in effect reduces α.

Effect (1) dominates in all models of Kitchatinov & Rüdiger (1999) leading to a solar-like (fast equator) surface rotation law.

Concerning the dependence of the "differential rotation strength" α on the rotation period P for a model of fixed spectral type, the following applies: For decreasing P (increasing Ω) the meridional flow becomes faster (Kitchatinov & Rüdiger, 1999, Fig. 2), thereby amplifying effect (2) and leading to a weaker differential rotation in terms of α.

Concerning the spectral type (or stellar evolution) dependence for a constant rotation period, the following statement can be made: A decreased thickness of the convection zone leads to a slow down of the meridional flow due to an increased (turbulent) viscous braking (of the oppositely directed upper and lower flows of the meridional circulation). Slowing down the meridional flow leads to a weaker effect (2) and hence to a stronger differential rotation in terms of α.[30]

Figure 2.15 gives an overview of the large-scale flows calculated from the outlined mean-field approach for a solar model. Figure 2.14 illustrates the differential rotation "strength" of the models as a function of the rotation period.

The mean-field approach appears as a "crude" approximation to the complex dynamics of the SCZ exhibited by spherical shell simulations. However, whether grasps the key ingredients of the SCZ dynamics is presently not settled.

The mean-field models reproduce the solar differential rotation quite successfully which clearly supports their approach. However, as a comparison to spherical-shell simulations shows, some of its predictions are not undisputed and can presently not be verified by solar ob-

[27] Keeping in mind the entropy expression for an ideal gas

$$S = c_v \ln\left(p/\rho^\gamma\right) = \gamma c_v \ln\left(\frac{\mathcal{R}}{\overline{\mu}} T p^{1/\gamma - 1}\right)$$

where γ represents the adiabatic coefficient, $\mathcal{R}$ is the ideal gas constant and $\overline{\mu}$ the mean molecular weight.

[28] The described influence of agent (b) on the meridional flow can equivalently be stated by saying that the anisotropic heat transport induces baroclinicity such that it significantly slows down the meridional flow driven by centrifugal acceleration.
Brun & Toomre (2002) also find that process in their spherical-shell simulations, but ascribe it less importance. Based on their models they propose that the Reynolds stresses play an important role in the meridional flow balance (see their Sec. 4.2).

[29] This applies irrespective of the equatorward *surface* flow velocities in the G2 V model of Kitchatinov & Rüdiger (1999, Fig. 2) for rotation periods $P \gtrsim 10$ days; this surface flow is caused by a near surface circulation cell (of unsettled "reality") and has no significant influence on the total angular momentum balance (Kitchatinov & Rüdiger, 1995, Fig. 1).

[30] The above qualitative discussion of the dependence of α on the rotation period P and (in effect) on the convective turnover time τ_c is directly related to the "preliminary estimation" of Kitchatinov & Rüdiger (1999, Sec. 2.3); this estimation results in their Eq. 30 which can be written as

$$\alpha \approx \frac{4}{\Omega^{*\,3/2}}$$

where $\Omega^* = 2\tau_c\Omega$ is the "local Coriolis number".
The effectivity of the centrifugal driving of the meridional flow relative to the viscous braking is measured by the Taylor number, $T_a = 4\Omega^2 R^4/\nu$ (Kitchatinov & Rüdiger, 1999, Eq. 27). Estimating the turbulent viscosity analogous to molecular velocity as $\nu \sim \ell u$ (L. Kitchatinov, priv. comm.), where ℓ is the mixing length and u is the convective velocity, and estimating the convective turnover time as $\tau_c \sim \ell/u$ leads to

$$\nu \sim \frac{\ell^2}{\tau_c} \quad .$$

This means that the turbulent viscosity decreases approximately inversely proportional to the convective turnover time.
Thus one finds that the Taylor number

$$T_a \sim \tau_c^2 \Omega^2 R^4/\ell^4 = \Omega^{*\,2}(R/\ell)^4 \quad ,$$

increases with τ_c. Since τ_c increases when going to later spectral types, so does the efficiency of the centrifugal driving of the meridional flow, leading to a decrease of α.

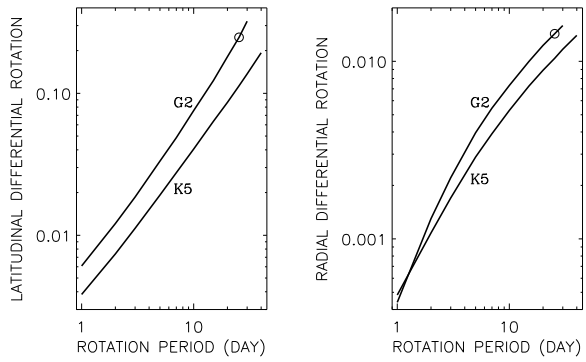

Figure 2.14: Latitudinal (left panel) and radial (right panel) differential rotation "strength" in terms of α (Eq. 2.6) as calculated from a mean-field hydrodynamic model of the convection zone (Kitchatinov & Rüdiger, 1999, Fig. 1). Note the different ranges of the y-axes. A comparison to observed values of differential rotation is made in Fig. 7.40.

servations (e.g. details of the meridional flow structure and the role of baroclinicity for the meridional flow).[31] These issues suggest that some care is appropriate when extrapolating the mean-field solar models to significantly deeper convection zones and/or faster rotation. This need for care is substantiated by some observational results of differential rotation on evolved stars which seem to exhibit a more complex behaviour than predicted by the results of Kitchatinov & Rüdiger (see Section 2.2.3).

However, presently the results of Kitchatinov & Rüdiger are the only quantitative theoretical results concerning the differential rotation of (ultra)fast rotating stars. Additionally, the mean-field approach has the advantage of yielding explicit equations governing the large-scale flows. Although these equations need to be studied numerically, they also yield some approximate analytic results.

[31] Stix (2002a, pp. 299-301) cautions that the pole-equator temperature differences of Kitchatinov & Rüdigers' models (which are vital in their context), appearing to be "slightly" too large compared to solar observations, may indicate a fundamental deficiency of their approach. He suggests further that "[there are possible indications] that meridional circulation is rather accidental to the problem of the Sun's differential rotation" (Stix, 2002a, p. 301). However, this appears presently as a rather isolated opinion.

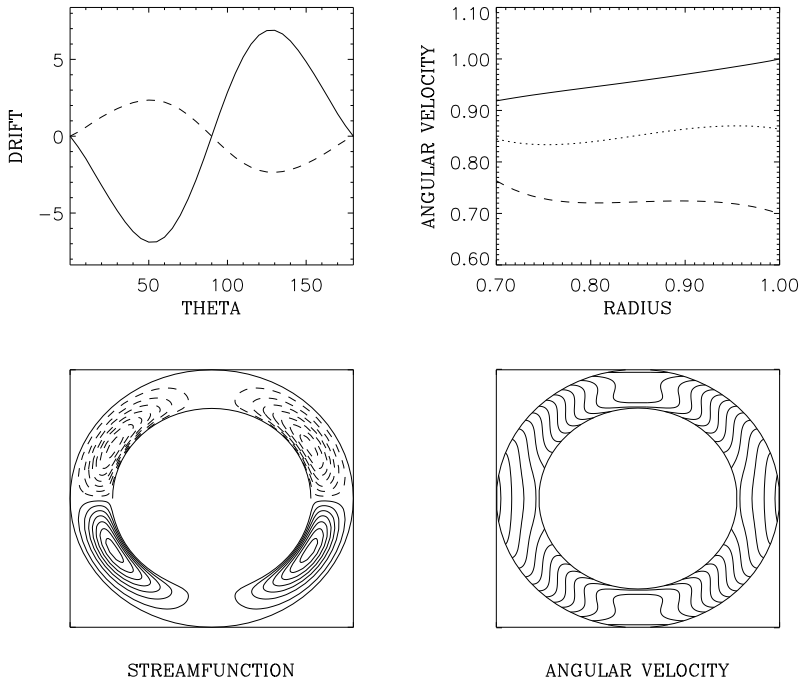

Figure 2.15: Meridional flow and differential rotation in the solar convection zone (SCZ) as modeled by a mean-field approach (Rüdiger et al., 1998, Fig. 1). *Upper left panel:* Meridional flow velocity (in m/s) as a function of colatitude; the solid and dashed curves are velocities close to the bottom and the top of the SCZ, respectively. *Lower left:* Streamlines of meridional flows; the flow is poleward at the top of the SCZ for all four cells. *Upper right:* Angular velocity as a function of radius (in units of $\Omega_{\odot,eq.}$); the curves represent the equator (solid), mid-latitudes (dotted) and the polar regions (dashed), respectively. *Lower right:* Iso-contours of angular velocity.

2.2.3 Stellar differential rotation observations

Several measures characterize the "strength" of differential rotation; the relative differential rotation measure α is preferably used in the following

$$\alpha = \frac{\Omega_{\mathsf{eq}} - \Omega_{\mathsf{pole}}}{\Omega_{\mathsf{eq}}} \tag{2.6}$$
$$= \frac{P_{\mathsf{pole}} - P_{\mathsf{eq}}}{P_{\mathsf{pole}}}$$
$$\frac{\alpha}{1-\alpha} = \frac{P_{\mathsf{pole}} - P_{\mathsf{eq}}}{P_{\mathsf{eq}}} \tag{2.7}$$

A different measure to characterize the differential rotation "strength", not considered here, is the pole-equator lap time (or beat period)

$$P_{\mathrm{beat}} = \frac{2\,\pi}{\left|\Omega_{\mathsf{eq}} - \Omega_{\mathsf{pole}}\right|} \quad . \tag{2.8}$$

There is no straightforward reason to assume that α is a physically meaningful measure of differential rotation. However, it is useful in the context of surface imaging because the shear $\Delta\varphi$ between the equator and the pole during one equatorial rotation is easily calculated from

$$\Delta\varphi = 2\,\pi \cdot \alpha \quad . \tag{2.9}$$

For the Sun, using the total equator-pole difference of angular velocity (Equation 2.3), Equation 2.6 yields

$$\alpha_{\odot\ \mathsf{magn.}} \approx \frac{0.83}{2.9} = 0.29$$

Using the rotation measurements of sunspots, a value of

$$\alpha_{\odot\ \mathsf{spots}} \approx 0.20$$

is more appropriate; however, it should be kept in mind that the sunspot measurements only extend from the equator to mid-latitudes.

For stars other than the Sun differential rotation can presently not be observed by directly imaging their surface. Instead, surface differential rotation is inferred from (a) rotational modulation of a star's disk-integrated brightness (or photometric colours) or (b) from a rotational modulation of disk-integrated spectral features or (c) from time-independent deformations of the disk-integrated spectral line profiles.

The rotational modulation of indicators (a) and (b) is caused by the different brightness and spectra of localized surface regions passing the stellar disk during rotation (e.g. photospheric spots or chromospheric emission features).

Doppler imaging belongs to category (b). Actually the idea of tracing line profile deformations with rotation phase and inferring angular velocities as a function of latitude can be detached from explicitly constructing an image (Collier Cameron et al., 2002; Donati et al., 2003).[32]

Apart from Doppler imaging (in different guises), methods of category (a) and (b) do not explicitly have to resort to localizing features on the stellar surface.[33]

[32] Such a technique is employed by Collier Cameron et al., they term it "direct starspot tracking" based on "matched filter analysis". It is inspired by techniques applied in the analysis of stellar non-radial pulsations (Collier Cameron et al., 2002, p. 700 and references there) and shows some resemblance to the time-series-analysis (TSA) backprojection developed for CLDI (Sec. 5.2.3). It differs from TSA by using curvature information (second derivatives) of the line profile as an indicator of spot-induced deformations (Collier Cameron et al., 2002, Sec. 3.1); while this is a straightforward idea, it runs the risk of introducing instabilities.
In a way "direct spot tracking" amounts to Doppler imaging without explicitly generating an image. The method has not been tested as a part of this work; however tests with similar approaches have been performed during the development of TSA. Based on experience with these tests and with TSA it is tentatively presumed that "direct spot tracking" may lead to *misinterpreted* ambiguities of the input data caused by complex (or ephemeral) spot patterns. While Doppler imaging is also hampered by such ambiguities, a careful analysis of Doppler images (including their phase sampling etc.) offers a chance of detecting them. Certainly, significant (i.e. not purely formal) error estimates are difficult to obtain for "direct starspot tracking".

[33] Inferring starspot latitudes from "few-spot" (usually two-spot) modelling of photometric lightcurves is a potentially highly ambiguous task (cf. e.g. Gray, 1988, p. 7-8). Eaton et al. (1996), studying syn-

Instead they can be based on different rotation periods observed at different epochs for the same star. Assuming non-rigid rotation of the surface, different stellar latitudes rotate with different angular velocities. As a result, if the surface latitudes dominantly covered by spots etc. change with time, different (dominating) rotation periods are observed at different epochs. In analogy to the Sun (e.g. Hempelmann & Donahue, 1997) such a change of dominant "active" latitudes would be expected to correlate with an activity cycle.[34]

Figure 2.16 gives an overview of stellar differential rotation measurements based on different methods. Solely results for late-type dwarf stars are shown, with the exception of the photometry-based observations of Hall (1991). Hall's stellar sample includes binary stars, while Donahue et al. (1996) do not discuss the multiplicity of their candidate stars; the remaining objects of Figure 2.16 are apparent single stars.

The measurements of Reiners & Schmitt (2003), see also Section 3.2, are the only direct measurements of photospheric plasma velocities (assuming the validity of the method which has been extensively verified, cf. Reiners & Schmitt, 2002a,b). The determined rotation periods for their objects are actually values of $P/sin\,i$, i.e. upper limits of the rotation period, because of the generally unknown stellar inclination i. They are not determined from photometry but inferred from stellar models and the observed value of $v\,sini$. Intrinsic to the method, their determined differential rotation measure are values of $\alpha/\sqrt{sini}$ (Reiners & Schmitt, 2003, Sec. 6), i.e. upper limits as well.[35] Reiners & Schmitt (2003, Tab. 3) also report a considerable number of stars with profile signatures compatible with rigid rotation or anti-solar rotation (alternatively a dark polar spot, cf. Reiners & Schmitt, 2002b). These stars are found in the whole rotation period range covered by their sample and are not plotted in Figure 2.16.

The measurements of Donahue et al. (1996) shown in Figure 2.16 are based on observed modulation periods of Ca II-H&K emission, i.e. they reflect the behaviour of chromospherically active regions. As noted by Donahue et al. (Sec. 5) the underlying chromospheric features may exhibit a differential rotation deviating from the photospheric plasma motions. The plotted values represent all 36 stars of their sample (covering about 100 late-type dwarfs) for which they did reliably detect modulation periods. The method is not able to detect the sign (i.e. solar or anti-solar orientation) of the differential rotation without further assumptions about the observed activity cycles. The values of α in Figure 2.16 for Donahue et al.'s measurements have been calculated using Equation 2.7 and adopting their observed minimum and maximum periods (Donahue et al., 1996, Tab. 1) as polar and equatorial rotation periods, respectively. As discussed in Section 3.3 of Donahue et al. (1996) the thus inferred strengths of differential rotation represent *lower limits* of the true differential rotation.

Hall's measurements are based on the spread of photometric modulation periods observed at different epochs for 85 stars "of different type" (including stars of different spectral type, luminosity class and multiplicity). Unfortunately the sample is not explicitly described by Hall.

The Doppler imaging results of Figure 2.16 (or from "direct starspot tracking" in the case of LQ Hya) are based on observations covering several days, up to a few weeks[36] with the exception of the value for V410 Tau (a K4 weak-lined T Tauri star) which is based on the comparison of two Doppler images taken about one year apart.

The differential rotation behaviour of evolved stars and binaries is not covered by Figure 2.16 (apart from the dotted line due to Hall, 1991). A similar plot to Figure 2.16, showing a smaller sample of RS CVn stars, can be found in Hatzes (1998, Fig. 12). All RS CVn stars in Hatzes's sample have an evolved primary component (spectral types ranging from G0 IV to K1 IV), they show a rigid or anti-solar differential rotation with $|\alpha|$ apparently increasing with increasing rotation period.

This apparent difference between the observed differential rotation of evolved stars and main sequence stars has been confirmed by more recent observations. Citing Weber & Strassmeier (2001, p. 985): "So far, there is cumulative evidence that differential rotation profiles on evolved stars (and possibly also on pre-main-sequence

thetic cases of *random* spot evolution, come to the conclusion that two-spot modelling of lightcurves can lead to sensible estimates of surface differential rotation even if the true spot pattern is much more complex than the adopted two spots. However, such results fail to evoke a deep-rooted confidence in the method.
A more promising approach is to deduce an upper limit of differential rotation from a correlation of starspot sizes with their apparent lifetimes for a specific star (Strassmeier et al., 1994). However such an approach requires extensive longterm observational data for a specific object.

[34] Donahue et al. (1996, p. 387) observe both, correlation as well as anticorrelation, with presumed activity cycle phases for different objects. Unfortunately, this is not indicated for individual stars in their Table 1.

[35] The method of Reiners & Schmitt yielding values of $\alpha/\sqrt{sini}$, i.e. an estimate depending on the unknown stellar inclination i, is illustrated by Reiners & Schmitt (2003, Fig. 11) showing a calibration of their method. It is due to their indicator of differential rotation, namely the ratio q_2/q_1 of the second and first zero of the Fourier transformed line profile, losing sensitivity in terms of α with decreasing inclination. This can be seen directly in Fig. 6 of Reiners & Schmitt (2002a).

[36] For Donati et al. (2003) this can be inferred from their Sec. 3.2, as well as their Tables. 1 and 2 when compared to e.g. Donati et al., 1999. The value of α=0.025 from Donati et al. (2003), plotted for LQ Hya in Fig. 2.16, is that which is apparently based on the longest observation time span and represents an approximate average of the individual measurements shown in their Fig. 3.

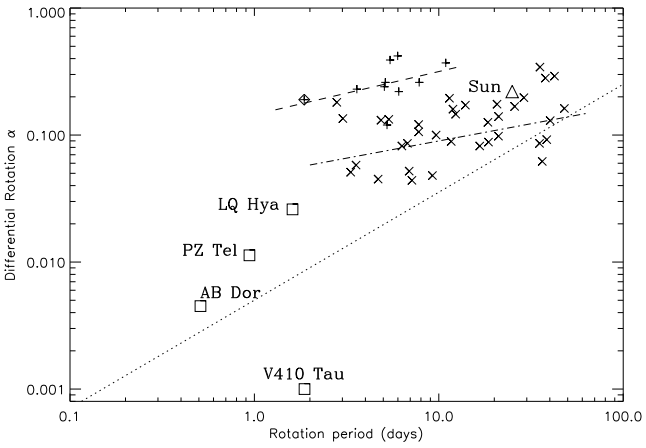

Figure 2.16: Measurements of stellar differential rotation, concentrating on single dwarf stars (companion to Fig. 7.40); the "relative differential rotation measure" α is defined in Eq. 2.6. Plusses indicate measurements by Reiners & Schmitt (2003), based on the analysis of photospheric line profiles of a sample of F4V - F9V stars; they include ψ Cap ($\diamond$) already studied in Reiners et al. (2001). Crosses represent all stars from Tab. 1 of Donahue et al. (1996), analysing the modulation periods of Ca II-H&K emission for a sample of F5V - K7V stars (see text for details). Squares mark measurements by Barnes et al. (2000, PZ Tel), Donati et al. (1999, AB Dor), Donati et al. (2003, LQ Hya) and Rice & Strassmeier (1996, V410 Tau) based on Doppler imaging or the related method of "direct spot tracking" (Collier Cameron et al., 2002). The dotted line shows the the fit given by Hall (1991, Eq. 1). It is determined from longterm photometry of a sample of 84 stars which includes binaries and giants; their rotation periods span the whole range of this diagram. The dashed and dash-dotted lines show the fits given by Reiners & Schmitt (2003) and Donahue et al. (1996) for their respective data.

stars) appear to be more complicated than on solar-type main-sequence or ZAMS [zero-age main sequence] stars."[37]

Donati et al. (2003), using "starspot tracking", report significant temporal fluctuations of the differential rotation strengths for the two ultrafast rotating single dwarfs AB Dor (K0V, P=0.51 days) and LQ Hya (K2V, P=1.61 days) with measured values of α varying by about $\pm 10\%$ between different epochs for AB Dor, observations spanning in total 6 years. Their measurements indicate a rigid or weak anti-solar differential rotation for LQ Hya at one epoch.

For the RS CVn star HR 1099 Donati et al. (2003, p. 1194) derive a "tendency of the differential rotation [...] to be solar-like" at the time of their observations. This deviates from results of Vogt et al. (1999) for the same object. Possibly, as Vogt et al. suggest, the large spots on HR 1099 show a resemblance to solar coronal holes, implying that their evolution may not significantly be influenced by the surface differential rotation i.e. by the photospheric plasma motions.

In addition, Donati et al. (2003) report significantly stronger values of α derived from magnetic features compared to those derived from photospheric "brightness" features. These recent results on the potential variability and tracer dependence of surface differential rotation would not be surprising given the analogy to the Sun (see e.g. Figure 2.5), though at present they certainly require further confirmation. However, they should be kept in mind when interpreting Figure 2.16.

Tentative summary

Judging from the available observations, the differential rotation of solar-like main sequence stars appears to be preferably solar-like (i.e. the equator rotates faster than the poles, leading to $\alpha > 0$) with a clear trend of decreasing relative strength α with rotation period. The precise functional dependence of this trend remains yet to be determined, it will have to take into account that the rotation period is certainly not the only parameter controlling the differential rotation of a star. However, limited measurement accuracies and stellar sample sizes render the search for other controlling parameters difficult at present (Hall, 1991, see also Reiners & Schmitt, 2003, Sec. 7).

Presently there is no clear evidence of anti-solar differential rotation in solar-like stars.

The differential rotation of evolved stars has only been treated shortly above. They appear to show a more complex behaviour, including cases of anti-solar differential rotation, which presumably deviates from rotation properties of main-sequence stars.[38]

[37] This view is supported by their findings for the RS CVn star KU Peg (G9II-III, P=24.9 days), comparing two Doppler images of consecutive stellar rotations (Weber & Strassmeier, 2001, Figs. 5 & 9). If the differences between the two images are attributable to differential rotation (and meridional flows) it has a solar-like orientation on KU Peg, but a much more complex latitudinal dependance.

[38] This is in conflict with theoretical models by Kitchatinov & Rüdiger (1999), see also Section 2.2.2, which predict a steady increase of the surface differential rotation α during post-main-sequence evolution (their Fig. 4) and a monotonic decrease of the angular velocity as a function of latitude (their Fig. 5). However, as shown by the same Figure, the meridional flow (MF) cell pattern of their models is becoming increasingly complex with increasing convection zone depth. If these complex MF patterns should not be appropriately modelled, the modelling of differential rotation would also break down since it depends crucially on the MF structure.

Chapter 3

Observation methods

This chapter describes methods for observing stellar surface structures and/or rotational properties of stars. Methods based solely on lightcurve analysis (including eclipse mapping etc.) are not discussed here, some related remarks can be found in Section 2.2.3. Doppler imaging is discussed in chapter 4.

3.1 Interferometry

The resolution of "direct" imaging observations is fundamentally limited by diffraction due to the finite aperture of the instrument. Until the advent of "100 m-class" optical telescopes (which can be made to operate at their diffraction limit), interferometric methods will provide the only means for "directly" imaging structures on solar-like stars.

This section summarizes a few aspects of optical interferometry, concentrating on the prospects of interferometric imaging of solar-like stars. A recent comprehensive review of optical interferometry is given by Monnier (2003), referred to as JDM03 in the following.
The angular resolution $\Delta\varphi$ of a an interferometer can be estimated from

$$\Delta\varphi = \frac{\lambda}{2\,b} \quad ,$$

where b represents the interferometer baseline. As an example, consider an interferometer with a baseline of 100 m operating at a wavelength of 1000 nm which results in

$$\Delta\varphi \approx \frac{1\cdot 10^{-6}\,m}{1\cdot 10^{2}\,m}\,\mathrm{rad} = 1\cdot 10^{-8}\cdot 57.3^{\circ} \approx 2\,\mathrm{mas} \quad (3.1)$$

with 1 mas = 1/1000 arcsecond = $1/(3.6\cdot 10^{6})$ degrees.[1] On the other hand, resolving features on the surface of a star of solar radius at a distance of a few 10 pc (which serves here as a typical distance of a highly active comparatively bright solar-like star) requires an angular resolution of the order of $\Delta\varphi \approx$0.01 mas.

By varying the parameters in the estimate of Equation 3.1 an angular resolution of 0.01 mas seems achievable for optical interferometry in the foreseeable future. However, besides the available baseline, optical interferometry is limited by the achievable limiting magnitude m (potentially improved by adaptive optics, here $m \gtrsim$10 mag is envisaged for e.g. the VLTI). For interferometric *imaging*, in addition the "(u,v) plane coverage" is crucial for the amount of image details that can be reconstructed from interferometric observations.

Aspects of interferometric imaging

In the following, the concept of the (u,v) plane is only superficially outlined to the degree required for the present discussion (see JDM03, Sec. 2 for references to more comprehensive discussions). The fundamental measured quantity of a stellar interferometer is somewhat misleadingly termed *visibility*, it is defined as the ratio of the amplitude of the interference "fringes" to their average intensity (JDM03, Eq. 5).[2]

Each available baseline orientation (vector) relative to the object contributes one value of the visibility. The relation between these visibility values and the image to be reconstructed is given by the Van Cittert-Zernike theorem (JDM03, Eq. 6); it states that the observed visibilities are the values of the *Fourier transform* of the "true" image brightness at the baseline vectors "suitably projected" onto the plane of the sky coordinates. This "suitable projection" defines the (u,v) plane (illustrative one dimensional examples are found in Fig. 2 of JDM03). This concept can be extended to include information on the phase of the fringe pattern in addition to its amplitude, leading to *complex visibilities*.[3]

[1] The "Very large telescope interferometer" (VLTI) allows baselines of up to 130 m. Currently planned future instruments reach up to baselines $\lesssim$1000 m (JDM03, Tab. 3), this includes NASA's space-based "Stellar imager".

[2] There are different ways to combine the interferometer beams and actually observe the interference fringes (JDM03, Sec. 3.3.3). The currently most used for optical interferometry in astronomy is the "Michelson" or pupil-plane combination where the two beams are overlapped in a beamsplitter. Varying the pathlength difference between the two interfering beams results in a varying transmission and reflection by this beamsplitter which can be used to scan the fringe pattern.

[3] The preceding discussion applies to monochromatic light. The ob-

The different interferometer baselines required to densely sample the (u, v) plane can be achieved by using many interferometer apertures (also possible by "aperture masking", i.e. subdividing the aperture of a single telescope), rearranging individual telescopes forming the apertures or by the apparent movement of the object in the sky (JDM03, Fig. 8). For observing spots on a fast rotating star, the latter two options would easily run into timing problems (if the spot pattern on the stellar disk to be observed changes fast, first of all due to rotation, compared to the effected changes of interferometer baselines). The above first option, namely masking the aperture of a single telescope seems hardly feasible in the near future due to the above estimated required large baselines.

Presently, optical interferometric imaging results (JDM03, Sec. 4) are limited to a rather coarse surface resolution of bright (super)giant stars with angular diameters of the order of a few 10 mas (cf. e.g. Young et al., 2000, Fig. 3 for the red supergiant star Betelgeuse, m_V=0.6 mag).

Summing up, the above estimates illustrate that optical interferometric imaging of solar-like stars is feasible in principle, but appears to be out of reach for the near future.

3.1.1 CLEAN

According to the Van Cittert-Zernike theorem, if the sampling of the visibility in the (u, v) plane were continuous (and noise-free) and not restricted by the available field-of-view, the reconstruction of the image from the interferometric observations would simply afford a Fourier transform. However, such a "perfect" sampling cannot be achieved for real observations.

The real case of a (usually sparse) discrete and restricted sampling can be obtained from the completely sampled (u, v) plane by multiplying it with a "spatial frequency mask" (nonzero for the points sampled by the available baseline vectors, zero otherwise). This multiplication turns into a convolution with the Fourier transform of this mask in the image plane; the Fourier transformed mask is termed "synthesized beam" or "dirty beam" (Högbom, 1974, Eq. 2, JDM03, Sec. 2.3.2).

The Fourier transform of the sampled points in the (u, v) plane, setting all points not sampled ("all unknown spatial frequency components") to zero is called the "dirty map".[4] It is an estimate of the input image, distorted by the sidelobes of the dirty beam (illustrative examples can be found in Högbom, 1974, Figs. 1-3, and Narayan & Nityananda, 1986, Fig. 5).

The dirty beam describes the response of the dirty map to an unresolved point source in the input image (it corresponds to the point-spread-function in the terminology of direct imaging). In the language of inverse problems it describes the forward problem.

Rationale of CLEAN

The starting point of CLEAN is to assume that the input image can be approximated by a set of unresolved point sources.[5] Given this assumption, there is a simple way of making use of the forward problem knowledge: By subtracting a dirty beam from the dirty map, scaled to the amplitude of the global maximum and centered on it, and enter a corresponding point source into the image to be reconstructed. This procedure can be iteratively repeated for the dirty map resulting from the subtraction; this iteration is the CLEAN algorithm. It is supposed to "clean" the dirty map from spurious features caused by the sidelobes of the dirty beam.

Justification

For the (trivial) case of a single point source this procedure is obviously successful. However, already for two point sources it could in principle fail if the dirty beam had (pathologically) strong side lobes and the sidelobes of the two sources would overlap by chance to exceed the two local maxima resulting from the individual sources. This serves to illustrate that CLEAN is a *heuristic* algorithm in the sense that its convergence to a sensible solution cannot be generally guaranteed.[6]

servability of interference fringes is reduced by enlarging the wavelength range (bandwidth) used for interference (JDM03, Sec. 2.4). This results in a trade-off between the limiting magnitude and the (u, v) plane coverage that can be achieved.

[4] For the case of equally weighted visibilities, this "dirty map" is identical to the so-called "principal solution". I.e. it is an analytic solution of the considered inverse problem which, in the absence of further knowledge about the input image, is as good as any other (Högbom, 1974, Sec. 2). The existence of a straightforward (although in general not directly sensible) *analytic* solution is a fundamental difference to the Doppler imaging problem discussed in Chapter 4.

[5] Citing Högbom (1974, p. 418): "A typical high-resolution map can usually be described by saying that it is empty but for certain exceptions which can be specified in a table."

[6] In the words of Högbom (1974, p. 420): "Observe that the interpretation of the dirty map in terms of a point source in an otherwise empty piece of sky is not based on synthesis theory."
This heuristic nature of CLEAN is not altered by the considerations of Schwarz (1978) who discusses a "mathematical-statistical" description of CLEAN. Schwarz develops an elegant interpretation of CLEAN as an iterative least-squares fit of sines to the observed visibilities. However, the "convergence criterion" of CLEAN which is discussed by Schwarz is not given any "practically relevant" interpretation. The convergence criterion for the realistic observational case of a finite sampling of the (u, v) plane appears to hinge on the case discussed in his Section 6.3 for which no *general* proof is given.

One way to reduce the unfavourable impact of "misplaced" point sources in the solution image is to reduce the *loop gain* g (Högbom, 1974), i.e. slow down the convergence by scaling the subtracted dirty beam only to a fraction $g < 1$ of the selected maximum.

The discussions of CLEAN found in the literature treat its application to interferometric observations, i.e. specifically in conjunction with Fourier transformed data. This applies to discussions of CLEAN's treatment of unobserved regions of the (u, v) plane ("unmeasured spatial frequencies", e.g. Högbom, 1974, Sec. 3); it also applies to the interpretation of CLEAN as a local optimization procedure (Schwarz, 1978, Secs. 6 & 7). For the application of a "CLEAN-like" algorithm to Doppler imaging (which is based on a transformation between image and data space completely unrelated to a Fourier transform) no immediate use of these aspects was found during this work. As a consequence, these aspects of CLEAN are not further discussed in Chapters 4 and 5.

3.2 Line profile analysis

This section gives a brief outline of the Fourier-transform-based line profile analysis developed by A. Reiners (Reiners, 2002), based on the pioneering work of D. Gray (Gray, 1977, 1988, 1992). A short outline of line profile broadening mechanisms can be found in Section 5.4, especially Section 5.4.3. Observational results of Reiners' profile analysis concerning differential rotation are discussed in Section 2.2.3.

Assuming that the spectral lines of a star are dominantly broadened by the star's rotation, the profile shape depends significantly on the surface rotation law (i.e. the dependence of the angular velocity on the surface latitude). This is illustrated in Figure 3.1: Assuming the equatorial angular velocity as fixed, "switching on" a solar-like differential rotation ($\alpha > 0$, i.e. the angular velocity decreases from the equator to the pole, see Equation 2.6) leads to a slow down of the surface regions away from the equator compared to rigid rotation. This slow down results in an increased contribution to the central regions of the disk-integrated line profile, causing an increase of its cental depth (the equivalent width remaining constant). Anti-solar differential rotation ($\alpha < 0$, i.e. "speeding up the pole") has the opposite effect, leading to a shallower line profile.

The profile deformation effected by differential rotation depends on the surface differential rotation law (adopted as "solar-type" by Reiners, i.e. a $\sin^2$ dependence of the angular velocity on latitude) and on the stellar inclination ($i = 0°$ corresponds to a pole-on observation, $i = 90°$ to an equator-on view of the star). As illustrated by Figure 3.2, the profile deformation "strength" decreases with an increasing inclination (i.e. it is weakest for an equator-on observation).

So far, deducing differential rotation from the line profile shape (given a sufficient rotational broadening) appears as fairly easy. However, this is not the case, because other stellar (atmospheric) parameters influence the shape of the line profile as well. If the line broadening is clearly dominated by rotation, the strongest additional influence comes from the limb-darkening, as shown in Figure 3.3. As can be seen by comparing the profiles of the same figure to those of Figure 3.1, the effect of limb darkening on the line profile is quite similar to that of differential rotation for (realistic) moderate differential rotation and high to intermediate stellar inclinations.

Following Gray (1992, Chs. 12 & 18), it can be fruitful to analyze the Fourier transform of the line profile instead of the profile "itself". Several reasons support such a procedure: (a) Spectral line broadening mechanisms can be well approximated by convolutions, these convolutions turn into (arithmetically simple) multiplications in the

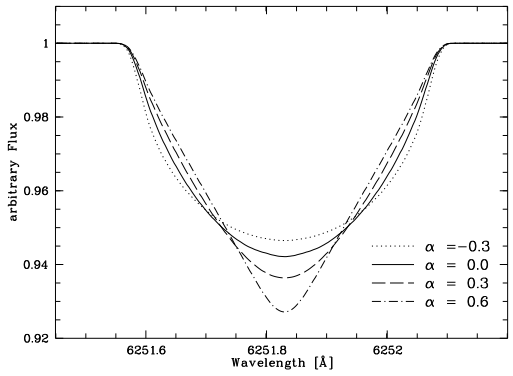

Figure 3.1: Modelled absorption line profiles for a projected rotational velocity of $v \sin i = 12\,\mathrm{km/s}^{-1}$ adopting a linear limb darkening with $\epsilon = 0.6$ and an inclination $i = 90°$. Different cases of differential rotation are indicated by the annotated line types. From Fig. 3 of Reiners & Schmitt (2002a).

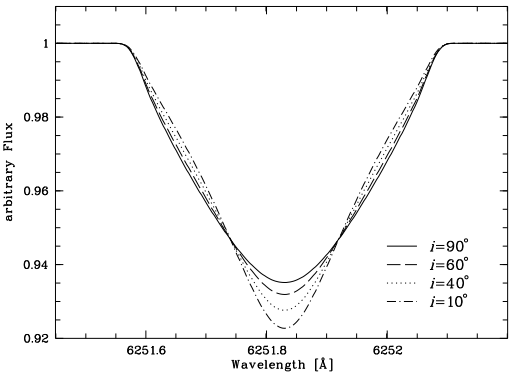

Figure 3.2: Absorption line profiles as in Fig. 3.1 for $\epsilon = 0.6$ and "strong" differential rotation ($\alpha = 0.35$). Different inclination angles, adopting a constant $v \sin i$, are indicated. From Fig. 4 of Reiners & Schmitt (2002a).

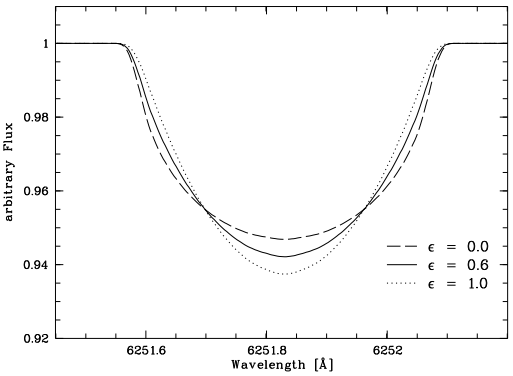

Figure 3.3: Absorption line profiles as in Fig. 3.1 adopting rigid rotation ($\alpha = 0$) and an equator-on observation ($i = 90°$). Three different values of the linear limb darkening parameter ϵ are indicated. Note the qualitatively similar deformations to the moderate differential rotation cases of Fig. 3.1. From Fig. 2 of Reiners & Schmitt (2002a).

Fourier domain. In particular, due to this multiplicative combination of broadening processes, zeroes introduced into the Fourier transform of the profile remain unaffected by other broadening processes. (b) Peak locations etc. measured in the Fourier domain can be turned into suitable *scalar* measures of the profile shape (e.g. Gray, 1992, Fig. 18.8). (c) Random ("white") noise is elegantly treated in the Fourier domain (e.g. Gray, 1992, Fig. 12.18).

Figure 3.4 shows Fourier transforms of the line profiles of Figure 3.1. As noticed by Reiners, the ratio q_2/q_1 of the second and first zero of the Fourier transformed line profile is a suitable measure to "quantify" the large-scale profile deformation, it is particularly sensitive to differential rotation. Given an unblended symmetric line profile (Reiners & Schmitt, 2003, Sec. 3), undisturbed by spots etc. and observed at sufficiently high spectral resolution and low SNR, the ratio q_2/q_1 can be calibrated as a measure of differential rotation, as illustrated in Figure 3.5.[7] This calibration (Reiners & Schmitt, 2002a, Sec. 2) uses synthetically modelled line profiles based on analytic approximations of the considered (non-rotational) line broadening mechanisms, the adopted (linear) limb darkening and the adopted solar-type differential rotation law.

Naturally, the above mentioned ambiguities of the line profile shape, with respect to inclination and limb-darkening, also affect the "deformation measure" q_2/q_1. As a result, the determined values of α depend on the (generally not directly known) stellar inclination and on the limb darkening (which is difficult to model in detail). However, broad intervals can be found for q_2/q_1, which cannot be achieved by rigid rotation under the mentioned assumptions, irrespective of the stellar inclination and linear limb darkening coefficient (these intervals are delimited by the dotted lines in Figure 3.5).

Other mechanisms than those considered above influence the large-scale line profile. Two scenarios, one of pronounced surface inhomogeneities (symmetric configurations of dark spots, Reiners & Schmitt, 2002b) and the other of extremely fast rotation (leading to a non-spherical shape of the star and gravity darkening, Reiners, 2003a) have been studied. These studies have confirmed the validity of the method, their results can be roughly summarized as follows (see the given references for details): Dark polar spots (also leading to a "flat-bottom" line profile core) can mimic anti-solar differential rotation using the measure q_1/q_2; other reasonable symmetric spot configurations are unlikely to mimic differential rotation in a similar way. For late-type stars, unrealistically fast rigid rotation (close to, or exceeding the break-up velocity) appears to be required to mimic a differential rotation signature in the line profile deformation as measured by q_1/q_2.

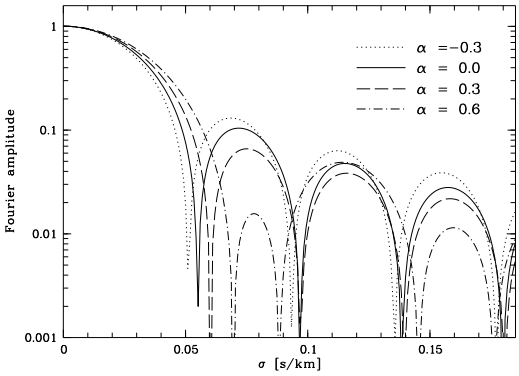

Figure 3.4: Fourier transforms of the line profiles shown in Fig. 3.1, using the same line types. For the Fourier transform the wavelength scale of the line profiles was converted into a velocity scale ($\Delta v = c \cdot \Delta\lambda/\lambda_0$, relative to the central wavelength λ_0), this results in the reciprocal velocity units on the x-axis here. Note the sensitivity of the zeroes of the Fourier transform to varying differential rotation "strengths" α. The position of the smallest zero is referred to as q_1 by Reiners, the second smallest zero as q_2. How many sidelobes can be analyzed in the Fourier transform of the line profiles depends on the quality and resolution of the spectra as well as on the stellar projected rotational velocity (cf. e.g. Reiners et al., 2001, Fig. 3). From Fig. 3 of Reiners & Schmitt (2002a).

[7] The demands on input spectra quality depend on the $v \sin i$ of the star to be analyzed; they are "high" for practical standards. As an example, a spectral resolution of R=235 000 and a SNR of about 800 was used in the case of Reiners et al. (2001, Fig. 3). Cf. also Gray (1988, Fig. 2.6).

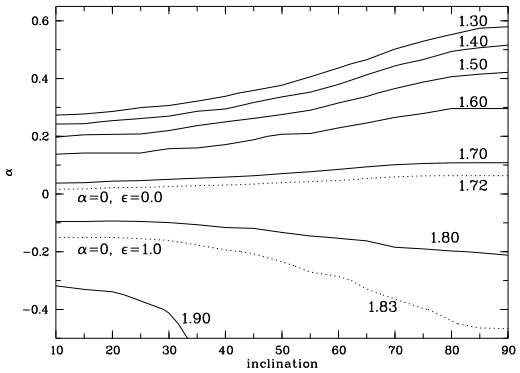

Figure 3.5: Calibration of the Fourier-transform-based line profile analysis in terms of differential rotation, based on a model grid of synthetic line profiles. Solid lines belong to the annotated constant values of the "profile deformation measure" q_2/q_1 as a function of stellar inclination i and differential rotation "strength" α, adopting a linear limb darkening with $\epsilon = 0.6$. The dotted lines delimit the interval of values of q_2/q_1 which can be accessed by rigid rotation *irrespective* of the adopted linear limb darkening. Fig. 6 of Reiners & Schmitt (2002a).

3.3 Asteroseismology

Inferences about the interior of the Sun can be made by studying its oscillations. In analogy to the application of sound waves for the study of the Earth's interior, such studies are called helioseismology. Helioseismology, apart from some information available from neutrino observations, offers the only "direct" means to investigate conditions *inside* the Sun.[8] The extension of these methods to stars other than the Sun, called *asteroseismology*, is presently rather limited. The potential and limitations of asteroseismology are discussed in the end of this section.

The following discussion conveys the basic aspects of rotation measurements using helioseismology, including some aspects of helioseismology as an *inverse problem*. A concise review can be found in Christensen-Dalsgaard (2002), indicated by CDG02 in the following. Foukal (1990, Secs. 1.6, 4.4, 7.4 & 7.5) provides a basic introduction to solar oscillations. Some useful remarks and references are supplied by Schrijver & Zwaan (2000).

The Sun acts as a resonator for a complex spectrum of oscillation modes. These oscillations are presumably excited by the (near) surface convection, supplying flows at near-sonic speeds with a broad frequency spectrum (CDG02, Sec. V. F). The strongest modes, essentially standing sound waves, are called p-modes (because pressure is their dominant restoring agent). They are concentrated around frequencies of 3 mHz ("5-min oscillations") at wavelengths greater than about 0.01 $R_\odot$. The resulting oscillatory surface displacements are predominantly radial and can be observed in the Doppler shift of a photospheric spectral line (CDG02, Sec. VI. A). However, the low velocity amplitudes of several 100 m/s require refined observation techniques including filtering out other velocity variations, e.g. due to granulation.

Spatially and temporally resolved observation of such Doppler shifts yields a signature of the oscillations. These observations can be combined into the frequency spectrum of the modes. Because the penetration depth into the solar interior depends on the mode, some depth information can be obtained already from this (surface position-independent) spectrum. However, to obtain spatially resolved information about interior rotation and flows, a *spatial analysis* of the observed oscillations is needed as a first step (CDG02, Secs. VI. B and X.).

The spatial analysis allows the separation of contributions from different spherical harmonic modes Y_l^m, limited by the given observational resolution and by the fact that only half of the surface is visible at a time. An example of observed frequencies ν_{nlm} thus separated is shown in Figure 3.6. For each mode the value of n gives the number of radial nodes; according to the geometry of the spherical harmonics, the indices l and m determine the number of nodal lines on the surface and their number crossing the equator, respectively.

In the absence of rotation, the frequencies of different azimuthal orders m ($-l \leq m \leq l$) for a given pair of (n, l) are degenerate. In the presence of rotation (or other departures from spherical symmetry), they split up (CDG02, Sec. V. E),[9] with a splitting $\Delta\nu$ approximately proportional to $m \cdot \Omega$. A complete description to first order in Ω leads to

$$\omega_{nlm} = \omega_{nl0} + m \cdot \int_0^R \int_0^\pi K_{nlm}(r,\theta)\, \Omega(r,\theta)\; r\, dr\, d\theta \tag{3.2}$$

with $\omega = 2\pi\nu$. Comparison with Equation 1.1 shows this to be a Fredholm equation of the first kind; actually the determination of the rotation law $\Omega(r,\theta)$ from the observed mode frequencies ω_{nlm} is an inverse problem. The kernels K_{nlm} need to be computed from a non-rotating solar model and describe the corresponding forward problem: The calculation of the response of individual mode frequencies to rotation.

Inversion techniques of helioseismology

Since Equation 3.2 describes an inverse problem, $\Omega(r_0, \theta_0)$ can be determined by the methods described in Section 4.3. However, other methods proved better suited for helioseismic inversions (CDG02, Sec. VI. C and references there), the usually applied methods are based on so-called *optimally localized averages* (Backus & Gilbert, 1970; Press et al., 1992, Ch. 18.6).

An advantage of these methods is that the reconstructed $\overline{\Omega}(r,\theta)$ can be interpreted as the convolution of the true $\Omega(r,\theta)$ with an *averaging kernel* $\mathcal{K}$ (not to be confused with the kernels defined in Equation 3.2)

$$\overline{\Omega}(r_0,\theta_0) = \int_0^R \int_0^\pi \mathcal{K}(r_0,\theta_0,r,\theta)\, \Omega(r,\theta)\; r\, dr\, d\theta \tag{3.3}$$

The averaging kernels provide information about the (position dependent) resolution of the inversion. Illustrative examples can be studied in Schou et al. (1998, Fig. 1) and Charbonneau et al. (1999), they are the basis for error maps like Schou et al. (1998, Fig. 4, cf. also the extensive discussion of errors in their Sec. 4).[10]

[8] An "exotic" potential signature of deep solar interior rotation is reported by Sturrock & Scargle (2001) who investigate modulations of the solar neutrino flux.

[9] Basically, because the propagation velocity of waves is different in the direction of rotation and against it.

[10] Citing Schou et al. (1998, p. 396): "[The averaging kernels] become poorly localized in the deep interior and near the poles: only modes of relatively low degree penetrate the deep interior, and likewise only modes of azimuthal order m close to zero feel the near-pole

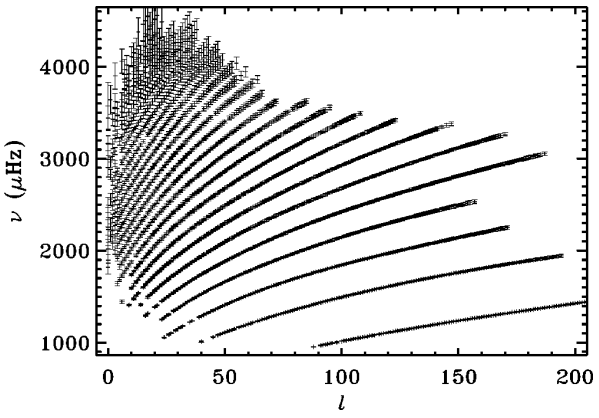

Figure 3.6: Observed (l, m)-multiplet frequencies ν of solar acoustic oscillations, analyzed and plotted as a function of spherical harmonic degree l ("$\nu - l$-diagram"). Each ridge corresponds to a radial order n, the ridge containing the lowest frequency belongs to $n = 0$, it is called the f-mode. Note that the error bars correspond to 1000 standard deviations, illustrating the precision of the measurements (Christensen-Dalsgaard, 2002, Fig. 12, showing data from SOI/MDI on board SOHO).

Local helioseismology

An alternative way of making use of the spatial information of the oscillations, is by studying correlations between different positions on the disc. This leads to the field of *local helioseismology*, in principle allowing the resolution of flows etc. below an individual surface region (CDG02, Sec. X). However, the solution of the forward problem is more complex than for the global frequency analysis described above: It requires the analysis and successful modelling of the oscillation *phases* in addition to their amplitudes. The basic idea of one of the methods of local helioseismology, called *time-distance analysis*, is inspired by terrestrial seismology: Measurements of travel times between many surface points along different paths can be combined into a subsurface reconstruction. The travel time information have to be obtained from correlation analysis of the oscillations.

Non-solar asteroseismology

The application of helioseismic methods to stars other than the Sun is called asteroseismology (CDG02, Sec. XII, including remarks on the etymology of the term).

The recent detection of solar-like p-mode oscillations on α Cen A (Bouchy & Carrier, 2001) is a promising "start"; however, asteroseismology is not only hampered by the weak (radial velocity or luminosity) signatures to be detected, but also by the restriction to disc-integrated observations. Although this restriction could in principle be overcome by space-based interferometry, it will remain valid for the "foreseeable future" (CDG02, p. 1114).

Due to the symmetry of the spherical harmonics, the restriction to disc-integrated observations leads to an upper limit of degree $l \lesssim 4$ for the observable modes (CDG02, Sec. VI B). In addition, a spatial analysis of the modes is not possible. This inhibits inferences on the interior rotation of stars other than the Sun analogous to solar observations.

As another example, Mazumdar & Antia (2001) conclude that the asteroseismic detection of stellar tachoclines from disc-integrated observations is feasible in principle, but out of reach for currently planned space-based instruments.

rotation". For the latter modes, the rotational splitting in frequency is smallest, according to Eq. 3.2. These limitations are the basis of the shaded "unreliable region" near the rotation axis in interior rotation maps like Figure 2.7.

Chapter 4

Doppler imaging (DI)

Inhomogeneities ("spots") on the surface of a rotating star cause distortions of the stellar spectral lines. Such inhomogeneities can e.g. be variations of abundance, magnetic fields or temperature. If the star is rotating sufficiently fast, the line profiles are significantly broadened by the Doppler effect and the distortions migrate through them (Figure 4.1). The shift of the distortions as a function of rotation phase contains information about the location of the features on the surface. In this way, information about the stellar surface is "modulated" into the stellar spectrum. Doppler imaging (DI) is the attempt to reconstruct a surface image from this information.

The resolution of DI is not limited by diffraction of the telescope. Instead, the resolution is determined by the projected stellar rotation velocity $v \sin i$, as well as by the spectral resolution and noise of the observed spectra. Imaging for example a star of solar radius at a distance of the order of 100 pc with a detailed resolution of surface features is feasible (e.g. Rice & Strassmeier, 2001, for the Pleiades star V1038 Tau), this corresponds to an angular resolution of the order of 0.01 milliarcseconds.[1] This is beyond the best diffraction limited resolutions of the order of 1 milliarcsecond available to interferometric methods at present (see Section 3).

Doppler imaging is an *inverse problem* (see Section 1.1). In general these problems are ill-posed, making additional "a priori" information necessary for their solution. This aspect is further discussed in Section 4.3.

Some history

Reconstruction of a stellar surface from a time series of spectral line profiles was first applied to surface abundances of Ap stars (Deutsch, 1958, 1970). Early approaches only used the equivalent width as function of phase, later Pyper (1969) included variations of the line center. The reconstruction was done analytically, expanding these quantities as a function of time into a Fourier series; the element abundance on the surface was expanded into spherical harmonics.

Using the same analytic methods as Deutsch, Falk & Wehlau (1974) divided the line profile into several segments, making partial use of shape information of the lines. Computational limitations and limited data quality made the surface resolution of these methods rather poor (e.g. Pyper, 1969, used spherical harmonics of only second degree for expanding the surface distribution).

Vogt & Penrod (1983) used an iterative trial and error scheme to fit a time series of 8 line profiles of the primary component of the RS CVn binary HR 1099. A few years later, Vogt et al. (1987) were the first to produce a Doppler image based on an automatic iterative algorithm using maximum entropy regularization.

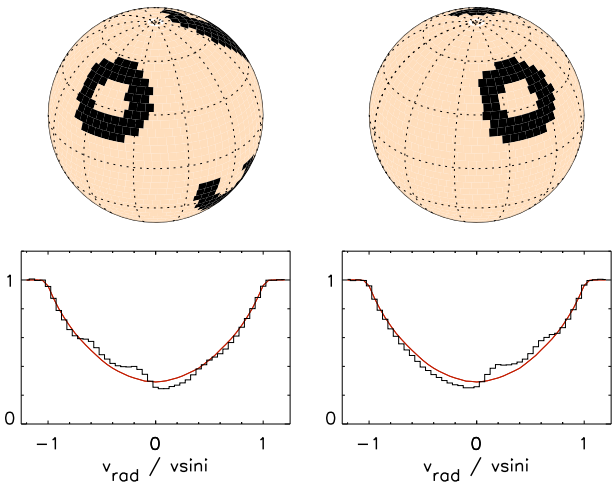

Figure 4.1: "Migrating" line profile features form the input information of Doppler imaging. The same star is shown at two rotation phases, the corresponding line profiles are shown below (black steps). An undisturbed profile is shown for comparison (red/gray).

[1] Resolving 0.1 solar radii at a distance of the order of 100 pc corresponds to an angular resolution of

$$\Delta\varphi \approx \arcsin \frac{7 \cdot 10^7\ m}{3 \cdot 10^{18}\ m} \approx 10^{-9}\ \mathrm{deg} \approx 5\ \mu\,\mathrm{arcsec}$$

This is approximately equivalent to resolving 1 mm at the distance of the moon ($4 \cdot 10^7 m$).

4.1 Rationale

If starspots are associated with line profile distortions, the rotationally broadened spectral line profiles are overlaid by a one-dimensional projection of the spots on the stellar disk (Figure 4.1). This projection is weighted by the relative contribution of different parts of the surface to the line profile. As a result of this weighting and the different velocity amplitudes of different latitudes during rotation, a *time series* of line profiles contains *two-dimensional* information. To some extent, longitude *and latitude* of the spots on the surface can be reconstructed from this information.

First, the case of a single unresolved (at the given resolution) spot on the surface is discussed. It is generalized later, with some restrictions, to complex and extended spot patterns.

Localizing a single spot

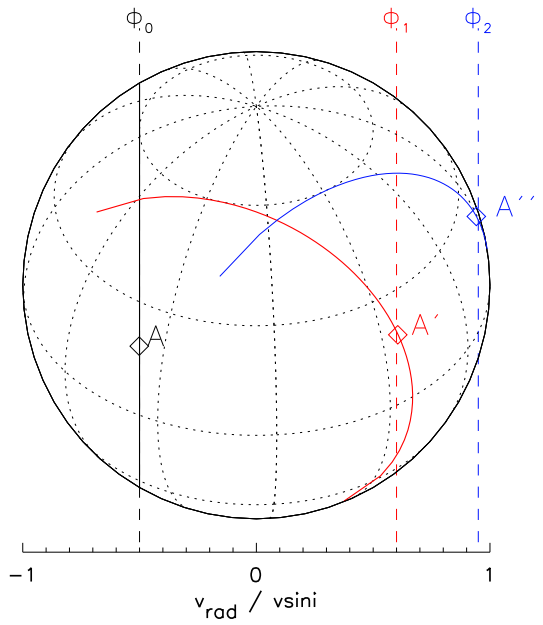

Figure 4.2: Doppler imaging: Localizing a feature "A" on a stellar surface from line profile distortions observed at three rotation phases ϕ_0, ϕ_1, ϕ_2. The solid line and the solid arcs represent the same loci on the surface, shown at three different phases; the dotted surface grid is only plotted for one phase to show the spherical geometry and the orientation of the rotation axis. See text for details.

Assume a star observed at three different phases ϕ_0, ϕ_1, ϕ_2 as shown in Figure 4.2. A resolved image would show the spot "A" consecutively at the three indicated positions. In the "Doppler imaging situation", the observer can only observe the varying *radial velocity* of the spot (i.e. the velocity component directed radially away from him).

For rigid rotation, all points on a plane parallel to the rotation axis containing the line of sight are seen at the same radial velocity. This radial velocity is independent of the stellar shape and proportional to the distance of the plane from the rotation axis. So for the situation in Figure 4.2, the observation at ϕ_0 locates the spot A *anywhere* on the vertical line drawn through A. Since the star is assumed spherical, this line actually is the plane projection of a circular arc. This becomes apparent at phase ϕ_1 where the same arc through A, fixed on the surface, is seen at a different angle. At phase ϕ_1 *the same* spot is observed at a different radial velocity. These two observations localize the feature either in the position shown or at the same longitude and latitude *south* of the equator (the pole oriented towards the observer is traditionally referred to as the north pole).

The radial velocity change between ϕ_0 and ϕ_1, i.e. for a constant phase difference, is a strictly monotonous function of the absolute value of the latitude, i.e. the angular distance from the equator. Consequently, the absolute value of the spot latitude is completely determined by the two observations. However, since the loci of equal radial velocities are symmetric to the equator, *absolutely no information* about the hemisphere of the spot can be gained from the radial velocity.

The hemispherical or "north-south ambiguity" so far can be resolved by an observation at a third phase, if the stellar inclination is not equal to 90 degrees.[2] At the phases ϕ_0 and ϕ_1 only the radial velocity information was used. Also the *amplitude* of the line profile distortion (i.e. the visibility of a spot) as a function of phase contains latitude information. An observation at ϕ_2 determines the phase when the spot vanishes from the visible hemisphere. This *limb visibility information* determines the hemisphere of the spots. Practically however, very little of this information is contained in the observed data. First of all it is observed at poor visibility near the stellar limb. It is easily lost in the noise, by slightly erroneous assumptions about the line profile, unrecognized line blends or the limb darkening. Second, it depends more strongly than the radial velocity information on a dense phase sampling of observations.[3]

[2] The stellar inclination is measured between 0 and 90 degrees. An inclination of $i = 90°$ means that the rotation axis is perpendicular to the line of sight; only in this case both poles are visible. For lower inclinations the visible pole and the corresponding hemisphere are termed *north*, their opposites *south*. Note, that these terms describe the orientation relative to the line of sight.

[3] Elements of this discussion can be found in several publications treating the basics of Doppler imaging, including Kürster (1993, Sec. 3.2). Kürster does not discuss the problem of "north-south ambiguity", his example avoids it by choosing a sufficiently large spot latitude (Kürster, 1993, Fig. 4).

Visibility information

Information gained from the profile distortion amplitude is highly ambiguous, because the size and contrast information of a spot are blended here. The distortions caused by a darker (i.e. cooler) spot at a poorly visible latitude are mimicked by a brighter and/or smaller spot at a better visible latitude. A similar ambiguity exists between spot size and contrast.

Although these ambiguities are reduced by dense phase sampling and low profile noise, removing them in practice requires additional information about the spot temperature(s), e.g. from multicolour photometry, line depth ratios or depth ratios of molecular bands.

This ambiguity has its merits: The relative stability of Doppler images against unknown stellar parameters ("nuisance parameters", see below) results from it. The image information contained in the line profile time series is largely contained in the radial velocity information. The radial velocity assigned to a line profile distortion is, apart from the projected rotational velocity $v \sin i$, independent of the nuisance parameters listed below.

Nuisance parameters

Some stellar parameters have to be known in order to perform the inversion of the observed line profile distortions into a Doppler image. Not without reason, some of them are occasionally referred to as *nuisance parameters*. Some of them have to be determined by trial and error as part of the Doppler imaging; this usually applies to the stellar inclination and the spot temperature distribution.
The parameters that need to be known are
(a) *stellar rotation parameters*: projected rotational velocity, rotation period, rotation law (i.e. angular velocity as a function of latitude, in case of differential rotation), stellar inclination
(b) *"photospheric" parameters*: limb darkening, spot temperature distribution (i.e. which temperature(s) to assume for the photospheric spots), line profile broadening parameters and the temperature dependence of the line parameters.

In the terminology of inverse problems, these parameters describe the forward problem, i.e. the synthesis of a line profile from a given spot distribution.

Differential rotation

For non-rigid rotation, the straight lines of equal radial velocity become warped. They are curved outward from the rotation axis in the (solar-like) case of higher angular velocity at the equator. In case of slower equatorial rotation, they are curved inward, towards the rotation axis. However, this effect only has to be taken into account, if the deviations from non-rigid rotation are well resolved by the velocity resolution corresponding to the spectral resolution.

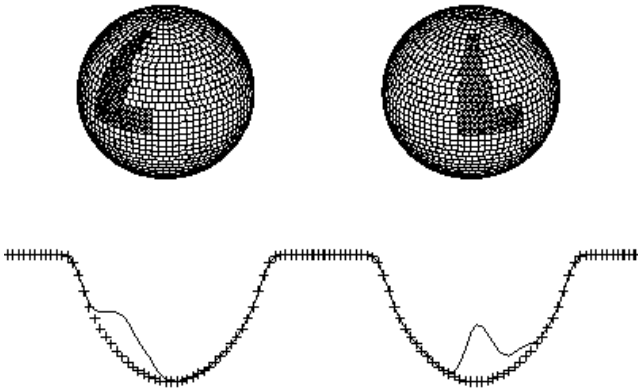

Figure 4.3: Phase-dependent "shadowing" of a spot's shape in the line profile information (Figure by A. Hatzes). See text for details.

Complex spot distributions: "Shadowing"

The above scheme of localizing features is only strictly valid for a single unresolved spot on the surface. A more complex distribution of several spots of resolved non-circular shape is the sum of such unresolved spots, but due to the one-dimensional projection of the surface for each phase, the spots may "shadow" each other for individual phases.[4] An example is sketched in Figure 4.3: For the first phase shown, the non-circular shape of the spot is not visible in the line profile (apart from a small hint of structure). At the second phase, a more complex shape is discernible in the line profile, revealing a concentration of the spot on a narrower longitude range.

The localizing scheme for a single spot remains valid, if the profile distortions of one spot(group) can be unambiguously distinguished from the distortions caused by other spot(groups). However, more and more observed phases at an appropriate spectral resolution and SNR are needed to resolve line profile structures of increasing complexity. This is confirmed by DI tests of synthetic data, described in Chapter 5. The reliability of the reconstructed image details is decreasing with an increasing complexity of the spot distribution.

Pseudoemission

Cool spots on the surface of a fast rotating star usually give rise to apparent emission features in its spectral line profiles (Figure 4.1), termed "pseudoemission bumps"

[4] Vogt et al. (1987, Sec. IV b) use the term *latitudinal shadowing* for this effect.

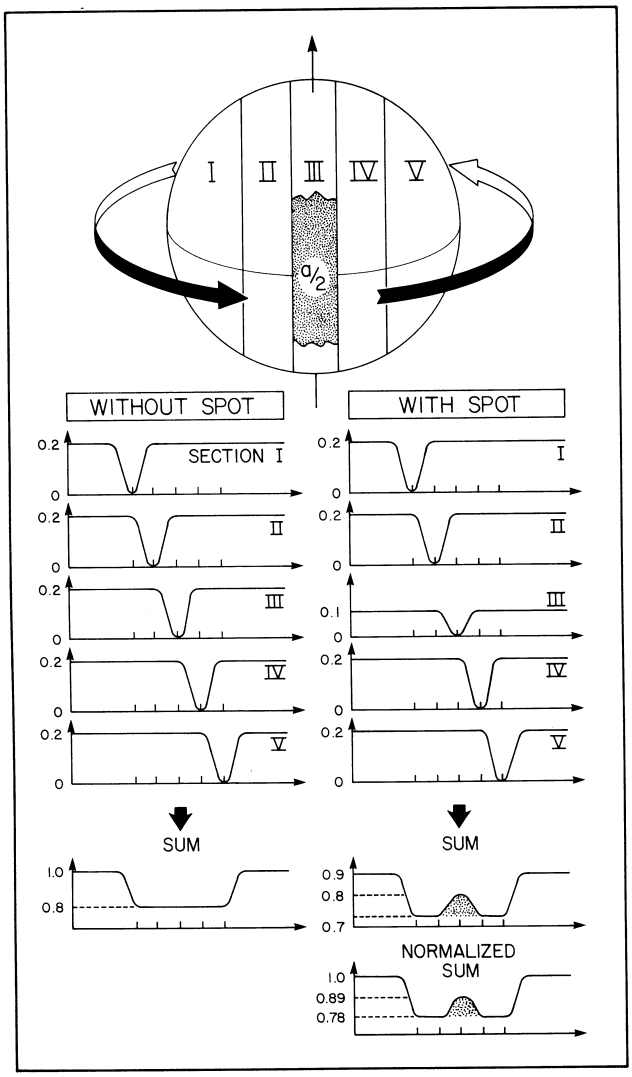

Figure 4.4: Schematic formation of a pseudoemission feature in the line profile of a rotating star, induced by a cool spot (Fig. 1 of Vogt & Penrod 1983).

in the following. The appearance of features mimicking emission in this situation is paradoxical at first glance.

The pseudoemission features are caused by "missing absorption" in the spots, Figure 4.4 illustrates how this comes about. The left column of line profiles ("without spot") illustrates the summation of line profile components from different regions of the surface, Doppler shifted due to rotation. Actually, this is a simplified analogue of the disc integration discussed in Chapter 5.

The right column shows the same process in the presence of a spot. Due to the lower continuum intensity emitted by the (colder) spot, less flux is absorbed there (or equivalently, the *absolute* line depth is reduced there). As the Figure nicely illustrates, this leads to a "bump" in the line profile. If region "III" did not emit any flux in the spotted case, the maximum of the bump would be at the resulting continuum level.

It is important to realize, that all absorption lines in Figure 4.4 have the same equivalent width W_λ; namely about one in the units of the wavelength ticks of the figure. This comes about, because W_λ is defined as normalized relative to the surrounding continuum flux F_C of a line described by the flux $F(\lambda)$:

$$W_\lambda = \int_{-\infty}^{\infty} \frac{F_C - F(\lambda)}{F_C}\, d\lambda \qquad (4.1)$$

If the equivalent width were increased in the spotted region, the amplitude of the bump would be diminished. Following the discussion of Vogt & Penrod (1983) and Kürster (1993), the following criterion applies:
For $\frac{I_c}{i_c} > \frac{w}{W}$, i.e. when the intensity contrast (ratio) is not compensated by the ratio of equivalent widths, a pseudoemission bump results. Otherwise, a dip appears in the profile; in the limiting case there is no deformation at all. Here, W and w denote the equivalent widths of the undisturbed and spot photosphere respectively, I_c and i_c the corresponding continuum intensities.

The case of the intensity contrast safely dominating the increase in equivalent width is often realized for metal lines in cool spots of solar-like stars. The resulting (approximately) constant equivalent width, independent of the spot filling factor, has one consequence to be kept in mind: A pseudoemission bump appearing in the profile is accompanied by a "sagging" of the profile as a whole; this effect can be seen in Figure 4.1. This "sagging" does not apply to line profile deformations primarily caused by changes of the equivalent width (as in the case of inhomogeneous surface element abundances).

4.2 Reconstruction capabilities

The following discussion concentrates on the *localization* of surface features by DI. The ambiguity of spot size and spot temperature (flux) is discussed shortly in Section 4.1. Complete knowledge of the stellar parameters needed for constructing a Doppler image is assumed. The effects of incorrectly assumed stellar parameters are to some degree discussed in Section 5.5, for more extensive discussions of this aspect, see the references in Section 4.2.1.

The dependence of the resolution and reliability of Doppler images on observational parameters (spectral resolution, phase sampling, signal to noise ratio "SNR") is discussed to some extent below. However, the detailed behaviour depends on the individual situation at hand. The effects of spot temperature contrasts, spot pattern complexity and effective line profile resolution can hardly be treated on a general basis. Consequently, the estimates of this section must be considered as very approximate.

For more detailed estimates, one has to resort to simulations. Simulation results for parameters similar to the observations described in Chapter 7 can be found in Section 5.5. Some more theoretical considerations along the lines of this section are discussed in Jankov & Foing (1992a,b).

The above named "shadowing" for complex spot distributions may cause neighbouring spots to wash out and merge in the reconstructed Doppler image. The deterioration of the image by this effect is usually small for good phase coverage and line profile resolution. However, it should be kept in mind that the resolution of a Doppler image does to some degree depend on the complexity and individual characteristics of the surface pattern to reconstruct.

Resolution estimation and observation layout

The line profile resolution is determined by the spectral resolution of the observations and by the stellar projected rotational velocity $v \sin i$ compared to the intrinsic (i.e. non-rotational) width of the local line profiles. Both agents, spectral resolution and intrinsic width, lead to a broadening of the line profile deformations. This results in a minimum possible width of the deformations. The ratio of this minimum width to the total (rotationally dominated) width of the line profile defines the *effective resolution* of the line profile for the purpose of DI.

To illustrate this, assume a star with a $v \sin i$ of 100 km s^{-1} and a spectral line observed at 6000 Å. If the intrinsic line broadening amounts to 5 km s^{-1} or 0.1 Å at the given wavelength, this results in a sampling of 40 resolution elements over the line profile. For the observation to resolve this, the spectral resolution would have to exceed 6000 Å / 0.1 Å$= 60\,000$.
The surface resolution resulting from a given line profile sampling can be estimated from

$$\begin{aligned} \Delta\varphi &= 2 \cdot \sin^{-1}\left(\frac{w}{W}\right) \\ &\approx 2 \cdot \frac{w}{W} \cdot 57^\circ \qquad \text{for small } \Delta\varphi \end{aligned} \tag{4.2}$$

Here w denotes the minimum resolved width, corresponding to the effective line profile resolution discussed above. $W \approx 2 \cdot v \sin i$ denotes the total (rotationally dominated) width of the line profile. This estimate yields the approximate longitude resolution $\Delta\varphi$ on the equator and the sub-observer meridian. It decreases towards the poles, because the spacing of the meridians decreases. Practical experience shows Equation 4.2 to be a useful estimate of resolution. As demonstrated below, the latitude resolution *at intermediate latitudes* is comparable to the longitude resolution for sensible combinations of phase coverage and spectral resolution.

For the numerical example above, i.e. 40 elements resolving the line profile, Equation 4.2 results in an approximate surface resolution of about three degrees. In order to make use of this resolution, two more parameter must be adjusted accordingly: exposure time and phase sampling; this is discussed in the following.

Evidently, the spots move through the field of view during exposure, the resulting blurring of the line profile deformations is called *phase smearing*. Assuming that the star of the considered example has a rotation period of one day, its angular velocity amounts to 0.25 degrees per minute. So the exposure time must not exceed about ten minutes, in order to avoid phase smearing as the reduction limiting factor. To provide a sufficient SNR at the resulting limited exposure times, comparatively large telescopes are required to perform Doppler imaging at high surface resolutions.

An upper limit of a "sensible" phase sampling density can roughly be estimated based on Equation 4.2: It yields the rotation angle that causes the radial velocity of a fixed point on the equator to a shift from one line profile resolution element to the next. So, exceeding a number $n_{\max} = 360^\circ/\Delta\varphi$ of equally spaced phases causes redundancy in the phase information of the time series, because the changes from one phase to the next are not resolved by the line profile resolution. If more phases have been observed, spectra of neighbouring phases should be summed in order to increase the SNR and reduce the computational overhead of the reconstruction. For the numerical example of this section, this results in $n_{\max} \lesssim 120$.

For practical purposes considerably lower $n_{\max}$ suffice; this is demonstrated by DI simulations in Section 5.5. Even at a rather poor phase sampling, many features of the spot distribution can be successfully reconstructed. This is due to the fact that the observation of an individual surface feature at a few, not too closely spaced phases usually suffices to model its radial velocity "behaviour". However, as stated before, to resolve increasingly complex surface patterns, an increasingly dense phase coverage is needed.

Reliably estimating the required SNR is based on a model of the stellar atmosphere and assumptions about the spot sizes and their temperature contrasts. Very roughly, for a solar-like star with $v \sin i \approx 100$ km s^{-1}, assuming a spot temperature contrast of 1000 K, line profile deformations with an amplitude of the order of 1% of the continuum flux can be expected. The typical noise amplitude should be kept "safely" below that level.

The preceeding discussion illustrates the layout of an optimum DI observation campaign for a given object and instrument. However, optimally dense phase sampling will in general be hard to provide. Most stars relevant in the context of this work have rotation periods ex-

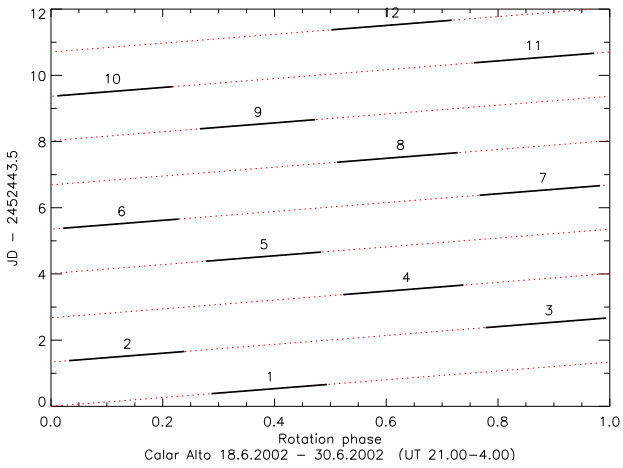

Figure 4.5: Schedule for an observation campaign of the solar-like star HD171488 (rotation period 1.34 days). Assuming a night duration of 8 hours, four consecutive nights are needed to observe all rotation phases; during four days, the star rotates quite exactly 3 times. In this example the observations cover nine rotations, each represented by a dotted line; the observation nights are numbered consecutively and are indicated by solid lines.

ceeding the duration of a single night. In those cases, due to the phase sampling limitations introduced by the object visibility and night duration, several nights are needed in order to observe most or all rotation phases. If longer gaps between the nights are needed, there is a fair chance that the total duration of the observation run exceeds the typical lifetime of the active regions on the star. In this case, the resulting Doppler image would be severely disturbed by artefacts. Certainly a rather limited lifetime of the spot distribution must be reckoned with, as clearly demonstrated by the results discussed in Chapter 7.

The main object observed in the context of this thesis, HD197890, was primarily selected because of its short rotation period; "backup" observations have been performed of a star with a longer, but still quite favourable rotation period. However, the necessary schedule of observations, shown in Figure 4.5, needs some sophistication.

If the stellar rotation period is considerably longer than the night duration, coordinated observations using telescopes on different locations on the Earth may help to improve the phase coverage. However the resulting inhomogeneity of the dataset due to the use of different instruments can be a serious problem (cf. e.g. Barnes et al., 2001).

Observation layout sanity check

One way to check the consistency of the above estimations is by comparing the resulting number of surface elements to be determined on the one hand to the number of input data points on the other.

However, this comparison can only be done very approximately, because (a) the information from different phases is not completely unrelated and the radial velocity bins close to the "line profile edges" carry practically no information. The last fact is due to limb darkening and low visibility of the corresponding surface elements. Due to the same reasons, (b) the brightness of the surface elements close to the "southern" stellar limb is practically not constrained by the input data. While (a) reduces the "effective" number of input data points, (b) lowers the "effective" number of surface elements of the solution; both facts should compensate each other to some degree. However, no attempt is made here to quantify their respective influence.

For the above numerical example, the surface resolution of three degrees corresponds to about 4600 surface elements (Section 5.4.1); depending on the stellar inclination, not all of them are visible. On the other hand, the estimated line profile sampling and upper limit of phase sampling density result in $40 \cdot 120 = 4800$ input data points. So the input and solution vectors resulting from the above estimation are of comparable dimensions. However, it should be apparent from the above discussion, that this is no more than an order of magnitude estimate.

Resolution inhomogeneity: Resolution grids

The latitude information, both from radial velocity and from visibility, becomes poorer towards the equator, i.e. with decreasing latitude. This is caused by the decreasing intersection angle of "radial velocity lines" belonging to different phases.

The *radial velocity line* belonging to a particular radial velocity resolution element $v_{\rm bin}$ (used to sample the line profile) and to a particular phase $\tilde{\phi}$ is defined as the locus of all points on the surface having the radial velocity $v_{\rm bin}$ at the phase $\tilde{\phi}$ and are visible at that phase.[5]

The intersection points of the radial velocity lines of a specific observation define the resolution of the Doppler image. These points become increasingly poorly defined for decreasing intersection angles, taking into account the "finite width" of the radial velocity lines due to the discrete wavelength sampling of the line profile.

This decrease of intersection angles towards the equa-

[5] Intersection points of radial velocity lines can e.g. be seen in Figure 4.2 where the radial velocity line of ϕ_0 (shown at three phases) intersects with two other lines at phases ϕ_1 and ϕ_2 .
See also Jankov & Foing (1992a, Fig. 11); however, their argument for a latitude bias close to the equator is hardly convincing. Actually it would lead to a "zone of avoidance" for the spots in Doppler images, which is not observed in typical DI reconstructions.

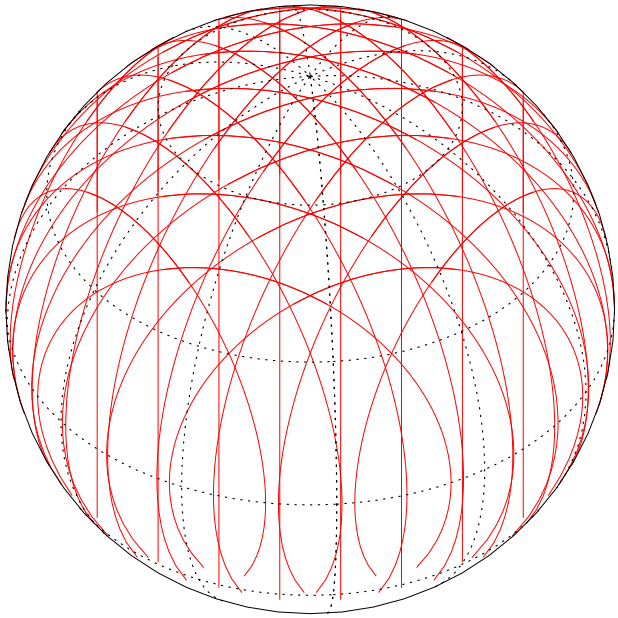

Figure 4.6: Doppler imaging resolution grid, constructed by projecting the radial velocity lines of all bins resolving the line profile at all observed phases onto the surface. The intersection points of the grid are the positions where a DI reconstruction of the given observation can localize an isolated "small" spot. This example shows the resulting grid for ten equidistantly observed phases and a line profile sampling by ten radial velocity bins; only the innermost eight of them have been used at each phase to account for poor limb visibility.

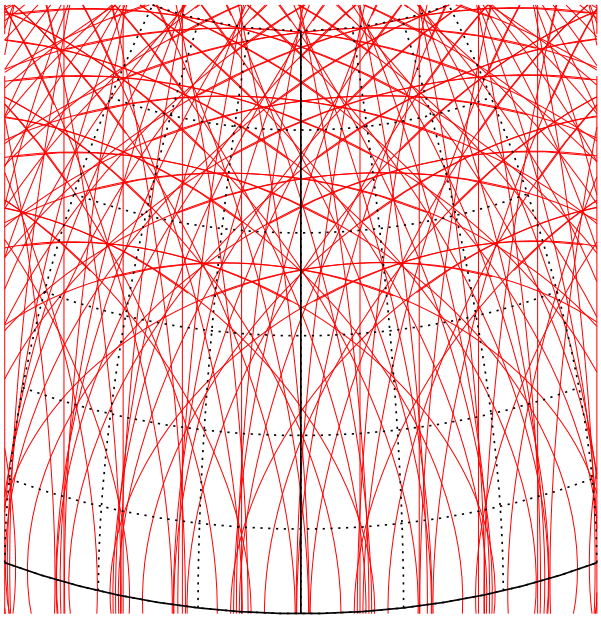

Figure 4.7: Zoomed in view of a DI resolution grid, companion to Figure 4.6. This grid is drawn for 30 equidistantly observed phases and a line profile sampling into 19 radial velocity bins. Thick lines mark the equator and the subobserver meridian. The dotted iso-longitude and iso-latitude lines have a spacing of 10°, so the intersection points of the grid have a spacing of typically less than 5° above about 25°latitude. This corresponds to the maximum attainable DI resolution from this observation when localizing an isolated feature on the surface.

tor reappears in the *Doppler imaging resolution grid* shown for an arbitrary sample observation in Figure 4.6. The decrease is a direct consequence of the spherical geometry and equally applies to the intersections of radial velocity lines with the stellar limb which determine the limb-visibility information.

> The intersection points of the resolution grid define the spot positions that can in principle be reconstructed from the input data for a specific DI observation. The grid is constructed by combining the radial velocity lines for all observed phases and for all radial velocity bins available to resolve the line profile.

Radial velocity lines corresponding to observations close to the stellar limb should not be included, because no significant profile deformations can be observed there in the case of real observations.

Actually the full resolution of the grid is only achieved for isolated, unresolved spots on the surface. As outlined in the discussion of complex spot distributions in Section 4.1, observations at more and more phases are required to reliably reconstruct increasingly complex spot patterns. For the resolution grid this means that "regions of several closely spaced" intersection points describe the resolution of the DI, instead of all individual intersection points; no attempt has been made here to quantify this.

Figure 4.7 shows a part of a resolution grid for observational parameters aiming at a higher resolution, compared to the case of Figure 4.6. This grid is constructed for 19 resolution elements of the line profile and 30 equally spaced observation phases.[6] Equation 4.2 yields about six degrees surface resolution for this line profile sampling; this is the approximate longitude spacing of radial velocity lines near the equator. The large number of nearly coinciding radial velocity lines around the equator shows that fewer observed phases would be sufficient to achieve that resolution in this case.

The pattern of radial velocity line intersection points becomes increasingly regular towards and above mid-latitudes; this corresponds to the improved resolution at those latitudes. There the typical spacing in longitude

[6] For a projected rotational velocity of $v \sin i = 100$ km/s this requires a velocity resolution of about $\delta v = \frac{200 \text{ km/s}}{19} \approx 10$ km/s; this corresponds to a spectral resolution of $R \gtrsim \frac{300\,000 \text{ km/s}}{10 \text{ km/s}} = 30\,000$. Additionally, it requires sufficiently narrow local line profiles.

and latitude of radial velocity line "intersection regions" comes close to the above estimated six degrees.

Reliability

Closely related to the resolution, image reliability in this context means judging to what certainty and degree features of the Doppler image correspond to "true" spot distributions of the original star. Since this is even harder to quantify than the resolution, it should definitely be tested by performing reconstructions of synthetic data. Only in this way the individual characteristics of the observation at hand can be taken into account.
However, the following general criteria can be used for judging the reliability of a Doppler image:

(i) The more phases contribute to localizing a feature, the more reliable it is. Resolution grids like Figure 4.6 help to judge this aspect for a given observational sampling. Those regions of the surface containing "quite well concentrated" intersection regions of several radial velocity lines, correspond to more reliable regions of the Doppler image. Conversely, regions of the resolution grid with relatively few intersection points are unreliable parts of the Doppler image.

(ii) The reconstructed Doppler image is completely based on the input information of the line profile time series. Consequently, "trustworthy" structures of the DI cannot show "more complexity" than significantly defined structures of the line profile time series. Although in a way trivial and only qualitative, this aspect is useful to keep in mind.

Error estimation of the image

A complete solution of the Doppler imaging problem would be a probability distribution of the solution surfaces for the given input line profiles.[7] Given such a probability distribution, a suitably defined standard deviation could be assigned to the value of each surface element of the solution surface. This would be a different (and more quantitative) way to treat the above discussed issues of reliability and resolution.

Such a "standard-deviation-map" is not supplied by CLDI (CLEANlike Doppler imaging, see Chapter 5), for a two-temperature solution, its equivalent would be a map giving the probability for each surface element to be "spotted".

As Piskunov & Kochukhov (2002) correctly point out, if the DI problem is treated explicitly as an optimization problem (as in the case of maximum entropy algorithms), such an error analysis is always possible: The curvature of the function to be minimized yields (formal) error estimates for the optimized parameters (cf. e.g. Press et al., 1992, Chapters 15.4 & 15.6).

The main potential weakness of this approach is that it estimates the error *completely local* (from the second-order derivatives forming the Hessian matrix) at the final solution. Consequently it fails in the case of several (more or less) isolated local minima of approximately equal value. Piskunov & Kochukhov (2002) suggest that this should not apply to a properly regularized problem. On the other hand, the above discussion of the DI resolution grid suggests that for poorly defined parts of the Doppler image (as below mid-latitudes in Figure 4.7), the behaviour of the solution may not be properly described by strictly local properties.

The problem of error estimation has not been studied analytically in the context of CLDI; presumably CLDI's approach to the Doppler imaging problem is not well-suited for that purpose (see however Section 5.6.3 for possible extensions).

In the light of the above general considerations, the problem of a reliable, practically significant, quantitative error estimate of Doppler images still appears as an open question at present.[8]

4.2.1 Applications and tests published elsewhere

A comprehensive list of Doppler images of late-type stars can be found in Strassmeier (2002).[9]

The tests described in Section 5.5 concentrate on con-

[7] This distribution is not identical to the *likelihood function* $\mathcal{L}(D, S)$, discussed e.g. by Berdyugina (1998b, Sec. 2.1), which gives the probability of an input data set D for a given (solution) parameter set S.
Instead, the hypothetical probability distribution considered here should give the probability of S for a given D. The two distributions can be related by the "principle of maximum likelihood" which is the sensible simplifying assumption that $\mathcal{L}(D, S)$ can also be used to "approximately" calculate the desired probability (Press et al., 1992, Secs. 15.1, 15.7).

[8] This statement includes to the "Occamian approach" to DI by Berdyugina (1998b). Berdyugina's approach yields formal *lower* limits of the errors of a Doppler image (Berdyugina, 1998b, Eq. 10); it does not yield any quantitative information about an upper error limit. In addition Berdyugina (1998b)'s error estimates make use of the above mentioned local curvature information of the minimized function (Berdyugina, 1998b, Secs. 2.3 & 4.1), so the above cautioning remark about local error estimates of DI also apply here.
The limited significance of these error estimates can be seen e.g. in Berdyugina et al. (1998a, Fig. 2 "December 1993"): In spite of a large phase gap of more than half a rotation, the error error map does not show any longitudinal variation; however, the image structures near the center of this phase gap at low and intermediate latitudes are undefined by the input data, so their error should be infinite in principle.

[9] Another version, updated at irregular intervals, can currently be found on the web-pages of the "Astrophysikalisches Institut Potsdam" (AIP) at *http://www.aip.de*.

ditions similar to those encountered in the observations described in Chapter 7. Experience with the "new" CLDI (CLEANlike Doppler imaging) developed in the context of this work, as well as with its "predecessor" (Kürster, 1993) show that its basic behaviour is very similar to that of other DI algorithms (see also Section 8.4).

This basic behaviour, i.e. the properties described as "reconstruction capabilities" in Section 4.2 and the reaction to wrongly adopted stellar parameters, is determined by the general properties (geometry, information loss, etc.) of the inverse problem associated with Doppler imaging. Consequently, test results of other Doppler imaging algorithms concerning these aspects also apply to CLDI.

A comprehensive review of issues concerning DI and test results is given by Rice (2002), see also references there. The following list is intended to give a compact orientation about extensive DI tests published; especially to allow efficient access to aspects not or only marginally covered by tests discussed in this work.

The tests described by Vogt et al. (1987) use synthetic input data to study the influence of data SNR, reconstruction inclination, phase coverage and spot-photosphere temperature contrast.[10] Rice et al. (1989), also using synthetic input data, concentrate on limitations of latitude recovery by DI. The influence of different regularization schemes on DI results is discussed in Piskunov et al. (1990a). The behaviour of three independent DI implementations is compared in Strassmeier et al. (1991), using the same observed input spectra.[11] The behaviour of the "old" CLDI is extensively studied in Kürster (1993).

Unruh & Collier Cameron (1995) perform a detailed investigation of the sensitivity of DI to wrongly adopted atmospheric parameters. Doppler images reconstructed from 15 different lines of the same observed input spectra are systematically compared in Stout-Batalha & Vogt (1999), including an image correlation analysis; unfortunately their phase coverage is rather sparse. Rice & Strassmeier (2000) perform extensive tests, studying the influence of data quality, phase gaps, atmospheric parameters and hot spots.

Kochukhov & Piskunov (2002) demonstrate the performance of magnetic DI, including a study of regularization influence (in the absence of a positivity constraint). They also include a short fundamental discussion of DI error estimation.

[10] Unfortunately, the reproduction quality of the figures is rather poor in the electronically available version of Vogt et al. (1987), cf. the printed version instead.

[11] Due to a rather sparse and uneven phase coverage (8-11 input spectra per DI), the attainable surface resolution was low in the case of Strassmeier et al. (1991); however, the comparison results are not very convincing.

4.3 Inversion techniques

As outlined in Section 1.1, Doppler imaging is an "inverse problem". In this context, inversion means reconstructing *some* stellar surface that "could have produced" the observed spectra. Given the limitations of Doppler imaging discussed above, generally a manifold of surfaces meet that requirement.

In mathematical terms, Doppler imaging is an *ill-posed, ill-conditioned, constrained optimization problem* (Section 1.1). Due to the ill-posed nature of the problem, the deviation between the synthesized and the observed line profiles need (and should) not be minimized to the absolute minimum. Instead, it should be brought to an "adequately low value" which depends on the accuracy of the input data (see the discussion of *proper solutions* below).

The Doppler imaging problem can be solved by suitable optimization algorithms. The algorithm needs to be "gagged" in order to ensure the mentioned "adequately close" fitting of the input data (given its quality) and avoid overfitting it. Maximum entropy DI is a powerful algorithm for this, it is further discussed in Section 4.3.1.

CLDI uses a different approach: It tries to reconstruct the stellar surface by analyzing structures of the line profile time series (using its "backprojections"). Since also CLDI iteratively makes use of the deviation between the synthesized and the observed line profiles, it behaves similar to an optimization algorithm. However, its philosophy is slightly different; it does not *explicitly* minimize any function.

Response matrix formulation

In the case of Doppler imaging, the integral of Equation 1.1 describes the surface integration of the local line profiles. The line profiles $\mathbf{D}$ observed at n phases are "produced" by a stellar surface described by $\mathbf{I}$. The latter is the stellar "image" to be reconstructed, i.e. the surface distribution of a parameter to be mapped. This "mapping parameter" is some measure of "spottedness", e.g. surface temperature, a brightness measure, a filling factor, etc.
Writing the surface integration as the operator $\mathcal{R}_{op}$, Equation 1.1 becomes

$$\mathbf{D} = \mathcal{R}_{op}\left(\mathbf{I}\right) \tag{4.3}$$

$\mathcal{R}_{op}$ maps a function describing the stellar surface onto a vector of functions, with each component containing a line profile as a function of wavelength for one observation phase

$$\mathcal{R}_{op} : \mathcal{C}(\Re^2 \rightarrow \Re) \rightarrow \mathcal{C}(\Re \rightarrow \Re^n)$$

Here $\mathcal{C}$ is used for the continuous functions between the designated real number spaces. The properties of $\mathcal{R}_{op}$ will

not be studied further. If the local line profile shape is not a function of the mapping parameter (i.e. it is independent of the value of $\mathbf{I}$)[12] and if the local line profile continuum flux can be approximated by a linear function of the mapping parameter, Equation 4.3 can be written as a matrix equation[13]

$$D = \mathbf{R} \cdot I \tag{4.4}$$

For this, the line profiles need to be discretely sampled and assembled end-to-end giving a *one-dimensional* vector D. Likewise, the surface has been divided into a discrete grid of zones whose mapping parameter values have also been packed into a one-dimensional vector I . The matrix $\mathbf{R}$ is the so-called *response matrix*. At the given resolution it describes the observable data as a function of the stellar surface.

Formally, solving the Doppler imaging problem means "inverting" the response matrix. Unfortunately, it is in general not invertible; in real cases it is usually not a square matrix either.

Solutions

Assume that a set of line profiles $D_{obs} = (d_1, d_2, \ldots, d_N)$ has been measured as a vector of N discretely sampled values.

Further assume that the d_i are uncorrelated and are normally distributed about the (unknown) "true values" D_{true} with variances σ_i.
In that case, the χ^2-measure

$$\chi^2[D] = (D - D_{true})S^{-1}(D - D_{true})^{\mathsf{T}} \tag{4.5}$$

is a sum of N terms, because the covariance matrix S is diagonal in this case, containing the squared variances

$$S = \mathrm{diag}(\sigma_1^2, \sigma_1^2, ..., \sigma_N^2)$$

If D for a moment is chosen as a random variable describing the normally distributed measurements, $\chi^2[D]$ would be a sum of N normally distributed random variables, each with mean zero and variance one. Then $\chi^2[D]$ would be a random variable with a probability distribution of a χ^2-distribution of N degrees of freedom. The expectancy value of this distribution is N, its standard deviation is $\sqrt{2N}$.
By minimizing

$$\chi^2[I] = (D_{obs} - \mathbf{R} \cdot I)S^{-1}(D_{obs} - \mathbf{R} \cdot I)^{\mathsf{T}} \tag{4.6}$$

the deviation between the modelled and the observed line profiles is minimized. The notation $\chi^2[I]$ conceals that the value also depends on the dataset D_{obs}, the measurement errors and the "physics and geometry" described by $\mathbf{R}$.

For (i) normally distributed errors and (ii) a linear model completely describing the problem which is (iii) parametrized by independent parameters, Expression 4.6 (suitably "regularized") is distributed as a χ^2 probability distribution (Press et al., 1992, Ch. 15.6). While (i) and (ii) are satisfied here by assumption, condition (iii) poses problems: The components of I, i.e. the "values" of the dicretized surface, cannot directly be considered as independent parameters controlling the modelled line profiles $\mathbf{R} \cdot I$ (see also the discussion of χ^2-regularization in Section 5.5).

However, it is common to use Expression 4.6 to judge the reconstruction quality. A surface reconstruction is considered "appropriately" good, if $\chi^2[I] \approx N$. This is reasonable (instead of strictly justified) assuming that the model contained in $\mathbf{R}$ describes the true line profiles well (condition (ii) above). Assuming further, that these true line profiles are smooth on the scale of the sampling, the small-scale structure of the observed profiles will be dominated by noise, instead of surface information.[14]

In this case, the expectancy value of the χ^2 calculated from Equation 4.6 is N. Fitting the line profiles to a χ^2-level far below N means that the noise structure is fitted, instead of the spot-induced deformations of the line profiles.

All stellar images I with a $\chi^2[I]$ in the range of $N \pm \sqrt{2N}$ are considered *proper solutions* of the given Doppler imaging problem.

4.3.1 Maximum entropy DI

Using the above notation, solving the DI problem does *not* mean looking for a global minimum of $\chi^2[I]$, called the *principal solution*. Instead, it requires minimizing $\chi^2[I]$ with the constraint of $\chi^2[I] \approx N$. This constrained optimization is performed by a scheme called regularization.

Regularization

Instead of directly minimizing $\chi^2[I]$, a suitable additional function f is introduced

$$\chi^2[I] + \lambda f(I) \stackrel{!}{=} \min \tag{4.7}$$

which leads to a family of solutions, parametrized by λ. From this family one selects a solution satisfying $\chi^2[I] = N$ by adjusting λ appropriately.

[12] This implies a constant equivalent width for local line profiles with a nonzero continuum flux.

[13] An example of a resulting response matrix is shown in Vogt et al. (1987, Fig. 2). Under the named assumptions, $\mathbf{R}$ can directly be used for line profile synthesis via Equation 4.4.

[14] The smoothing effect of this on the solution of the DI problem is discussed by Hendry & Mochnacki (2000).

This f is called a *regularizing functional* (less usual *stabilizing functional*). In the case of discretely sampled functions, its input argument is simply a vector, and f is a function. It stabilizes the search for the solution, because in the ideal case, it selects a single solution from the manifold of proper solutions. In this way it removes the ill-posedness of the problem, albeit at a price: All solutions not "favoured" by the regularizing function are discarded.

Consequently, the function f can be used as a *penalty function*. This means it should be minimum for solutions known to be "good" due to some *a priori* knowledge or assumptions about the problem. Thus, by choosing a suitable function f, unwanted solutions (in the light of the a priori knowledge) can be suppressed.

Information theoretical aspects of the matter just described have been important for the historic development of maximum entropy methods (Jaynes, 1957, 1982; Press et al., 1992). This view emphasizes that the function f supplies *additional information* which is "missing" in the observed data to completely constrain the solution. At this point it makes plausible that the influence of the regularizing function diminishes with decreasing noise of the data. However, it *does not vanish in the ideal case of noisefree data*, because of the inherent ill-posedness due to the geometry of the DI problem (Section 4.2).[15]

In order to stabilize the solution process f should favour the "smoothness" of the solution (Lucy, 1994). This is reasonable, because small-scale variations of the solution are usually not determined by the "true" information of the input data. Instead, they tend to be sensitive to small-scale variations in the data, i.e. they are unstable against noise.

In the following list of regularisation functions, the M elements of the discretized surface are written as

$$I = (u_1, u_2, \ldots, u_M)$$

The "total intensity" of the image is denoted by U

$$U = \sum_{j=1}^{M} u_j$$

The *zeroth-order* regularisation function (Press et al., 1992) reads

$$f = I \cdot I = \sum_{j=1}^{M} u_j^2 \tag{4.8}$$

The *Tikhonov* regularisation function is

$$\begin{aligned} f &= I \cdot (\mathbf{B} \cdot \mathbf{B}^{\mathsf{T}}) \cdot I \\ &= \sum_{j=1}^{M-1} |u_j - u_{j+1}|^2 \end{aligned} \tag{4.9}$$

[15] An example of the influence of the regularization for "noisefree" input data is given in Piskunov et al. (1990a, Fig. 2).

Here $\mathbf{B}$ is the $(M-1) \times M$ first difference matrix

$$\mathbf{B} = \begin{pmatrix} -1 & 1 & 0 & 0 & \cdots & 0 \\ 0 & -1 & 1 & 0 & \cdots & 0 \\ \vdots & & & \ddots & & \vdots \\ 0 & \ldots & 0 & -1 & 1 & 0 \\ 0 & \ldots & 0 & 0 & -1 & 1 \end{pmatrix}$$

Finally, the *maximum entropy* regularisation function, is defined as

$$f = \sum_{j=1}^{M} u_j \ \ln(u_j/U) \tag{4.10}$$

Actually, Function 4.8 works, but is not normally used in practice. It satisfies

$$\|a\| > \|b\| \quad \Leftrightarrow \quad f(a) > f(b) \tag{4.11}$$

thereby favouring solutions of low total intensity U. It is "weakly" smoothing, because it penalizes high values of the u_j with an exponent exceeding one; thus it discourages solutions oscillating around smooth solutions of comparable χ^2.

The *Tikhonov* regularisation function 4.9 is a straightforward choice, because it measures *local contrasts* of *neighbouring* pixels. It favours locally smooth solutions by penalizing high first order derivatives. In the given form it only measures pixel-to-pixel contrast to only *one* neighbour pixel, but it can be generalized to higher order derivatives. The term "Tikhonov-like", used in the following, includes this generalization.

If controlling small-scale instabilities of the solution is the primary aim of the regularisation, "Tikhonov-like" regularisation functions are a good choice. An example is the sLSD (*selective* least-squares deconvolution) algorithm discussed in Chapter 6.

Maximum entropy regularisation

As mentioned above, the maximum entropy regularisation function was originally inspired by information theoretical considerations. Expression 4.10 is (at least formally) the negative of an "entropy-like" measure containing the image pixel values. One motivation of the method is to presume that it *actually is* a sensible measure of information content of the image. In that case minimizing expression 4.10 minimizes the information content of the solution image. By adjusting λ in Equation 4.7, this minimization is carried as far as the information contained in the observed data allows. As far as the above presumption is valid, the maximum entropy solution thus acquired can be said to be "maximally noncommittal with regard to missing information" (Jaynes, 1957).

The information theoretical context of expression 4.10 is further discussed below. However, it appears that the power of maximum entropy regularization can be understood without it. Instead, the following properties of Expression 4.10 appear to be vital for its operation. Other functions sharing these properties can be used yielding practically indistinguishable reconstructions (Narayan & Nityananda, 1986; Press et al., 1992).[16]

1. Constant solution trend: For a given total intensity $U = U_0$, the Function 4.10 is minimized for the constant solution $u_j = U_0/M$. In this way, non-constant solutions are penalized.

2. No neighbourhood treatment: Expression 4.10 does not explicitly compare neighbouring pixels, *it has the same value for any permutation of the solution pixels*. This makes it less sensitive than "Tikhonov-like" regularisation schemes to local contrasts, e.g. (quite) isolated bright pixels. If the desired solutions may contain such pixels, this is an advantage.

3. Enforcing positivity: Unlike Functions 4.8 and 4.9, Function 4.10 enforces a positive solution $u_j \geq 0$, because $\frac{\partial f}{\partial u_j}$ approaches negative infinity as any u_j approaches zero. This makes potentially cumbersome explicit sign constraints of the optimization unnecessary.[17]

4. Nonlinear first derivatives: This is relevant if the observables (i.e. the input data of the optimization) are Fourier transforms of the image to be reconstructed; this is the case for interferometric observations (see Section 3.1). The nonlinear first derivatives of f create nonzero values for unmeasured frequency components; this suppresses ripple otherwise introduced by localized sources (e.g. point sources). For a detailed discussion see Narayan & Nityananda (1986).

Actually, the Function 4.10 has an additional property helping to stabilize the solution process. As zero-order regularisation, and unlike "Tikhonov-like" regularisation schemes, *maximum entropy regularisation favours solutions with low total intensity* U; this is a direct consequence of Function 4.10 fulfilling Condition 4.11. This is beneficial for many applications; in the case of Doppler imaging it potentially introduces a *sub-observer latitude bias* of the reconstructions, as discussed further below.

There has been an intensive and rather widespread dispute about the relevance of the information theoretical justification of the maximum entropy regularisation. There have been statements like "Entropy maximization is the only consistent regularization technique for images" (Gull & Skilling, 1983, p. 267). No attempt is made here to review that discussion.[18] From a practical viewpoint, at least in retrospect, this dispute seems partially obsolete for three reasons.

(a) As outlined above, there are other regularizing functions sharing the "relevant" properties 1.-4. of function 4.10. They can be used instead with practically indistinguishable results (Narayan & Nityananda, 1986). In the context of information theory or statistical mechanics, these functions have different interpretations or no interpretation at all.

(b) Concerning Doppler imaging, tests using synthetic input data indicate that maximum entropy reconstructions yield well comparable results to Tikhonov-regularized reconstructions (Piskunov & Wehlau, 1990) and CLDI-based reconstructions (Kürster et al., 1994 and Chapter 8.4), certainly in the case of low-noise data.

(c) Regarding the invariance of expression 4.10 for any scrambling of the solution pixels (item 2 of the above listed properties), it does not necessarily measure what an unprejudiced observer would consider the "*complexity*" of the solution. As an example, assume two images with the same number of nonzero pixels. In one image, the pixels of this image are arranged as a single, coherent spot. In the other image, they are randomly distributed over the image. Although their values assigned by Function 4.10 are the same, their respective "complexity" can be different depending on a strict definition of the term. Indeed, proper input data should discern unambiguously between the two example images. Anyway the fact remains, that "complexity" or "simplicity" are rather fuzzy concepts and not easily measured by a simple function; statements about the "simplest" solution to a given problem should be considered with some care.

Sub-observer latitude bias

To the degree the reconstruction image is not constrained by the input data, it seems reasonable to look for a solution of minimum total spot filling factor. This leads to a potential preference of the reconstruction to place spots

[16] Examples are

$$f = \sum_{j=1}^{M} \sqrt{(u_j/U)}$$

$$f = \sum_{j=1}^{M} \ln(u_j/U)$$

[17] For applications where the positivity constraint is not appropriate (e.g. Zeeman-Doppler imaging of magnetic fields), expression 4.10 can be modified (Piskunov & Kochukhov, 2002).

[18] The conflicting positions can be studied for example by comparing Gull & Skilling (1983) and Jaynes (1982) on the one hand to Narayan & Nityananda (1986) and Cornwell (1983) on the other. A compact discussion can be found in Titterington (1985).

near the sub-observer latitude, because this is where a spot of given size and contrast has the strongest influence on the line profile.

As a consequence of Condition 4.11, this is the case for maximum entropy regularized DI reconstructions. As outlined in Section 5.2.2, this tendency is also present in CLDI reconstructions; however, as discussed in Section 5.5.5, it is very small and can be neglected for densely phase-sampled data.

However, it should be kept in mind when interpreting poorly constrained Doppler images and measuring the latitude distribution of spots based on them.

Use of the response matrix

Because of the key role of the response matrix $\mathbf{R}$ for CLDI, its use in different implementations of maximum entropy Doppler imaging is briefly examined in the following.

While $\chi^2[I]$ in Equation 4.7, describing the "cost function" to be minimized, is evaluated in data space (i.e. among the line profiles), the regularization function $f(I)$ is evaluated in image space. For determining the partial derivatives of the cost function needed for the optimization, "feedback from data space to image space" is frequently needed (Skilling, 1984, p.115). This feedback can be supplied at low computational cost by the transpose of the response matrix $\mathbf{R}^\mathsf{T}$. However, strictly the inverse of $\mathbf{R}$ would be needed here (which generally does not exist). As outlined in Section 5.2, use of $\mathbf{R}^\mathsf{T}$ is well justified in this context, but nevertheless causes imperfections.

Unfortunately, Rice, Wehlau & Khokhlova 1989 do not describe details of their optimization routine. The algorithm used by Piskunov, Tuominen & Vilhu (1990a) is described in Piskunov (1985), an improved version is presented in Piskunov & Kochukhov (2002). None of these references discusses details of the cost function gradient computation.

The implementation of Vogt et al. (1987) and the code used by Collier Cameron, Donati and coworkers (Brown et al., 1991, Sec. 3.1) both use the optimization algorithm developed by Skilling (1984). One of its key ideas is to construct, at each iteration step, a low-dimensional (e.g. three-dimensional) subspace from the multi-dimensional (typically a few thousand) image space. During each step, the minimum is sought only along the vectors spanning the subspace. The gradient of $\chi^2[I]$ is needed for the construction of the subspace, and $\mathbf{R}^\mathsf{T}$ is used to estimate it.

This scheme has proved effective in practice, greatly reducing the number of iteration steps needed for convergence. The large-scale structure of the solution settles already after a small number of steps. Consequently only a small number of search directions are explored to define the global appearance of the solution. Obviously these few search directions suffice, because a proper solution is found, however the large-scale structure of the solution should be influenced by the structure of $\mathbf{R}^\mathsf{T}$.

4.3.2 CLEANlike DI

CLEANlike Doppler imaging (CLDI) adopts a strategy quite different from those outlined in the preceding section. Instead of continuously "adjusting" the solution surface until the corresponding line profiles fit the data, CLDI iteratively "assembles" the solution surface, monotonically increasing the spot coverage. This procedure resembles the strategy of the CLEAN algorithm originally developed for applications in radio astronomy (Section 3.1.1).

For this solution assembly, CLDI iteratively tries to extract information about spot locations from the line profile time series, proceeding to weaker and weaker line profile features. CLDI is described in Chapter 5.

Chapter 5

CLEANlike Doppler imaging (CLDI)

This chapter describes the Doppler imaging (DI) algorithm developed and realized as a part of this thesis. It is called "CLEANlike Doppler imaging" (CLDI) because its iteration strategy is inspired by the deconvolution algorithm CLEAN (Section 3.1.1). Actually, this strategy is merely one of the ingredients of the algorithm; the use of "tentative backprojections" of the input data is equally important for its philosophy. However, the name was coined at an early stage and survived further developments of the method.

In its present form, CLDI consists of two separate components. The construction of the line profiles from the observed spectra is performed by a method called "least squares deconvolution", it is described in Chapter 6. From these line profiles, the reconstruction of the stellar surface is done by the imaging algorithm itself which is described in Section 5.3.

The imaging algorithm of CLDI is based on the work of M. Kürster and J. Schmitt (Kürster, 1991, 1993; Kürster et al., 1994). Differences and improvements of CLDI compared to the algorithm developed by Kürster are discussed in Chapter 5.6.2.

5.1 Rationale

Motivation

CLDI is intended as an alternative to regularized optimization schemes for the inversion of Doppler imaging data.[1]

Looking for such an alternative was originally motivated by the fundamental properties of MEMDI reconstructions contradicting the properties of sunspots. MEMDI solutions are iteratively constructed by a continuous optimization algorithm, usually a gradient-based (i.e. "downhill") method. In order to converge, such an algorithm needs to adjust the solution by (at least quite) continuous increments. Consequently, MEMDI solutions are *continuous* functions of the surface coordinates. The influence of the regularisation function makes MEMDI solutions *smooth*, in the ideal case deviating from smoothness only as far as the observed data requires.

On the other hand, in order to characterize the brightness distribution of spots on the solar surface, neither "smooth" nor "continuous" would be appropriate terms on scales usually observed. Sunspots normally have pronounced umbrae and penumbrae. They show discrete quite well defined temperature contrast steps compared to the undisturbed photosphere (see Section 2.1.2).

Another motivation of CLDI was the development of an inversion scheme *specifically adapted to Doppler imaging* with the aim of possibly extracting information from the observed data more efficiently.

Guidelines

The following list summarizes the central guidelines followed during the development of CLDI:

1. Steep spot-photosphere contrast:
   Instead of a continuous distribution of spot temperatures on the resolved image scales, CLDI constructs a solution with discrete steps of a spot filling factor. To this aim, it assumes *two discrete temperatures* for the spotted and undisturbed photosphere, respectively.

2. No regularization:
   CLDI constructs a solution *without an explicit smoothing* (regularization) prescription.

3. Feature tracking:
   Instead of an explicit χ^2-minimization, CDLI constructs a solution by iteratively *interpreting temporal patterns* in the time-series of line profiles.

The aims motivating these guidelines, and how far they have been achieved, are further discussed in Section 5.6.3.

[1] Only maximum entropy DI (abbreviated as MEMDI "Maximum entropy method DI") is named in the following; the discussion is equally valid for other regularization functionals described in Section 4.3.1.

Combinatorial optimization

The discrete-contrast assumption of CLDI changes the mathematical context of the problem. It is turned from a continuous into a *combinatorial optimization* (i.e. "discrete") problem. There is still a function to be minimized, but it is not a function of continuous parameters; instead it is defined on a discrete (albeit in general very large) configuration space.[2] As a concrete example, assume a stellar surface discretized into 2000 surface elements (a typical number for the DI applications considered here. If each surface element is further assumed to be either "spotted" or not, the number of possible configurations would be

$$2^{2000} = 10^{\log_{10}(2)\cdot 2000} \approx 10^{600}$$

So the number is large indeed, blindly trying out each, for example in a nanosecond, is not feasible. For considerably lower numbers of possible configurations, solution algorithms can make use of the "finite" number of potential solutions; for the orders of magnitudes involved here, this is not directly possible.

One more aspect is characteristic for the solution of combinatorial optimization: The concept of direction is not necessarily defined in the configuration space, in such cases "downhill" or gradient methods cannot be used.

Realisation

Actually, CLDI does not treat the discrete-temperature DI problem as one of combinatorial optimization; some prospects of such a treatment are discussed at the end of this chapter. Instead, CLDI iteratively builds up a solution using an imperfect but "quite appropriate" *backprojection* of the observed line profiles onto the stellar surface. With the restrictions of the response matrix formulation of the DI problem, the inverse of the response matrix would perform such a backprojection properly (see Section 4.3); unfortunately it does not exist.

However, tests have indicated at an early stage (Kürster, 1991), that the *transpose* of the response matrix provides the required backprojection "quite appropriately". The justification of this use of the transposed response matrix is discussed in Section 5.2.

[2] A classical example of a combinatorial optimization problem is the "Travelling salesman" (cf. e.g. Press et al., 1992): The shortest route between N cities of given positions is sought, connecting the cities by straight lines and visiting each exactly once.
There are $N!$ such routes, their number increases roughly exponentially for large N. The travelling salesman problem belongs to the class of *NP-complete problems* (Kirkpatrick et al., 1983), whose general solution cannot be guaranteed after N^k iteration steps for any k.

CLDI's *strategy* can be described as follows:

> CLDI iteratively assembles a solution image by summing up "point sources" (spotted surface elements). Once set, a "point source" is never removed from the solution. The positions of the "point sources" are determined from estimates based on deviations between the reconstructed and observed data (line profiles) at the current iteration step.

This strategy describes an "irreversible" solution assembly; it is equally valid for the deconvolution algorithm CLEAN originally developed for reconstructing images from radio interferometric observations (Högbom, 1974). This provided the name "CLEAN-like" for CLDI.

However, the behaviour and properties of the original CLEAN rely strongly on the Fourier transformation associated with interferometry (Schwarz, 1978). In that sense, the connection between CLEAN and CLDI does not extend beyond the described general procedure.

CLDI, like CLEAN, is a *heuristic*[3] method. No attempt is made in this work to justify it mathematically on a general basis. It seems doubtful that a general proof of convergence or solution properties can be given for any relevant general class of problems. Instead, this work demonstrates CLDI to be quite robust and successful in performing Doppler imaging inversions.

5.2 Backprojections

As stated above in its strategy, CLDI needs a position estimate of the spot(components) responsible for the remaining line profile deviations, i.e. the difference of the observed and the synthesized line profiles. This estimate is renewed for each iteration step. An attempt is made to project the deviations "back" onto the stellar surface, creating a temporary map for each step. Large values of this map indicate, which parts of the surface are presumed to be responsible for the deviations. These maps are called *backprojections* in the context of CLDI.

Kürster uses the term "probability maps" for backprojections. This nicely conveys the purpose of the backprojections: At each iteration step, they are CLDI's answer to the question "Where are the spots most relevant for the strongest line profile deviations presumably located?". However, it should be emphasized that *there is no strict probability interpretation* of the backprojections.

[3] The term *heuristic* is used here as in the context of computer science. It characterizes an algorithm "reasonably expected" to find a solution, without a formal guarantee of convergence or an optimal solution.

5.2.1 Response matrix backprojections

The simplest way to obtain a backprojection is by applying the transpose of the response matrix $\mathbf{R}$. Actually, CLDI uses a modified response matrix $\tilde{\mathbf{R}}$, which is further discussed in Section 5.2.2. Since the following discussion is completely valid independent of these modifications, the reader is advised to ignore this aspect at first reading.

Using the notation of Equation 4.4, the backprojection $B^{(n)}$ at the n'th iteration step can be written as

$$\begin{aligned} B^{(n)} &= \tilde{\mathbf{R}}^{\mathsf{T}} \cdot \left(D^{(\mathsf{obs})} - D^{(n-1)} \right) \\ &= \tilde{\mathbf{R}}^{\mathsf{T}} \cdot \Delta^{(n)} D \end{aligned} \tag{5.1}$$

Here, $D^{(\mathsf{obs})}$ denotes the vector of observed line profiles (i.e. the input data at all observed phases). $D^{(n-1)}$ is the vector of line profiles synthesized from the reconstructed surface at the preceding iteration step. For $n = 1$ it contains the line profiles synthesized for an unspotted star.

The symbol $\Delta^{(n)}$, sometimes referred to as *spot signature* in the following, is used as an abbreviation for this difference between the observed and the reconstructed

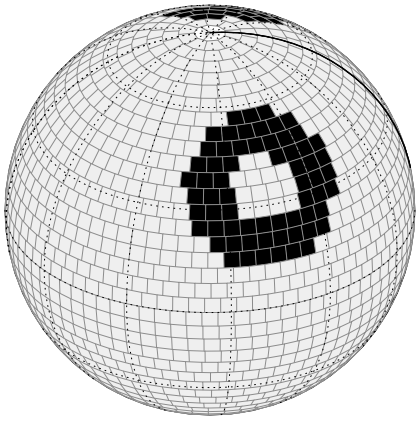

Figure 5.1: Test star surface; the zero-phase meridian is emphasized. The limb darkening is not rendered in this plot.

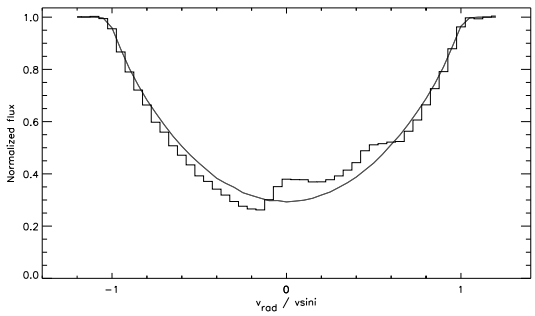

Figure 5.2: Line profile generated by the star of Figure 5.1 (steps) compared to the profile generated for the same parameters by an unspotted star (smooth graph). Both profiles are continuum normalized to one.

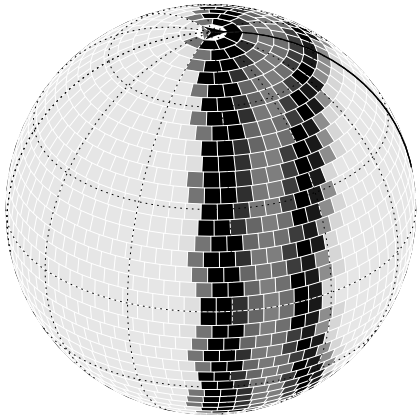

Figure 5.3: Single phase backprojection of the line profile shown in Figures 5.2. A darker shading indicates a larger backprojection value, the gray scale is shown in Figure 5.6. In the terminology of Sec. 5.2.2 an unweighted response matrix has been used for this backprojection.

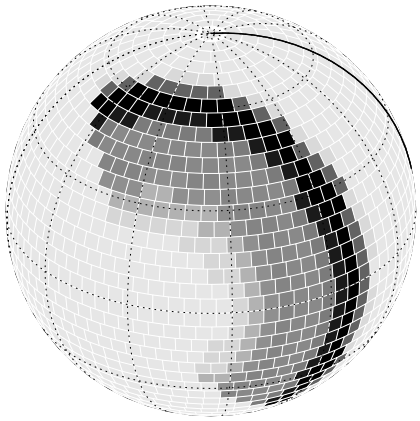

Figure 5.4: Backprojection from a different single phase, rotated to the same projection angle as the map of Figure 5.3.

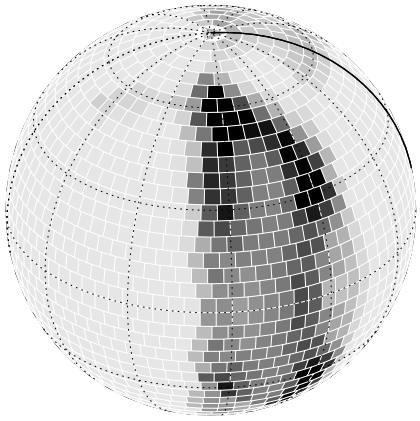

Figure 5.5: Combined backprojection of two phases: This map is the sum of the above two maps, renormalized to a maximum value of one.

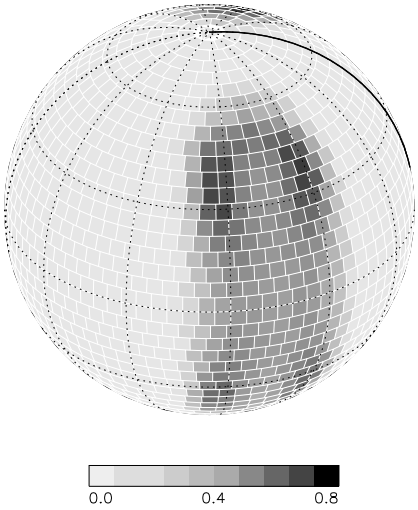

Figure 5.6: Response matrix backprojection of 30 observed phases. While the map of Fig. 5.5 is the sum of two single-phase backprojections, this map is obtained by summing up 30 of them. The map is normalized to maximum value of one, values between 0.8 and unity are rendered black for better contrast.

line profiles

$$\Delta^{(n)} \equiv D^{(\mathsf{obs})} - D^{(n-1)} \tag{5.2}$$

As an example, Figure 5.6 shows a backprojection of the line profile deviations (compared to an undisturbed line profile) for the test star shown in Figure 5.1.

Geometric interpretation

Calculating a backprojection from Expression 5.1 is closely related to the localization principle of a single spot, discussed in Section 4.1.

Figure 5.2 shows the line profile of the test star compared to the line profile of an unspotted star with otherwise equal parameters. The rotation phase is the same as in Figure 5.1, called ϕ_1 in the following. Comparing the two line profiles in the figure, we can be sure that one or more spots are *somewhere* in the shaded areas of Map 5.3. This map, named $B^{(n)}_{\phi_1}$, is generated by applying the transpose of the (modified) response matrix to "a part" of the difference vector $\Delta^{(n)}D$:

$$B^{(n)}_{\phi_1} = \tilde{\mathbf{R}}^{\mathsf{T}} \cdot \Delta^{(n)} D_{\phi_1} \tag{5.3}$$

"A part" means, that only those line profile components observed at phase ϕ_1 are nonzero: The vector D_{ϕ_1} is defined as having the same values as D for the components belonging to phase ϕ_1, all other components zero.

While Map 5.3 shows the backprojection of the single phase ϕ_1, Map 5.4 shows the same for a different phase ϕ_0. The vertical stripes of a single-phase backprojection at ϕ_0 have been rotated and are now (shown at ϕ_1) discernible as circular arcs. Adding the two single-phase backprojections yields the combined backprojection of both phases together, shown in Figure 5.5. The situation is completely analogous to the discussion of spot localization on intersecting radial velocity lines belonging to Figure 4.2.

Finally, for obtaining Map 5.6, the single-phase backprojections of all 30 simulated observations can be added. This means adding terms like Expression 5.3 for all observed phases. Actually, this is done by applying the (modified) response matrix to the whole vector of line profile deformations. Consequently, the backprojection map of Figure 5.6 is obtained by directly using Expression 5.1.

As Map 5.6 is the sum of all single-phase backprojections, the resolution grids discussed in Section 4.2 (e.g. Fig. 4.6) are a superposition of all radial velocity lines defined by the phase coverage and line profile resolution. This close analogy provides a geometric interpretation of the response matrix backprojection:

> The response matrix backprojection of all observed phases is a "weighted" resolution grid defined by the sampling parameters (i.e. line profile resolution and phase sampling) of a particular line profile time series. The weight of each radial velocity line of the grid is determined by the corresponding line profile deviation $\Delta^{(n)}$.

Consequently, intersection points of *several* strongly weighted radial velocity lines result in large values of the backprojection map.

This geometric interpretation explains, why only the large amplitude features of the backprojection are directly correlated with the spot distribution on the surface: Any such weighted resolution grid will contain many intersection points of low amplitude, resulting from "accidentally" intersecting radial velocity lines of e.g. only two phases.

This is the fundamental reason, why CLDI's iterative strategy of only selecting close-to-maximum regions of the backprojection at each step (Section 5.3) is necessary and yields successful reconstructions although the individual backprojections only poorly resemble the solution surface.

5.2.2 Response matrix modifications

As mentioned above, CLDI uses a modified response matrix for its backprojections. These modifications are motivated by the above geometric interpretation of the backprojections. They serve to enhance the contrast of

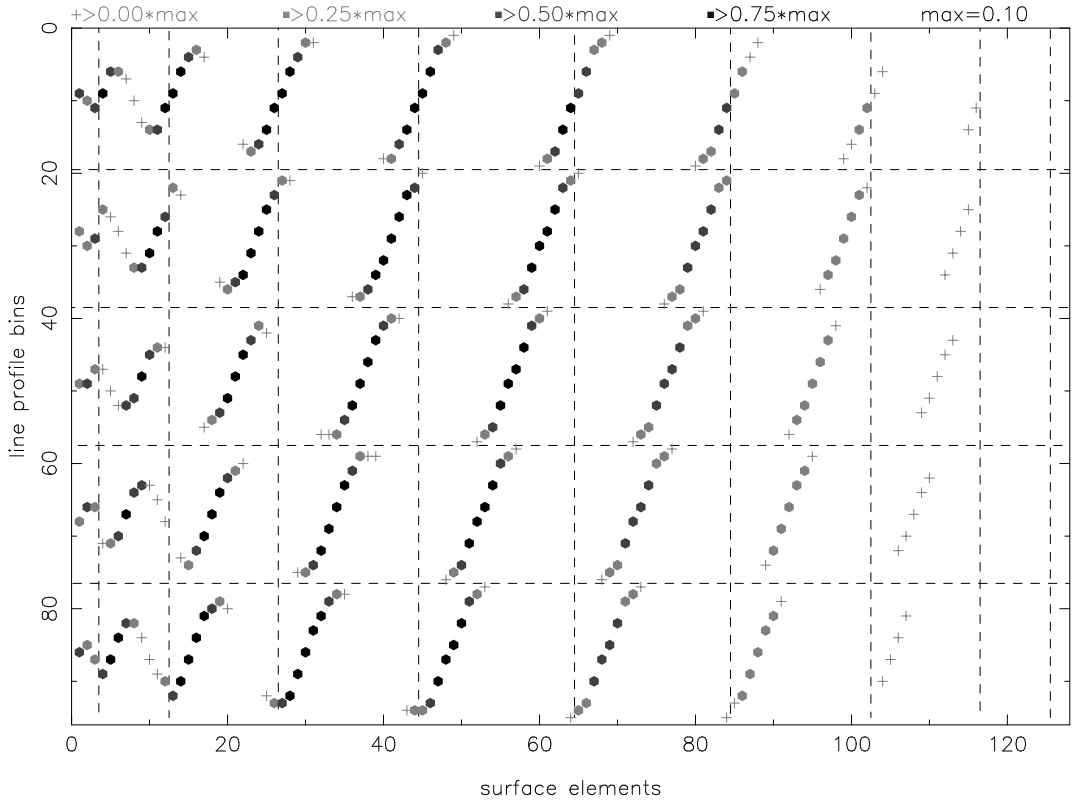

Figure 5.7: Graphic representation of a modified response matrix. Each symbol indicates a non-zero matrix element, giving the visibility (including limb darkening) of one surface element at a particular phase. Dark symbols represent large matrix elements (see gray scale above), zero elements are left blank. This $128 \times 95 = 128 \times (5 \cdot 19)$ matrix represents observations at five equally spaced phases (separated by horizontal lines), discretely sampled into 19 bins each. The surface is divided into 128 elements, arranged in ten latitude rings. The latitude rings are separated by vertical lines, starting with the north pole on the left. The star is inclined $60°$, the limb-darkening is weak ($\epsilon = 0.2$). In the terminology of this section, this is a single-entry, zero-continuum, fully visibility weighted matrix, see text for details.

the backprojection maps and (partially) remove a latitude bias.

The modified response matrices are "tuned" for the purpose of backprojection; this tuning makes them unsuitable for the line profile synthesis, which they are not used for in CLDI (see Section 5.4). Decoupling the response matrices from the line profile synthesis allows to keep their dimensions smaller than what would generally be required for a synthesis with acceptably low synthesis jitter (Section 5.4.2). The smaller dimensions of the modified response matrix reduce the memory required for storing it and the computational load for applying it.[4]

A rough surface discretization and poor phase sampling are chosen for the following examples to keep the resulting response matrix dimensions small, facilitating their graphic representation.

Response matrix structure

The matrix elements of a sample modified response matrix are plotted in Figure 5.7. In accordance with the matrix multiplication in Equation 4.4, each matrix column is assigned to one surface element (one component of I), each row to one line profile bin at one particular phase (one component of D). [5] A similar figure is shown by Vogt

[4] The memory requirements may become an issue for realistic observational situations. Applications described in Chapter 7 are based on surface grids comprising about 2000 surface elements and time series of up to more than sixty line profiles, resolved into about 50 bins each. The resulting dimensions of the response matrix are of the order of $2000 \times (60 \cdot 50) = 2000 \times 3000$, resulting in $6 \cdot 10^6$ matrix elements. Using single-precision float variables (typically 4 bytes long) for storage this requires more than 20 Mbyte of memory for storage.
Using the response matrix for line profile synthesis, given "narrow" local line profiles, the binning resolution would have to be increased by at least a factor of 10 (Section 5.4.2) to sufficiently reduce the synthesis jitter required for low-noise input data, thereby increasing the size of the matrix by the same amount.

[5] As discussed in conjunction with Equation 4.4, the line profile vector is created by stringing the line profiles of all phases end-to-end. In the same way, the surface vector is created by joining all latitude rings of the surface, one after another. The horizontal and vertical dotted lines in Figs. 5.7 to 5.9 reflect this substructure of the vectors, they separate regions of the matrix assigned to each phase and latitude ring respectively.
For example the leftmost region of the matrix, delimited by a vertical

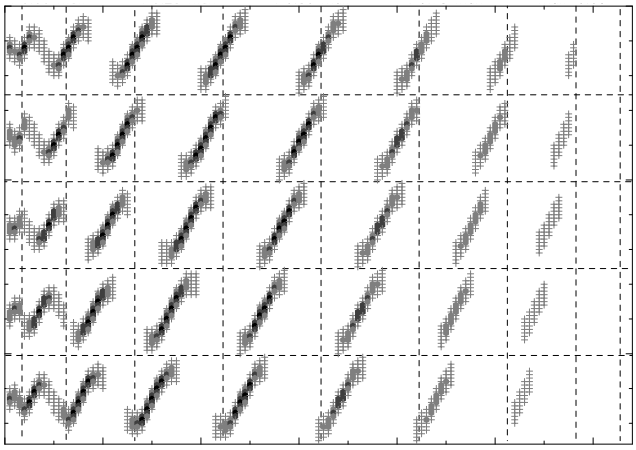

Figure 5.8: Response matrix for the case of resolved local line profiles. All other parameters are the same as in Fig. 5.7, see text for discussion.

et al. (1987, Fig. 3).

The modified matrix of Figure 5.7 is no "proper" response matrix which means that it could not be used to synthesize absorption line profiles via Equation 4.4. Instead, the matrix is generated by applying *three modifications* discussed below. These modifications concern the representation of the line profile shape and continuum as well as the weighting of the matrix elements. An instructive representation of a "proper" response matrix with well-resolved local line profiles and a non-zero continuum is shown in Vogt et al. (1987, Fig. 2); it should be rotated counter-clockwise by 90° for direct comparison with the matrix representations shown here.

As in the preceeding discussions, a modified response matrix is marked by a tilde (and additional indices) to distinguish it from a "proper" response matrix, represented by a plain R.

The "line profile modification"

In its present form CLDI is optimized for the imaging of fast rotating stars, in this case the local line profile can be assumed to be narrow compared to the total width of the rotationally broadened line profile, determined by the value of $v \sin i$. For a reasonable spectral resolution of the observations, the local line profiles are usually only poorly resolved.

As a consequence CLDI uses a *single-entry* (one entry for each surface element and phase) response matrix for its backprojection (Figure 5.7). Here, the entries of a matrix with resolved local line profiles (Figure 5.8) are summed up and entered at the center of each local line profile. This summing up corresponds to replacing the local line profiles by delta functions.

A concentration of the local line profiles in this way leads to a larger "dynamical range" of the matrix elements. Using the single-entry matrix for backprojection leads to enhanced contrasts in the backprojection map compared to a matrix with resolved local line profiles.[6]

The "continuum modification"

Using the response matrix for the actual synthesis of an absorption line profile (Equation 4.4) requires non-zero continuum values of its local line profile entries (as in Vogt et al., 1987, Fig. 2). For the purpose of backprojection, the common offset of *all* matrix elements due to the local line profile continuum can be omitted: It only contributes a constant offset to the backprojection map.
As a consequence, CLDI uses a zero-continuum matrix $\tilde{\mathbf{R}}^0$ for backprojection with

$$\tilde{\mathbf{R}}^0 = c \cdot \mathbf{U} - \mathbf{R} \quad . \tag{5.4}$$

Here $\mathbf{U}$ represents a "uniform matrix" (with all matrix elements equal to 1), multiplied by the constant continuum level c. Since CLDI always uses a zero-continuum matrix, the superscript 0 is omitted elsewhere in the discussion. The order of terms on the right hand side of Equation 5.4 turns the "absorption dips" of the true response matrix (for absorption lines) into positive values in the modified response matrix. This sign reversal causes positive backprojection entries when applying Equation 5.1 to pseudo-emission "bumps".

The "visibility modification"

The value of the nonzero elements of the Matrix 5.7 are determined by their visibility at each phase, proportional to their projected area times the limb-darkening factor. Using the transpose of this *visibility weighted* response matrix for backprojection has two consequences in the light of the geometric interpretation discussed in Section 5.2.1:

(a) From the subobserver latitude on the surface, the visibility of elements decreases towards the poles. As a result, the maximum element of each row in Matrix 5.7 is that closest to the subobserver latitude. This reflects that the surface elements at the subobserver latitude have the

dashed line, is assigned to the three surface elements at the north pole. They show a small radial velocity amplitude during rotation and are visible at all phases, since the stellar inclination is below 90°here.

[6] However, tests on synthetic data, using early versions of CLDI, have not shown a significant influence of this "single-entry" modification of the response matrix on the reconstruction results; in the current version of CLDI it is not optional.
Actually, the "single-entry" modification makes the modified response matrix sparser (i.e. reduces the number of its nonzero or non-continuum entries). This has been used to reduce its storage memory size in earlier versions of CLDI, currently this is not implemented.

largest influence on the line profile deformations. If this matrix is used for backprojection, the values of the backprojection map will be largest close to this latitude, i.e. it introduces a potential *subobserver latitude bias*. This is not justified by the radial velocity information, the subobserver latitude is just the location where the "weakest" possible spot would be found. The bias can be seen by comparing the backprojection maps in Figures 5.4 and 5.10

(b) For any latitude on the surface, the visibility of elements decreases towards the stellar limb, causing a decreasing contribution to the line profile deformations when approaching the limb. If the visibility weighted matrix is used for backprojection, the contribution of line profile deformations to the backprojection is additionally suppressed with increasing distance from the line center. For poor input data quality (and possibly imperfectly adopted line parameters) this may stabilize the reconstruction process, because the profile deformations far from the line center become increasingly unreliable. However under favourable condition it leads to an information loss, because these deformations do not significantly contribute to the backprojection.

The discussed properties of the visibility weighted response matrix backprojection can be eliminated by equal weighting of all nonzero matrix elements. This leads to the *unweighted* Response matrix shown in Figure 5.9. The effect of this for the backprojection can be studied by comparing Figure 5.6 to 5.11.

While property (a) of the visibility weighting increases the contrast of the backprojection map by concentration of features on the subobserver latitude, (b) has no pronounced effect on the backprojection contrast, due to the low amplitude of the line profile deformations further from the line center.

It should be noted that CLDI reconstructions using response matrix backprojections are intrinsically unable to distinguish southern hemisphere spots from those at the same longitude on the northern hemisphere. This is valid independently of the visibility modification.

As discussed in Section 4.1, the information about a spot's hemisphere is completely contained in its visibility as a function of phase, especially in its visibility near the stellar limb. For a stellar inclination $i \neq 90^\circ$ a northern hemisphere spot is better visible and visible for a longer phase interval than its counterpart mirrored to the southern hemisphere.

The resulting larger amplitudes and longer visibility of line profile deformations induced by northern spots lead to larger entries in the northern hemisphere of the backprojection map. However, the converse is not true: smaller amplitudes and shorter visibility of southern spots

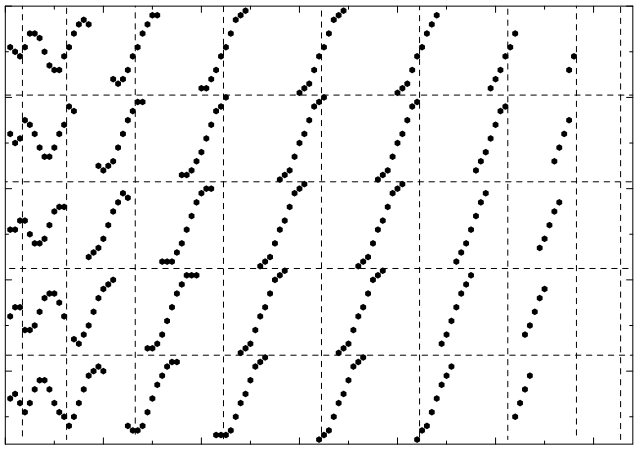

Figure 5.9: "Unweighted" response matrix. The parameters are the same as in Fig. 5.7. Here, all nonzero matrix elements are equal. A value of one indicates that a surface element is visible at a given phase, otherwise the matrix element is set to zero.

do not increase the backprojection values in the southern hemisphere. As a consequence, CLDI using response matrix backprojections only reconstructs spots on the northern hemisphere unless these northern spots have already reached the maximum possible filling factor.[7]

More generally, the *response matrix backprojection only exploits the radial velocity information of the migrating deformations* in the line profile time series (as discussed in Section 5.2.1). It does not make explicit use of the visibility information of the deformations as a function of phase. Even if visibility information is intrinsically ambiguous and sparse for a realistic input line profile time series, this aspect is a fundamental deficiency of the response matrix backprojection.

Response matrices used by CLDI

The concentration of maxima in the visibility weighted backprojection improves the convergence of the CLDI reconstruction for noisy data or near the end of the iteration. However this stability comes at a price: A bias towards the subobserver latitude and the relative ignorance of line profile deformations far from the line center.

Using the unweighted backprojection, on the other hand, makes better use of off-center line profile deformations. By decreasing the subobserver latitude bias, it enlarges the latitude range in which CLDI tends to put spots. Both properties may lead to slightly better fits to densely

[7] This also applies to the "old" CLDI of Kürster (1993), where the visibility weighting of the response matrix and the problem of "north-south ambiguity" of DI are not discussed.
However, the absence of southern hemisphere spots in the reconstruction, unless the corresponding northern regions are already "spotted", can be nicely seen for the "crescent-shaped" spot in Figs. 6-17 of Kürster (1993). Here, "corresponding" means mirrored at the equator to the opposite hemisphere.

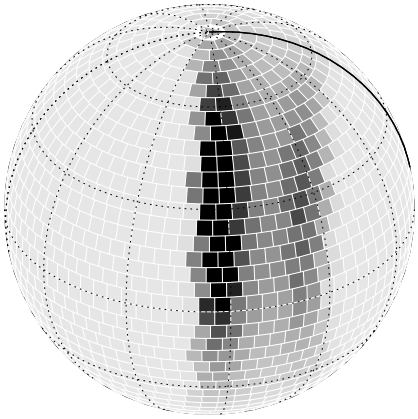

Figure 5.10: Backprojection from a single observed phase using a visibility-weighted response matrix (α=1 in Equation 5.5). A comparison with Fig. 5.3 shows that the visibility weighting leads to local maxima of the backprojection at the subobserver latitude.

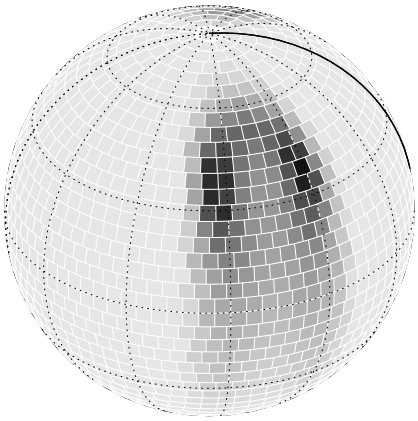

Figure 5.11: Backprojection of 30 equidistantly observed phases, using a visibility-weighted response matrix. Compare to Fig. 5.6, where an unweighted matrix has been used; also here the visibility weighting leads to a "concentration" of the backprojection on the subobserver latitude.

phase sampled, low-noise data. However, a precise line profile modelling is needed to correctly detect the feeble deformations far from the line center.

As the preceding discussion shows, there is a tradeoff between more stability for the visibility weighted backprojection and potentially extracting more line profile information for the unweighted backprojection. To adjust this balance, CLDI uses a continuous parameter $\alpha \, \epsilon \, [0, 1]$

$$\tilde{\mathbf{R}}_\alpha = \alpha \cdot \tilde{\mathbf{R}}^{[\mathsf{viswgt}]} + (1 - \alpha) \cdot \tilde{\mathbf{R}}^{[\mathsf{unwgt}]} \qquad (5.5)$$

$\tilde{\mathbf{R}}^{[\mathsf{viswgt}]}$ and $\tilde{\mathbf{R}}^{[\mathsf{unwgt}]}$ denote the visibility weighted and unweighted *single-entry* response matrices, respectively. The resulting backprojections are termed $\mathtt{RM}_\alpha$-backprojections.

Choices of α for practical applications of CLDI are discussed in Section 5.5.1; as shown there, the influence of α on the CLDI reconstruction results is small. This small influence indicates that the profile deformations originating near the stellar limb contribute little information to the DI reconstruction for realistic input data. In addition it indicates that the mentioned latitude bias of backprojections is outweighted by the latitude information contained in adequately densely phase sampled input data.

In summary, the *modified* response matrices $\tilde{\mathbf{R}}$ used by CLDI for backprojection differ from a "true" response matrix $\mathbf{R}$ in three respects: (i) the integrated depth of each local line profile is entered as one matrix element, all other elements are set to zero; (ii) the continuum offset is set to zero; and (iii) the visibility-weighting of the resulting nonzero elements is adjusted according to the parameter α in Equation 5.5.

5.2.3 Time-series-analysis backprojection

The amplitude $a(t)$ and radial velocity $v_{rad}(t)$ of the line profile deformations caused by a *single unresolved* spot can (approximately) be calculated analytically as a function of time. The pair $(a(t), v_{rad}(t))$ describing the deviation from the undisturbed line profile as a function of time (not including the deviation shape) is called "*spot signature*" in the following.[8]

$v_{rad}(t)$ of the spot is a sine of the rotation angle (or time), its phase depends on the spot longitude; for differential rotation, its period is a function of latitude. For

[8] Assume the star placed as a unit sphere in a right-handed (xyz) Cartesian coordinate system, with the observer located on the positive x-axis. The rotation axis is on the z-axis for an inclination $i = 90°$, otherwise the star is inclined in the xz-plane with the upper (north) pole towards the observer.
The rotation is right-handed around the z-axis ($i > 0°$), i.e. the right half of the star ($y > 0$) "moves away from the observer" so that the radial velocity is proportional to y (Section 4.1). This convention is the same as in Fig. 1a of Kürster (1993).
In this situation, the visibility ν of a surface element is proportional to its normal vector's projection on the x-axis x_{rt} ("rotate-tilt") times the adopted limb-darkening factor

$$\begin{aligned} x_{rt} &= \cos(\phi_{rot}) \sin\theta \sin i + \cos\theta \cos i \\ \nu &= x_{rt} \cdot ((1 - \epsilon) + \epsilon \, x_{rt}) \end{aligned} \qquad (5.6)$$

Since the surface element is located on the unit sphere, x_{rt} is identical to the x-component of its location vector. Here θ is the colatitude of the surface element, ϵ is the limb darkening coefficient and ϕ_{rot} is the rotation angle measured from the x-axis. ϕ_{rot} is calculated from the rotation phase and the position on the surface, possibly taking account of differential rotation. The corresponding radial velocity $v_{rad} \propto y$ can be calculated from

$$y = \sin(\phi_{rot}) \cdot \sin\theta$$

linear limb darkening, also $a(t)$ is a simple function proportional to the visibility of the spot as a function of time.

If *(i)* the time series of line profiles for a complex spot pattern were simply the sum of independent "single spot signatures" superimposed on an undisturbed profile and if *(ii)* the signatures of all surface elements were a set of complete *orthogonal* functions, the observed profile time series could be expanded in those signatures. In the limit of continuously sampled input profiles, the expansion coefficients would be the solution of the DI problem.

Concerning issue (ii), the single spot signatures of different surface elements are linearly independent functions (for an inclination $i \neq 90°$, if they are of the type of Equation 5.6), so they could be orthogonalized by a suitable transformation. This means that condition (ii) could be fulfilled to construct such an expansion (even if it presumably would be numerically unstable for finite sampling and in the presence of noise).

However, condition (i) poses a fundamental problem: The spot induced deviations from the *undisturbed* line profile are in general not a sum of *independent* terms attributable to different spots. This is discussed in detail in Section 5.2.4. Basically this mutual dependence of different spot signatures is due to each spot deforming the whole *continuum normalized* line profile, instead of just placing a localized bump on it (for the case of approximately equal equivalent widths for spotted and undisturbed surface regions).

As a consequence of the preceding discussion, the time series of line profiles cannot be analytically "decomposed" into contributions attributable to different regions on the surface. Actually, such a decomposition would be an analytic solution of the DI problem.

However, the "Time-series-analysis" (TSA) of CLDI constructs a backprojection guided by the idea of such a decomposition. The procedure of TSA is illustrated in Figures 5.12 and 5.13. For each surface element, the profile deviations $a(t)$ "along" $v_{rad}(t)$ are extracted as a function of phase.[9] These extracted profile deviations are compared to the analytically computed visibility of the given surface element; this comparison results in a value measuring the "amount of agreement". This value is entered in the TSA backprojection map at the position of the surface element. While the CLDI iteration proceeds, the profile deviations are not determined as the difference to an undisturbed profile, as described above, but as the difference to the line profiles synthesized for CLDI's current solution surface.

[9]This is done by binning the profile deformations on a two-dimensional grid as a function of v_{rad} and rotation phase, as shown in Figure 5.12. From each phase-row of this grid the deformation amplitude is extracted with a narrow filter centered on the radial velocity of the considered surface element.

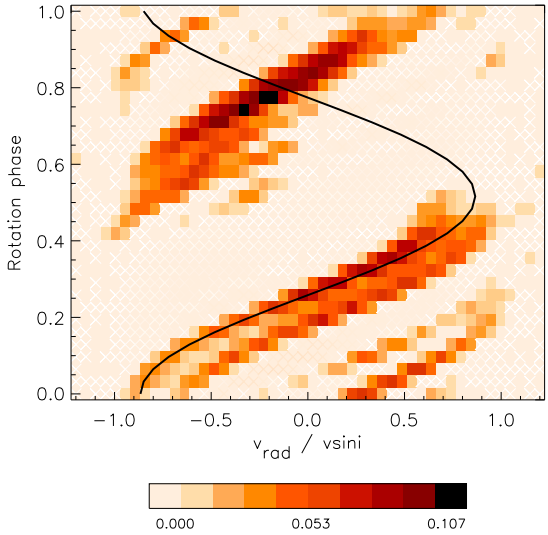

Figure 5.12: "Phase portrait" of a time-series of line profile deviations. Positive deviations from an undisturbed line profile are indicated by dark shades shown in the colour scale, negative deviations are weakly indicated by light crosses. This portrait shows line profiles of the "OvE" star (Fig. 5.25) at an inclination of 60°, covering a complete rotation. The deviations centered at about phase 0.2 are induced by the "O", those at phase 0.8 by the "E". The solid curve shows the radial velocity as a function of phase for a surface element at 30° latitude and 270° longitude, located in the left part of the "O".

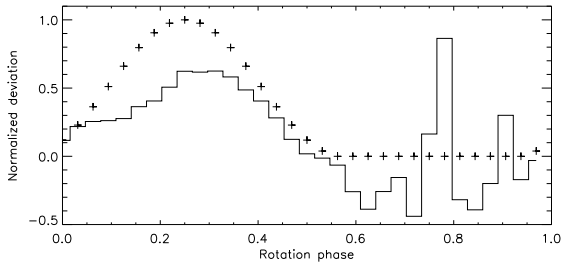

Figure 5.13: Line profile deviations (steps) extracted from the "phase portrait" shown in Figure 5.12. The deviations were extracted along the radial velocity curve shown in the same figure, i.e. for a surface element at 30° latitude and 270° longitude. The plusses show the analytically computed visibility of this surface element (Eq. 5.6).

The visibility calculated for a *single* surface element and the profile deviation extracted for a *complex* spot pattern cannot be expected to agree in any strict sense. Consequently, the above named "amount of agreement" can only be measured tentatively, also turning TSA into merely a heuristic scheme (see Section 5.1). In analogy to the above idea of an expansion, a scalar product can be used, with the sum extending over all sampled phases:

$$\sum_{j=1}^{M} a_j \nu_j \tag{5.7}$$

Here a_j and ν_j represent the sampled values of the corresponding continuous quantities $a(t)$ and $\nu(t)$, respectively. This approach works, but does not yield any contribution for the phase interval of zero visibility $\nu(t) = 0$. For the purpose of backprojection a modified version of Expression 5.7 was found to be better suited. For this modification the above values $\nu_j = 0$ are replaced with $-\overline{\nu(t)}$, i.e. the negative of the average visibility of the surface element. This leads to a positive (nonzero) contribution to the sum for overlapping intervals of zero visibility and extracted negative deviations.[10]

Using the average visibility $\bar{\nu}$ makes this contribution decrease with decreasing visibility of the considered surface element's latitude. Otherwise, the resulting TSA backprojection map contains in general quite irregular large values at poorly visible latitudes. The latter do seriously destabilize the CLDI reconstruction process.

An example of a TSA backprojection map is shown in Figure 5.14, in comparison to a response matrix based backprojection. Their similarity is quite striking, it indicates that the two backprojection schemes extract very similar information from the line profile time series. This is supported by experience with CLDI and by the reliable convergence of the combined RM×TSA backprojection demonstrated in Section 5.5.

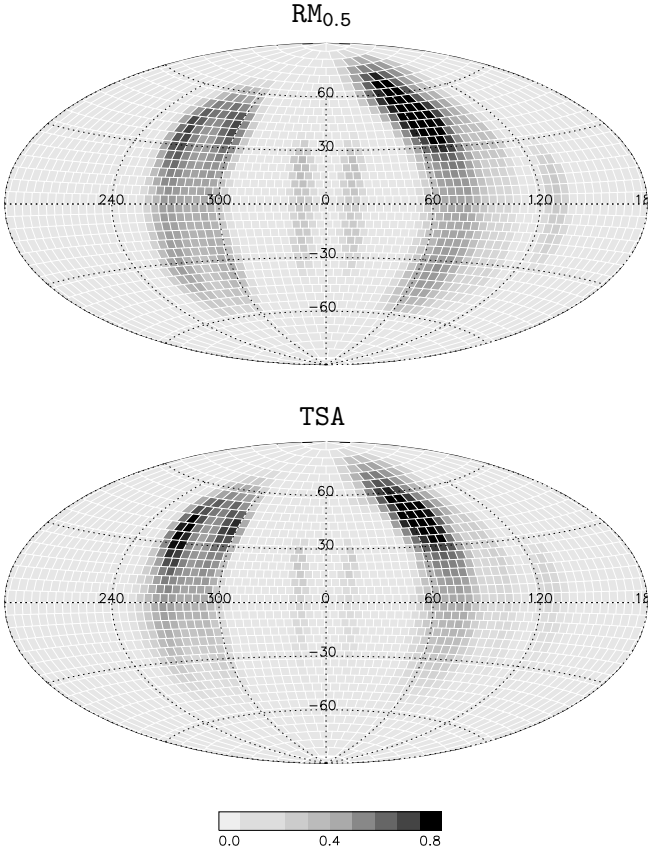

Figure 5.14: Different backprojections at the first CLDI iteration step. The type of backprojection is noted above each map, "$\mathtt{RM}_{0.5}$" and "TSA" indicating a response matrix and time-series-analysis backprojection respectively. The "OvE" test surface (Fig. 5.25) observed at 32 equidistant phases and a SNR of 300 was used to synthesize the input line profiles. Each map is normalized to a maximum value of 1, dark regions represent large backprojection values, rendered black above 0.8.

Mixing the backprojections: "RM×TSA"

Experience with CLDI has shown that using TSA-backprojections alone is superseded by response matrix backprojections. As may be expected, the TSA-backprojections are not robust against strong noise or grossly incorrectly adopted stellar parameters like the inclination; this is due to the TSA trying to make use of the visibility information of the spots.

Combining TSA- and response matrix backprojections leads to slightly improved reconstructions in many cases. Several kinds of combinations have been tried out during the development of CLDI including weighted linear combinations etc.. However, only a simple multiplicative combination proved useful, it is termed RM×TSA-backprojection in the following. The RM×TSA-backprojection is determined by independently computing a response matrix backprojection without visibility weighting ($\mathtt{RM}_{0.0}$, i.e. $\alpha = 0$ in Equation 5.5) and a TSA-backprojection. After that the two backprojection maps are multiplied to obtain the RM×TSA-backprojection.

This simple procedure has two effects: The $\mathtt{RM}_{0.0}$-backprojection contains no latitude bias, leaving "elbow room" for the latitude information supplied by the TSA-backprojection. On the other hand, potential instabilities of the TSA-backprojection can be inhibited by small values of the $\mathtt{RM}_{0.0}$-backprojection. Actually the mul-

[10] This modification of Expression 5.7 is intended to (and does) increase the contrast of the TSA backprojection map. Interestingly, it also enables CLDI, in principle, to successfully localize a feature on the southern hemisphere under the favourable conditions of an isolated small southern spot not "too close" to the equator.
However, this has had no effect for realistic (even favourable) tests carried out with CLDI. No modification of Expression 5.7 could be found that is truly successful in reconstructing southern hemisphere spots.

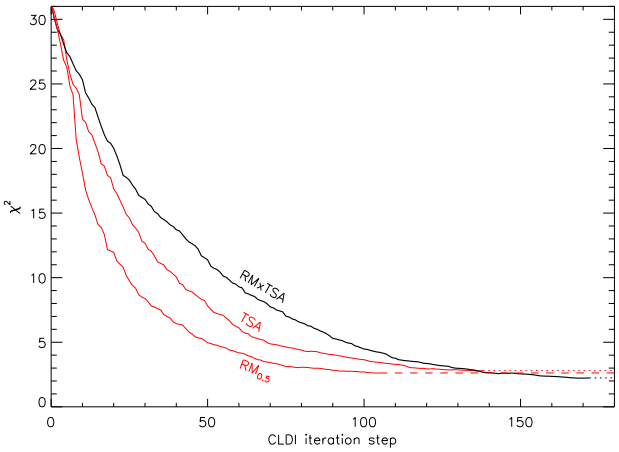

Figure 5.15: Convergence history of CLDI using different backprojections: Deviation of input and reconstructed line profiles in terms of χ^2 as a function of the number of CLDI iteration steps. Each curve is continued by a dotted or dashed line after the corresponding CLDI reconstruction stopped further convergence. Using the RM×TSA-backprojection causes the slowest convergence of CLDI, but also attains the best fit to the line profiles. The difference of the achieved final χ^2-values are significant, although not well visible at this scale: 2.77 (TSA), 2.58 ($RM_{0.5}$) and 2.23 (RM×TSA). The "irregular" test surface (Fig. 5.32) observed at 32 equidistant phases and SNR 300 was used to generate the input line profiles.

tiplicative mixing of the backprojections implements a *veto scheme*: In regions where either the $RM_{0.0}$- or the TSA-backprojections are (close to) zero, the RM×TSA-backprojection is small.

An example where the RM×TSA-backprojection prevails over other backprojections is illustrated in Figure 5.15. Here CLDI achieves the closest fit to the input line profiles when using the RM×TSA-backprojection. Another feature of RM×TSA-backprojections is clearly visible in Figure 5.15: They significantly slow down the convergence of CLDI. This has been observed for all applications of CLDI using RM×TSA-backprojections. The slow convergence confirms RM×TSA-backprojections as the "most conservative" backprojections of CLDI which is due to their veto scheme discussed above.[11]

5.2.4 Spot signature correlation

As discussed in Section 4.1, the contributions of individual spot groups to the line profile deformations cannot be separated at all phases. This "shadowing" is a direct consequence of the one-dimensional projection at each phase.

If the line profile deformations ("pseudoemissions", see Section 4.1) are predominantly due to the spot-photosphere brightness contrast, with the total equivalent width of the considered line roughly constant, another effect correlates the profile deformations caused by different spots when measured relative to a (quite) undisturbed profile.

As in the preceding Sections, the term "spot signature" is used for the deviations between the observed and the so far by CLDI reconstructed line profile. As can be seen in Figure 5.2, the spot-induced bumps do not simply appear on an otherwise unchanged profile, instead the whole line profile also "sags" compared to the undisturbed profile. This sagging is a result of the (in this case adopted) exactly constant total equivalent width which would otherwise be reduced by the bumps.[12]

A more pronounced example is given by Figure 5.22 where several large spots are simultaneously present on the visible hemisphere. Here only the strongest one-dimensional projection of the spots (the right wing of the "v" together with the upper half of the "E") suffices to cause a bump rising significantly above the undisturbed profile. This sagging has an important consequence for the backprojection of the shown line profile, when using a (quite) undisturbed profile for comparison: Some spot-induced bumps do not appear as positive deviations from the comparison line profile.

Following the geometric interpretation of the response matrix backprojection (Section 5.2.1), only positive deviations at several phases lead to a strong signature of a spot in the resulting backprojection map. As a consequence, smaller features can get lost in the backprojection, especially for unfavourable phase sampling, when much larger features are mostly present simultaneously on the visible surface.

Such "lost" features will appear in the backprojections later during the CLDI iteration, once the strong spots have partially been reconstructed and the comparison profile starts sagging itself. This contributes to the need for CLDI to iterate: It is necessary to allow the backprojections to get hold of the weaker surface features.

The effect of line profile sagging can also be studied in Figure 5.12, where it leads to the asymmetries of the spot signatures with respect to $v_{rad} = 0$.

Both, TSA and response matrix backprojections are hampered by the line profile sagging. However, the re-

[11] Examples where the RM×TSA-backprojection leads to slightly superior DI reconstructions can be found in Figure 5.24. There the CLDI reconstructions based on RM×TSA-backprojections lead to an improved image reconstruction and better line profile fits for densely sampled low-noise input line profiles when compared to other tested backprojections.

[12] Actually, this "sagging" of the whole line profile results from the continuum normalization *of each individual profile* of a time series to unity. For strictly flux-calibrated spectral line profiles the profile would instead be shifted by a constant amount due to the reduction of the disk-integrated flux caused by the spots on the visible hemisphere. However, the latter case is irrelevant for practical applications of Doppler imaging and is not further discussed here.

sponse matrix backprojection can mostly compensate for it for an even and dense phase coverage, because the negative differences between the sagging observed profile and the undisturbed profile lower the backprojection values in unspotted surface regions. Such a compensation is not possible for the TSA which only successfully detects regular, positive deviations from the comparison profile. This leads to the weaker backprojection of the "v" in the TSA-backprojection map of Figure 5.14, compared to the response matrix backprojection shown above it.

5.3 Algorithm

The core of an implementation of CLDI is the iteration loop "assembling" the reconstruction image. A short outline of this loop is given to allow the discussion of fundamental parameters of the CLDI algorithm.

Preparatory steps:

- Calculate the response matrix; it depends on the surface geometry, the limb-darkening and the observed phases. CLDI's modified response matrices are independent of the local line profile.
- Initialize the solution surface as "spotless", setting the values of all surface elements zero.

Iteration steps:

- Synthesize the line profiles of the solution surface for all observed phases.
- Determine a backprojection map from the difference of the synthesized and observed line profiles.
- Select the close-to-maximum surface elements from the backprojection. Increase their value by the filling factor increment δ_{FF}, up to a maximum value of one.

Termination:

- Terminate the above iteration, when a predefined number of steps do not yield a significant decrease in χ^2 (calculated from the difference of the synthesized and observed line profiles).

The construction of the response matrix, the line profile synthesis and the backprojection are discussed in the corresponding sections of this chapter. The filling factor increment δ_{FF} and the "close-to-maximum" criterion are discussed below.

Naturally, additional termination criteria can be employed. Certainly a predefined number of maximum allowed steps makes sense; once the input data quality is reliably known, a lower χ^2 threshold can be defined. However, the above criterion has proven most useful in practice.[13]

"Close-to-maximum" selection of surface elements

The synthesis of the line profiles with sufficiently low noise is the most time-consuming part of the CLDI iteration. In order to reduce the number of iterations needed to construct the final solution, CLDI usually selects more than one surface element from the backprojection at each iteration step.

This is done by selecting all surface elements with a backprojection value above typically 95% of the maximum value of the backprojection map. This *selection threshold* should be set by experiment for a given input data quality; setting it too low (i.e. selecting too many elements per step) will reduce the quality of the final line profile fits attained by CLDI.

It happens occasionally, that all surface elements thus selected have already reached their maximum allowed filling factor. In this case, the above selection criterion would lead to no change of the reconstructed surface at the given iteration step, inhibiting further convergence of CLDI. To ensure convergence, CLDI must adaptively lower the selection threshold in this case.

The filling factor increment

A constant increment δ_{FF} is added to the value of each selected surface element, however the maximum result allowed is one. This increment per iteration step δ_{FF} is a free parameter of the CLDI algorithm.

Since the imaged quantity of CLDI is defined to be in the range $[0, 1]$, choosing $\delta_{\mathsf{FF}} = 1$ results in a "two-temperature surface", i.e. each element is either spotted or unspotted. Choosing smaller values $\delta_{\mathsf{FF}} < 1$ will result in more and more continuous surfaces which may improve the reconstruction capabilities of CLDI, as discussed in Section 5.5.1. Actually this agrees with experience from

[13] The number of tolerated iteration steps without decreasing χ^2 can be set to e.g. 5. Note that this number is not critical.
Depending on the data quality and the backprojection used, CLDI performs typically about 90-95% of its converging iterations without any increase of χ^2. However, the χ^2-decrease for each iteration step decreases quite monotonically during the iteration (see Fig. 5.15).
Only for the remaining "final" steps, an occasional increase in χ^2 occurs (when the very well-defined line profile deformations have already been fitted). For a given dataset, it is a matter of experimentation to set the number of tolerated χ^2-increase steps such that CLDI iterates until no more significant improvement in χ^2 is achieved.

other applications of CLEAN (see Section 3.1.1) - slowing down convergence is generally helpful for finding (globally) optimal solutions.

Decreasing δ_{FF} increases the computational effort of a CLDI reconstruction, because more iteration steps are needed. Lowering δ_{FF} so far that the backprojections do not change significantly between two CLDI steps is meaningless because CLDI will simply perform several subsequent incrementations of the same surface elements. This explains the asymptotic approach of χ^2_{final} towards a lower limit in Figure 5.28. As demonstrated in Section 5.5.1, choosing $\delta_{\mathsf{FF}} = 0.5$ is a useful compromise in practice between improving CLDI's convergence, a computationally effective reconstruction and obtaining a solution with strong filling factor contrasts.

5.4 Line profile modelling

In case of the Sun we can perform spatially resolved spectroscopy, i.e. we can observe spectra as a function of position on the solar disk. The absorption line profiles of such spectra, belonging to a particular portion of the stellar disc, are called *local line profiles* here. For stars other than the Sun practically only *disk integrated* spectra can be observed, their line profiles are weighted integrals of local line profiles, Doppler shifted by the stellar surface rotation.

The line profile synthesis of CLDI is based on the assumption that the rotational broadening is by far the dominating line profile broadening mechanism. The typical width of the adopted local line profiles of 5-10 $\mathrm{km\,s^{-1}}$ is of the order of the spectral resolution, $\lambda/\Delta\lambda$ of about 40 000 used in the context of this work (corresponding to a velocity resolution of $\Delta v = c/40\,000 \approx 7.5\ \mathrm{km\,s^{-1}}$).

In addition, these velocities are considerably smaller than the stellar projected rotational velocities considered $v \sin i \gtrsim 100\ \mathrm{km\,s^{-1}}$, so a simplified modelling of the line profiles is justified. DI has been found to be quite robust against errors of the local line profile shapes under the named assumptions (see Section 4.2.1).[14]

5.4.1 Surface discretization

In order to represent the spot distribution on a stellar surface as a one-dimensional vector (as required for Equation 4.4), the surface needs to be subdivided into a number of zones. These zones are called *surface elements* in the context of CLDI. The set of resulting zones is called *surface discretization* or *surface grid*. Following e.g. Vogt et al. (1987), the surface is divided into elements of approximately equal area. The elements are arranged in rings of equal latitude extent.[15] A surface discretization is shown in Figure 5.16.[16]

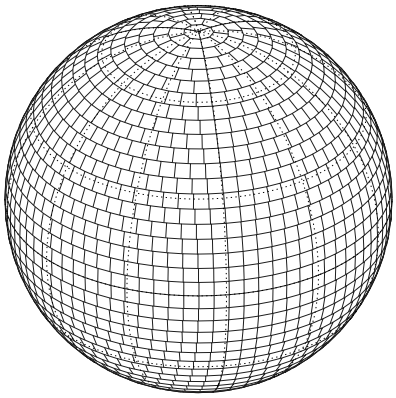

Figure 5.16: Example of a surface discretization (surface grid). The surface shown has 2020 elements of approximately equal area, arranged in 40 rings of equal latitude extent of 4.5°.

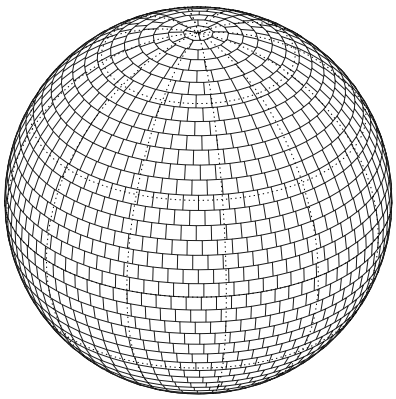

Figure 5.17: "Warped" surface discretization used by CLDI, compare to Figure 5.16. Using the same surface elements, the latitude rings are sheared relative to one another. This helps to reduce jitter of the line profile synthesis based on this discretization.

In this way, the sphere is approximated by a convex polyeder. The faces of the polyeder are quadrangles (approximately squares near the equator), apart from the face at the pole.

The resulting number of surface elements n_{sel} as a function of the number of elements at the equator n_{eq} can be estimated from[17]

$$n_{\mathsf{sel}} \approx \frac{4\,\pi}{(2\,\pi/n_{\mathsf{eq}})^2} = n_{\mathsf{eq}}^2/\pi \tag{5.8}$$

The resulting grid has a resolution of about $360^\circ/n_{\mathsf{eq}}$ in longitude and latitude near the equator, decreasing in longitude towards the poles. As an example, the surface grid used for the reconstructions of Chapter 7 has 80 elements along the equator and 2020 surface elements in total. The corresponding resolution near the equator is 4.5°.

[14] Citing Stout-Batalha & Vogt (1999, p. 251):
"The quality of the fit to the average disk-integrated line profile is found to be more important to DI analysis than the exact parameters used to generate the fit when the shape of the disk-integrated line profile is dominated by rotational broadening."
Although this is is only a singular statement, it is based on the careful comparison of 15 individual Doppler images reconstructed from the same input spectra, albeit at a rather low surface resolution.

[15] Such a discretization can be constructed by dividing the sphere into n of rings of equal latitude extent. The ring(s) closest to the equator are divided into $2n$ zones of equal area A_0. Each remaining latitude ring is divided into zones of equal area $A_\theta < A_0$ and $A_\theta \approx A_0$.

[16] Note, that the surface element covering the pole appears as a triangle in colour representations elsewhere in this work. This is due to a simplification of the graphics rendering routine. However, it is a regular polygon bounded by the adjacent surface elements. Note in passing, that this polar surface element is different from that shown in Fig. 1 of Vogt et al. (1987), who do not have a single surface element centered on the pole.

[17] This results from the surface area 4π of the unit sphere, approximately divided into squares of equal area $(2\,\pi/n)^2$.

Besides storing the spot distribution on the surface, the grid is used for the line profile synthesis (see Section 5.4.2). The condition of approximately equal area surface elements is motivated by the requirements of the profile synthesis. It makes all surface elements contribute to the line profile with comparable amount (depending on visibility and limb-darkening though).

The arrangement in rings is not required at all, it is motivated by the simplicity of the construction. The resulting regularity of the discretization is not an optimum choice for the line profile synthesis, because it amplifies jitter of the (discretely) synthesized profiles. This jitter arises because of the "*clumping*" (non-uniform distribution) of the radial velocities of the surface elements. The clumping can be inferred from the tendency of surface elements to concentrate along vertical lines in a plane projection of the surface grid, as in Figure 5.16. Another indication of the problem is the rather large scatter of the distribution of visibilities during rotation (see Figure 5.20).

This problem has to be handled by the line profile synthesis algorithm (see Section 5.4.2). A simple means to reduce the jitter (to some degree) is to slightly twist the latitude rings relative to each other, also disturbing the symmetry between the hemispheres, as shown in Figure 5.17. For the applications discussed in this work, this typically reduces the synthesis jitter mean amplitude by typically more than 30%.[18]

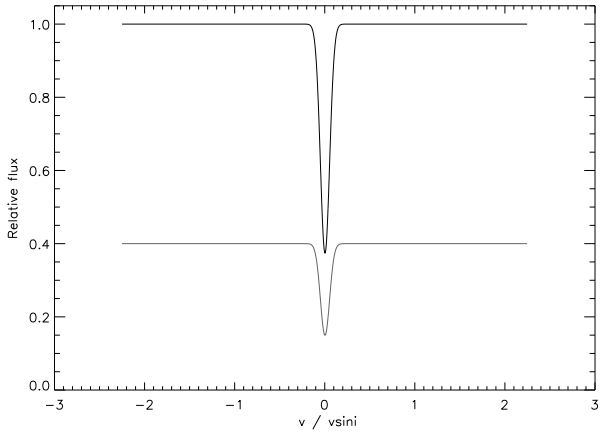

Figure 5.18: Local line profiles used by CLDI. The different continuum flux of the undisturbed-photosphere profile (upper, black) and the spot line profile (lower, gray) is apparent; it is caused by the different temperatures of the surface regions emitting them. The two profiles shown are purely Gaussian of equal equivalent width and FWHM; both parameters can be chosen differently in general.

5.4.2 Disk integration

CLDI uses local line profiles with a *shape* independent of the position on the stellar disk. In this context, the shape is meant to be independent of depth, i.e. two profiles are defined to have the same shape if they are identical after scaling to the same depth. Following the "two-temperature assumption" named above, CLDI uses two constant local line profiles $H^{\mathsf{spot}}(\lambda)$ and $H^{\mathsf{nospot}}(\lambda)$, for the spotted and undisturbed ("unspotted") stellar surface respectively. In the example shown in Figure 5.18 the two profiles are even of the same shape - in the above sense.

This approach does not take into account changes of the local line profile *shape* due to limb darkening and gravity darkening. However it incorporates changes of depth caused by these effects; presently only the limb darkening option is used in CLDI.

The numerical disk integration proceeds by summing up the individual local line profiles for all surface elements. These individual profiles are determined for each surface element by the following steps:

1. Mixing: The actual profile $H(\lambda)$ is calculated by mixing the spotted and unspotted profiles according to the spot-filling-factor σ. As can be seen in Figure 5.18, this incorporates possibly different continuum fluxes

$$H(\lambda) = \sigma \cdot H^{\mathsf{spot}}(\lambda) + (1-\sigma) \cdot H^{\mathsf{nospot}}(\lambda) \quad (5.9)$$

2. Scaling: The resulting $H(\lambda)$ is multiplied by a factor proportional to its visibility towards the observer, determined by the projected area and the limb darkening.

3. Shifting: The scaled $H(\lambda)$ is shifted in wavelength according to the radial velocity of the surface element towards the observer.

Actually, Equation 5.9 is the definition of the spot filling factor $\sigma \,\epsilon\, [0,1]$ in the context of CLDI: It is defined as a linear mixing parameter of the two adopted line profile models.

Synthesis jitter

For typical surface discretizations used by CLDI, directly applying the above procedure approximates the disk integral by a sum of about a thousand local line profiles, a significant part of them contributing only at low visibilities. Numerically, depending on the actual resolution of the line profile, this is usually too poor an approximation.

[18] In the example of synthesis jitter shown in the lower panel of Figure 5.19, using Grid 5.17 instead of Grid 5.16 increases the SNR due to the jitter from 2000 to 3500. In particular it reduces the maximum jitter amplitude for "unfavourable" phases of particularly strong clumping by a factor of typically two. These improvements come at very little computational cost.

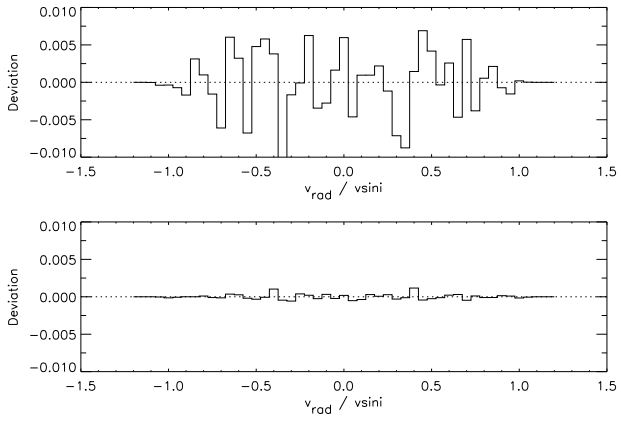

Figure 5.19: Examples of line profile synthesis jitter, caused by the finite number of terms used to approximate the disk integration. Both panels show the *difference* of a line profile synthesized by CLDI from a profile analytically computed from Equation 5.11 and convolved with a suitable Gaussian profile. For the profiles corresponding to the upper and lower panel, about 4000 and 40 000 local line profiles were summed up, respectively.

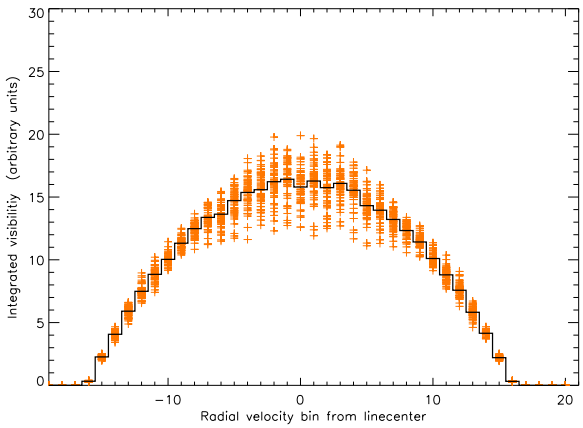

Figure 5.20: Scatter of the radial velocity distribution of the visible surface elements due to the discrete binning of their velocities during rotation. The surface grid shown in Figure 5.17 was rotated to 72 roughly equidistant phases covering a full rotation. Each plus indicates the integrated visibilities of all surface elements falling into the corresponding velocity bin at a particular rotation phase. The thick line shows the distribution which results from averaging all rotation phases.

Because only relatively few terms contribute to each part of the line profile, it may show considerable irregularities, referred to as *synthesis jitter* in the following. An example is shown in Figure 5.19.

Apart from being simply a problem of numerical resolution, this jitter is significantly amplified by the "clumping" of the radial velocities of the surface element centers, discussed in Section 5.4.1.

Figure 5.20 offers another view of this clumping, based on a "warped" surface grid of 2020 elements (as in Figure 5.17). Averaging many phases, the binned integrated visibilities come close to the rotation profile of Equation 5.11. However, for individual rotation phases, there is significant scatter around this average distribution. This scatter is due to radial velocity clumping in conjunction with the radial velocity binning of the surface elements (it is significantly increased when instead using a "straight" surface grid as that shown in Figure 5.16).

The jitter decreases with increasing width of the local line profiles, since it is smoothed by the corresponding convolution. However, this width is dictated by the physical parameters of the star (and the observational resolution). The usual way to reduce the jitter is the use of a finer surface discretization and a finer sampling of the line profiles during synthesis, finally rebinning the resulting profiles to the observationally required resolution.

CLDI does use a finer line profile sampling during synthesis which is later rebinned onto a coarser sampling (Piskunov & Kochukhov, 2002, Sec. 2.6, describe a similar procedure). CLDI also uses an appropriately finer surface discretization, but in a slightly simplified way: As outlined in Section 5.4.1, the stellar surface is approximated by a convex polyeder, bounded by quadrangles. For the line profile synthesis each surface element is further subdivided into smaller quadrangles *in the same plane* as the original surface element. A local line profile is added for each smaller quadrangle, their number is determined by the line profile sampling chosen. This simplified refinement of the surface grid reduces memory requirements and computational effort of the line profile synthesis.

The refinement of the sampling during the synthesis comes at a considerable computational cost. The number of operations for an n-fold finer sampling roughly increases proportional to n^2, because the number of line profiles to be summed up and the number of bins of each line profile are about proportional to n. The actual degree of refinement needed is determined by the required noise level of the synthesized profiles, some examples can be seen in Figure 5.19. Experience with CLDI has shown that typically of the order of several 10 000 local line profiles need to be summed up to attain a SNR of several hundred.[19]

[19] This corresponds well to numbers given in (Gray, 1988, p. 1-28) or Reiners (2003a, Sec. 3). A reasonable safety margin should keep the SNR of the synthesized profiles well above the SNR of the observed profiles to be processed. This is necessary because of the non-normally distributed synthesis jitter, showing occasional high amplitude outliers due to the irregular "clumping" of the binned radial velocities.
If a low-noise profile of a *homogeneous* surface is to be synthesized, it is most effective to compute the average of several profiles synthesized at irregularly spaced phases.

Limb darkening approximation

The line of sight (defined e.g. to extend to unit optical depth) extends less deep into the stellar atmosphere at the stellar limb than it does at the disk center. As a result, the continuum and spectrum are predominantly formed in increasingly higher layers of the atmosphere when approaching the stellar limb (cf. e.g. Fig. 9.3 of Gray, 1992).

Because of the decreasing temperature of the photosphere with height, this leads to a decreasing continuum brightness towards the limb at optical wavelengths, observed as limb darkening. Since also the formation depths of individual lines are affected, line profiles and equivalent widths depend on the limb distance. However, the latter line dependencies are generally small; following the fast-rotator-assumption of CLDI's line profile synthesis, they are currently not modelled by CLDI. They could be incorporated quite easily by using a lookup table of local line profiles, depending on limb distance.

Instead, the limb darkening is approximated by a linear limb darkening law, leaving the shape (including the equivalent width) of the local line profile constant. The stellar continuum flux $\mathcal{F}$ observed at an angle θ to the surface normal ("limb angle") is calculated from

$$\mathcal{F}(\theta)/\mathcal{F}(0) = 1 - \epsilon + \epsilon \cos\theta. \qquad (5.10)$$

It is parametrized by the limb darkening parameter ϵ . Values of $\epsilon \approx 0.6$ to 0.7 are typical for G and K stars respectively at a wavelength of about 6000 Å (e.g. Fig. 17.6 of Gray, 1992).

This linear approximation of the limb darkening adopting a constant-profile-shape is appropriate in many cases, as illustrated by Figure 5.21. Significant deviations only occur at the extreme limb; this has little effect on the resulting total disk-integrated line profile because of the small contribution of the corresponding outer disk annuli.

The limb darkening massively influences the overall shape of the disk-integrated line profile (see Figure 3.3). In addition, it influences the amplitude of the line profile deformations when spots approach the stellar limb. While the first aspect is very important for DI to ensure a correct undisturbed line profile (to avoid symmetric imaging artefacts, see Section 5.5.6), the second aspect is of minor importance: Spot-induced profile deformations close to the outer boundaries of the line profile are hardly detectable for realistic input data.

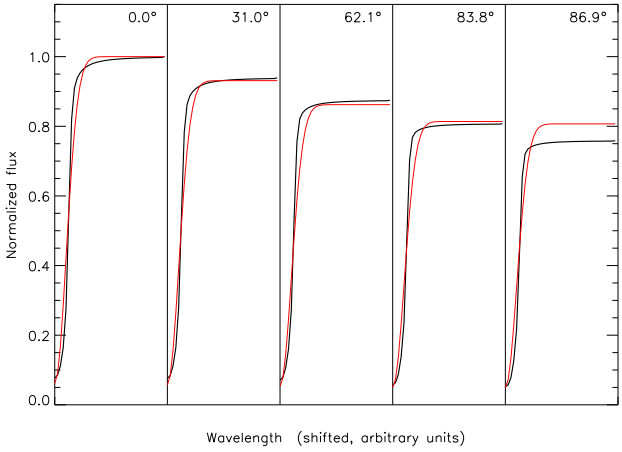

Figure 5.21: Local line profiles for selected limb angles θ given at the top, note the uneven spacing of angles. The black profiles were synthesized using a stellar atmospheric model for a star of 6400 K effective temperature (supplied by A. Hatzes). The red/gray profiles are Gaussians of constant shape scaled by a linear limb darkening law (Eq. 5.10), with a limb darkening parameter adjusted to approximately fit the fully synthesized black profiles. The FWHM of the profiles is 0.13 Å at 4750 Å, i.e. they are hardly resolved at a spectral resolution of 40 000. Note that significant deviations only occur very close to the stellar limb, i.e. for large values of θ.

5.4.3 Local line profiles

Line broadening mechanisms

Several mechanisms predominantly determine the profiles of stellar photospheric lines. Often termed "broadening mechanisms", they can be summarized as follows for the "local" profiles, i.e. including *everything but rotational broadening*:

1. Thermal broadening: The Maxwell distribution of thermal motion leads to a Gaussian line profile with a width depending on temperature and atomic mass. For heavier elements like iron, the width of this profile is about 1 km/s at 5000 K (Gray, 1988, Table 1-1).

2. Pressure broadening: Collisional interactions of particles in the photosphere influence the atomic energy levels. This results in a Lorentzian profile parametrized by a damping constant γ, depending on the individual transitions, the temperature as well as on electron and gas pressure (Gray, 1992, Chapter 11).

3. Turbulent broadening: Velocities of convective motions lead to a broadening of the line profiles. In order to get a formally simple approximation, the turbulent motions can be split up into micro- and macroturbulence with typical scales small and large compared to unit optical depth, respectively. Microturbulent velocities are of the order of 1-2 km/s; macroturbulent velocities are about 2 km/s for a K dwarf star, increasing with effective temperature and total luminosity (Gray, 1992, Figure 18.9)

The thermal and microturbulence broadening (assumed to have an isotropic and Gaussian velocity distribution) can be combined into a common Gaussian profile. The pressure broadening effects, together with the natural width of a line can be summed into one damping constant describing a Lorentzian profile. Together with the Gaussian broadeners, they can be combined into a Voigt profile.

The treatment of the anisotropic macroturbulence can be approximated by a "radial-tangential" model, it can be incorporated into the local line profile, resulting in a limb angle dependent shape

Assuming the above listed processes to be independent of the position on the stellar disc, the line profile resulting from their combination can be represented by a convolution of the profiles for each process (Gray, 1992, Ch. 17). This includes the description of rotational line broadening by a suitable broadening function, like e.g. Expression 5.11, cf. also Reiners & Schmitt (2002a).

Local line profiles used by CLDI

The spectral resolution of observations used for Doppler imaging of stars with $v \sin i \gtrsim 100$ km/s is sensibly chosen of the order of 50 000, corresponding to a velocity resolution of $\Delta v = c/50\,000 \approx 6$ km/s. The above quoted typical local broadening values for G and K dwarf stars make them barely or not resolved at all at this resolution except for the pressure broadening of stronger lines and the thermal broadening of light elements.

In the context of this work, CLDI has only been applied to "average line profiles" (rotational broadening functions) deconvolved by sLSD (see Chapter 6). The template spectra used for the deconvolution were observed for slowly rotating stars or "fully synthesized", i.e. their modelling includes the above broadening mechanisms.

Consequently, the local line profiles necessary to analyze these deconvolved rotation profiles should be predominantly Gaussian, describing the observational resolution (for the case of synthetic spectra) and possibly approximating a limited resolution of the deconvolution process. No significant deviation from this expected behaviour was found during the applications described in Chapter 7, so they have been carried out using purely Gaussian local line profiles for the disk integration of CLDI. It should be noted that, depending on the surface grid resolution, a sufficient width of the local profiles is necessary to avoid excessive jitter otherwise introduced by the discrete disk integration (see Section 5.4.2).

According to the discussion of Section 5.4.2, the shape of CLDI's local line profiles is currently independent of the position on the disk (this could be remedied by a limb angle-dependent lookup table); however, the shapes can be chosen differently for the adopted spotted and undisturbed photosphere.

This approach, sufficient for the application to ultrafast rotating stars, would need to be extended for applying CLDI to slower rotators.

The rotation profile

If the local line profile $H(\lambda)$ is assumed to be independent of the position on the stellar disc, and adopting a linear limb darkening, the disk integrated line profile can be obtained by a convolution with a function $G(\Delta\lambda)$; here $\Delta\lambda$ is the (Doppler) wavelength shift from the line center (Gray, 1992, Ch. 17).

This function is termed "rotation profile" by Gray, it can be expressed analytically for the case of rigid rotation. For $\Delta\lambda/W \leq 1$, with W representing the rotational half width of the line, and a linear limb darkening coefficient ϵ it reads[20]

$$G(\Delta\lambda) = \frac{2(1-\epsilon)\mathsf{A}^{\frac{1}{2}} + \frac{1}{2}\pi\epsilon\mathsf{A}}{\pi W(1-\epsilon/3)} \quad ; \qquad (5.11)$$

here the symbol $\mathsf{A} \equiv 1 - (\Delta\lambda/W)^2$ has been used, computed from the center wavelength λ_0 by

$$W = \frac{v \sin i}{c} \cdot \lambda_0 \quad .$$

Expression 5.11 is defined as zero for $\Delta\lambda/W > 1$.

[20] Abney (1877) suggests that a star's rotation should have an effect on its line profiles. However, he does not give a quantitative treatment: "I have calculated what the shade would be; but I have not thought it necessary to bring forward the formulae to-night." (Abney, 1877, p. 278).
Instead, such a treatment was performed by Vogel (1877) who (incorrectly in retrospect) expresses doubt that a stellar projected rotational velocity could exceed ten times the solar value (Vogel, 1877, p. 75).

5.5 CLDI: Tests

This section describes tests of CLDI using line profiles synthesized for "artificial stars". The Doppler imaging reconstructions are compared to the known input surfaces to study the behaviour of CLDI.

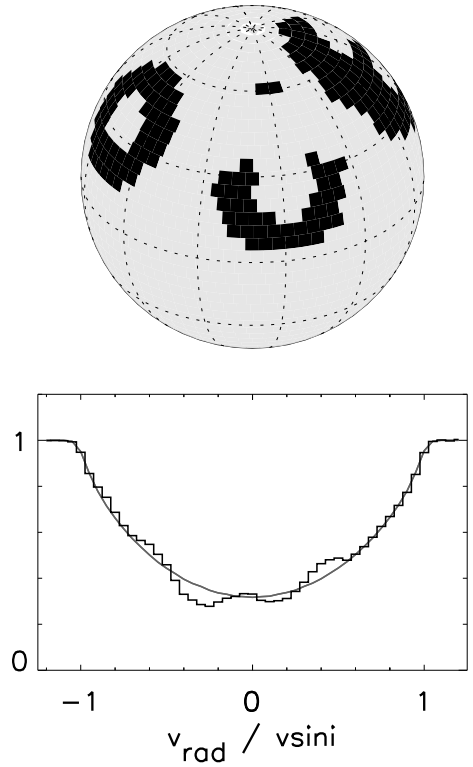

Figure 5.22: "OvE" test surface and the synthesized line profile (SNR 300) at the corresponding rotation phase. The smooth graph shows the line profile of an unspotted surface for comparison.

Doppler imaging is quite robust against (reasonably) incorrect assumptions of stellar parameters as inclination and atmospheric parameters. As outlined in Section 4.2, this is due to the fact that most of the image information is contained in the radial velocity information of the spots, much less in their visibility. The radial velocity information primarily depends on a correctly known $v \sin i$ and rotation period, it is much less dependent on other stellar parameters. This robustness has been extensively demonstrated and tested elsewhere (see Sec. 4.2.1).

The purpose of this section is different, its focus is twofold: (a) Adjusting the parameters specific to CLDI, governing its reconstruction behaviour. Two "standard settings" of CLDI result from this adjustment. (b) Studying the behaviour of these CLDI settings with observational parameters similar to the conditions of observations encountered in Chapter 7.

At present it is not known, whether stars show regular and "monolithic" spot distributions qualitatively similar

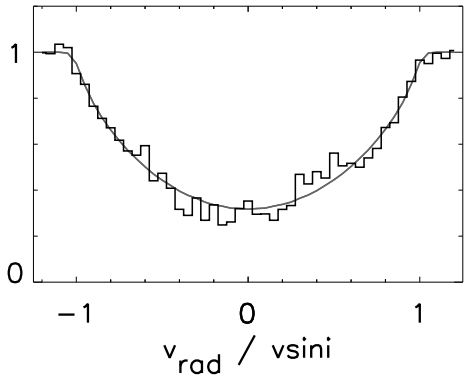

Figure 5.23: Synthetic line profile belonging to the same surface and phase as Fig. 5.22; however, here the SNR is 25.

e.g. to the test surface shown in Figure 5.25); certainly the Sun does not show them. As demonstrated below, the behaviour and resolution of CLDI depend to some degree on the regularity of the stellar surface to be reconstructed. Consequently, many of the tests described in this section use a tentative irregular test surface as input. It is shown in Figure 5.32.

At first reading, the reader is advised to start with a look at Section 5.6.1 to get an overview.

Input data and remarks on SNR values

The input surfaces used to synthesize the input line profiles have a resolution of $4.5^\circ \times 4.5^\circ$ near the equator. As will be shown this is comparable to the resolution attainable for the favourable cases of the simulations. The inclination of the "input star" was adopted as 60° for all simulations.

The non-continuum region of the line profiles is sampled into 42 bins; that means that it is effectively resolved into about 20 resolution elements, assuming a requirement of twofold oversampling as the limiting factor. The intrinsic width of the local line profiles is 0.05 (FWHM in units of $v\,sini$) which would otherwise permit a resolution into up to $2/0.05 = 40$ elements. Using the estimate of Equation 4.2, the effective resolution of the line profile into 20 elements allows for a surface resolution of about 5.5°.

The synthetic input data of the tests are superimposed by "Gaussian noise", i.e. random numbers normally distributed around zero were added to the data bins. The errors of the synthetic line profiles are completely dominated by this noise, the synthesis jitter plays no significant role (Section 5.4.2). Naturally, for real input data also systematic errors have to be expected. These can be introduced by data reduction errors, errors of sLSD (if used), unrecognized line blends etc.. As a consequence,

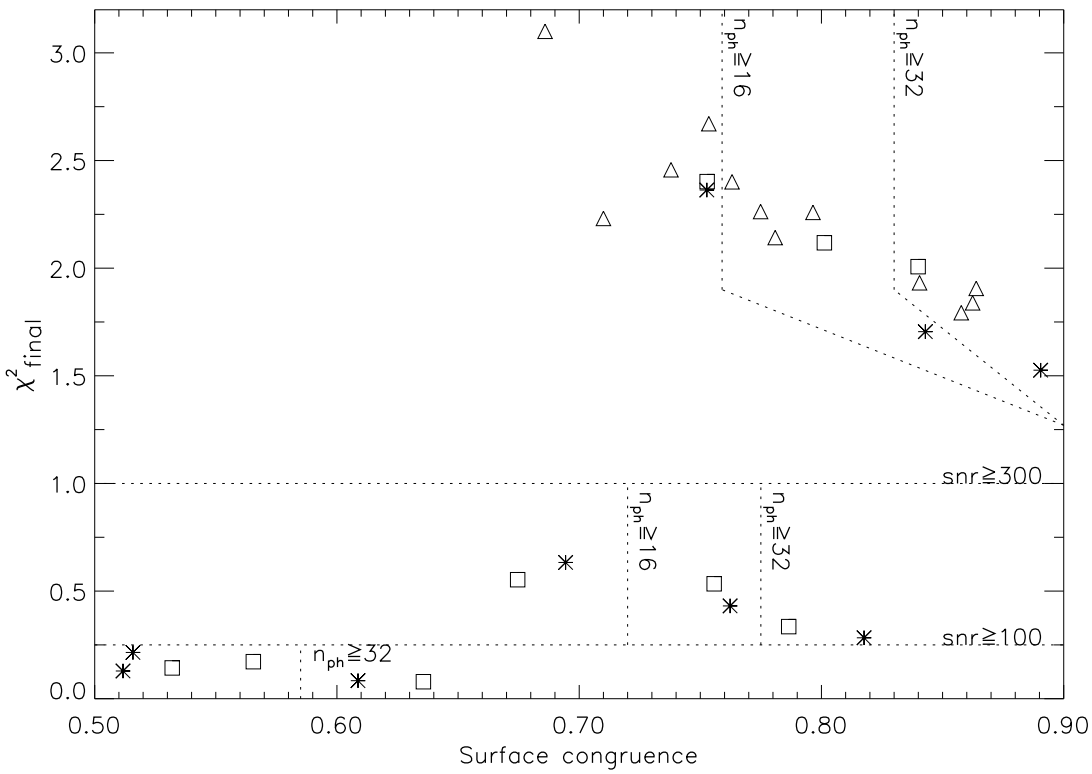

Figure 5.24: Overview of CLDI reconstructions of the "OvE" surface (Fig. 5.25), adopting a stellar inclination of 60°, for different numbers of observed phases n_{ph}, SNR and CLDI parameter settings. The y-axis shows the regularized χ^2 values of the line profile fit at the last iteration step. The congruence measure, comparing the input and CLDI reconstruction surfaces, is defined in the text. Stars represent RM×TSA, squares $\mathtt{RM}_{1.0}$ reconstructions, respectively. The triangles indicate $\mathtt{RM}_{0.0}$, $\mathtt{RM}_{0.3}$, $\mathtt{RM}_{0.5}$ and $\mathtt{RM}_{0.7}$ reconstructions which are not distinguished here.

the χ^2-values given for the synthetic tests of this section are significantly lower than for reconstructions of "real" observed data.

The signal-to-noise ratio (SNR) of the synthetic line profiles is defined as the inverse of the standard deviation σ of the superimposed noise, i.e. the continuum (normalized to one) is used as the "signal level"

$$\mathrm{SNR} = \frac{1.0}{\sigma_{\mathrm{noise}}} \tag{5.12}$$

However, measuring the noise amplitude relative to the continuum is of limited relevance for judging the imaging information contained in the profiles. For this purpose the noise mean amplitude must be compared to the typical line profile deformations caused by the spots.

The three SNR values used for the tests below represent three different regimes of the noise amplitude: For SNR 300 it is "safely below", for SNR 100 about twenty percent and for SNR 25 it is of the same order of magnitude as typical line profile deformations. This is illustrated by comparing Figure 5.22 to Figure 5.23.

For comparison of the following results with reconstructions from real observation data, such an estimation of the noise level must be performed.

Regularization and scatter of χ^2_{final}

The χ^2_{final}-values given in this work are defined as

$$\chi^2_{\mathsf{final}} = \frac{1}{M} \cdot \frac{\sum_{j=1}^{M} (D_{\mathsf{obs},j} - D_{\mathsf{recon},j})^2}{\sigma^2_{\mathsf{noise},j}} \tag{5.13}$$

The sum extends over all data points, M is the product of the number of phases times the number of line profile bins per phase. D_{obs} represents the input line profiles, D_{recon} the line profiles computed by CLDI after the last (final) reconstruction step.

The M in the denominator of Equation 5.13 is intended to normalize χ^2_{final} to values of the order of one. However, even for appropriate reconstructions, the χ^2_{final} value may deviate substantially from one. For real data, the SNR may be wrongly estimated or rebinning during the data reduction may introduce correlations of the noise in neighbouring data bins.

More importantly, D_{recon} is the result of a fit to D_{obs}. If this fit were performed with a known number γ of uncorrelated parameters, M should be replaced by $M-\gamma$ in

Table 5.1: Estimated scatter of CLDI surface reconstruction quality (as measured by $\mathcal{C}$) and line profile fit quality χ^2_{final} caused by random noise of the input line profiles. Each pair $\Delta\mathcal{C}$ and $\Delta\chi^2_{\mathsf{final}}$ was computed as the standard deviation of the respective quantity, using ten input datasets with differently seeded random noise. n_{ph} indicates the number of observed equidistant phases. The reconstructions marked with "*irr.*" used the "irregular" test surface (Fig. 5.32) as input, all other reconstructions used the "OvE" test surface. All reconstructions used a `RM×TSA` backprojection; however, other backprojections result in a similar scatter.

$n_{\mathsf{ph}} \times \mathsf{SNR}$	$\Delta\mathcal{C}$	$\Delta\chi^2_{\mathsf{final}}$	$\sqrt{2/M}$
16×100 *irr.*	0.03	0.10	0.051
16×100	0.02	0.09	0.051
16×300	0.01	0.10	0.051
32×100	0.01	0.04	0.036
32×300	0.01	0.09	0.036
32×300 *irr.*	0.03	0.12	0.036

the denominator of Equation 5.13. This is due to the reduced number of degrees of freedom of the resulting χ^2-distribution (Press et al., 1992, Ch. 15.6). Consequently, χ^2_{final} values below unity do not necessarily mean that the data has been "overfitted".

Estimating γ in the Doppler imaging case is difficult. It is certainly related to the number of surface elements of the solution surface, but their values are correlated according to the ambiguities of the solution. In addition, different regions of the solution surface influence the profile fit with different weights, according to visibility and phase sampling. Line profile bins close to the edges of the profiles are practically unaffected by the solution surface (due to low visibility and limb darkening). Lacking a proper estimate of γ, Equation 5.13 is used instead. It should be clear, that the *absolute* values of the resulting χ^2-values are of limited significance.

The expected statistical scatter of χ^2_{final} resulting from the noise is

$$\Delta\chi^2_{\mathsf{final}} \approx \frac{\sqrt{2M}}{M} = \sqrt{2/M} \tag{5.14}$$

The actual scatter for some simulation cases has been estimated from a random ensemble of datasets. The results are summarized in Table 5.1 and compared to the values resulting from Equation 5.14. Estimated from a low number of datasets, these are crude estimates. They are only intended as an orientation for judging the significance of χ^2-differences, as in Figure 5.24.

Actually, the scatter is comparable to the expected values, but systematically exceeds it. That indicates, that a slight instability of CLDI remains even for low-noise data. Due to ambiguities of the line profile information,the input data does not completely define (parts of) the solution surface. CLDI sets surface values quite "randomly" within the limits of this ambiguity, applying no explicit smoothing condition to the solution. This can be seen e.g. by comparing the maps in Figure 5.33. Since CLDI assembles its solution "irreversibly", these quasi-random placements of surface values to some degree influence CLDI's final solution.

Measuring image congruence

Comparing two images is to some degree a subjective task. In the following sections, a simple *tentative image congruence measure* is sometimes used to compare a stellar input image and its reconstruction. Given two discretely sampled surfaces represented by the M-element nonzero image vectors $I^{(1)}$ and $I^{(2)}$, their congruence measure is defined as

$$\mathcal{C}(I^{(1)}, I^{(2)}) = \frac{\sum_{j=1}^{M} I_j^{(1)} \cdot I_j^{(2)}}{\sqrt{\sum_{j=1}^{M} (I_j^{(1)})^2} \cdot \sqrt{\sum_{j=1}^{M} (I_j^{(2)})^2}} \tag{5.15}$$

Geometrically, this is the cosine of the angle between the two image vectors. Consequently $0 \leq \mathcal{C}(I^{(1)}, I^{(2)}) \leq 1$ holds true, a value of one indicates parallel image vectors, i.e. two surfaces whose corresponding surface elements are multiples with a common factor. This is especially satisfied by two identical or *congruent* surfaces. A value of zero indicates that the two images have no nonzero surface elements in common.

The above description indicates that $\mathcal{C}$ is some measure of image "likeness". It performs a "pixel-by-pixel comparison" of the images; this is a proper procedure if the resolution of the images is comparable to their sampling by surface elements. Otherwise, for *significantly oversampled* images, the values of $\mathcal{C}$ should be interpreted with some care.

Summing up, the values of $\mathcal{C}$ do not make a visual inspection of the images obsolete. However experience in the context of CLDI tests has shown it to be a quite *reliable measure for comparing surfaces originating from similar parameter sets*.

Its reliability is illustrated by the $\mathcal{C}$-values given for the images in Figure 5.30: Higher $\mathcal{C}$-values correspond to "better" reconstructions. It is also supported by Figure 5.24. Here the reconstructions from input data with a SNR of 300 and 100 each show a significant trend of increasing surface congruence $\mathcal{C}$ with decreasing χ^2_{final}. It reflects that a more complete extraction of information from the line profiles generally leads to an improvement of the surface reconstruction.

The nearly complete absence of this trend for the reconstructions from the SNR of 50 input data is mostly

caused by exceeding a "critical noise level", where the input data only very poorly define the solution at the resolution aimed for. Also, it reflects the diminishing sensitivity of $\mathcal{C}$ for oversampled images.

5.5.1 Adjusting CLDI parameters

Two basic properties of CLDI need to be adjusted for its application: The filling factor increment per iteration step δ_{FF} (Section 5.3) and CLDI's way to construct the backprojections. CLDI's backprojections are controlled by the "visibility-weighting" parameter α of the response matrix (Equation 5.5) and the role of the "Time-series-analysis" (TSA) backprojection (see Section 5.2.3).

The results of a comparative test of different backprojection modes are plotted in Figure 5.24. Each point in this figure represents one CLDI reconstruction, different symbols mark different CLDI settings. The figure shows that RM×TSA supersedes the other backprojection settings, for the case of a "regular" input surface observed from densely phase sampled low-noise data. It yields the closest fit to the input line profiles as well as reconstructions closest to the input surfaces.

Although the improvements are small, they are recognizable when comparing the surfaces in Figure 5.25 and 5.26. Keeping in mind the estimated scatter of χ^2_{final} of about ± 0.1 (see Table 5.1), the line profile fit quality is significantly improved for a sampling of 16 or 32 phases at a SNR of 300. This advantage of RM×TSA over the other backprojections is diminished or lost with decreasing phase sampling and increasing noise.

For a phase sampling of 8 phases and/or a SNR of 25, the line profiles contain too little information to define spot locations at the resolution of the used surface grid. This agrees with estimates discussed in Section 4.2.

Visibility weighting

As outlined in Section 5.2.2, the visibility weighting of the response matrix can be modified for generating the backprojections, i.e. $\alpha \neq 1$ can be chosen in Equation 5.5. This can improve the CLDI reconstructions for densely sampled, low-noise input data, since better use is made of information further away from the line profile center. As Figure 5.27 shows, there is an influence of the visibility weighting on the line profile fit quality, but the differences are at the limit of significance. For the Figure, seven sets of data were computed by adding differently seeded random noise to line profiles generated from the "OvE" test surface.

On average, the reconstructions using the $\mathtt{RM}_{0.5}$ backprojection yield the closest fit to the data. This reflects a

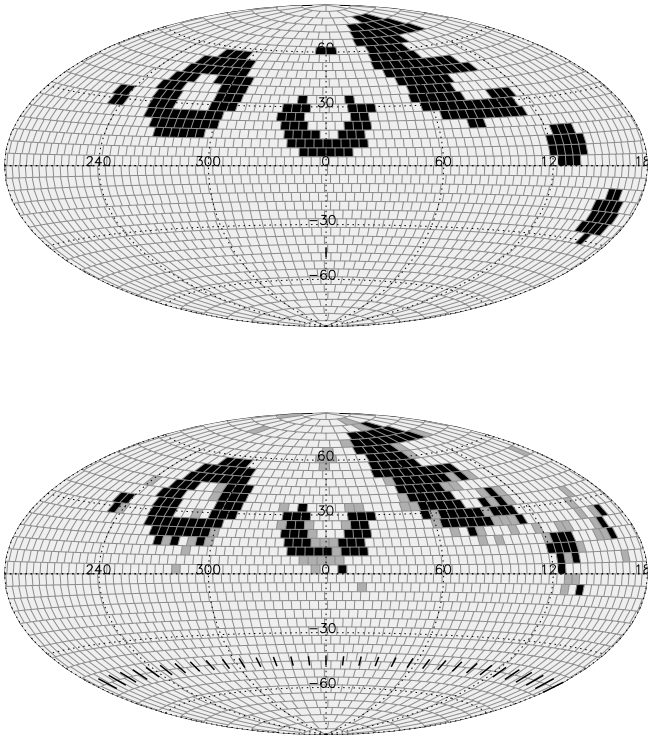

Figure 5.25: *Upper panel:* "OvE" test surface used for adjusting CLDI parameters and other tests. For all tests described in this section the stellar inclination is chosen as 60°. *Lower panel:* CLDI reconstruction (RM×TSA) for 32 phases and a SNR of 300. The ticks on the southern hemisphere mark the 32 equidistant observation phases; the grayscale is shown in Figure 5.26. Note that the near-equator southern spot appears in the CLDI reconstruction mirrored to the northern hemisphere.

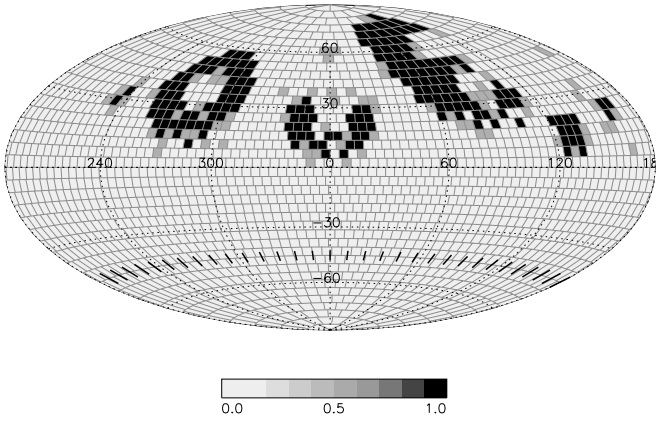

Figure 5.26: CLDI reconstruction ($\mathtt{RM}_{1.0}$) for 32 phases and a SNR of 300. Different gray shades indicate different spot filling factors ranging from zero to one. This Doppler image was computed from the same input data as the DI in Fig. 5.25, but yields a slightly poorer reconstruction of the "input surface" (upper panel of the same figure). This illustrates the small, but significant superiority of RM×TSA backprojections over their $\mathtt{RM}_{1.0}$ counterparts for high-quality input line profiles.

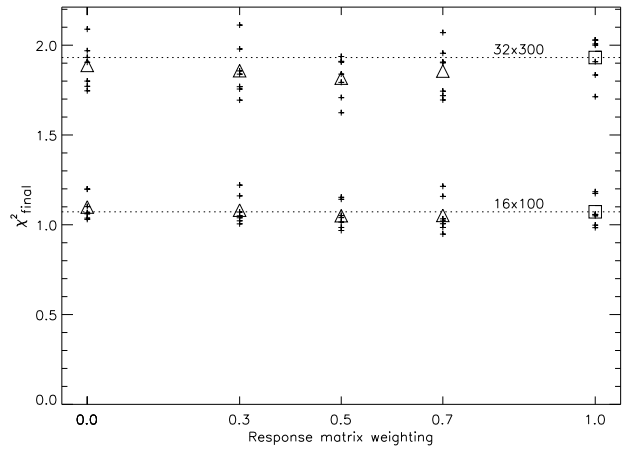

Figure 5.27: Fit quality of CLDI reconstruction line profiles χ^2_{final} as a function of response matrix visibility weighting α (Eq. 5.5). Phase sampling and noise level of the input data is annotated. The individual reconstruction results are marked by plusses, each triangle and square marks the mean value of χ^2_{final} averaging all reconstructions at the given α and phase sampling. See text for details.

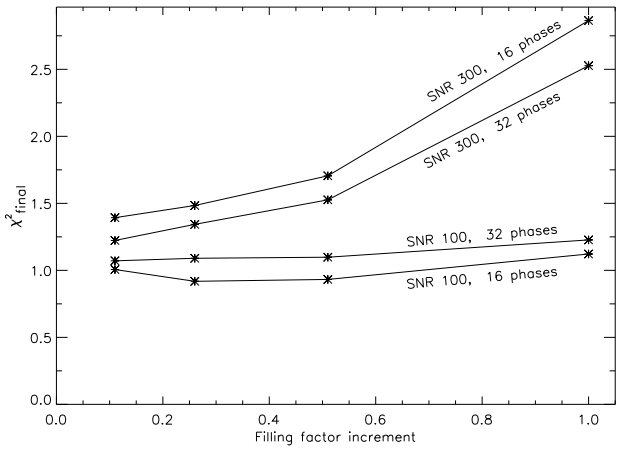

Figure 5.28: Quality of CLDI line profile fits χ^2_{final} as a function of filling factor increment per step δ_{FF}. Note that reducing δ_{FF} from one to 0.5 results in a considerable improvement of χ^2_{final} for cases of low-noise input data (SNR 300).

trend shown by CLDI reconstructions of a variety of synthetic and observed input data.

Even though the differences between $\mathtt{RM}_{1.0}$ and $\mathtt{RM}_{0.5}$ reconstructions are minor, the latter have been used in this work for applications of CLDI with "pure" response matrix backprojections. This makes $\mathtt{RM}_{0.5}$ backprojections the second "standard setting" of CLDI besides RM×TSA backprojections.

Adjusting the filling factor increment

The increment δ_{FF} which CLDI adds to the value of each selected surface element controls the contrast of the resulting reconstruction (Section 5.3). As Figure 5.28 shows, it also influences the quality of the resulting fit to low-noise input data.

This may be expected, since CLDI can approach the solution more "carefully". Occasional surface elements not optimally selected by the backprojection have a lower effect on the solution. Apparently, this uncertainty of the backprojection to discern between neighbouring surface elements only matters for very high SNR. Only in that case the input data reliably defines the surface solution on such a small scale.

Choosing $\delta_{\mathsf{FF}} = 0.5$ for low-noise data is a sensible compromise between improving the final line profile fits and the computational load of CLDI. That choice was usually made for applications of CLDI in the context of this work.

Unfortunately the resulting reconstructions, so suggestive of an umbra/penumbra structure do not allow this interpretation. This aspect is discussed in Section 5.5.3.

5.5.2 Influence of noise and phase sampling

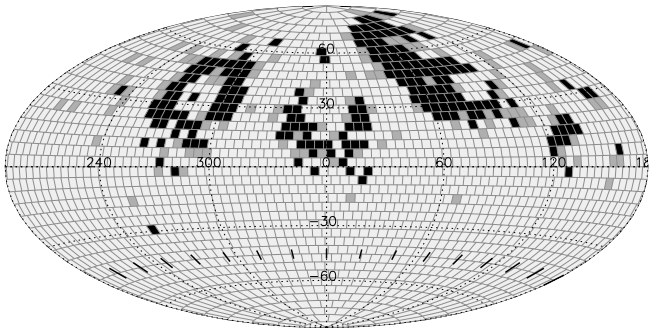

Figure 5.29: CLDI reconstruction (RM×TSA) for 16 phases and a SNR of 100. A comparison with Figure 5.25 which shows a reconstruction with equal parameters, but based on denser phase sampled, less noisy input line profiles, illustrates the influence of input data quality on the Doppler image.

As Figure 5.30 illustrates, the quality of CLDI reconstructions increases *monotonically* with improved phase sampling and decreasing line profile noise. This holds true for the resulting surface congruence $\mathcal{C}$ between input and reconstruction, and for the line profile fit quality.

This result is confirmed for irregular test surfaces (Section 5.5.4). Although not surprising, it is a valuable indication of CLDI's stability in the sense that it reacts smoothly to different information content of its input data.

At first glance it is astounding that even poor phase sampling allows the reconstruction of many features of the spot distribution. At second thought this is less surprising; for example 8 observations equidistantly sampling one full rotation mean that the star is observed at

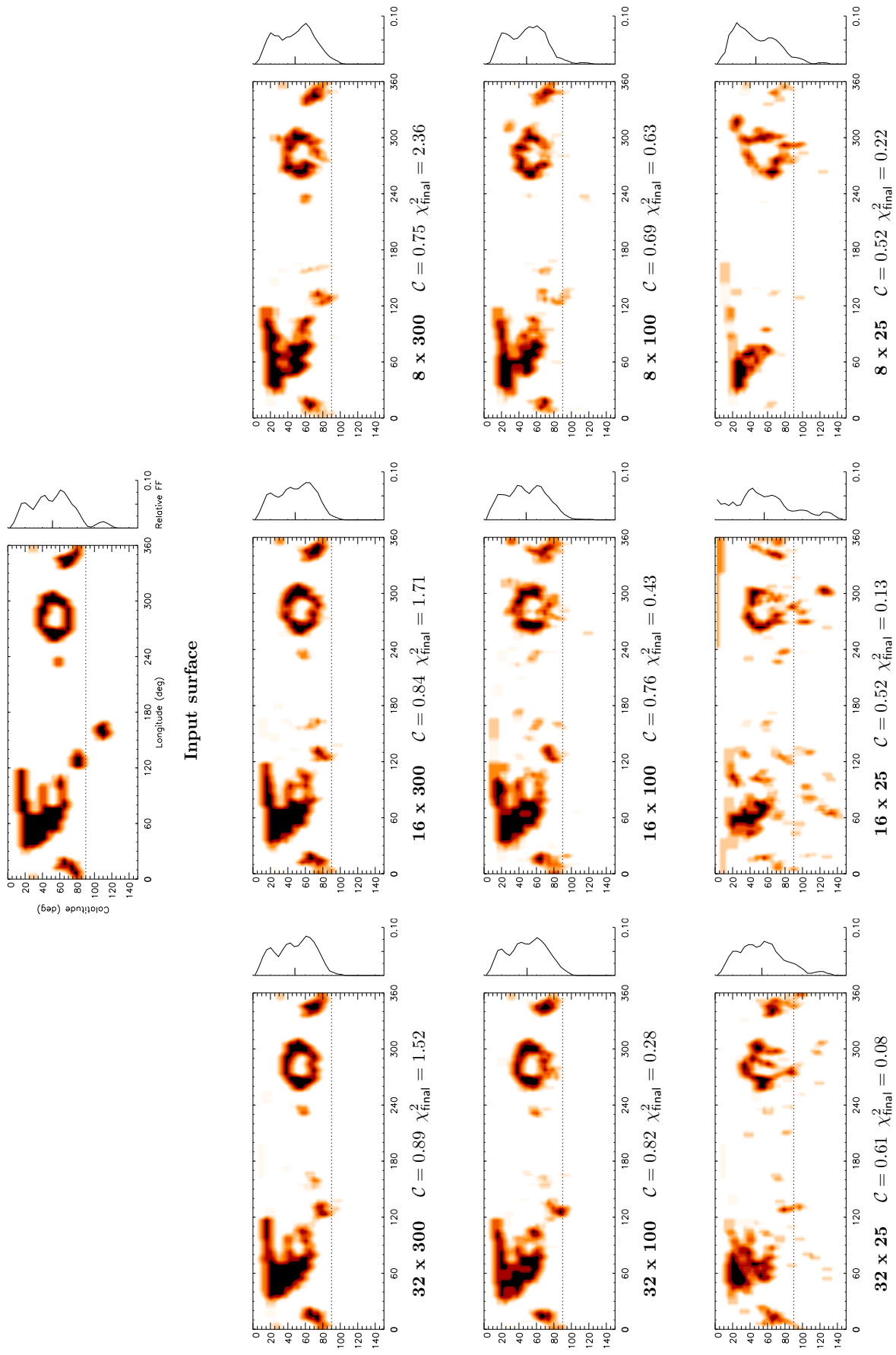

Figure 5.30: Quality of CLDI reconstructions (RM×TSA) as a function of the input data quality which is given as "**number of sampled phases** × **SNR**". The $\chi^2_{\rm final}$ and congruence values $\mathcal{C}$ (Eq. 5.15) are measured relative to the input line profiles and input test surface, respectively. The shown images correspond to the asterisks in Fig. 5.24. The narrow graph right of each map shows the latitude distribution of spots (Sec. 5.5.5).

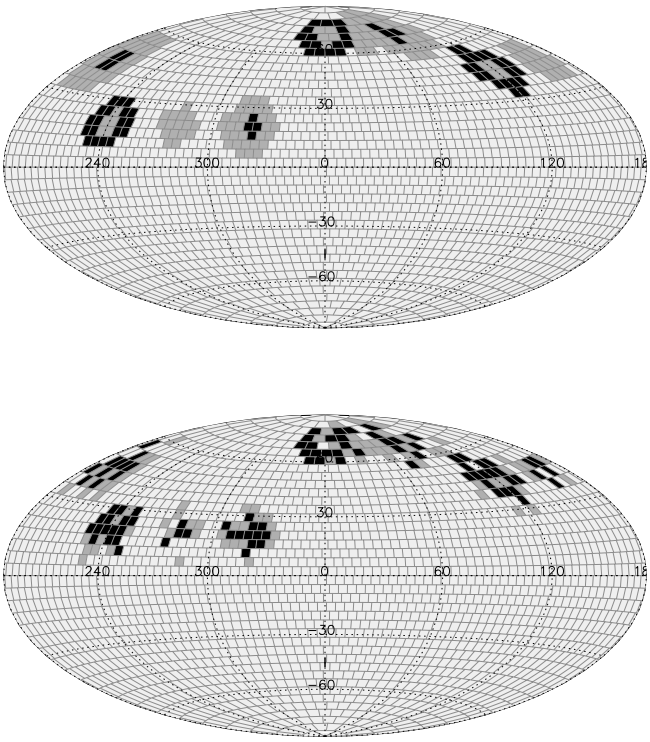

Figure 5.31: *Upper panel:* "Penumbra" input surface *Lower panel:* CLDI reconstruction (RM×TSA) for 32 equidistant phases and a SNR of 300. The grayscale is shown in Figure 5.26.

intervals of 45° turns. This means that every feature is observed three times during its passage over the stellar disk. According to the considerations of Section 4.1, this allows a reconstruction of its position.

However, already for the regular "OvE" input surface a dense phase sampling is needed to avoid shadowing (Section 4.1) and to fully resolve some detailed features. Especially the horizontal bars of the "E" are prone to shadowing. Since increasingly complex spot patterns increase the influence of shadowing, they require a sufficiently dense phase sampling for their reconstruction.

5.5.3 Umbra-/Penumbra reconstruction

As shown in the example of Figure 5.31, CLDI is not able to successfully reconstruct several steps of flux brightness. This is primarily caused by intrinsic ambiguities of the line profile information (see Section 4.1). Additionally, CLDI's irreversible solution assembly, making little use of visibility information, is not well suited for this purpose.

This failure of CLDI to reconstruct penumbrae-like structures agrees with results of Kürster (1991, 1993) for the "old" CLDI. An explicit optimization of the solution surface may improve this situation, at least in the ideal case of completely known stellar parameters. Actually, spot contrasts are partially recovered by careful maximum entropy DI *for well-extended homogeneous spots* (cf. e.g. Rice & Strassmeier, 2000, Fig. 2). However, the same example shows that this is not the case for small or intermediate-scale penumbra-like structures.

5.5.4 Reliability: An irregular teststar

As suggested by the Sun, real spots on stellar surfaces may be far from the "regularity" displayed by teststars like the "OvE" surface of Figure 5.25.

To test the influence of surface fine structure and complexity on the quality of the Doppler images, test results for the "OvE" surface were compared to those of a tentative "irregular" surface, shown in Figure 5.32. Actually, this is a preliminary DI of HD197890, as can be seen by comparing it to Figure 7.13. Although *not containing significant southern features*, it possibly better simulates the case of real observations than more regular test surfaces.

Comparing Doppler images of the irregular surface (Figures 5.33 and 5.34) with corresponding reconstructions of the "OvE" surface (Figure 5.30) indicates, that the latter are reliably reconstructed down to smaller scales. This is supported by a comparison of the respective surface congruences in Table 5.2.[21]

Apparently, CLDI manages to reconstruct the boundaries of regular, medium-scale spot patterns with a better resolution than small-scale patterns. To some degree this can be expected from the discussion of mutual "shadowing" of spots during the one-dimensional projection onto the line profiles (Section 4.1).

However, the χ^2_{final}-values of Table 5.2 show that CLDI is also less successful in fitting the line profiles in the irregular surface case. This indicates limitations of CLDI's backprojections for such irregular small-scale features.

An explicit optimization of line profile fits, like maximum entropy DI, can improve these fits by small-scale adjustments of the solution. The irreversible assembly of the solution by CLDI does not allow this. If the additional information thus extracted by maximum entropy DI could improve the small-scale resolution in the irregular case was not tested in the context of this work; this is due to

[21] For the CLDI reconstructions of the irregular input surface described in this section, RM×TSA backprojections were used. The slight superiority of RM×TSA over $\mathtt{RM}_{0.5}$ backprojections for synthetic data has been demonstrated for a *regular* input surface in Section 5.5.1; it remains valid in the irregular case. The values of $\mathcal{C}$ and χ^2_{final}, describing the image reconstruction and line profile fit quality respectively, are more than 10% poorer when using $\mathtt{RM}_{0.5}$-backprojections compared to the values of Table 5.2 which describe RM×TSA backprojections.

Table 5.2: CLDI reconstruction quality of a regular ("OvE") and an irregular input surface (Fig. 5.32) with otherwise equal reconstruction and stellar parameters. The values of $\mathcal{C}$ and χ^2_{final} measure the achieved image reconstruction quality and the line profile fit quality, respectively.

$n_{\mathsf{ph}} \times \mathsf{SNR}$	16×100		32×300	
	χ^2_{final}	$\mathcal{C}$	χ^2_{final}	$\mathcal{C}$
"OvE"	0.4	0.76	1.5	0.89
"Irregular"	1.0	0.56	2.2	0.67

the limited resolution that could be handled by the maximum entropy DI program used for comparison (see Section 8.4).

The (at least subjectively) very small deviations between the synthetic input line profiles and their reconstructions by CLDI (an example is shown in Figure 5.35) illustrates that CLDI is quite successful in its line profile fits. The minuteness of the deviations suggests that a significantly higher resolution of the reconstructions may be hard to achieve. However the profile deviations are not randomly distributed (e.g. for the broad bump around phase 0.3 in Figure 5.35); consequently they show that CLDI does not extract *all* information from the profile time series and that CLDI's reconstructions are not strictly optimal.

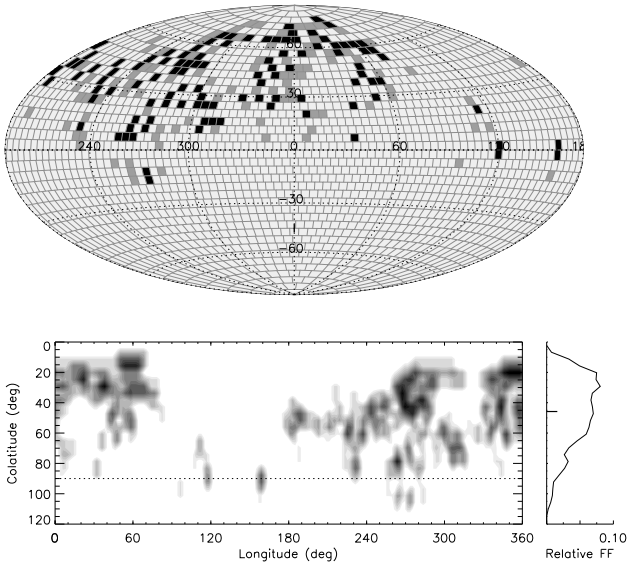

Figure 5.32: "Irregular" input surface, shown in Hammer-Aitoff projection (upper panel) and pseudo-Mercator projection (lower panel) respectively. The small graph right of the lower map shows the fractional spot filling factor for each latitude (Sec. 5.5.5).

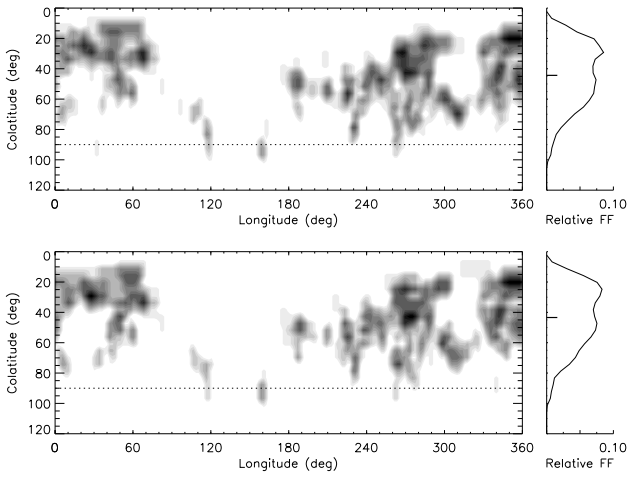

Figure 5.33: Doppler images of the above "irregular" surface reconstructed from 32 equally spaced observation phases; the corresponding line profiles are shown in Fig. 5.35. Both panels show CLDI reconstructions with the same parameters, but the input line profiles were superimposed by differently seeded random noise of SNR 300. Note the pronounced similarity of both images and the "input" surface on scales down to about 10-20°. Note also the small-scale differences on scales $\lesssim 10°$.

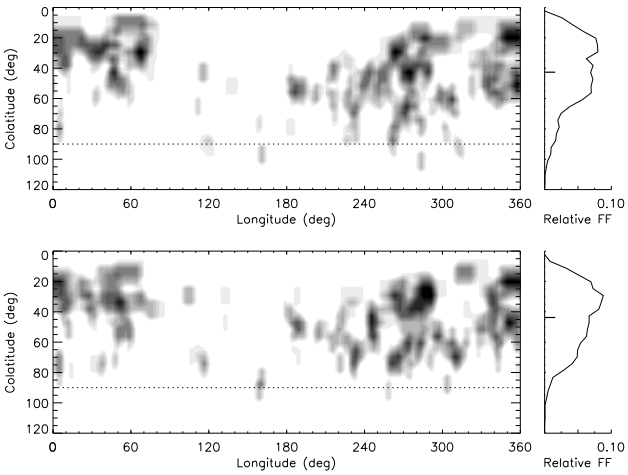

Figure 5.34: Companion to Figure 5.33, but for 16 equally spaced observation phases and superimposed by differently seeded random noise of SNR 100. Due to the coarser phase sampling and higher noise level, the correspondence of these images with the input surface is poorer, compared to the images of Fig. 5.33. Note reconstruction artefacts like the spot at 100° longitude and 30° colatitude in the lower image which do not appear in Fig. 5.33.

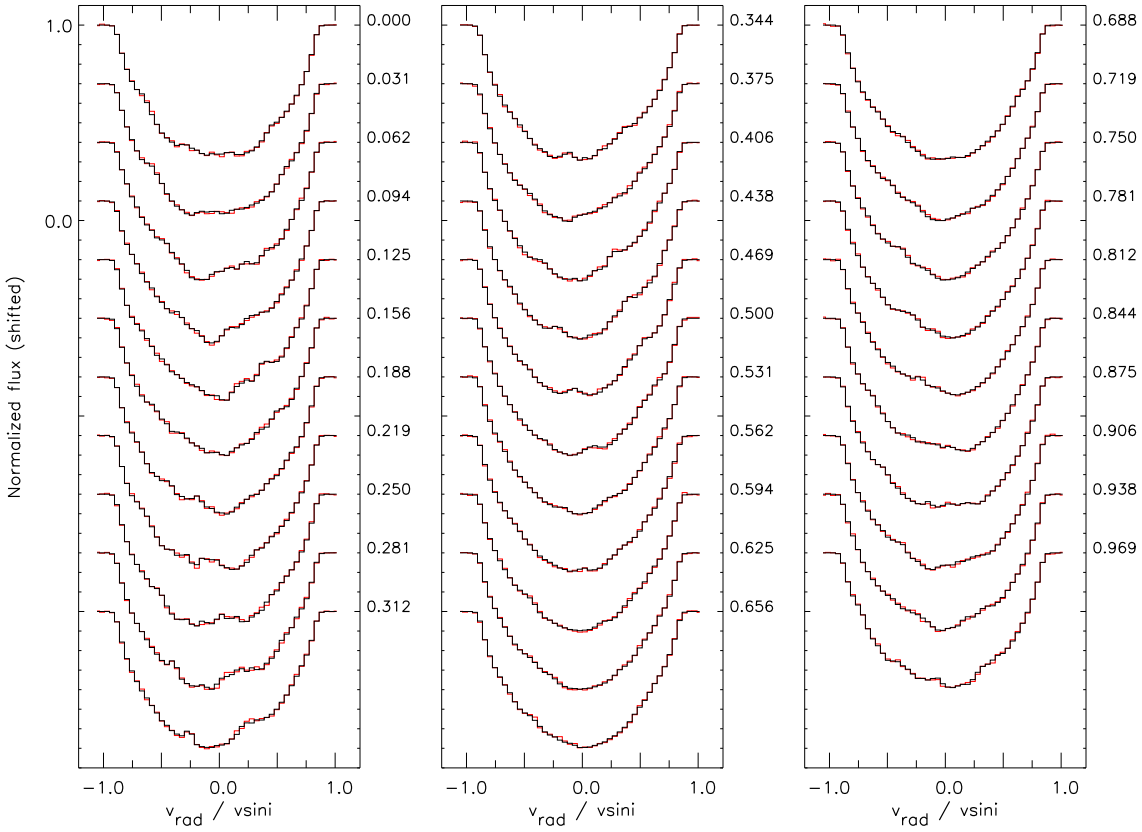

Figure 5.35: Line profile time series of the "irregular" test surface of Fig. 5.32, synthesized at 32 evenly spaced phases and superimposed by random noise of SNR 300 (red/gray curves). The black curves show the line profiles fitted by CLDI, belonging to the image shown in the upper map of Fig. 5.33. The attained line profile fit quality is $\chi^2_{\rm final}$=2.2. Note that due to the quite successful reconstruction the input and fitted profiles are difficult to distinguish for most phases at this scale.

5.5.5 Inclination determination

As discussed for a schematic example in Kürster (1993, Sec. 4.4), Doppler imaging can be used for determining stellar inclinations, if spots occur on a sufficiently wide range of surface latitudes.

The procedure is to adopt the inclination for which the DI reconstruction yields the best fit to the observed line profiles. This has been applied to many objects, yielding a wide range of inclinations usually compatible with other stellar parameters (e.g. Hatzes et al., 1989; Kürster et al., 1994; Piskunov et al., 1990a, who incorrectly claim that this procedure was proposed by Vogt et al. 1987). This includes close binaries for which the inclination of rotation axis can presumably be inferred from the orbital inclination (e.g. Hatzes, 1998, Sec. 3.2). Occasional synthetic tests support a successful recovery of the stellar inclination by minimizing the line profile fit deviation (e.g. Rice & Strassmeier, 2000, Sec. 4.4).

As illustrated by Figure 5.36, CLDI does also successfully recover the inclination i of an artificial input star; this applies to both "standard settings" of the backprojection. However, the $\mathtt{RM}_{0.5}$ shows a more symmetric, better defined minimum in $\chi^2(i)$, especially for the intermediate noise case. As a consequence, it has been used for the inclination determination of HD197890, discussed in Section 7.5.2.

As also illustrated by Figure 5.36, even for dense phase coverage a sufficiently low noise level is required to successfully determine the inclination. This is caused by the failure to reliably detect line profile deformations sufficiently far from the line center for too strong noise.

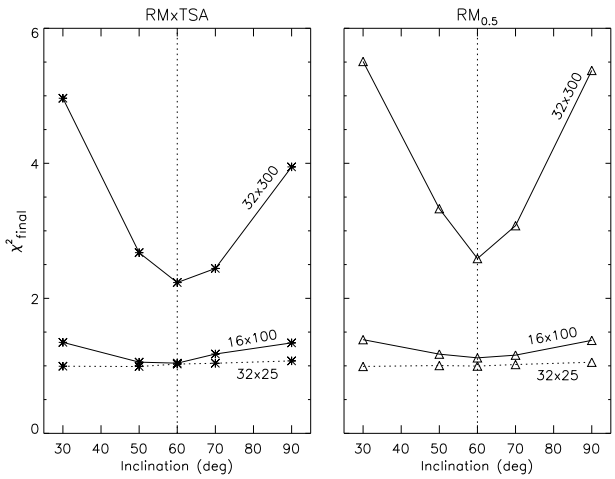

Figure 5.36: Quality of CLDI line profile fits χ^2_{final} as a function of the inclination of the reconstruction star. Different data qualities are given as "number of sampling phases x SNR". The left and right panels show results using the given backprojections. The "irregular" test surface (Fig. 5.32) at an inclination of 60°(marked by the vertical dotted lines) was used to synthesize the input line profiles. Note that for the high-noise case (SNR 25) no inclination information can be recovered, in spite of the dense phase sampling.

Sub-observer-latitude bias

As discussed in Sections 4.3.1 and 5.2.2, maximum entropy DI and CLDI reconstructions may exhibit a latitude bias by putting spots preferably on the sub-observer latitude. Since CLDI assembles its solution by "irreversibly" positioning spots, this could hamper the convergence of CLDI. One motivation for possible modifications of the response matrix used by CLDI (see Section 5.2.2) was the study of this effect.

A quantitative *measure for the spot latitude distribution* is useful for such an analysis. The measure used here is the fractional filling factor per colatitude interval, i.e. the percentage of *area* covered by spots for each latitude ring of surface elements.[22] The small graphs right of the

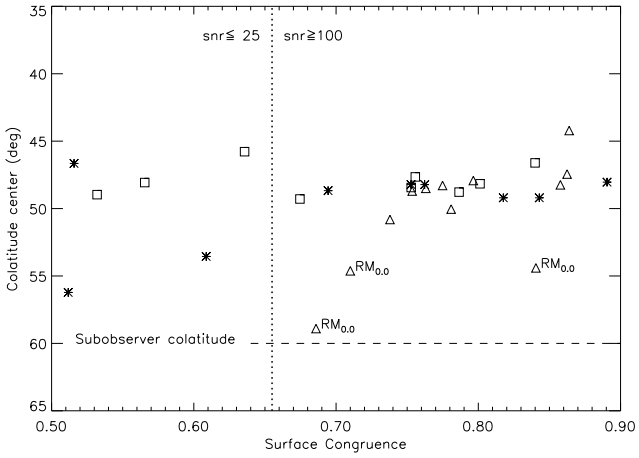

Figure 5.37: Center of the spot colatitude distribution θ_c for the same CLDI reconstructions as in Fig. 5.24, using the same symbols. Note that the different reconstructions (apart from the indicated $\mathtt{RM}_{0.0}$ reconstructions and some "high-noise cases" with an SNR of 25) show no apparent trend relative to the subobserver colatitude of 60° (equal to the stellar inclination). Only the $\mathtt{RM}_{0.0}$-reconstructions (no visibility weighting of the backprojection response matrix) show a marked shift of spot colatitudes towards 60°.

[22]The center colatitude θ_c of this spot latitude distribution $\rho(\theta)$ is occasionally used in this chapter. It is defined as

$$\theta_c = \int_0^\pi \theta \cdot \rho(\theta)\, d\theta$$

pseudo-Mercator maps of this chapter show this fractional filling factor (annotated by "relative FF"). The tick on the y-axis of these plots indicate the center colatitude θ_c of the spot distribution.

Experience with CLDI has shown, that a latitude bias of the reconstructions is not encountered in practice, definitely not for reasonable phase sampling. As Figure 5.30 shows, the spot latitude distribution of an input surface is quite well reproduced by CLDI reconstructions (not including spots on the southern hemisphere); significant deviations occur only for very poor SNR or phase sampling of the input line profiles. Individual spot patterns show no apparent tendency of being "drawn" towards the subobserver latitude of 30° (=60°colatitude).

The absence of a significant latitude bias in CLDI reconstructions is further supported by Figure 5.37: Only a very weak visibility-weighting of the backprojection response matrix (the $\texttt{RM}_{0.0}$ cases) disturbs the latitude distribution of the spots reconstructed by CLDI. This is due to the increased tendency of $\texttt{RM}_{0.0}$ reconstructions to "mirror" parts of the spot pattern to the southern hemisphere, thereby shifting the center of the latitude distribution towards the equator.

Actually, also for very high line profile noise (some cases in Figure 5.37 with a SNR of 25) there seems to be a subobserver latitude bias in the RM×TSA reconstructions. However, as Figure 5.30 illustrates, such a high noise level allows only very poor reconstructions anyway, so that this case is of little practical relevance.[23]

Summing up, a subobserver latitude bias is inherent to CLDI (due to its response matrix backprojections, see Section 5.2.2) and maximum entropy DI (due to properties of the regularization function, see Section 4.3.1). However, as the examples discussed in this section indicate, this bias is not of practical relevance for reasonably dense phase coverage and moderate or low line profile noise. Apparently, the latitude information contained in the line profile time series is sufficiently pronounced to override such a bias.

5.5.6 Other stellar parameters

Profile shape errors

Incorrectly assumed limb-darkening, $v \sin i$ or line equivalent widths lead to deviations of the reconstructed line profiles from the input line profiles, which are independent of rotation phase. CLDI, as any other DI algorithm tries to compensate this by image structures also independent of rotation phase, i.e. rotationally symmetric spot patterns in the solution. Depending on the location of the deformation in the line profile, this leads to polar caps or "spotted belts" in the reconstruction. Examples can be found in Kürster (1993, Fig. 9), as well as in Unruh & Collier Cameron (1995, Figs. 5 and 6). An extensive discussion is performed in Kürster (1991, Ch. 4).

Incorrectly adopted rotation period

In contrast to inclination, choosing a different rotation period has a marked influence on the resulting Doppler images. Three different mechanisms influence the DI reconstruction, when the adopted period is changed: (a) "reshuffling" of phases from different rotations, (b) "warping" of the image in longitude, and (c) a latitude shift of features.

(a) is caused by the fact that profile distortions observed during different stellar rotations will not show the correct migration behaviour through the line profile, when "phased" with a wrong period.[24] Since the example in the upper map of Figure 5.38 is reconstructed from the data of a single rotation (as the reconstructions of Chapter 7), mechanism (a) does not lead to overall inconsistencies of the phased time series. However, inconsistencies arise where the observations from the start and the end of the observed rotation overlap on the reconstructed surface. In the given example, this is the case around 0° longitude and leads e.g. to the massive reconstruction artefacts at about 30° longitude.

The assignment of each observation time to a longitude on the surface depends on the adopted rotation period, which causes effect (b). An example can be seen by comparing the input surface (Figure 5.25) to a Doppler image based on a wrongly adopted, too large a period (upper map of Figure 5.38). Such a comparison reveals that the wrong-period reconstruction is increasingly "warped"

[23] Another way of studying a potential latitude bias of CLDI is by comparing reconstructions for differently adopted stellar inclinations. Comparing the two maps of Figure 7.19, two effects are visible: Adopting a higher inclination (70°) produces (i) an increased number of spots "mirrored" to the southern hemisphere and (ii) on average darker spots at intermediate latitudes. Effect (ii) is due to the poorer visibility of intermediate latitudes for the higher inclination, requiring spots of stronger contrast to produce line profile deformations of the same amplitude as in the case of $i = 50°$. The mirrored south features of effect (i) also act to increase the amplitude of the line profile deformations, they are amplified by the increasing north-south ambiguity of DI for increasing stellar inclinations (approaching the complete lack of hemispherical information in Doppler images for $i = 90°$, see Section 4.1). Both effects are also discussed in Section IV e) of Vogt et al. (1987).
However, also in this example, no obvious latitude shift of features is taking place, although the sub-observer latitudes of the considered reconstructions differ by 20°.

[24] Hatzes (1990) presents an example of (a), with an initially slightly wrong adopted reconstruction period of about 1.3 days and observations spanning more than a year.

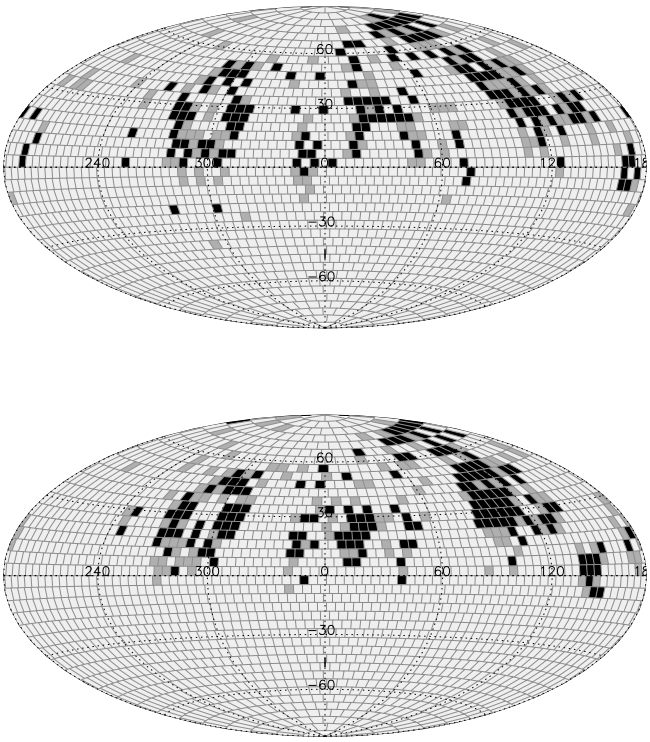

Figure 5.38: CLDI reconstructions ($\mathtt{RM}_{0.5}$) with wrongly adopted rotation parameters. The "OvE" test surface (Fig. 5.25) in rigid rotation, observed at 32 equidistant phases and a SNR of 300 was used as input. *Upper panel:* Adopting a rigid rotation, with a 20% too long period. *Lower panel:* Adopting a roughly correct equatorial rotation period, but a differential rotation with α=0.25 (i.e. slower-pole, see Eq. 2.6). The gray scale is shown in Figure 5.26.

in longitude with decreasing value of longitude.[25]

(c) is due to the differently interpreted migration speed of the deformations through the line profile. For an increasingly larger adopted rotation period, the migration speed of the spots over the projected stellar disk decreases. To keep up their observed migration speed through the line profile, they need to be shifted to lower latitudes. This shift of the spot pattern towards the equator is quite pronounced for the "O" and the "E" in the upper map of Figure 5.38.

Since a latitude shift of the spots also changes their radial velocity amplitudes, it leads to *intrinsic inconsistencies* of the line profile time series. These intrinsic inconsistencies arise because the radial velocity amplitudes no longer match (the visibilities and shape of) the observed line profile deformations. In conjunction with (a) this presumably leads to the reconstruction deficiencies of the upper map of Figure 5.38. It should be kept in mind that detecting such intrinsic inconsistencies requires a very good line profile modelling, dense phase sampling and low noise for real observations.

Strong differential rotation

In the context of Doppler imaging, "strong" differential rotation has two meanings, one related to the overall line profile shape the other related to the resulting surface shear.

As outlined in Section 3.2, differential rotation leads to a deformation of the rotationally broadened line profile, compared to rigid rotation. Differential rotation is "strong" for Doppler imaging if this deformation becomes significant compared to the spot-induced deformations. Very roughly this may be the case for $\alpha \gtrsim 0.1$. However, as also outlined there, the deformations due to differential rotation are quite similar to those caused by strong limb darkening.

In addition to deformations of the line profile shape, a differently adopted differential rotation affects the DI reconstruction with mechanisms analogous to (b) and (c) discussed above for rigid rotation. An example reconstruction for an incorrectly adopted differential rotation is shown in the lower panel of Figure 5.38. While effect (c) is clearly visible for this example in the equatorward shift of the "O" and the "E", compared to the input test surface (Figure 5.25), effect (b) is less pronounced: Only the "E" looks slightly warped (first of all it is sim-

[25] Since rotation takes place with decreasing subobserver longitude and starts at $0^\circ \hat{=} 360^\circ$ longitude, the effect of the differing rotation period increases with *decreasing* latitude.
As a result, the "O" and the left half of the "v" are reconstructed at quite correct longitudes, while the "E" is found at too large longitudes, compared to the input surface.

ply poorly reconstructed). Note that the nearly correctly adopted equatorial rotation period manifests itself in the quite successful reconstruction of the "equatorial spot" at about 130°latitude.

For observations covering more than one rotation period also the above mechanism (a) becomes relevant (this is not the case for Figure 5.38). Even if less than one rotation period is observed, mechanism (a) plays a role in those surface regions where observations from the start and the end of the observed rotation overlap.

Concerning the discussed image distorting effects, differential rotation is strong when its longitude shear during the observed rotation exceeds the resolution of the resulting Doppler image. Again very roughly, for high resolution Doppler images as those discussed here, with a surface resolution of the order of 10 degrees, this may also become significant for $\alpha \gtrsim 0.1$.[26]

Currently CLDI does support the modelling of surface shear due to an adopted differential rotation law $\Omega = \Omega(\theta)$; given a correct $\Omega(\theta)$ it could compensate the effects (a)-(c) above. However, CLDI's line profile modelling does presently not take differential rotation into account. As mentioned above, its effect on the overall line profile shape can to some degree be approximated by adopting a stronger limb darkening.

5.6 Evaluation and outlook

5.6.1 Evaluation of test results

CLDI's reconstruction capabilities have been tested for a wide range of input data qualities (Figures 5.24 and 5.30). These tests show CLDI to react in a stable way to an increase of input noise as well as to a decreased phase sampling density. Here stability means that the line profile fit quality (measured by a decreasing χ^2_{final}) and the surface reconstruction quality (measured by the image congruence $\mathcal{C}$, Equation 5.15)[27] improve monotonically with increasing input data quality. The behaviour of CLDI in the presence of phase sampling gaps has not been tested, because it is not relevant for the observations of Chapter 7.

The described tests of CLDI also demonstrate the ability of CLDI's backprojections to successfully extract fine structure of the spot pattern to be reconstructed, given high input data quality. However, the reconstructions of the "irregular" test surface (Figure 5.32) indicate that *the resolution achieved by CLDI for a given phase sampling density depends to some degree on the complexity of the spot pattern*.

The influence of "shadowing" (due to the *one-dimensional* projection of spots onto each line profile, see Section 4.1) increases for increasingly complex spot patterns. As a consequence some decrease of the resolution is intrinsic to Doppler imaging (at least for finitely dense phase sampling) for irregularly shaped and positioned spots. However, also CLDI's line profile fit quality is getting poorer (increasing χ^2_{final}) for more irregular spot patterns (Table 5.2). This indicates that the backprojections of CLDI extract spot position information less successfully for increasingly complex spot patterns.

The χ^2_{final} values for all test cases studied here (including the low-noise cases which allow the most detailed reconstruction) are of the order of unity; this indicates "nearly immaculate" line profile fits (which is also the case, see Figure 5.35). Whether an even closer fit to the line profiles could yield a significantly higher resolution of the resulting Doppler images cannot be checked with the current performance of CLDI. However, for many practical applications this question is of limited significance, because for real observed data the reconstruction parameter uncertainties and spectral line extraction or line synthesis deficiencies (due to minor unrecognized blends etc.) are likely to destroy the required very "high-fidelity" line profile information.

Several algorithm-specific parameters control the CLDI reconstruction process, including the backprojection used for translating line profile deformations into spot pattern information. Two "standard settings" of CLDI (termed `RM×TSA` and $\texttt{RM}_{0.5}$) have been selected based on the test results. Their achieved image resolution for high-quality input data (i.e. densely phase-sampled low-noise line profiles) are very similar. For the ideal conditions of the performed tests (for a perfect line profile synthesis and completely known stellar parameters) the `RM×TSA` reconstructions supersede their $\texttt{RM}_{0.5}$ counterparts marginally but significantly. The `RM×TSA` setting of CLDI provides a *conservative mode* of CLDI in the sense that it is not prone to produce features on the solution surface without "properly" evolving deformations in the line profile time series.

CLDI increases the local spot filling factors of its solution surface strictly monotonically by *discrete* increments. Lowering this increment slows down the convergence of CLDI and improves the finally achieved line profile fit quality and image resolution.[28] A value of δ_{FF}=0.5

[26] $\alpha = 0.1$ results in a pole vs. equator shear of 36°during one equatorial rotation (Equation 2.9), correspondingly in a shear of the order of 20°between well-resolved latitudes.

[27] The rather simple measure $\mathcal{C}$, defined by Equation 5.15 proved to be a useful quantitative proxy for "image congruence" if the resolution of the compared images is of the order of the resolution of the surface grid.

[28] Decelerating convergence is often a "good idea" (although naturally no guarantee) for solving *global* optimization problems (e.g. Lucy, 1994) in order to avoid the algorithm getting hooked on some

for this increment (adopting a maximum filling factor of one for each surface element) has been found to be a sensible value for this parameter, leading to a significant improvement of the CLDI reconstructions for high-quality input data compared to δ_{FF}=1.

The above aspect can be put as: The CLDI reconstruction is significantly more successful when enabled to build up solution surfaces containing several steps of the spot-photosphere contrast, instead of constructing a strictly "black and white" solution. However, CLDI was found to be unable to reconstruct penumbra-like spot patterns, more generally it can presently not successfully reconstruct different spot-photosphere contrasts.[29] As a consequence the spot brightness grades in the CLDI Doppler images are an intrinsic result of its solution algorithm, they cannot be identified with true contrasts found on the stellar surface to be reconstructed.

There is a trade-off between a dense phase sampling and low-noise of the line profiles of a time series: For any time series the profiles of adjacent phases can be summed up ("phase-binned") to achieve a lower SNR. Given the choice between a dense phase sampling and low-noise line profiles, the latter should be preferred for the purpose of Doppler imaging. This is illustrated by Figure 5.30, comparing e.g. the "32×25" Doppler image (32 equidistantly sampled phases at an SNR of 300) to its "8×100" counterpart. Although the input data of the latter image could be directly generated from that of the former by phase-binning, the latter has a better reliability and resolution. Once the line profile noise exceeds the "critical level" (not sharply defined) of the typical profile deformation amplitude, additionally sampled phases add only very little Doppler imaging information to the time series. However, the above recommended choice is no more than a rule of thumb, because the reconstruction of increasingly complex spot patterns requires increasingly dense phase sampling (*and* a sufficiently low noise level).[30]

CLDI's backprojections more or less "turn blind" when a critical noise level is exceeded. Although explicit optimization strategies for Doppler imaging (e.g. maximum entropy Doppler imaging, MEMDI) presumably can fit up to higher noise levels, also they will fail in the absence of well-defined profile deformations due to excessive noise. The above discussion suggests that there is an "optimum" phase sampling density for Doppler imaging, given the total available exposure time for the line profile times series, the achievable SNR and the amplitude of the profile deformations to be detected. This optimum is found between the extreme cases of summing up all spectra into one (which yields no Doppler imaging information, apart from revealing rotationally symmetric structures like polar spots) and "far too noisy" spectra resulting from splitting the time series up into too shortly exposed spectra. Of course these considerations are only of interest if the phase sampling is not, as often in practice, mostly determined by other factors like telescope scheduling, object visibility etc..

5.6.2 CLDI old and new

The term "old CLDI" refers to the Doppler imaging algorithm developed by M. Kürster. The publications describing it (Kürster, 1991, 1993; Kürster et al., 1994) were the starting point of the "new CLDI", developed as a part of this work. The new CLDI makes use of the basic idea and construction principles of its "old" predecessor.[31] The following aspects have been improved comparing the old and new CLDI:

- A deeper understanding of its "working principles"
- Use of the visibility information contained in the time series of line profile deformations.
- An "interface" to line profiles determined from spectrum deconvolution
- High surface resolution

local minimum far from the "true" solution. This decelerating idea can be found in global optimization strategies like e.g. *simulated annealing* (Kirkpatrick et al., 1983).

[29] Given high-quality data, spot contrasts far weaker than on the stellar surface to be reconstructed (i.e. spots adopted far too "bright") do lead to poorer line profile fits. Excessively large spots need to be put onto the solution surface in this case which leads to conflicts with the visibility information of the line profile deformations (this agrees with the results of Kürster et al., see Kürster, 1993, Sec. 4.3 and Kürster et al., 1994, Secs. 5.1 & 6.1).
So a rather high *upper* limit can be determined for the spot brightness from Doppler imaging high-quality input profiles of a single line or extracted from a single spectral region. But, citing Kürster et al. (1994, p. 916): "There is no measure against an *underestimate* of spot brightness from single-line spectroscopy alone".

[30] Statements like "increasing the number of phases adds mostly redundant information to the dataset [for the purpose of Doppler imaging]" (Kürster, 1993, p. 863) are easily misunderstood outside their specific context: They depend sensitively on the complexity of the spot pattern to be reconstructed.

[31] Preliminary tests were carried out using the original FORTRAN77 implementation of the old CLDI, kindly supplied by M. Kürster. These tests indicated soon that the given source-code was not suitable for further extensions and improvements. This triggered the development of the new CLDI as a completely new realization in the programming language of the data analysis environment IDL (Interactive Data Language, see Section 8.5) A manifest result of the mentioned tests was that the line profile synthesis of the old CLDI was not well-suited for synthesizing low-noise line profiles of high effective resolution (i.e. using narrow intrinsic line profiles) in the regime required for the VLT/UVES data of HD197890. This made the development of a suitable line profile synthesis algorithm the seed of the new CLDI. Originally by accident, this has resulted in a separation of the response matrix treatment and line profile synthesis (in contrast to the old CLDI) which proved fruitful for the development of the new CLDI.

Obviously, the items of this list are of different character. The mostly *conceptual issues* are given first, while concerning their *practical impact*, the ordering of the list is presumably upside down. These two aspects are separated in the following discussion.

In the context of this work the observed input line profiles of CLDI have exclusively been generated by spectrum deconvolution (using "selective least squares deconvolution", sLSD). CLDI can operate without sLSD, directly using a spectral line cut out from a spectrum. CLDI's line profile synthesis should be completely appropriate for such an application on ultrafast rotators (it is more versatile than the synthesis of the old CLDI which has been successfully used for this purpose, cf. Kürster et al., 1994). For slower rotators a more sophisticated spectral line modelling may be required.

Conceptual improvements

The response matrix contains a complete description of the specific Doppler imaging problem at hand (if the linear approximation is appropriate, see Section 4.3), including the geometry, spectral (sampling) resolution and phase sampling information. The Doppler imaging problem is in general ill-posed. As a consequence *the response matrix is not invertible*; this means in particular that that its transpose does not have any mathematically strict connection to its (nonexisting) inverse.

The problem of CLDI's working principle could be stated as: "Why does the iterative application of the transposed response matrix lead to an appropriate solution of the Doppler imaging problem?"

The following answer summarizes the discussion of Section 5.2, using the term backprojection map (named "probability map" by Kürster) for the surface map obtained for each CLDI iteration by applying the transposed response matrix to the difference of synthesized and observed line profiles:

> Most regions of the backprojection map contain spurious structures based on information from very few observation phases. No relevant Doppler imaging information can be obtained from very few phases. But the values near the maximum of this map result from summing up line profile deformations of (*often*) as many phases as possible. As a result, CLDI selects these close-to-maximum regions of the backprojection map at each iteration step which (*should*) contain very reliable Doppler imaging information.

The parenthetical words above are of central importance, because they underline the heuristic nature of CLDI.

As outlined by the above working principle, the response matrix backprojection makes efficient use of the *radial velocity information* of the line profile deformations, i.e. their position in the profile. But, metaphorically speaking, the response matrix backprojection ignores the visibility information contained in the profile deformation *amplitude*. A symptom of this ignorance is the intrinsic inability of the old CLDI to successfully reconstruct spots on the southern hemisphere.[32]

The modifications of the response matrix for the purpose of backprojection (Section 5.2.2) were originally studied to remedy this ignorance of visibility information. While the modified response matrices could not fulfil this purpose, they are conceptually simpler and computationally more efficient than their fully resolved counterparts.

The new CLDI possesses a second kind of backprojection termed "time-series-analysis" (TSA) which is independent of the response matrix. Also a heuristic approach, it attempts to expand the time series of line profile deformations into contributions from different surface regions. Developing the TSA backprojections was intended to make the visibility information of line profile deformations available to the CLDI reconstruction. TSA proved partially successful in this respect, leading to improvements of the Doppler images for high-quality input data. However, it is no satisfactory solution to the "southern hemisphere problem" which demonstrates that CLDI still leaves available information of the line profile time series unused.

Apart from resulting in minor improvements of the solution, an interesting aspect of the TSA backprojection maps is the striking similarity to their response matrix counterparts (Figure 5.14). This similarity is surprising because of the conceptual difference of the two backprojection methods. However, this similarity (and the resulting *only minor* improvements of the solution by TSA backprojections) give rise to the conjecture that the response matrix backprojection already extracts nearly all *unambiguous* information from the line profile time series which can be extracted by a direct "backprojection" (in the sense of a semi-analytic scheme applied to the in-

[32] The close relation between the localization principle of Doppler imaging for a single spot (Section 4.1) and the application of the transposed response matrix has been noted by Kürster (1991, Sec. 4.2), less pronounced it is found in Kürster (1993, Secs. 3.2 and 3.3). However, Kürster does not further analyze the properties of the response matrix and he does not discuss its intrinsic limitations (including a "southern blindness") due to ignoring the visibility information.
Kürster et al. (1994, Sec. 6.3, Figs. 23 & 24) nicely demonstrate that the profile deformations of a large southern spot can very well be mimicked by a weaker spot mirrored to the northern hemisphere. However, that this mimicry depends on ambiguous limb visibility information and hence on the spot size and phase sampling density is not further discussed there.

put data). Of course, this is by no means a strict proof.

Performance improvements

Apart from studying fundamental issues of Doppler imaging, the development of CLDI concentrated on the processing of "high-quality" input line profile time series. This "high quality" is defined by a dense phase sampling, low-noise input data and a high "effective" line profile resolution (i.e. a large ratio of the rotationally broadened width of the line profile to the intrinsic width of the used spectral line(s)). Although hard to quantify, the resolution parameters of the new CLDI, as verified by systematic tests, are about three times higher compared to the old CLDI. This factor characterizes the achieved surface resolution as well as the effective profile and phase sampling resolution. However, its value should not not be taken as a strict quantitative measure, it is given for illustration purposes only.[33] No "upper limits" have been determined for the current implementation of the new CLDI. Instead, the systematically tested parameter regimes were closely guided by the available input data quality (as in the case of Kürster, 1993 and Kürster et al., 1994).

The new CLDI can perform reconstructions adopting "moderately strong" differential rotation. "Moderate" means here that the differential rotation is strong enough to significantly distort the spot pattern during the observation time span of one image (see Section 5.5.6, this feature has been used for tentative rotation "scenarios" studied in Section 7.8.3). In addition, "moderate" means that the overall line profile shape deformation due to differential rotation (see Figure 3.1) is small compared to the spot-induced deformations used for the Doppler imaging. Presently CLDI cannot treat "strong" differential rotation cases appropriately, because its line profile synthesis does not model the overall profile shape resulting from non-rigid rotation.

The current implementation of CLDI's line profile synthesis is computationally rather ineffective; this can be improved if more bulky reconstructions should require it (see Section 5.6.3). Otherwise several features of CLDI, used in conjunction with "selective least squares deconvolution" (sLSD), keep its computational and memory requirements quite low: (a) Use of a modified response matrix for backprojection and a line profile synthesis independent of the response matrix; (b) extracting the line profiles from the input spectra by spectrum deconvolution *previous* to the Doppler imaging reconstruction itself.

It should be kept in mind that item (b) comes at a price: Working on the rotational broadening functions resulting from the spectrum deconvolution must be an appropriate approximation to a full-grown spectrum synthesis. However, if it is appropriate, it considerably reduces the computational effort of the line profile synthesis *during* the Doppler imaging reconstruction.

The new CLDI and the programs related to it are realized as a transparent modular package (Section 8.5). This has been a "tacit" guideline during CLDI's development to allow future extensions and modifications.[34]

[33] As mentioned above, Kürster's original implementation of the old CLDI was not sufficiently "revitalized" (in spite of kind remote support by M. Kürster) to systematically study its behaviour. As a result any quantitative comparison of the performance of the old and new CLDI is based on the quantitative information found in Kürster (1991, 1993); Kürster et al. (1994).
Kürster (1993, studying synthetic input data) and Kürster et al. (1994, working on observational data) use nearly the same resolution parameters. These parameters (Kürster, 1993, Sec. 4.2 and Kürster et al., 1994, Secs. 4.1 and 4.3) result in each line profile sampled into 34 bins with an intrinsic line width of 2.5 bins, i.e. the profile was effectively resolved into about 34/2.5≈14 elements. One rotation was sampled into up to 26 phases which apparently was at the limit of the old implementation and computing capacities at the time (Kürster et al., 1994, p. 906).
These values can be compared to their counterparts used for CLDI in Sections 5.5 and 7.5, which translate into up to 49 bins sampling the profile, effectively resolved into up to 40 elements.
Due to the sampling theorem (cf. e.g. Press et al., 1992, Ch. 13), requiring at least a twofold oversampling for a given resolution, this resolution is not fully available to the reconstruction (although the profile synthesis was performed on an about tenfold finer sampling, see Section 5.4). However, if the profile is assumed to be effectively resolved into about 25 elements, Equation 4.2 yields a surface resolution of about 5° which is fully appropriate for the presented applications.
The maximum number of sampled phases for a DI reconstruction presented in this work is 72 (for the 2002 August 7 time series of HD197890 in Chapter 7). However, an "upper limit" for the current implementation of CLDI has not been studied (and is presumably of limited practical significance); cases of up to 100 sampling phases have been studied during this work.
The synthetic test surfaces of Kürster (1993, Figs. 5 & 18) show structures down to scales of about 30° on the surface. The test surfaces studied in this work (Figs. 5.25, 5.31 and 5.32) resolve scales down to about 10°.
Summing up the above collection of numerical values, the parameters describing the resolution each differ by a factor of two to three between the old and new CLDI (and the new CLDI has not been driven "to the limit" by these applications). The tested noise-levels of the new and old CLDI are of comparable magnitude (e.g. SNR=300 for the cases of Section 5.5 and SNR≈400 for Kürster, 1993, e.g. Tab. 1). However, a detailed comparison of noise levels is difficult and should take the "typical" amplitudes of line profile deformations into account to be truly appropriate (Section 5.5). The SNR values of Tab. 1 of Kürster (1993) must be seen in conjunction with the lower profile resolution and the rather coherent and large structures of the test surfaces (which have a massively smoothing effect on the resulting profile deformations).

[34] CLDI is not a result of "software engineering" in the sense that a catalogue of well-defined performance characteristics was set up *before* its realization and regularity monitored during the development. Instead, features "waxed and waned" during its development, especially when working on real observational data. However, the performance of the individual modules remained well defined and a reasonable transparency of the overall structure could be retained.

Concluding remark on CLDI's "philosophy"

CLDI (in contrast to e.g. maximum entropy Doppler imaging, MEMDI) is not an optimization algorithm. As a (rather long) slogan, CLDI's approach to the Doppler imaging problem can be formulated as

> Extract surface information from the line profile time series using estimators based on the knowledge of the geometry (and sampling) of the Doppler imaging problem. Stop the surface reconstruction when these estimators cannot retrieve any more information.

Although this applies in a similar way to an optimization method, the role of the deviations between the observed and synthetic line profiles is fundamentally different. For an optimization routine these deviations are typically quantified by a χ^2-measure and treated as a function of the surface values. The behaviour of this χ^2-function "guides" an optimization routine *during the whole reconstruction process* (e.g. by following local gradients).

On the other hand, CLDI uses the value of χ^2 only for its termination criterion: CLDI stops when it cannot achieve a further improvement of χ^2. Naturally the deviations between the observed and synthetic line profiles also form the input information of CLDI. However, CLDI interprets them in a different way by using its backprojections.

As illustrated by the exemplary comparison of MEMDI and CLDI reconstructions in Section 8.4, both methods produce the same global (or large-scale) solution. These large scales of the solution are unambiguously defined (apart from a partial north-south ambiguity) by high-quality input data and can be said to belong to the "well-posed component" of the Doppler imaging problem. But CLDI and MEMDI differ in their treatment of the poorly defined (or even conflicting) components of the input information, i.e. the "ill-posed component" of the problem. MEMDI continuously tries to reduce the line profile deviations, filling up ambiguous (i.e. strictly speaking missing) information based on its regularization function. Thereby MEMDI attempts to reduce the χ^2 down to a value which is determined from the estimated random noise level of the input data. In this way, the regularization function of MEMDI strongly influences image structures that are ill-defined by the input data. In case of "moderate" random noise this poor definition only affects the small-scale structure of the solution, leading to the small-scale smoothing of MEMDI reconstructions up to the resolution "properly defined" in accordance with the estimated random noise of the input data (which is a nice and sensible feature of MEMDI).

However, a poor definition of the solution by the input data is also partly due to intrinsic (geometric) ambiguities of the Doppler imaging problem (including a coarse or irregular phase sampling)[35] or even conflicting input information. Such conflicting information in the profile time series can arise due to fast spot evolution (fast compared to the observation time span), uncorrected measurement errors, unrecognized spectral line blends etc..

On the other hand, CLDI stops convergence after having extracted all "structural" information that its backprojections can discern in the profile time series. It does not (and it presently cannot) "fine-tune" its reconstruction after that by slightly adjusting the solution surface values according to the remaining line profile deviations. While such a fine-tuning may (and in favourable cases certainly does) lead to the extraction of more information from the input data, it certainly also leads to reconstruction artefacts where the extracted information happens to be ambiguous. In that sense CLDI's surface reconstructions can be called "conservative", because they are only based on the structures of the input data that CLDI recognizes as "properly evolving" with the adopted rotation.

Practical relevance of CLDI

The strength of the optimization approach of MEMDI lies in its ability to better fit the observed line profiles by *explicitly* minimizing their deviations from the synthesized profiles. This is a mathematically straightforward approach, employing the elegant concept of a regularization function. In this way MEMDI extracts more information from the input data than CLDI. However, part of this information is ambiguous or even conflicting for unfavourable conditions. For this part of the input information the MEMDI reconstructions are "biased" by the maximum entropy regularization.

CLDI, on the other hand, is a heuristic scheme using different estimators than MEMDI to extract information from the input data. These estimators are not intrinsically superior, but specifically adapted to the geometry of the Doppler imaging problem. As a consequence,

[35] Cases of MEMDI "overfitting" its input data, in the sense of extracting more surface information from the profile deformations than unambiguously contained in it are illustrated by some Doppler images of Vogt et al. (1999). Vogt et al.'s (quite successful) "thresholding" of their images after the Doppler imaging reconstruction proper is actually a removal of image artefacts. The thus removed (comparatively weak) spot groups are revealed as artefacts because only *after their removal* the quasi-simultaneous photometric lightcurves are appropriately fitted.
Unfortunately, cases of poor phase sampling and CLDI's reaction to it have not been systematically studied in this work. However, it is conjectured here that CLDI would tend to stop converging (which it can be quite obstinate at in cases of ill-defined input data) instead of constructing extensive artefacts.

CLDI's reconstructions provide to some degree an independent means of checking the reliability of features in e.g. MEMDI Doppler images.

A second attribute of CLDI, fundamentally different from MEMDI, are the images with discrete contrast steps it produces. That their appearance is rather like that of spots on the Sun is unfortunately only an aesthetic argument. Due to the surface resolution being intrinsically limited by the "effective resolution" of the observed line profiles, the reality of this cannot be proved on the basis of the observed input line profiles. However, the CLDI images offer a "different view" of the star to be reconstructed.[36] Together with the above issue of image reliability this "different view" can be a helpful tool for judging the reality of features found in Doppler images.

5.6.3 Outlook

The following items discuss desirable extensions of the present status of CLDI and their prospective feasibility.

An easy modification of the implementation of CLDI would be a computationally more efficient line profile synthesis.[37] The efficiency of the profile synthesis is crucial for CLDI's computational performance because it currently performs a synthesis of all profiles of the considered time series at each iteration step. Since CLDI (by construction) only applies changes to a few elements of the solution surface during each iteration (depending on the precise settings typically 3-5), many iteration steps (typically a few hundred) are necessary to reach the final solution. Apart from minor technical optimizations, an "incremental" synthesis would massively improve the computational efficiency: Instead of synthesizing all profiles "from scratch" during each CLDI iteration, the already synthesized profiles could be corrected according to the few changed surface elements.[38]

Optionally including photometry information in the CLDI reconstruction may be crucial for sparsely phase sampled observations (for which the behaviour of CLDI has not been systematically tested, see however the discussion in Section 7.7). Also for cases of dense phase sampling a strictly simultaneous high-quality photometry may play an important role (as its absence demonstrates in the discussion of Section 7.8.3). Photometric information could quite easily be supplied to the CLDI reconstruction by "wrapping" it as an additional backprojection map (which would contain mostly longitudinal information). This "photometry backprojection map" could be combined with CLDI's line profile backprojection maps by a (preferably weighted) mixing similar to those described in Section 5.2.3 or Equation 5.5. While such an approach would be easy to integrate into CLDI, its success and influence on the reconstructions would need systematic testing.

As outlined in Section 5.1, adopting a solution with discrete contrast steps turns Doppler imaging into a problem of discrete optimization. As also outlined there, CLDI does not use an explicit optimization approach. The disadvantages and potential merits of this non-optimizing approach of CLDI have been discussed above. A few considerations along the lines of the following can be found in Kürster (1991, Secs. 3.3.3 and A.1), as well as in Kürster (1993, Section 2.4).

What could be gained by an explicit (discrete) optimization approach, compared to CLDI's current "unidirectional" solution assembly?
(i) An improved surface resolution by extracting more information from a closer fit to the input data. (ii) Explicit information about the ambiguity of the solution of a specific Doppler imaging problem.

As discussed above, item (i) alone may also lead to the extraction of considerably ambiguous information; this relates it quite closely to item (ii). Nevertheless item (i) is an important aim, it presumably also motivated the mentioned discussions of Kürster (1991) who suggests a potential solution by a global optimization strategy called *simulated annealing* (Press et al., 1992, Sec. 10.9). Simulated annealing, not restricted to discrete optimization, belongs to a class of optimization strategies sometimes referred to as "intelligent optimization techniques" (cf. Pham & Karaboga, 2000, Ch. 1 for a compact overview). It is proposed in the following that there is another technique of this class which is better suited for Doppler imaging.[39]The fundamental weakness of simulated annealing

[36] As an example, the presumable reality of weak spot groups like that close to the equator at around 210° longitude in the August 7 CLDI images of HD197890 (Fig. 7.33) would easily go unnoticed in "smoothed" reconstructions; compare to Fig. 7.34.

[37] Currently CLDI spends nearly 90% of its computational effort on the line profile synthesis. The reconstructions described in Chapter 7 (typically 150-250 CLDI iterations) take about 5-10 min on a 2.4 GHz Pentium 4-based PC, using the current implementation of CLDI.

[38] Since the numerical disk integration is a sum extending over all surface elements, such an incremental correction could be easily incorporated. To avoid a pile-up of numerical round-off errors, a full profile synthesis may be necessary regularly after a suitable number of iterations.

[39] Simulated annealing has been successfully applied to other problems of discrete optimization (the most "renowned" of them being the travelling salesman problem, cf. Kirkpatrick et al., 1983). However, there is a substantial difference between e.g. the travelling salesman problem and the Doppler imaging problem: While the cost function (the function to be optimized) of travelling-salesman-like problems is computationally rather cheap to evaluate (e.g. basically two multiplications and a square root for each "city", using the Euclidean distance travelled by the salesman) it affords a complete synthesis of a line profile time series in the Doppler imaging case (which involves up to several hundred multiplications for each surface element to achieve realistic noise levels, see Section 5.4.2). A computationally expensive

in the context of Doppler imaging is its "short memory" of configurations previously tried out during the optimization. Keeping (suitably selected) previously successful configurations would be favourable for Doppler imaging problems because it could help to avoid unnecessarily (computationally expensive) trying out configurations. In addition, such a set of successful configurations would contain valuable information about the above issue (ii).

"Genetic" optimization schemes avoid the above listed disadvantages of simulated annealing and are proposed here as more suitable for Doppler imaging. The basic idea of genetic algorithms is inspired by natural evolution (Holland, 1975; Charbonneau et al., 1995; Pham & Karaboga, 2000): Instead of working on only one solution, they "breed" a *population* of potential solutions (termed "individuals") trying to improve its individuals by selection and reconfiguration processes. Naturally, *(a)* the criteria for selecting successful individuals need to be well-defined, as needs *(b)* the reconfiguration-scheme to successfully generate new individuals from the current population. Finally, the success of genetic algorithms depends *(c)* crucially on a population of potential solutions spanning a wide range of "qualitatively" different configurations (i.e. probing a sufficiently large parameter subspace to find a "proper" global solution). These issues are certainly non-trivial for Doppler imaging but not further discussed here.

As mentioned above, successfully applying a genetic optimization scheme to Doppler imaging would offer a chance of getting a concrete view of the "variance" of the set of feasible solutions (i.e. the surfaces leading to appropriate fits of the input line profiles). In this way it would contribute information to the error estimation of a Doppler image. As outlined in the summary of Section 8.4, unless discrete-spot-photosphere-contrast solutions are explicitly desired (although their reality cannot be verified on the basis of the available observational data), a "polishing" of CLDI's solutions towards a better profile fit is presumably most effectively done by a continuous optimization approach (like maximum entropy Doppler imaging).

Systematic and significant error estimates of Doppler images are still rare (see Section 4.2), they do presently not comprehensively cover all sources of solution ambiguity. "Standard deviation maps" etc. computed from Doppler images of different wavelength regions (e.g. Strassmeier et al., 2003) cannot completely resolve that issue, because all compared images are usually affected by similar ambiguities due to the given phase sampling and other fundamental geometric effects (however, they do help to analyze the influence of the spectrum or line profile synthesis).

Possibly semi-analytic error estimates of Doppler images could be obtained along the lines of the response matrix structure analysis and the geometric interpretation of the response matrix backprojection (Section 5.2). Such a future study could follow e.g. Christensen-Dalsgaard et al. (1993) who perform a study of response matrices appearing in helioseismic inverse problems. Their study is based on "generalized singular value decomposition" (cf. also Christensen-Dalsgaard, 2002, Sec. VI c). Possibly, the method of "optimally localized averages" (Backus & Gilbert, 1970; Press et al., 1992) which is e.g. used for helioseismic inversions, and supplies error estimates of the solution, could be successfully adapted to Doppler imaging (see Section 3.3 of this work, Pijpers & Thompson, 1992; Schou et al., 1998).[40]

Currently the spot brightness contrasts of a CLDI reconstruction result from the two adopted local line profiles for the undisturbed and spot photosphere (including the level of their continua). These local line profiles are supplied as input parameters to CLDI; as a result the brightness contrasts of the CLDI reconstructions are indirectly set a priori to the reconstruction and not determined from the observed line profiles during it.

Possibly CLDI could be extended to truly reconstruct spot temperature contrasts by simultaneously "imaging" several (ensembles of) lines of different temperature sensitivity. As outlined in Section 7.9.1, sLSD (*selective* least squares deconvolution) could be applied to carefully *selected* wavelength ranges containing spectral lines of similar temperature sensitivity. As outlined in Section 6.5 the average profiles extracted from different spectral regions clearly reflect the characteristics of the spectral lines dominating them. By determining average line profiles for several such ranges, dominated by lines with different temperature sensitivities, several line profile time series could be constructed. The spot-induced deformations in the profiles of each time series could have a "quite well-defined" temperature sensitivity.

As a first step different spot-photosphere contrasts could be adopted for different reconstructions, to see if they lead to fits of significantly different quality when *simultaneously* fitting the input time series of different tem-

cost function is very unfavourable for simulated annealing, because it is founded on "quite randomly" trying out many configurations to achieve a "good" global solution. In addition, not discussed by Kürster (1991), the efficiency of simulated annealing depends crucially on a "rearrangement prescription". This rearrangement prescription should generate "significantly different" new configurations from the current preliminary solution without falling back on "blindly" trying out completely random configurations.

[40] Citing Press et al. (1992, p. 816): "Backus-Gilbert is often recommended as the method of choice for designing, and predicting the performance of, experiments that require data inversion."

perature sensitivity. The simplest way of such a simultaneous fit by CLDI could be done by constructing a common backprojection map as a (weighted) average of the backprojections of the different input time series. As a second step the backprojection map of each input time series could be used separately to (possibly) reconstruct spots of different contrast.

The last issue discussed, namely trying to adapt CLDI to the (coarse) reconstruction of "true" surface brightness contrasts deserves to be critically scrutinized. Its feasibility needs to be checked by tests using synthetic data, including a cross-check of results with an "independent" spot temperature indicator (multi-colour photometry or molecular band heads). Possibly, such an approach will require the above mentioned "polishing" of CLDI's present solutions to achieve even closer line profile fits. However, whatever optimization method will be used for polishing the solutions (discrete optimization or e.g. maximum entropy Doppler imaging), CLDI in conjunction with sLSD could possibly fill a gap between broad range LSD (blind to characteristics of individual spectral regions) and a full-grown spectral synthesis *during* the Doppler imaging reconstruction.

Chapter 6

Least squares deconvolution (sLSD)

Deconvolving spectra with the aim of extracting "average line profiles" for Doppler imaging was introduced by Donati et al. (1997b), originally in the context of magnetic Doppler imaging to allow the detection of the extremely weak signatures of polarization components. Donati et al. also coined the name "least-squares deconvolution (LSD)" for their implementation of this idea.

Donati et al. apply LSD to wide spectral ranges with the aim of massively increasing the SNR of the extracted line profiles compared to individual profiles from the input spectrum. Thereby they attempt to make use of the e.g. more than 1000 Å wide spectral ranges simultaneously observed by modern Echelle spectrographs. However, such wide ranges contain several hundreds or thousands of "stronger" spectral lines in the spectrum of a solar-like star. This effectively inhibits studying the contribution of individual line (groups) and limits the possibilities of a careful template spectrum optimization.

The application of CLDI (CLEANlike Doppler imaging) presently requires a time series of "practically unblended" line profiles. In the context of this work these line profiles have been generated by a variant of LSD, called "*selective* least-squares deconvolution (sLSD)".

In contrast to the LSD of Donati et al., sLSD concentrates on the analysis of *narrower wavelength ranges*, typically several 10 Å wide, containing only a handful of "stronger" lines. While this comes at the price of requiring a higher SNR of the input spectra, it avoids the relative "blindness" of LSD to local characteristics of the spectra.

In the following discussion the abbreviation (s)LSD is sometimes used to indicate aspects applying both to "classical" LSD and sLSD.

6.1 Basics

Motivation

The line profile deformations used for high-resolution Doppler imaging, as demonstrated in Chapters 5 and 7, are often rather feeble. Depending on the contrast of effective temperature between spots and the undisturbed photosphere spots of a surface extent of the order of 10 degrees typically cause disturbances at a 1% level of the spectrum continuum (see e.g. Figure 6.1). Because of the limited exposure times (to avoid phase smearing) and the required high spectral resolution, the necessary signal-to-

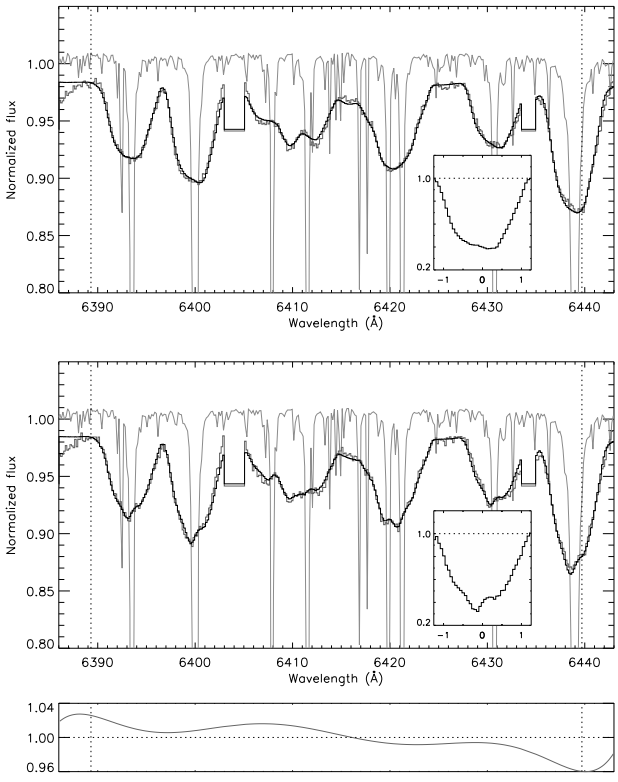

Figure 6.1: Two sample spectra from the August 2 time series of HD197890 and the "rotational broadening functions" (RBF) extracted by sLSD from the "6400Å" wavelength region. The inset panels show the RBFs, their x-axes are annotated in units of 120 km/s. The gray broad-lined curve represents the observed spectrum, the black broad-lined spectrum is the fit by sLSD. The narrow-lined graph shows the template spectrum used for the deconvolution (synthetic PHOENIX 5200 K, same as in Fig. 6.6). The dotted vertical lines delimit margin regions of reduced weighting for the fit by sLSD, the narrow flat regions around 6404 Å and 6434Å have been excluded from the fit. The lowermost panel shows the "continuum correction function" (CCF) used for both spectra (see text).

noise ratios (SNR) is usually not easy to attain from the information of a *single* line.

In order to increase the SNR it is a straightforward idea to combine the information of several spectral lines into a "suitably averaged" line profile; this is the aim of LSD and sLSD.

Rationale: Rotational broadening functions

With the restrictions discussed in Section 5.4.3, the line profiles of a sufficiently fast rotating star can be approximated by convolving the narrow-lined spectrum of a (ideally non-rotating) slowly rotating star with a suitable broadening function. This narrow-lined spectrum is called *template spectrum* in the following. The broadening function describes profile shaping mechanisms not confined to small regions of the stellar surface; namely (differential) rotation, limb darkening, macroturbulence and spots. Although they describe more than just rotation, they are called *rotational broadening Function* (RBF) in the following. Using this terminology, sLSD tries to construct a RBF (approximately) common to the selected spectral lines.

If the spectrum contained sufficient numbers of *unblended* lines and the individual characteristics of those lines could be neglected, this process would be a "simple" averaging. The main problem would be the determination of a suitable template spectrum used to sample the rotationally broadened spectrum. Mathematically this sampling and averaging could be performed by a cross-correlation.[1] Unblended lines in the visible spectrum of an ultrafast rotating solar-like star are virtually non-existent. Several weakly blended lines can be found in the spectra of fast rotating G- and K-stars, they constitute the "popular" choices for Doppler imaging of solar like stars, most of them are found above 6000 Å (a selection, including a thorough discussion of properties, can be found in Bruls; Solanki & Schüssler 1998). However some deblending is necessary even for those lines in order to extract a RBF. This *need of deblending* turns the above averaging problem into a problem of *deconvolution* - in addition to the remaining (more difficult) problem of finding suitable template spectra.

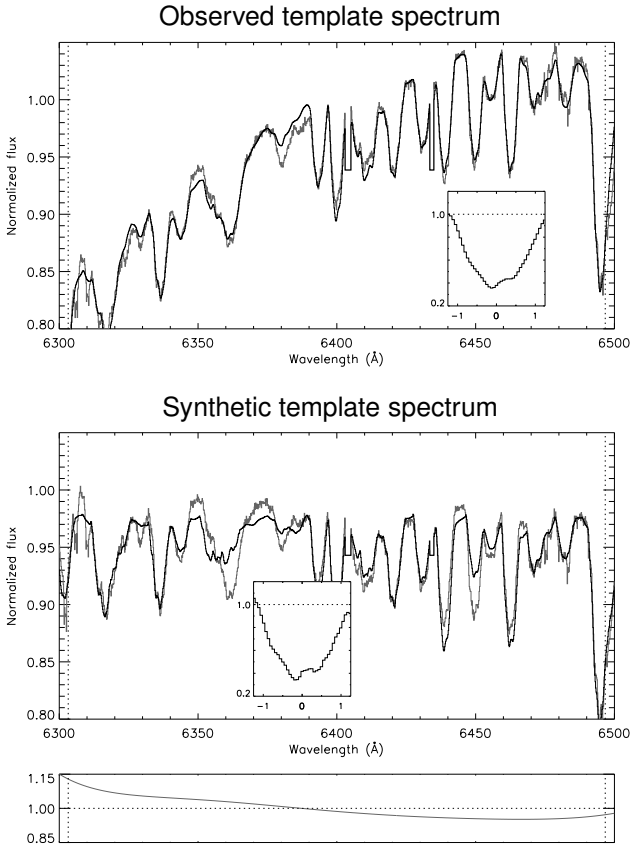

Figure 6.2: Examples of moderately wide-range applications of sLSD. See Fig. 6.1 for annotations; the input spectrum for the deconvolution is the same as in the lower panel of that Figure (JD 2452488.853). The *upper panel* shows a deconvolution based on the observed template spectrum (Gl 472), the *lower large panel* is based on a synthetic template (PHOENIX 5200 K). The CCF for the synthetic template case is shown in the narrow lowermost panel, note its rather large slope (performing about a 20% correction); this slope compensates the different "instrumental" and "physical" quasi-continua of the observed and template spectrum respectively.

Realisation of sLSD

Donati et al.'s descriptions of LSD (cf. Donati et al. 1997b, Sec. 4.1, Collier Cameron 2000, Sec 3.1) focus on a matrix formulation of the deconvolution problem. To some degree this veils the very simple idea of the (s)LSD procedure, which is apparent e.g. in Figure 6.1: The RBF (seen in the inserted small plot) is convolved with the template spectrum (narrow-lined upper spectrum), yielding the broadened spectrum (broad-lined dark).[2] The RBF is chosen such that this broadened spectrum optimally fits the observed spectrum (broad-lined gray); i.e. minimizing the sum of squared deviations in each wavelength bin, optionally weighted by their estimated standard deviations.

[1] Such methods have already been applied using opto-mechanical devices. For example Mayor (1980) sampled photographically recorded stellar spectra with oscillating masks containing up to several thousand slits. In the above terminology, their extracted averaged line profiles are actually RBFs, their masks represented the template spectra. However, Mayor only made use of the width and area information of their extracted RBFs.

[2] Actually, all RBFs shown here are plotted "as normalized absorption line profiles"; i.e. relative to a continuum of one. The "true" RBF, i.e. the function used for the convolution, is one minus the plotted RBFs.

Although this formulation of the problem leads to an optimization problem with typically 20-50 parameters to be optimized (the number of radial velocity bins of the RBF at the chosen resolution), this procedure leads to a surprisingly stable convergence.[3] Several optimization algorithms can be used for its implementation. Donati et al.'s LSD uses a solution of the normal equations (based on Choleski decomposition, cf. the above references).

The optimization routine of sLSD uses a Levenberg-Marquardt algorithm[4] , approximating partial derivatives by finite differences; although this is not a very sophisticated solution numerically, it turned out to be completely appropriate for sLSD. A roughly sensible RBF as a start value is needed in some cases to ensure convergence; for example a triangular profile can be used.

6.2 Ingredients of sLSD

The application of sLSD to relatively narrow wavelength intervals leads to two additional issues to be handled by the algorithm: (i) The treatment of end-effects at the borders of the wavelength interval. (ii) The suppression of "small-scale oscillatory" solutions.

The continuum-correction-function (CCF)

An example of issue (i) can be seen by comparing the region around 6390 Å in Figures 6.1 and 6.2: The error of the spectral fit is rapidly increasing below 6390 Å, most certainly due to a deficiency of the template spectra. Even in the absence of template deficiencies, a strong line "just outside" the fitted wavelength region would lead to some deformations inside the region, due to rotational (and possibly other) broadening mechanisms.

These problems can be reduced by carefully selecting the wavelength range including its exact boundaries. sLSD handles the remaining deviations by iteratively adjusting the continuum of the fitted spectra, i.e. by dividing the observed spectrum by a smoothly varying function (i.e. *varying on larger scales than the individual line profiles of the spectrum*). These functions can be seen in the narrow lower panels e.g. of Figure 6.1, they are called "continuum-correction-function" (CCF) in the context of sLSD. The CCFs serve three purposes:

- Continuum adaption
- End-effect treatment
- Tentative correction of small template deficiencies

The CCFs used by sLSD are Legendre polynomials of a degree defined before starting the iteration. By adjusting this degree, the "stiffness" of the CCFs can be adjusted, e.g. a degree of three leads to a pure adaption of slope and offset between the observed and template spectra.

The continuum adaption by the CCF brings about that the observed and template spectra need not be continuum normalized, a task which is often very difficult for spectra of (fast rotating) solar-like stars. Naturally, the CCF encounters the same difficulties inherent to continuum normalization. However, the advantage of the CCF is that its behaviour is *transparent during the line profile deconvolution itself* and not potentially hidden in a prior spectrum reduction procedure.

For treating the end-effects of the fitted wavelength range the degree of the CCF must be chosen sufficiently high to give it "adequate flexibility", depending on the strength of deviations near the ends of the fitted range. In addition, in order to treat end-effects, optionally a *wavelength margin* at the boundary of the fitted region can be defined (these margins are delimited by dotted lines in Figure 6.1 and similar figures of this section). Inside this margin, the relative weights of deviations between observed and fitted spectra, entering the χ^2 optimized for the fit, are continuously reduced towards the boundaries; the weights are reduced from one down to a lower predefined value, usually zero.[5]

Certainly the most delicate task of the CCF is the "tentative" correction of template deficiencies. To understand what is meant precisely by this correction, sLSD's basic purpose should be kept in mind: Finding an RBF *approximately common* to the fitted spectral region. In order to reliably "sample" the (especially rotation-induced) deformations of this common RBF, the fitted spectrum should be close to the observed spectrum in a wavelength interval as broad as possible, covering a large number of discernible spectral lines. If the CCF is chosen flexibly

[3] Instead of treating the value of each radial velocity bin as an independent parameter, sLSD can optionally expand the solution into Chebyshev polynomials. This can reduce the number of parameters considerably for sufficiently smoothly varying line profiles. However for the line profiles of ultrafast rotators, studied in conjunction with CLDI, this turned out to be ineffective. The reason is that the "relatively sharp edges" (higher order derivatives) at the profile boundaries are not well approximated by polynomials *of moderate order*. The resulting deviations of the polynomial fit, evenly distributed over the approximation interval for Chebyshev polynomials (e.g Press et al., 1992), tend to swamp the profile deformations relevant for Doppler imaging.

[4] The Levenberg-Marquardt method (e.g Press et al., 1992) uses a mixture of an inverse-Hessian (unstable far from the minimum) and a steepest-descent optimization (ineffective close to the minimum). The IDL routine "CURVEFIT" supplies an implementation, optionally calculating partial derivatives, required for the Hessian matrix, from finite differences. The latter procedure is not recommended, if analytic partial derivatives can be obtained, generally losing much of the convergence speed.

[5] Currently, sLSD uses a linear ramp for reducing these weights. In practice, this smooth reduction of weighting has proved effective to allow the CCF to adjust at the boundaries, without end-deviations affecting the fitted RBF.

enough and the RBF is sufficiently well-defined, this may lead to additional wavelength regions supplying information to the fit. An example of this can be seen by comparing the group of lines around 6410 Å in Figures 6.1 and 6.2 (lower panel). In both cases, the order of the CCF is the same, but due to the narrower wavelength interval in the first case, the CCF "can" adapt to features as narrow as 10 Å in the spectrum.

In this way, slightly wrong equivalent widths (including missing weak lines) in parts of the template spectrum can be corrected for in suitable wavelength ranges. This feature of the CCF is controlled by setting its degree, it should be used "under thorough supervision".

A partly different approach to a tentative template correction is described in Reiners & Schmitt (2003). Their variant of LSD, "Physical LSD (PLSD)" iteratively optimizes the template spectrum, starting out from a δ-function spectrum based on the atomic line database VALD (Kupka et al., 1999). This template is broadened, in some cases according to effective temperature and atomic weights, and the equivalent widths and central wavelengths are iteratively adjusted to yield an optimum spectral fit.

Applications of PLSD as in Reiners & Schmitt (2003) show that it is a powerful method, especially because wide ranges of synthetic template spectra almost always contain a few "grossly wrong" lines, often caused by sporadic errors of atomic data. PLSD, compared to sLSD, is able to deal with more serious errors of the template spectra during the deconvolution itself. Using sLSD, it would be necessary to eliminate the massive template spectrum errors *before* starting with the deconvolution (which may be a tedious procedure, even hardly feasible, for a large number of lines).

The apparent robustness of LSD-methods for many applications (given a "roughly" correct template spectrum, see Section 6.3) allows determining additional corrections to improve the fit of the observed spectrum. Both methods, sLSD and Reiners & Schmitt's PLSD, iteratively construct such a correction. PLSD's approach is more "radical", quite freely constructing a "suitable" template. However, it is limited to synthetic δ-function templates. On the other hand sLSD's procedure is more flexible in the sense that it can make use of synthetic *and observed* template spectra. This was one of the aims of the development of sLSD and has been used extensively in conjunction with CLDI.

Iteration outline

The sLSD iteration loop starts with a constant CCF at value one. With this CCF held constant, the RBF (line profile) is iteratively optimized, until the improvement of χ^2 decreases below a pre-defined threshold, or a maximum number of optimization steps has been performed. Now, with the resulting RBF held constant, the CCF is optimized in the same manner; since the number of parameters describing the CCF (typically 4-10) is much lower than for the RBF (often about 40), this optimization converges very stably and much faster. After that, again the resulting CCF is held constant, and starting out from the current RBF, the RBF is further optimized. This *alternating optimization of RBF and CCF* is performed until the improvement in χ^2 drops below a predefined value for a given number of steps.[6]

Regularization

An important issue of sLSD is stabilizing the solution against "small-scale ripple"; some examples of such ripple can be seen in Figure 6.9 (e.g. at JD 2452493.915 or JD 2452493.712). Such ripple is brought about by fitting narrow wavelength intervals (i.e. few spectral lines) at a high resolution of the RBF (i.e close to the spectral resolution of the spectra). [7] As visible in the same Figure, the rippled RBFs do usually "envelope" the ripple-free RBFs of the same rotation phase.

Such small-scale ripple often inhibits a proper convergence of the alternating RBF and CCF optimization. In those cases, neither the RBF nor the CCF converge to a stable solution, they mutually destabilize each other. This results in the fitted RBF oscillating around the "true" solution, only reorganizing the (irrelevant) small-scale ripple, without further converging to a solution.

A simple means of reducing this instability of the alternating RBF and CCF optimization is to use the smoothed RBF of the previous iteration step as the start value for the next iteration. However, in many cases this is not sufficient. As a consequence, sLSD optionally employs a *Tichonov* regularisation (see Section 4.3.1) to support convergence towards a reasonably smooth solution.

Any measure effectively penalizing bin-to-bin oscillatory ripple in the RBF, and being (as much as possible) insensitive to longer-scale gradients or curvature can be used for the regularization. sLSD currently uses a penalty functional based on the third-order finite difference (in the continuous case, this would measure local changes of curvature). This has proven to be effective for the current ap-

[6] This number of "no-improvement-steps" is somewhat arbitrary; for the sLSD applications shown here, it was typically chosen about 5. It can easily be adjusted, depending on data quality etc., after a few test applications of sLSD. It should be chosen safely larger than the number of iterations necessary after the start to settle "close" to a stable solution.

[7] It should be noted that the RBFs shown in Figure 6.9 are not oversampled (binwidth of 7.3 km/s) in relation to the resolution of the spectra ($\approx$ 40 000).

plications of sLSD. The use of a penalty functional based on Fourier methods has not been studied, it may be a powerful alternative for future applications.

The relative weight of this penalty functional (corresponding to λ in Equation 4.7) *is currently not adjusted according to a χ^2 level aimed at*. Instead, the penalty functional weight is adjusted "manually" by reducing it (with a safety margin) to above a value, where the described small-scale ripple sets in and starts inhibiting convergence. If the penalty functional weight is adjusted properly, the small-scale ripple typically disappears after one or two RBF and CCF optimization steps.

6.3 Using sLSD

The "ideal" template spectrum for applying sLSD to a given star would be a disk-integrated spectrum seen by a co-rotating observer. Since such a spectrum is not available, an approximate choice of a template spectrum has to be made, mainly based on spectral type and element abundances (if available). Either an observed spectrum of a suitable star with sufficiently low $v \sin i$, or synthetic spectra can be used, examples for both choices can be seen in Figure 6.2.

Synthetic vs. observed template spectra

Synthetic template spectra have the obvious advantage of (quite) freely adjustable parameters. The synthetic spectra shown in this chapter were generated using the stellar atmosphere code PHOENIX (Hauschildt et al., 1999), identification of lines was mostly based on line lists from the database VALD (Kupka et al., 1999). The main disadvantage of synthetic spectra is that they may contain grossly incorrect equivalent widths for some lines or line groups; usually this is due to some seriously incorrect atomic transition parameters. An example of such template deficiencies can be seen in Figure 6.2 around 6360 Å: This region is quite successfully fitted using the observed template, but not fitted at all using the synthetic template.[8] The only way to deal with such massive template deficiencies is an iterative optimization of the template (Reiners & Schmitt, 2003), shortly described in Section 6.1. Otherwise such regions should preferably not be used for optimizing the RBF, examples of such *cut out wavelength regions* can be seen around 6405 Å and 6435 Å in Figures 6.1 and 6.2 (lower panel).

[8] As its complex shape suggests, this line group in the broadened spectrum is a blend of several lines of roughly equal equivalent widths, the strongest identified belonging to Fe I, Ni I, Ca I and Cr I. Extensive experimenting with varying the abundances of these and other "candidate" elements could not significantly improve the fit.

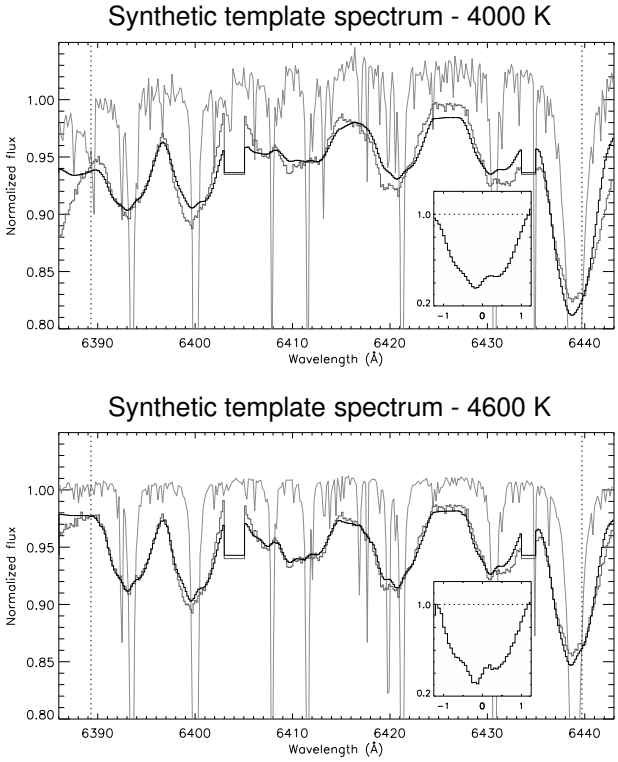

Figure 6.3: Trying out template spectra for sLSD on the "6400Å" wavelength region, see Fig. 6.1 for annotations. The input spectrum (JD 2452488.853) is the same as in the lower panel of that Figure. The *upper panel* shows a deconvolution based on a PHOENIX 4000 K template spectrum, while the *lower panel* uses a PHOENIX 4600 K template. The equivalent widths of both templates have been approximately scaled down by 40% (see text).

Apart from lacking such "unnatural" deficiencies, template spectra observed with the same instrument may have the advantage of sharing (similar or identical) instrumental features with the target spectra. This effect is partly responsible for the misfit, *using a synthetic template*, around 6440 Å in the lower panel of Figure 6.2, where two echelle orders overlap; using an observed template spectrum (Figure 6.2, upper panel), this region is fitted much better. Although considerable effort has been put into merging the echelle orders (see Section 8.1.2), these reduction deficiencies could not be completely removed for all echelle orders. Certainly the safest way to proceed is by excluding such order-overlap ranges from the fit (as e.g. in Donati et al., 1997b).

Figure 6.2 also demonstrates the quite remarkable *robustness* of (s)LSD against template deficiencies in parts of the fitted wavelength region, meaning that a "roughly sensible" RBF is extracted despite of them. Apparently, there are two reasons for this robustness: (i) Spectral regions like that around 6360 Å, very poorly fitted using the synthetic template (lower panel of Figure 6.2), produce a massive offset in χ^2. However, presumably this

offset is only weakly dependent on the precise shape of the RBF and consequently only weakly influences the resulting fit. (ii) For spectral regions where the equivalent width of a quite isolated strong line is wrong, the fitted spectrum runs roughly parallel, quite close to the observed spectrum (if intermediate-scale corrections by the CCF are not successful or not enabled). Also in such cases, there is an offset in χ^2, but it certainly still depends on the shape of the RBF, although presumably only on its large-scale structure. Such a situation can be studied around the Ca I λ6439 line in both panels of Figure 6.2.

On the one hand, the named robustness of (s)LSD facilitates the choice and construction of template spectra; on the other hand, it limits the amount of information that can be gained (e.g. on element abundances) from optimizing the template. Actually this robustness is a necessary requirement for the successful application of (s)LSD to very wide wavelength ranges (as e.g. in Donati & Collier Cameron 1997a).

Selection and adjustment of template spectra

Although guided by the known properties of the target star, finding a suitable template spectrum requires some experimentation. By varying the effective temperature (possibly abundances) of the template star or atmospheric model, a close and stable fit to the observed spectrum needs to be obtained. The process of finding a suitable template spectrum is illustrated in Figure 6.3, especially in comparison with Figure 6.1 which shows a more successful choice.

In conjunction with choosing a template, suitable wavelength regions must be found, excluding critical wavelength ranges containing telluric lines, massive template deficiencies or regions with uncorrected instrumental features (e.g. echelle order overlap regions need to be carefully checked).

Finally, some approximate common *fine-tuning of the template equivalent widths* can be applied. If the continuum of the template spectrum were perfectly normalized to one[9] , multiplying deviations of the template spectrum fluxes from one by a given factor, say 0.95, reduces the equivalent widths of all lines by 5%, while approximately conserving their shape.

If such an overall correction of template equivalent widths is necessary but not performed, the resulting RBF is shifted by a constant offset and reduced in amplitude. In this way, the RBF compensates the (roughly) constantly off equivalent widths yielding a fit of similar quality.

[9]For practical purposes and not too wide wavelength ranges, this can usually be achieved approximately by multiplying the template fluxes with a linear function of wavelength, i.e. by adjusting the offset and the slope.

Extracting time-series of RBF

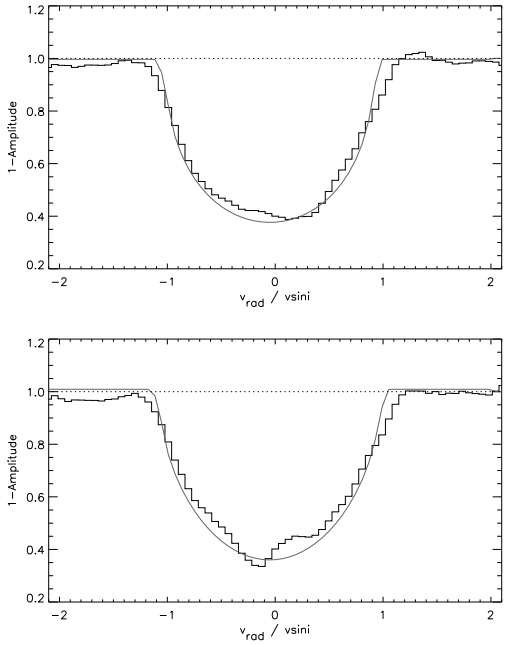

Figure 6.4: Each panel shows an RBF ("rotational broadening functions", stepped graphs) extracted from the same observed spectra on the same wavelength range, using the same template as in Fig. 6.1; again the x-axes are annotated in units of 120 km/s. Differing from Fig. 6.1 the RBFs here are defined on a wider radial velocity range, namely [-2.1, 2.1]. The smooth graphs show the same analytic rotation profile for both panels (Eq. 5.11); it is a rather poor fit to the RBFs and only intended to facilitate a comparison. Note the variations of the continuum regions comparing the two RBFs.

sLSD has been developed for the extraction of line profile time series for the purpose of Doppler imaging. In this case, *the CCF should be held constant* for all spectra of the time series in order to avoid introducing artificial RBF variations caused by variations of the CCF. The required constant CCF can be determined from an application of sLSD to an average spectrum of the whole time series. With the CCF held constant, the overall level of each spectrum (depending on exposure time etc.) needs to be adjusted. If individual variations of the spectra are small (as in the Doppler imaging case), this can be done by determining the median flux of each spectrum. Each spectrum is multiplied by a factor to adjust this median to a value common to all spectra in the time series.

Another means to avoid artificial RBF variations in a time series is the extraction of narrow RBFs, without broad "continuum collars" (i.e. regions of the RBF with $|v_{rad}/v \sin i| > 1$). As can be seen in Figure 6.4, such continuum collars show (usually small) temporal variations; the information of these variations cannot be used by the subsequent Doppler imaging. Using a RBF only defined on $|v_{rad}/v \sin i| \lesssim 1$ "forces" these variations

into the line profile proper.

According to experience with applying sLSD to time series, both named effects are usually small. However, they should be carefully monitored, if non-constant CCFs and/or "wide" continuum collars are used.

6.4 sLSD and CLDI

A fundamental issue

If the intrinsic spectra of the unspotted and spotted photosphere *were identical*, extracting a RBF common to the whole stellar surface would be strictly correct. Because of the strong temperature contrast and other differing atmospheric parameters, these spectra are certainly not identical. However, Doppler imaging based on (s)LSD apparently works to quite some degree. This is supported by the discussion of sLSD's reliability in Section 6.5 as well as the results presented in Chapter 7.

The main reason for this is illustrated in Figure 6.3: Even for a temperature contrast exceeding 1000 K, most of the strong lines of the template spectra remain strong in the wavelength domain considered. In this way, the mechanism of line profile deformation by cold spots, discussed in Section 4.1, is an acceptable approximation for these lines: They show pseudo-emission bumps, dominantly produced by the spot-induced change of continuum flux.

Following the discussion of pseudo-emission in Section 4.1, spectral lines intrinsically strongly varying with temperature need to be treated with care for Doppler imaging; they should be avoided when using sLSD for the line profile extraction.

Practical issues

Apart from the aspects of extracting RBFs from a time-series of spectra, discussed in Section 6.3, an adaptive correction is usually necessary to use the extracted RBFs as an input of CLDI.

The reason is that CLDI, using symmetric intrinsic line profiles (see Section 5.4.3), synthesizes equally symmetric rotationally broadened profiles (if the visible surface is unspotted). If CLDI's input line profiles show a *phase-independent* deviation from symmetry, this will lead to reconstruction artifacts, similar to those described in Section 5.5.6.

Significant phase-independent deviations (as in the uppermost panel of Figure 6.5) will massively disturb the convergence of CLDI. The reason is that even weak deviations of this kind "mislead" CLDI's backprojection at all phases. However, they are intrinsically impossible to fit for Doppler imaging, because they are outside the line

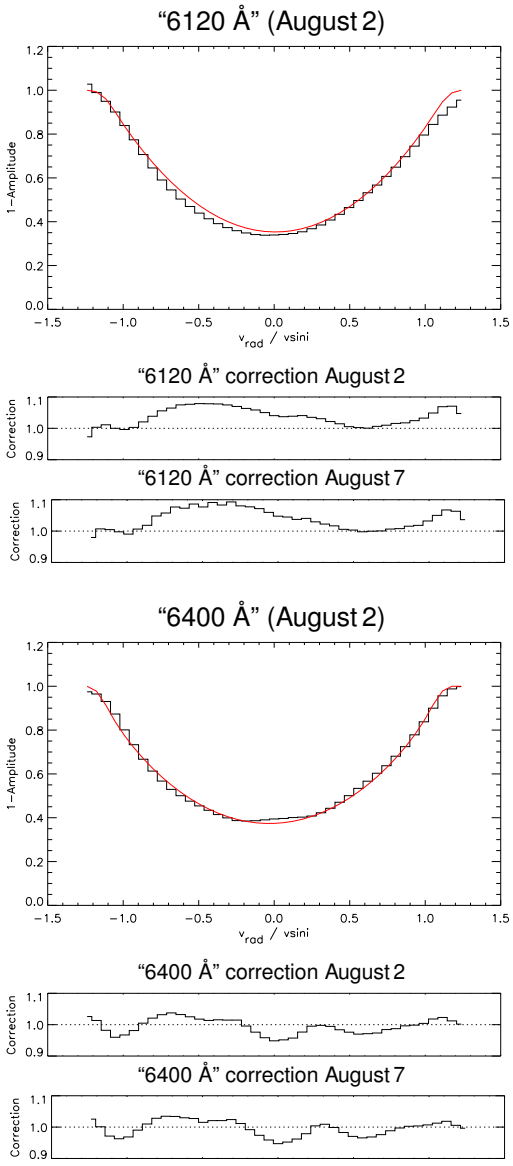

Figure 6.5: *Large panels*: Average RBFs of HD197890 (stepped graphs) extracted by sLSD from the wavelength region given above each plot; the radial velocity is annotated in units of 120 km/s. The shown RBFs were extracted from an average of all spectra of HD197890 taken on August 2; these spectra sample a whole stellar rotation quite evenly, so that spot-induced line profile deformations should largely cancel out. Overplotted (smooth graphs) are fitted analytical rotation profiles, their parameters are given in Table 7.4. The average RBFs extracted from the August 7 spectra have a very similar shape for the same wavelength range, yielding the same fit parameters within ± 1 km/s for $v \sin i$ and within ± 0.1 for the limb darkening coefficient; however, the August 7 average RBFs are shifted by about -2 km/s in radial velocity compared to their August 2 counterparts (see text). *Small panels*: Correction functions ξ computed from Eq. 6.1. These correction functions are applied to each RBF extracted from spectra of the corresponding night and wavelength region (Eq. 6.2) before using them as input for CLDI.

center without migrating through the profile with rotation phase.

Such asymmetries demand care when the shape of the RBF is to be interpreted in terms of stellar parameters (cf. Reiners & Schmitt, 2003, Sec. 7.2).[10] For the purpose of Doppler imaging these asymmetries are less crucial, if they are small compared to the spot-induced line profile deformations; in contrast to the latter deformations, they are phase-independent.

Assuming that these asymmetries are indeed small compared to the deformations relevant for Doppler imaging, the RBFs are transformed to a symmetric "proper" rotation profile in the following way.

A symmetric rotation profile is determined by fitting an analytic rotation function (Equation 5.11) to an average RBF of the time series. If possible, care should be taken, to avoid incomplete or uneven rotation phase coverage. In this way, asymmetries of the average RBF due to spot-induced deformations can be reduced. In addition to Equation 5.11, the fitted analytic profile is convolved with a Gaussian of predefined constant width (about 10 km/s) to mimic the "rounded edges" of the RBFs (i.e. the transition of the RBF into the surrounding continuum) computed by (s)LSD.[11]

The average RBFs of the "6120 Å" and "6400 Å" ranges and the corresponding analytic fits $f_{\rm rot}$ are shown in Figure 6.5. The parameters of those fits are given in Table 7.4 and were adopted for the line profile synthesis of CLDI for the reconstructions of HD197890. These fits yield a radial velocity shift of about -2 km/s for the August 7 RBFs compared to their August 2 counterparts. This corresponds well with the results of the radial velocity measurements described in Section 7.1.1. This velocity shift does not exceed the estimated radial velocity measurement uncertainty and is possibly due to intrinsic variations of the average line profiles between the two observing nights caused by spot evolution.

A correction function ξ is computed *from the average* rotational broadening function $\mathsf{RBF}_{\rm ave}$ and the corresponding analytic fit $f_{\rm rot}$:

$$\xi(v_{\rm rad}) = \frac{f_{\rm rot}(v_{rad})}{\mathsf{RBF}_{\rm ave}(v_{\rm rad})} \tag{6.1}$$

Each individual RBF of the time series is then corrected by applying *the same* correction function

$$\mathsf{RBF}_{\rm corr}(v_{\rm rad}) = \mathsf{RBF}(v_{\rm rad}) \cdot \xi(v_{\rm rad}) \tag{6.2}$$

The thus corrected $\mathsf{RBF}_{\rm corr}$ are used as the input to CLDI. Using the same correction ξ for the whole time series is a natural requirement; it avoids introducing artificial phase-dependent deformations of the RBF, which could cause artefacts in the resulting Doppler images.

Care should be taken that *symmetric deviations* of the average input profile and CLDI's undisturbed synthetic profile are not "blindly corrected away" during this process. Such symmetric deviations are induced e.g. by *polar spots* (and other rotationally symmetric spot configurations). Analysis of several wavelength ranges is certainly advisable to safely identify such symmetric line profile signatures (Bruls; Solanki & Schüssler, 1998). As illustrated by Figure 6.5, such signatures were not detected for the average profiles of HD197890.

6.5 Reliability of sLSD

Analogous to the discussion of the reliability of Doppler images (Sections 4.2, 5.5.4 and 7.5.1), estimating the reliability of sLSD means answering the question: "Which line profile (rotational broadening function, RBF) deformations are presumably real, which are artefacts?". Actually, this question is adapted to the needs of Doppler imaging, the more general question (much harder to answer) would be: "How reliably can the RBF *shape* be physically interpreted". The following discussion focuses on the first question.

A general discussion of this issue would require tests based on synthetic data. Such tests have not been performed in the context of this thesis; instead, the discussion is based on consistency considerations of the HD197890 results. Although this abundant set of spectra and extracted RBFs constitute quite an extensive basis for the discussion, its limited generality should be kept in mind.

Consistency of different wavelength ranges

The following discussion is based on the comparison of RBFs extracted from the same input spectra in different

[10] It is interesting to note, that the two examples of RBF asymmetries shown in the left and right panels of Fig.4 of Reiners & Schmitt (2003) are of similar type as the asymmetries of the lower and upper panel of Figure 6.5 here. No explanation for these asymmetries is given by Reiners & Schmitt.

The simplest explanation for such asymmetries in average line profiles of a heavily spotted star like HD197890 would be asymmetric phase coverage of the averaged spectra or massive spot evolution. However, for the shown average RBFs of HD197890 this explanation seems unlikely. First, because the averaging intervals quite evenly sample roughly one whole rotation period; second, because the average RBFs of the August 2 and August 7 observations are practically identical for each wavelength region.

The different RBF asymmetries for the two wavelength regions suggest that they are largely due to template deficiencies, specific to the individual wavelength regions.

[11] Presumably, these "rounded profile edges" are related to the limited resolution of the (s)LSD deconvolution over the whole line profile. This limited resolution is presumably in part caused by "slight" template deficiencies differing for each individual line; such deficiencies limit the accuracy to which a *common* RBF can be determined by deconvolution for these lines.

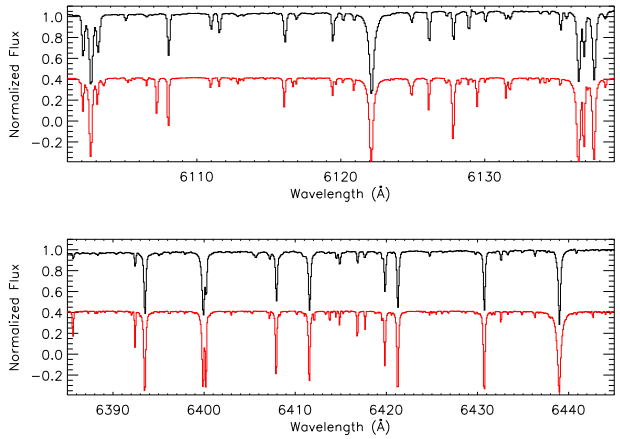

Figure 6.6: Comparing observed (Gl 472, black) and synthetic (PHOENIX 5200 K, red/gray) template spectra around the "6120 Å" and "6400 Å" wavelength ranges used for HD197890. For both panels the spectral quasi-continua have been roughly normalized to one, the red/gray spectrum is shifted in flux by -0.6.

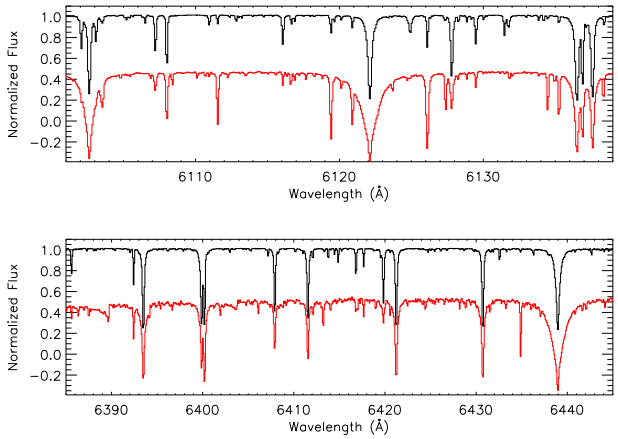

Figure 6.8: Selected ranges from synthetic spectra, not rotationally broadened. The PHOENIX 5200 K spectrum (black) has been used as the template spectrum for applying sLSD to the "6400 Å" wavelength range; the PHOENIX 4000 K spectrum (red/gray) is presumably a rough proxy for the spectrum of the spots on HD197890. For both panels, the quasi-continua have been roughly normalized to one, the red/gray spectrum is shifted in flux by -0.5. See Section 7.4 for the complete parameters of the spectra.

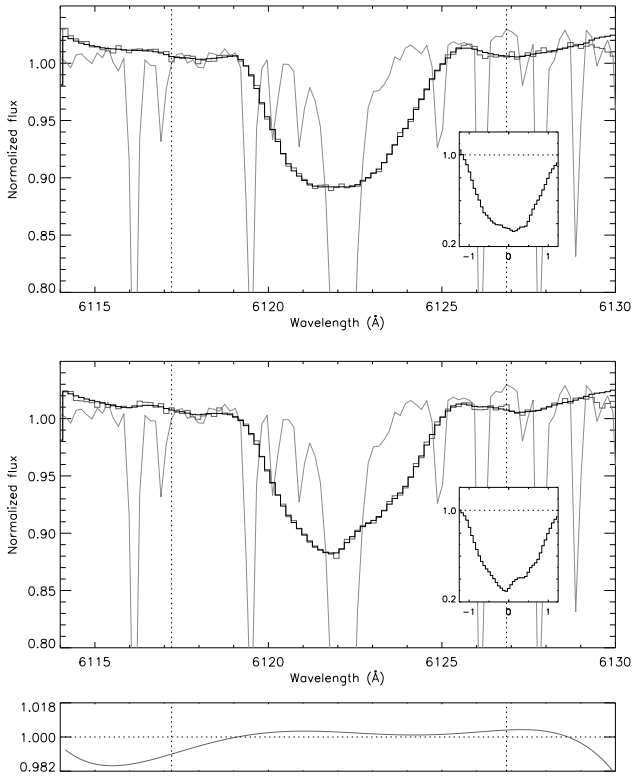

Figure 6.7: Application of sLSD to the "6120 Å" wavelength region; the shown spectra are the same as in Fig. 6.1 (JD 2452488.738 and JD 2452488.853). For this wavelength range an observed template spectrum (Gl 472) was used, also shown in Figure 6.6. The vertical dotted lines delimit margin regions contributing to the spectrum fit with reduced weights.

wavelength ranges, shown in Figure 6.9. Concerning the input information, the "6120 Å" and "6400 Å" time series are quite independent: They are extracted from disjunct wavelength regions, using different template spectra (and slightly different regularisation settings of sLSD). However, since each pair of RBFs is taken at the same rotation phase, they should share "well-comparable" spot-induced deformations.

Already the substantial consistency of the Doppler images extracted from the two time series (Section 7.5.1, especially Figures 7.13 and 7.14) is an indication of the consistency of the RBF time series used as input of the DI reconstructions. This is supported by the Doppler images extracted from subsets of the time series of RBFs (Figures 7.16 and 7.17); their consistency indicates that the position and shape of the migrating deformations have been successfully extracted by sLSD.

Comparing the RBFs of the same rotation phase in Figure 6.9 shows a substantial correlation of the deformations. However, significant differences are present as well. It is immediately apparent that the "6120 Å" RBFs show much smoother (and apparently weaker) deformations than their "6400 Å"-counterparts.

It is important to note, and has been extensively tested, that this is not due to the slightly different regularisation weights used (see Section 6.2).[12] Decreasing the regularisation weight λ for the "6120 Å" range does not lead to a significant "sharpening" of the deformation fea-

[12]The regularisation weighting parameters are $\lambda = 0.01$ for the "6120 Å" and $\lambda = 0.0025$ for the "6400 Å" range, respectively.

tures, it only leads to small-scale oscillatory instabilities of the solution. Increasing λ for the "6400 Å" range on the other hand suppresses the remaining oscillatory instabilities (e.g. visible at JD 2452493.712) and smoothes "discontinuous" steps (like e.g. at JD 2452493.892). Naturally, a massive increase of λ (exceeding about a factor of 50) finally smoothes the deformation features.

Characteristics of the wavelength ranges

Qualitatively, the differences between the "6120 Å" and "6400 Å" RBFs can be explained by the properties of the spectral lines in the corresponding wavelength regions. Unbroadened spectra, presumably very roughly representing the undisturbed and spotted photosphere, are shown in Figure 6.8.

Obviously, the "6120 Å" region is dominated by a single line, see Figure 6.7 for the exact boundaries of the region. This dominating line is the Ca I λ6122 line, the two other "stronger" lines of the region are Ti I λ6121 and Ti I λ6126.[13]

First of all, the Ca I λ6122 line is considerably wider than strong lines in the "6400 Å" region.[14] Consequently, the same surface feature leads to a broader line profile deformation in the "6120 Å" RBFs, compared to their "6400 Å" counterparts. In the terminology of Section 4.2, the attainable *effective resolution* of the Ca I λ6122 line is lower than that of the lines in the "6400 Å" region.

Additionally, the width of the Ca I λ6122 line increases substantially with decreasing temperature (i.e. inside the spots); following the discussion of Section 4.1, this leads to even broader line profile deformations. If these broad deformations are deconvolved with the higher temperature photospheric template containing a comparatively narrow Ca I λ6122 line, they lead to broadened deformations in the resulting RBFs.

Finally, the Ca I λ6122 line shows a marked increase of equivalent width with decreasing temperature.[15] Following the discussion of Section 4.1, such an increase in equivalent width reduces the amplitude of pseudo-emission line profile deformations caused by cool spots.

Summing up, due to the relatively large intrinsic width and temperature dependence of the Ca I λ6122 line, the "6120 Å" RBFs should exhibit broader and weaker deformations than their "6400 Å" counterparts; this is indeed observed. The broader deformations reduce the "effective resolution" of the "6120 Å" RBFs, the deformation weakness reduces the sensitivity of the RBFs (for a given SNR) to small and/or low-contrast spots.

As a result, the "6400 Å" Doppler images should have a higher resolution than their "6120 Å" counterparts. However, to conclusively check this, more independent wavelength regions would have to be analyzed; this has not been done in the context of this work.

Self-consistency of individual RBF time series

A quite compelling evidence of the successful extraction of RBFs by sLSD, albeit more indirect than the above comparison, is their good fits obtained by Doppler imaging. Spurious line profile deformations lacking a "proper" (rotation induced) migration during the time series cannot be fitted by a DI reconstruction.[16]

The RBFs of Figure 6.9 are shown with their corresponding fits by CLDI reconstructions in Figures 6.10 and 6.11, anticipating results of Chapter 7.[17]

Assuming simultaneously

(o) a correct extraction of all RBFs by sLSD
(i) a stable spot configuration on HD197890 during each observation night
(ii) that all observed line profile variations are induced by those stable spots
(iii) a correct DI reconstruction, including correctly adopted stellar and line profile parameters

would imply that *all* RBFs of each time series were perfectly fitted. The following discussion tries to study the validity of item (o) in conjunction with (i)-(iii) on the basis of the presented RBF fits by Doppler imaging. This study does not at all have the character of a proof, strictly speaking items (i)-(iii) are hypotheses whose appropriateness is considered in the following. To truly support them, some information about the spot pattern independent of the line profile deformations would be needed, e.g. from high-precision multi-colour photometry simultaneous to the DI observations. However, such independent

[13] Compared to the observed Gl 472 spectrum (shown in Figure 6.7), finally used as the template for the "6120 Å" region, two lines are much weaker in the 5200 K PHOENIX spectrum of Figure 6.8: Si I λ6125.02 (not named above) and Ti I λ6121.00. Apart from the shape of the Ca I λ6122 line itself, these differences cause the relative "superiority" of the Gl 472- over the PHOENIX-template for this region.

[14] At 5200 K, about 0.4 Å (FWHM) for Ca I λ6122, compared to typically about 0.25 Å for strong lines in the "6400 Å" region. This difference is even increasing at 4000 K: 2.0 Å (FWHM) for Ca I λ6122 compared to about 0.4 Å in the "6400 Å" region.

[15] Measured relative to the surrounding quasi-continuum (which is the relevant quantity for the observed line profile), the equivalent width increases from 0.5 Å at 5200 K to 1.4 Å at 4000 K.

[16] Although naturally the DI reconstruction may be misled and try to mimic them. A possible example of this are the somehow inconsistent RBF deformations around phase 0.287 in the August 7 "6120Å" time series (Fig. 6.12).

[17] More precisely, the RBFs of Figure 6.9 have been corrected according to Equation 6.2, using the correction functions of Figure 6.5 to produce the two latter figures. However, this minor correction is not visible at this scale.

information is not available for the August 2002 data of HD197890.

While the RBF fits are not faultless, most of the RBFs are fitted quite well, including their (rotation induced) migration from the blue ($v_{rad} < 0$) to the red wing ($v_{rad} > 0$) of the RBF. This indicates that condition (iii) is quite well met.

As mentioned above, given the dense and even phase sampling of the time series of each observation night, "isolated" RBF deformations, appearing only at a single phase without migrating counterparts at neighbouring phases, would not be fitted by the DI reconstruction profiles. Some (more or less) isolated profile deformations, poorly fitted by the DI reconstruction can be found in the August 2002 RBF time series of HD197890; most pronounced in the "6120 Å" RBFs (Figure 6.12, e.g. around phase 0.823 for the August 2 data or at phases 0.287 and 0.754 for August 7). The preliminary results of Section 8.3 indicate that some of these ill-fitted profile deformations are correlated with localized chromospherically active regions. However, apart from not yet conclusive, this would only affect "a few" deformations of the "6120 Å" RBFs and apparently not significantly any of their "6400 Å" counterparts. This would restrict the validity of (ii) for some phase ranges of the "6120 Å" RBFs, but it would remain valid for the remaining phases and completely for the "6400 Å" time series.

While the results of Chapter 7 clearly indicate intermediate-scale variations of HD197890's spot pattern on time scales of about 2.5 rotations during the August 2002 observations, most spot groups apparently remained largely stable during the totally covered 13 rotations. No evidence could be found for significant variations of spots during their passage over the stellar disk (and no conclusive evidence for significant variations when reappearing after one rotation). Trying to assemble the above aspects into a coherent picture, most spot(groups) on HD197890 seem to have evolved slowly on time scales of the rotation period, while a few spot(groups) have evolved gradually on the same time scale. This would make item (i) a "nearly completely" correct assumption.

Summing up, the overall close fit of the observed line profiles (RBFs) of HD197890 by DI-reconstructions are a strong indication, but no independent "proof", for the above item (o), i.e. their (overall) correct extraction by sLSD.

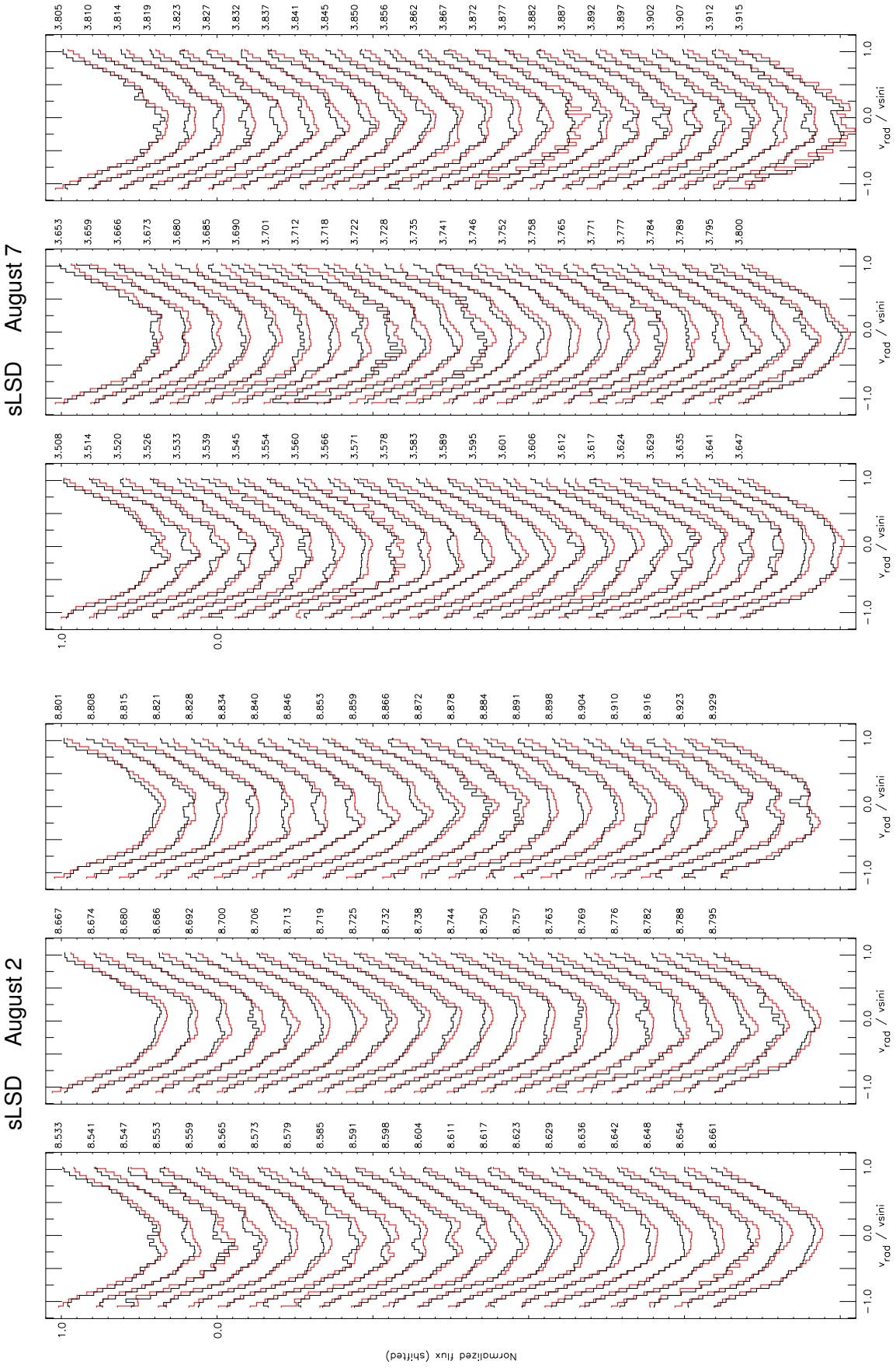

Figure 6.9: Line profiles of HD197890, extracted by sLSD in the "6120 Å" (red/gray) and the "6400 Å"-region (black). Subsequent profiles of the time series are shifted, the flux scale is valid for the topmost profile of each panel. The mid-time of the exposures is given right of each profile as JD-2452490.0 for August 2 and JD-2452493.0 for August 7, respectively.

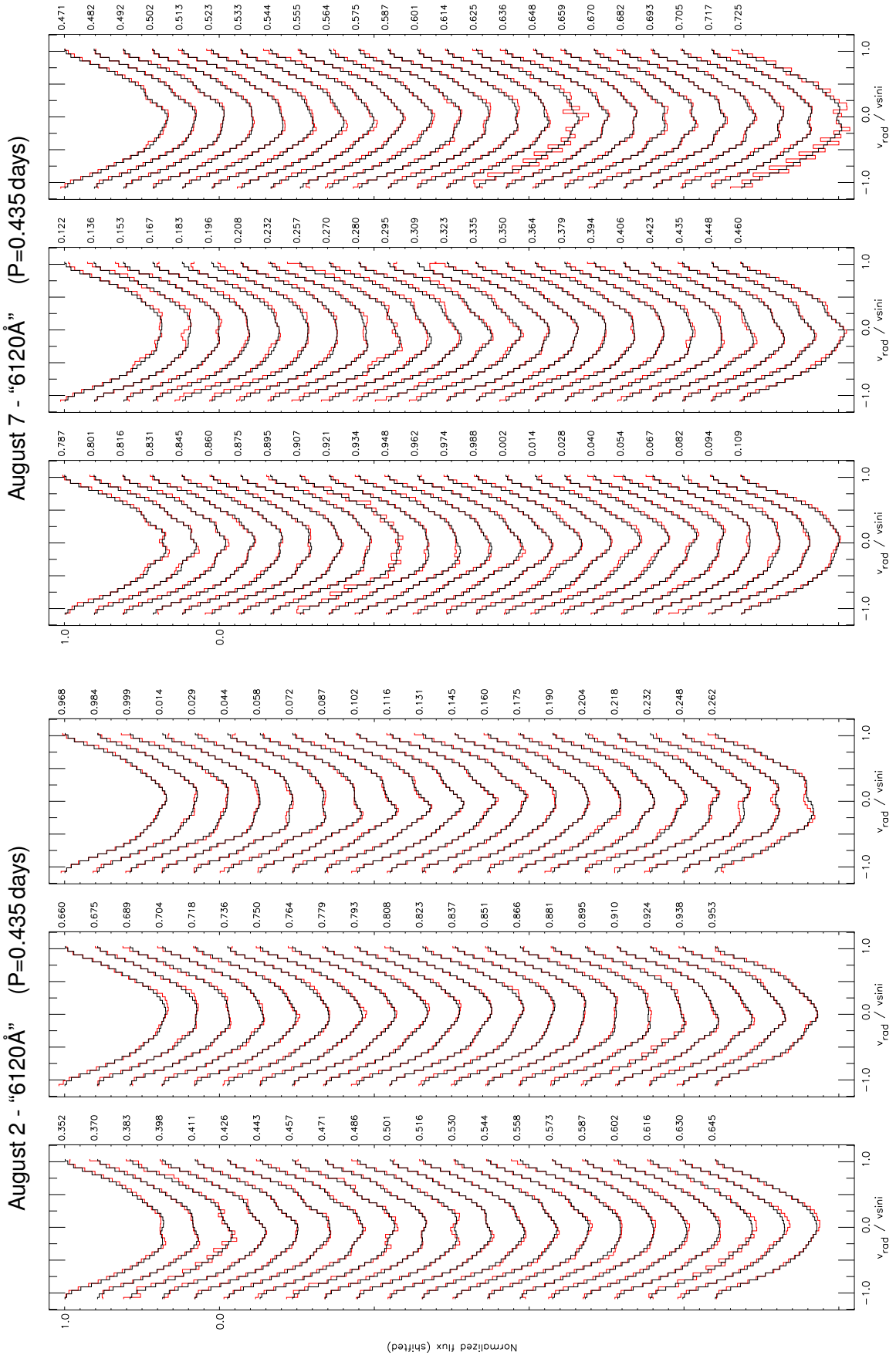

Figure 6.10: Line profiles of HD197890, extracted by sLSD in the "6120Å"-region (red/gray) and fitted by CLDI (black). The adopted rotation period is 0.435 days, the detailed reconstruction parameters are listed in Tab. 7.4. Subsequent profiles of the time series are shifted, the flux scale is valid for the topmost profile of each panel. The mid rotation phases are given right of each profile, with the phase zero-point at $\mathrm{JD}_{\phi=0} = 2448000.05$

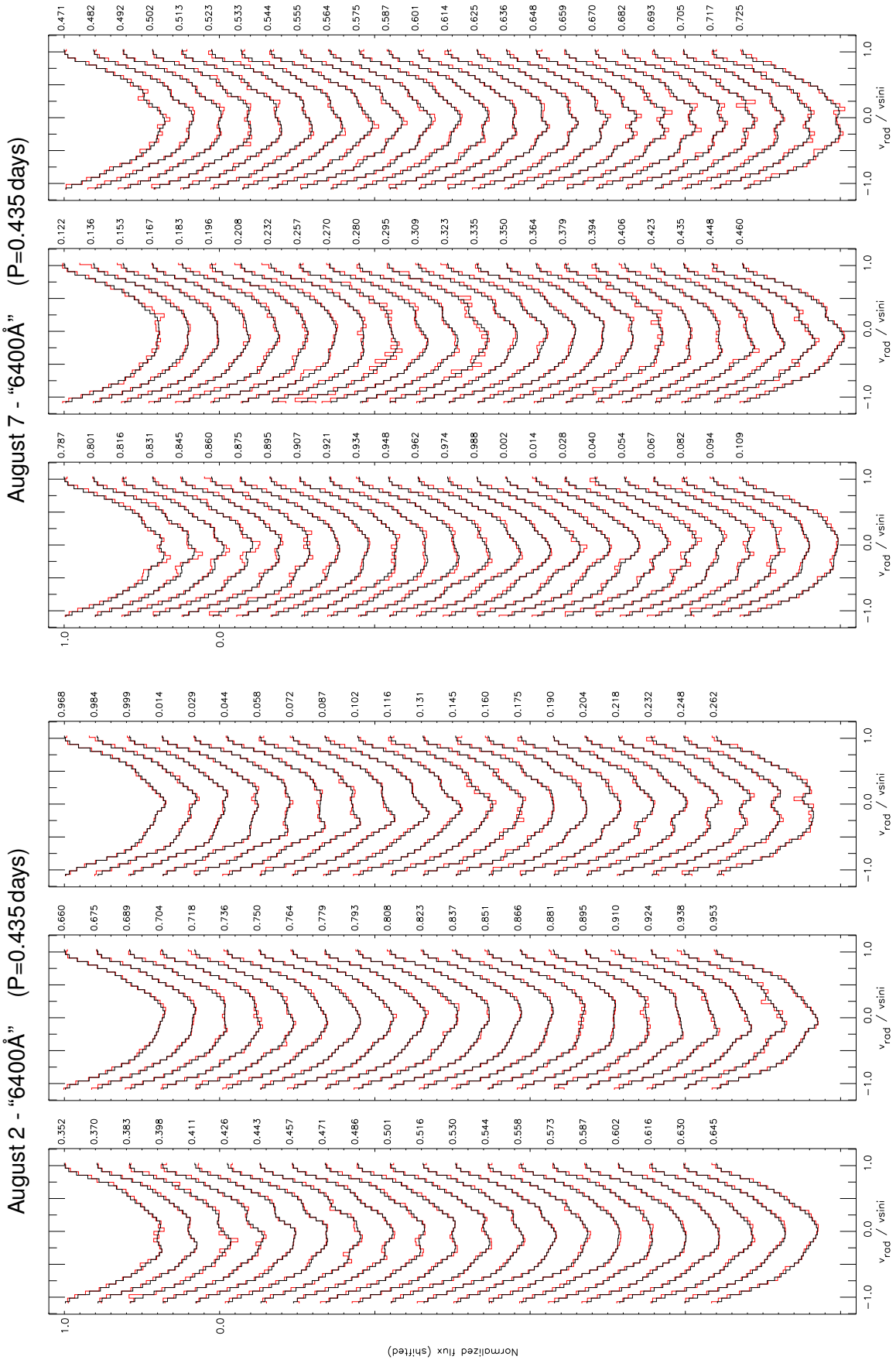

Figure 6.11: Same as Figure 6.10, but for line profiles extracted in the "6400Å"-region

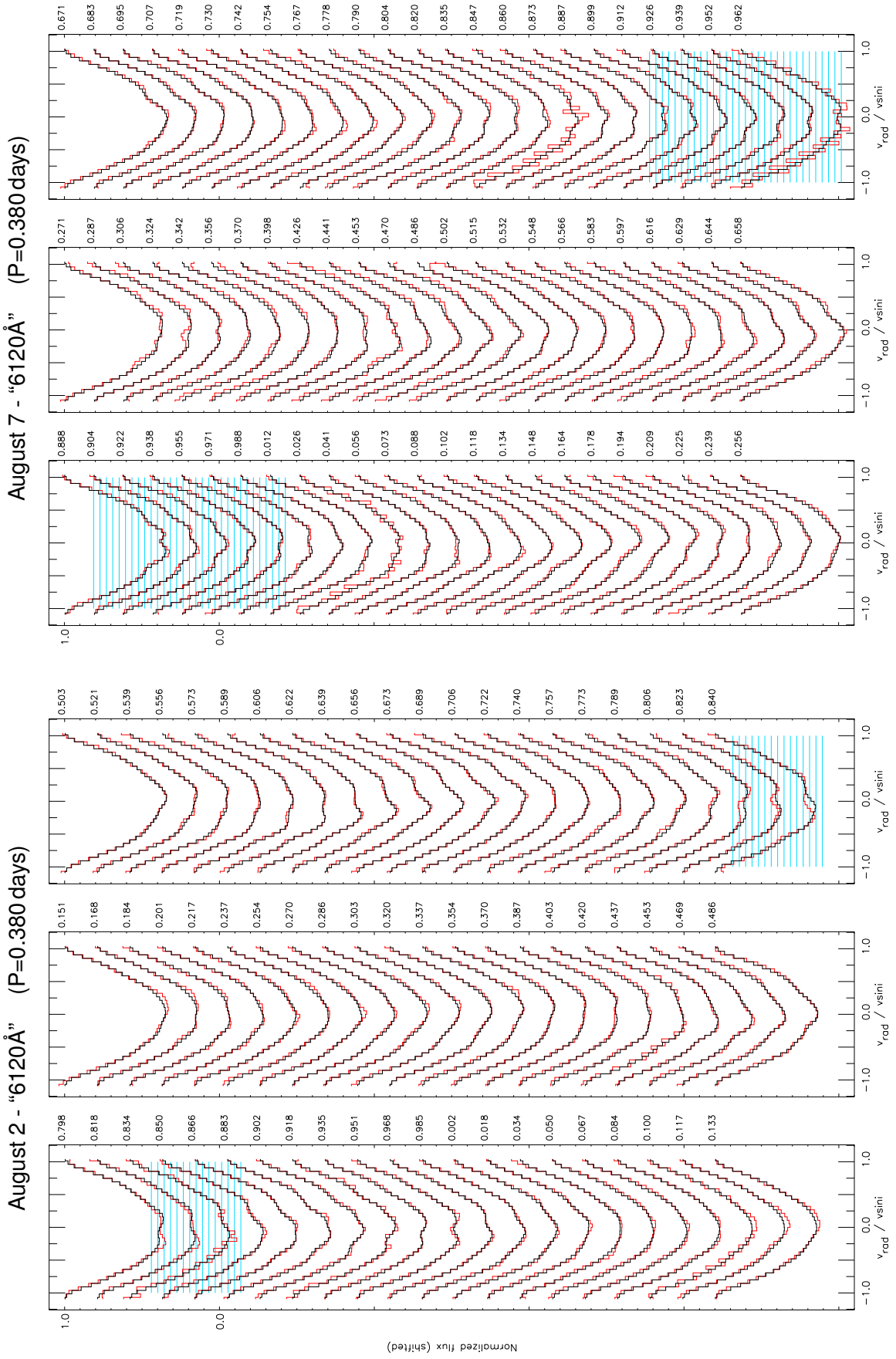

Figure 6.12: Same as Fig. 6.10, adopting a reconstruction period of 0.380 days with the same phase zero-point chosen at $JD_{\phi=0} = 2448000.05$. Both observation nights were longer than this adopted period; the hatched regions mark the *cores* of the profiles in the phase overlap interval of the beginning and the end of each night.

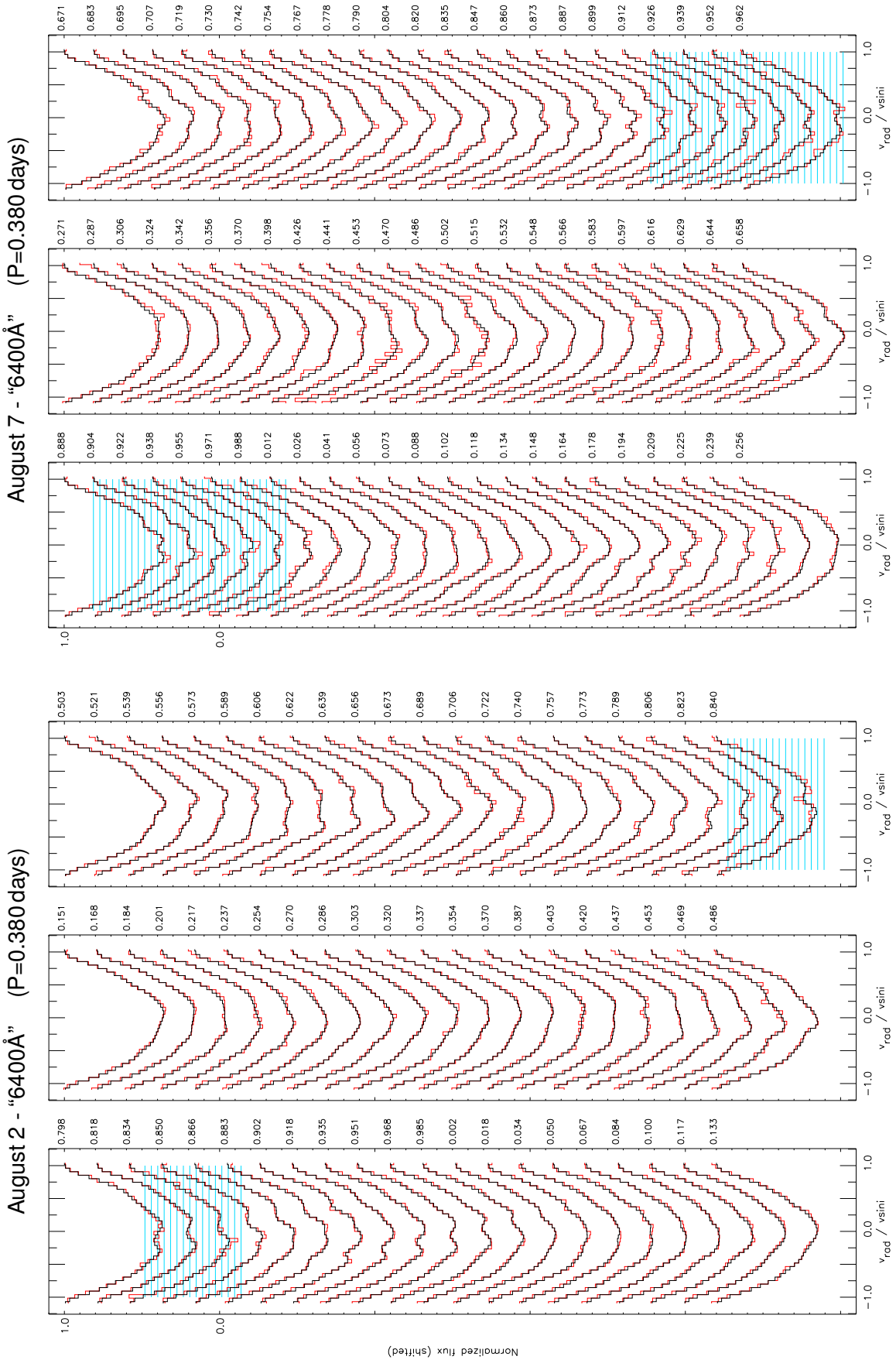

Figure 6.13: Same as Figure 6.12, but for line profiles extracted in the "6400Å"-region

Chapter 7

Observations of "Speedy Mic"

The ultrafast rotating dwarf star HD197890 ("Speedy Mic") was chosen as the main observational target for this thesis. Observations of two other objects have been performed and partially analyzed (SV Cam=HD44982, V889 Her=HD171488). However, when the HD197890 data became available, work was concentrated on them, so the other objects are not discussed here.

The properties of HD197890 are discussed in Sections 7.1 and 7.9, they make it well suited for Doppler imaging (DI) studies; especially its rotation period allowing the observation of a complete rotation during a single night. HD197890's short rotation period for an apparently single star of its spectral type also make it an interesting object for studying differential rotation, because the differential rotation behaviour of ultrafast rotators is still not well known and incompletely understood (Section 2.2).

The input data for the Doppler imaging were obtained from spectroscopic observations performed in August 2002 at the "Very Large Telescope" (VLT) of the "European Southern Observatory" (ESO). As far as the different locations and weather conditions allowed, simultaneous photometric observations were performed in collaboration with F. Wijk and D. Kilkenny at the "South African Astronomical Observatory" (SAAO). They were originally intended for checking the consistency of the DI results and possibly "tuning" some input parameters (like spot temperature contrast) of the Doppler images. While the latter aspect has not been treated in this thesis, the August 2002 photometry turned out to be crucial for the former, namely assessing the consistency of the resulting Doppler images and their interpretation. The rotation period tentatively deduced from the photometric observations deviates by about 10% from the rotation period of HD197890 observed during other epochs (Cutispoto et al., 1997). Due to this situation, termed the "two-period puzzle" below, Doppler imaging reconstructions adopting both potential rotation periods have been performed and are presented in the following.

Because of the continuous and dense phase sampling of the available spectra, adopting the two different rotation periods mostly leads to a quite regular transformation affecting all individual Doppler images in the same way (Section 7.5.2). Consequently the discussions of image consistency and reliability, based on the comparison of images *derived for the same reconstruction parameters*, is only carried out for one of the rotation periods.

The standard "pipeline" data reduction[1] of the VLT spectra turned out to be insufficient for the given purpose. This created the need for an individual reduction of the data. Some aspects of this reduction are discussed in Section 8.1, concentrating on aspects specific to the treatment of low-noise spectra.

7.1 Object properties

Previous observations

Attention was drawn to HD197890 by Bromage et al. (1992), reporting a large flare observed during the EUV all-sky-survey of ROSAT. The integrated energy output in the passband of the mainly used filter (λ=115-180 Å), was estimated to 10^{33} erg.[2]

Bromage et al. also reported results of optical follow-up observations: A radial velocity of 6.5 ± 2.0 km/s with "no evidence for binarity" (based on 11 spectra covering 6 days). They estimated a $v \sin i$ of 120 ± 20 km/s, earning HD197890 its nickname "Speedy Mic". Their V-band photometry yielded a peak-to-peak amplitude of 0.2 mag, indicating modulation by extended cool spots. In addition, they reported an unusually broad Ca K emission line and a large equivalent width of 220 ± 50mÅ for the Li I 6708Å line, the latter suggests a young evolutionary status.

The data used by Bromage et al. was further analysed by Anders et al. (1993). However, in retrospect their analysis appears rather unsuccessful. The sparse sampling of their photometry did not allow a reliable period de-

[1] For observations in visitor-mode, i.e. not performed by observatory staff alone, ESO provides only a crude "quick-look reduction" for VLT/UVES data. This standard procedure is only rudimentarily adapted to the requirements of individual observations.

[2] This may be compared to the *total* energy output of large solar flares of about 10^{32} erg.

termination, so their reported values of P=0.31 days (alternatively P=0.28 days) are presumably artefacts. Their value of $v \sin i = 170 \pm 20$ km/s is most certainly too large, possibly due to the narrow analyzed wavelength range and an insufficient atmospheric modelling (based on Gustafsson et al. 1975). Their estimated spectral type of K5 ($T_{\rm eff} = 4350$ K for their models) is presumably inaccurate due to the same reasons.

A satisfactory rotation period was finally determined by Cutispoto et al. (1997), yielding P=0.380 ± 0.004 days. Their photometry also yielded multicolour lightcurves showing a consistent phase behaviour and

$$\begin{aligned} \overline{U-B} &\approx 0.56 \pm 0.02 \\ \overline{B-V} &\approx 0.94 \pm 0.01 \\ \overline{V-R} &\approx 0.57 \pm 0.02 \end{aligned}$$

(approximate average $\pm$ amplitude of modulation).

Analyzing their complete photometric data shown in Figure7.10, spanning observations from 1993-1996 (Cutispoto et al. only used the 1996 data) yields

$$\overline{m_V} \approx 9.42 \pm 0.07$$

The Hipparcos distance of 44.5$\pm$3.2 pc implies a distance modulus of $(m_0 - M) = 3.24 \pm 0.16$ mag. This makes use of the definition

$$m_V - M_V = (m_0 - M) + A(V) \quad , \qquad (7.1)$$

approximating the extinction $A(V)$ as zero.[3] Finally, this results in an "observed" visual magnitude of

$$\overline{M_V} \approx 6.2 \pm 0.1$$

Parameters estimated from photometry

The observed colours are not consistent with a main sequence star (Cox, 2000, Sec. 15.3.1):
$\overline{B-V} \approx 0.94$ matches a K3V classification with an effective temperature $T_{\rm eff}$ $\approx$4800 K and an absolute visual magnitude of M_V $\approx$6.5.
$\overline{V-R} \approx 0.57$ matches a G7V with $T_{\rm eff}$ $\approx$5400 K and M_V $\approx$5.4

Calculating M_V and $T_{\rm eff}$ from Strömgren photometry published by Hauck & Mermilliod (1998) and using the program "UBVYBETA" (Moon 1984, 1985, including a calibration for dwarf stars by Napiwotzki et al. 1993) yields $T_{\rm eff}$=5200 K and M_V=5.9. These values are close to mean values of the above "main sequence" estimates from colour indices. The corresponding radius is $R \approx 0.8 R_\odot$, equal to the radius of a main sequence star of this effective temperature.

Parameters estimated from rotation

The mismatch between the observed absolute magnitude and that deduced from the colour indices could be removed by a slightly lower effective temperature. However, a "main sequence" radius of $R \approx 0.8 R_\odot$ for HD197890 is not consistent with its rotational data as discussed in the following.

Using the inclination of 70$\pm$10° and a $v \sin i$ of 134$\pm$10 km/s, both discussed in Section 7.5.2, (the uncertainty of $v \sin i$ is adopted rather large for the following estimation to "safely" include all measurement errors), results in an equatorial rotation velocity of v_{eq}=$143\,^{+23}_{-17}$ km/s. This further corresponds to a radius of $R = 1.07\,^{+0.19}_{-0.14}\ R_\odot$ when using the above cited rotation period of 0.380$\pm$0.004 days.[4]
Combining this radius and $T_{\rm eff}$=5200 K, using

$$\frac{L}{L_\odot} = \left(\frac{T}{T_\odot}\right)^4 \cdot \left(\frac{R}{R_\odot}\right)^2$$

with $T_{eff,\odot} = 5780$ K, yields a luminosity of $0.74\ ^{+0.29}_{-0.19}\ L_\odot$. This already rather wide range of luminosities would be enlarged, if an uncertainty in effective temperature were also included.

The bolometric correction for a main sequence star with $T_{\rm eff}$=5200 K is $BC = 0.3$ (Cox, 2000). Using

$$M_V = BC + M_{bol,\odot} - 2.5 \log \frac{L}{L_\odot}$$

with $M_{bol,\odot} = 4.74$ mag, this yields an absolute visual magnitude of M_V=5.4$\pm$0.3 mag.

So the enlarged radius considerably increases the mismatch between the observed absolute magnitude and that calculated from the estimated stellar parameters. This has already been noticed by Barnes et al. (2000) based on a different calculation.

Summing up, the "observed" absolute magnitude of $\overline{M_V} \approx 6.2 \pm 0.1$ and the radius estimate of $R = 1.07\,^{+0.19}_{-0.14}\ R_\odot$ can be considered reliable. The photometric colours and the resulting estimated effective tem-

[3] The visual extinction $A(V)$ can most certainly be neglected in this case. Unsöld & Baschek (1988) give a "typical" value for $A(V)$ in the galactic plane of $\gamma \approx 0.3$ mag kpc^{-1}, resulting in an extinction of 0.01 mag for a distance of 50 pc. Even if the large inhomogeneity of the interstellar medium is taken into account, this value is considerably smaller than the uncertainties of the visual magnitudes considered here.
The corresponding reddening $E_{B-V} \approx 0.003$ (Cox, 2000, Sec. 21.2.1) can be neglected.

[4] The equatorial rotation velocity v_{eq} of a star, given its radius and rotation period P, can be calculated from

$$v_{eq} = \frac{R}{R_\odot} \cdot \frac{1}{P_{\rm [days]}} \cdot 50.9 \ {\rm km/s}$$

perature are not consistent with these values, *if a spectral flux distribution similar to a main sequence star is assumed*.

Instead, in order to attain the "low" observed visual magnitude (luminosity) of HD197890, the effective temperature (averaged over the surface) needs to be a few hundred Kelvin lower than the above adopted 5200 K. Additionally, a spectral flux distribution significantly deviating from a main sequence star with a homogeneous surface temperature must be assumed for HD197890. Apart from the cool spots covering a substantial part of the surface, a pole-equator temperature difference of the order of 100 K is presumably induced by HD197890's fast rotation (Section 7.1.2).

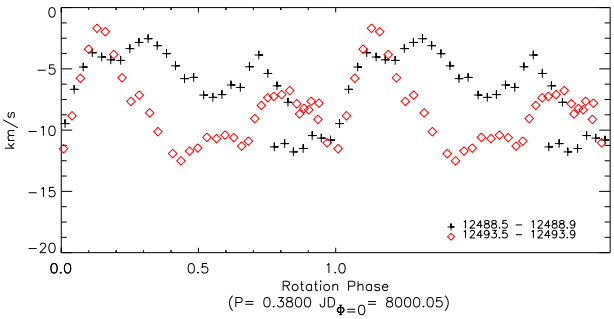

Figure 7.1: Apparent radial velocity variations of HD197890 as a function of rotation phase, as determined from cross-correlation with a narrow-lined template spectrum. These variations are due to the spot-induced deformations of the line profiles, mimicking Doppler shifts of line centers and flanks.

Evolutionary status

Using the evolutionary models of Siess (2000), including their colour-calibrations, leads to a partly clarified picture.

The above absolute magnitude $\overline{M_V} \approx 6.2$ together with $\overline{B-V} \approx 0.94$ or $\overline{V-R} \approx 0.57$ are nearly *consistently matched* by a M=0.9 $M_\odot$ model yielding the following approximate parameters:

Age	4.0 $\cdot 10^7$ yr
R	0.9 $R_\odot$
$T_{\rm eff}$	4900 K
L	0.5 $L_\odot$
M_{bol}	5.6 mag

Note that this corresponds to a bolometric correction of about 0.6, substantially differing from the above value of 0.3 approximately assumed for a main sequence star.

To bring this radius estimate roughly in agreement with the above estimate of R $=1.07^{+0.19}_{-0.14}$ $R_\odot$, derived from HD197890's rotation, an inclination at the lower end of 70±10° and a projected rotational velocity at the upper end of 134±10 km/s appear as unlikely.

The above cited Li λ6708 equivalent width of 220 ±50 mÅ for HD197890 translates into a Li abundance of 2.3±0.4 dex, assuming $T_{\rm eff}$=4900 K. (Soderblom et al., 1993c, Tab. 2).[5] Inspecting Figure 9a of Soderblom et al. shows that such an abundance would be moderate to low for a member of the Plejades cluster (age ≈ 70 Myr). For members of the Hyades cluster (age ≈ 600 Myr) no lithium is significantly detected at effective temperatures below about 5400 K. Actually for members of M34 (age ≈ 200 Myr) an abundance of 2.3 dex is about the upper limit detected at this effective temperature.

In summary, the Li λ6708 equivalent width indicates an age below "a few" 100 Myr for HD197890 and is certainly compatible with the above value of 30-40 Myr.

It is interesting to note that the angular velocity of the rotation evolution models of Keppens et al. (1995, Fig. 3, based on a "simple" core-envelope coupling model) reach their maximum at an age of about 20-40 Myr, quite irrespective of the assumed coupling dynamo parameters . However these models do not cover extremely fast rotators as HD197890.

7.1.1 Radial velocity and binarity

Measuring the radial velocity v_R of an ultrafast rotating cool solar-like star is hampered by two effects: (i) the massive blending and large width of its spectral lines and (ii) spot-induced line profile deformations. While (i) can to some degree be overcome by considering a wide spectral range, (ii) can only be properly corrected by averaging a suitable set of spectra, symmetrically covering a whole rotation.

Effect (ii) is illustrated in Figure 7.1 for HD197890. It indicates that "blindly" applying a cross-correlation measurement of v_R to a single spectrum may introduce an error of ±5 km/s, possibly more for an unfavourable spot configuration. Stout-Batalha & Vogt 1999 (Fig. 4) observe the same effect with a similar v_R-amplitude for objects quite similar to HD197890.

The available radial velocity measurements for HD197890 are summarized in Table 7.1.[6] Neither Bro-

[5] Because of the large scatter of Li-equivalent widths and abundances for individual stars, they alone do not allow "hard" statements about the age of HD197890. As an example, the Li λ6708 equivalent width ranges from about 100 to 1000 mÅ at an effective temperature of 4900 K for the Plejades cluster, age ≈ 70 Myr (Soderblom et al., 1993c, Fig. 9a).

[6] Montes et al. (2001) do not give a source for their radial velocity value (-6.5±1 km/s), it is apparently the value of Bromage et al. (1992). While Bromage et al. conclude that the estimated space motion of HD197890 is compatible with a membership of the Pleiades moving group, Montes et al. (2001) do not come to that result.

mage et al. (1992) nor Barnes et al. (2000) discuss the absolute calibration of their measurements. The given errors must presumably be considered lower limits, because of aspect (ii) above. The value and error given here for Barnes et al. (2000) are the average value and standard deviation of five separate values given by them.

For the 2002 radial velocities, the relative accuracy is about 1 km/s (the stability of the wavelength calibration was checked using telluric lines). However, the *absolute* calibration of the 2002 radial velocities is certainly poorer, it was performed by correcting the used template spectrum (Gl 472 on the wavelength range λ=6150-6450 Å) to laboratory wavelengths using a synthetic spectrum. The March 2002 value, based on only two spectra is considerably less accurate than the other values of the table.

Given the above discussed uncertainties of a radial velocity determination of ultrafast rotators and the lack of a common calibration of the values from different sources in Table 7.1, they contain no indication of radial velocity variations of HD197890.

As illustrated by the spectrum fits (e.g. Figure 6.1) and the deconvolved line profiles (rotational broadening functions, RBFs, e.g. Figure 6.5), the analyzed spectral ranges of HD197890 do not show signatures of a secondary companion (this has been confirmed by applications of sLSD to numerous wavelength ranges between 6000Å and 6700 Å).

The potential "background object" discussed by Barnes et al. (2000, in conjunction with their Fig. 2), used to explain a phase-independent distortion in the blue wing ($v_{rad} < 0$) of their deconvolved line profiles of HD197890, appears as a mystery in this context. Our average line profiles of HD197890 do not show such a feature (see Figure 6.5), although individual phases may mimic them due to spot-induced deformations (e.g. in the *red* wing of the profiles of Figure 6.4).[7]

To cause a line profile deformation of the strength found in the disturbed wing of the profiles of Barnes et al. and be a physical companion to HD197890, the hypothetical secondary could not be much fainter than a factor of ten in the visual, compared to HD197890. For this, it would need a mass certainly not smaller than 0.2 $M_\odot$, presumably larger.[8]

If the profile wing feature of Barnes et al., appearing at a radial velocity of about 100 km/s, were caused by a secondary companion of the mass estimated here (which they do not claim), radial velocity variations of the order of $\frac{0.2\ M_\odot}{0.9\ M_\odot}\cdot$100 km/s≈20 km/s for the primary should be expected. Such variations are not observed.[9]

Table 7.1: Compilation of radial velocity measurements for HD197890. The given errors are approximate estimates.

Date	v_R [km s^{-1}]	Remark
1991 August	-6.5±2.0	Bromage et al. (1992)
1998 July 10-14	-9.5±1.0	Barnes et al. (2000)
2002 March 13-14	(-7.7±5)	only 2 spectra
2002 August 2	-6.5±2.5	full rotation average
2002 August 7	-8.4±2.5	full rotation average

7.1.2 Rotational deformation

The surface of a fluid sphere in equilibrium under the influence of gravitation and rotation is an equipotential surface of the combined gravitational and rotation potential (Kippenhahn & Weigert, 1990, § 41). Such a potential exists for rigid rotation, more general for iso-rotation on cylinders aligned with the rotation axis; only the former case is treated here. In the Roche approximation, deviations of spherical symmetry are neglected for the computation of the gravitational potential, in that case the body can be treated as a point mass concerning gravitation.
A useful dimensionless parameter is

$$K = \frac{\Omega^2 \cdot R^3}{G \cdot M} = \frac{\Omega^2}{G \cdot \rho_{ave}} \qquad (7.2)$$

where Ω denotes the angular velocity, R the *polar* radius, G the gravitational constant and M the mass of the body; ρ_{ave} denotes its average density.
The ratio of centrifugal acceleration a_{rot} to gravitational acceleration g in the equatorial plane at a radius R is

$$\frac{a_{rot}}{g} = K \quad . \qquad (7.3)$$

This allows to compute the resulting (rotationally symmetric) shape from

$$x^2 + y^2 = \frac{1}{(1 - K \cdot x^2)^2}$$

[7] The preliminary average RBFs extracted by sLSD from the (inferior) quick-look pipeline reduced data did show a similar feature. However, this was apparently due to reduction deficiency and an unsuitably chosen *narrow* wavelength range for the application of sLSD.

[8] The evolutionary models of Baraffe et al. 2002, Fig. 2, yield a luminosity of 0.03 $L_\odot$ and an effective temperature of 3200 K for a 0.2 $M_\odot$ model at an age of 10 Myr.

[9] Concerning an unresolved cooler companion, Becklin et al. performed coronographic imaging of HD197890 using the near-infrared instrument NICMOS (Camera 2, λ=1.4-1.8 μm) of the HST. This yielded no other object with $dm \lesssim 4.0$ at a distance of 0.1-0.4″from HD197890 and no object with $dm \lesssim 7.0$ from 0.4″out to several arcseconds (P. Lowrance, priv. comm.). Here dm denotes the magnitude difference compared to HD197890 at the observed wavelength.

using the dimensionless variables $x = \bar{\omega}/R$ and $y = z/R$ ($\bar{\omega}$ and z denote cylindrical coordinates, namely the distance from the rotation axis and the height from the equatorial plane, respectively).
For $K \ll 1$, neglecting terms of $\mathcal{O}(K^2)$, this turns into the equation of an ellipsoid

$$\left(\frac{x}{1+K}\right)^2 + y^2 = 1$$

which means that, to first order in K, the equatorial radius is

$$R_{eq} = (1+K) \cdot R \quad . \tag{7.4}$$

In conjunction with Equation 7.2, this shows, that the aspheric deformation of the body decreases with increasing density. This is sensible, since the gravitational forces increase for a more compact body, while the centrifugal acceleration decreases towards the rotation axis.

Finally, combining Equations 7.3 and 7.4, the ratio of effective gravitational accelerations at the pole and equator is

$$\frac{g_{eq}}{g_{pole}} = \frac{g_0(1-K)}{g_0(1+K)^2} \approx 1 - 3 \cdot K \tag{7.5}$$

where $g_0 = \frac{G \cdot M}{R^2}$ is the polar gravitational acceleration (unaffected by rotation) and again higher order terms in K have been neglected, using $1/(1+\epsilon)^2 \approx 1 - 2\epsilon$ for $\epsilon \ll 1$.

As a generalization of von Zeipel's law of gravity darkening (e.g. Tassoul, 2000, Sec. 3.3.1) for the case of stars with convective envelopes, a gravity-darkening exponent β_1 can be introduced to describe the dependence of the effective temperature on effective gravity g (Claret, 2000)

$$T_{\rm eff} \propto g^{\beta_1}$$

For the pole-equator temperature ratio this yields

$$\frac{T_{eq}}{T_{pole}} = \left(\frac{g_{eq}}{g_{pole}}\right)^{\beta_1} \quad . \tag{7.6}$$

For the parameters of HD197890 deduced above from evolution models and a rotation period of 0.38 days, Equations 7.2 and 7.5 yield $K = 0.076$ and $\frac{g_{eq}}{g_{pole}} = 0.77$ respectively.

Using a value of $\beta_1 \approx 0.4$ for a 1 $M_\odot$ model at an effective temperature of 4800 K (Claret 2000, Fig. 3, the dependence on the two parameters is weak for the purpose of this estimation)[10], Equation 7.6 yields $\frac{T_{eq}}{T_{pole}} = 0.97$ corresponding to an effective temperature about 100 K higher at the pole than at the equator.

This estimate of the pole-equator temperature difference should be considered with some care. Assuming that the above estimate of rotational deformation is approximately correct, Equation 7.6 and certainly the adopted value of β_1 may well be poor approximations. The reason is that Claret's models do not include meridional circulations. As outlined in Section 2.2.2, they should have a significant influence on the temperature balance of the convection zone. However, models reliably including this are presently not available for ultrafast rotators; actually the precise solar pole-equator temperature difference and its explanation are still a matter of dispute.

The above calculated equator/pole ratio of effective gravities corresponds to a difference of $\log 0.77 \approx 0.1$ dex in $\log g$. The influence of this on the corresponding local line profiles may be expected to be negligible for the rotationally broadened profile.

Concerning the influence of the non-spherical shape (Equation 7.4) and the pole-equator temperature difference, they also should have a very small influence on the rotationally broadened line profiles of HD197890.[11]

[10] This is quite close to the value of $\beta_1 = 0.32$ computed by Lucy (1967) for convective envelopes based on older stellar envelope models.

[11] This is supported by Figure 2 of Reiners & Schmitt (2003), studying the influence of asphericity and gravity darkening on the line profiles of a G0V star, as a function of equatorial rotation velocity v_{eq}. Their modelled G0V line profiles start showing significant deviations from rigid, spherical rotation profiles without gravity darkenening at $v_{eq} \gtrsim 250$ km/s. This is considerably faster than HD197890, even allowing for the difference in spectral type and evolutionary status to a G0V star.
As that figure also illustrates in conjunction with Equation (3) of the same paper, the combined effects of asphericity and gravity darkening roughly mimic an increase in limb darkening.

7.2 Observations

Overview

The observations used for the analysis described in this chapter are summarized in Table 7.2.

The "Hipparcos" (HIP) lightcurves shown here are taken from the "Hipparcos and Tycho Photometry Annex" (where HD197890 is found as TYC 7469-997-1 and HIP 102626). The HIP observations have a very irregular sampling, mostly covering a few hours, with weeks in between. All data continuously sampling more than two rotation periods of HD197890 have been analyzed.

MBO represents observations performed at the "Mt Burnett Observatory" of the Monash University, Australia; they are available as Table 1 of Anders et al. (1993), it is same photometric data as that reported by Bromage et al. (1992).

ESO indicates data kindly supplied by G. Cutispoto, the 1996 data are published in Cutispoto et al. (1997).

Photometry:

- ○ HIP 1990 March 22 - 1991 June 6
- ○ MBO 1991 August 3 - September 8
- ○ HIP 1993 March 8-11
- ○ ESO 1993 November 20 - December 3
  ESO 1995 October 2-13
  ESO 1996 October 7-13
- • SAAO 2002 August 3-5, September 12,13,15

Spectra:

- • VLT/UVES 2002 March 13,14,15
- • VLT/UVES 2002 August 2,7

Table 7.2: Observations of HD197890. Filled bullets indicate observations performed in the context of this thesis, empty bullets mark datasets collected from other sources (see text).

7.2.1 Observation layout 2002

Timing issues

Given HD197890's rotation period of about 0.4 days, two nights of quite continuous observations were required for the construction of two independent Doppler images, the minimum number required to derive results on spot evolution and differential rotation.

Assuming a "weak" differential rotation with $\alpha \lesssim 0.01$ for HD197890, suggested by some observations and modelling results for ultrafast rotating dwarf stars, requires a sufficiently large gap between the two observation nights to allow its detection. A differential rotation with $\alpha = 0.01$ would result in an equator-pole shear of 3.6° during each rotation (Equation 2.9). Even for ideal conditions the latitude resolution near the equator and the longitude resolution near the poles are comparatively poor in Doppler images (see Section 4.2). Including a safety margin to account for the latter aspect, more than 10 rotations seem necessary between the two Doppler images to observe the resulting shear at a surface resolution of 5-10°. As a result of these estimates (obviously rather uncertain) an interval of four to eight nights was applied for between the two observing nights.

HD197890's rotation period corresponds to an angular velocity of about 0.7° per minute. Allowing the resulting Doppler images to resolve scales below 10° on the surface limited the exposure times to about 600 s to avoid intolerable phase smearing.

Wavelength issues

Experience with the spectra of ultrafast rotating G and K stars ($v \sin i \gtrsim 100$ km/s) suggested observing the spectral region between 6000 Å and 7000 Å, offering several lines not "fatally" blended by rotational broadening. In spite of the wide spectral range of the spectrograph UVES (Section 8.1.1), wavelengths above 7000 Å were not observed, because of the decision to observe the Ca H&K lines (3934 Å and 3968 Å) during the whole time series instead. A switching of the wavelength ranges during the observations was not possible without massive observation time loss.

While the Ca H&K lines offer a valuable tool for activity diagnostics (Section 8.3), the TiO bands e.g. at 7055 Å and 8860 Å may have have allowed further spot temperature analysis along the lines of O'Neal et al. (1998).

The "standard" spectral resolution of UVES (assuming typical VLT seeing values and not using an image slicer) of about 40 000 at 6000 Å was very well suited for the DI surface resolution of 5-10° aimed at and needed no modification.

7.2.2 Observations carried out 2002

Spectroscopic observations

Although partially offering comparatively poor observing conditions, both VLT nights in August 2002 could be used for observations from dusk to dawn, Figure 7.2 summarizes the observing conditions encountered. The nights were quite different in character: The first observing night (2002/08/01 23:50UT to 2002/08/02 10:25UT) offered quite stable conditions. For the second night (2002/08/06 23:04UT to 2002/08/07 10:01UT) the strongly variable sky transmission due to clouds moving through the field

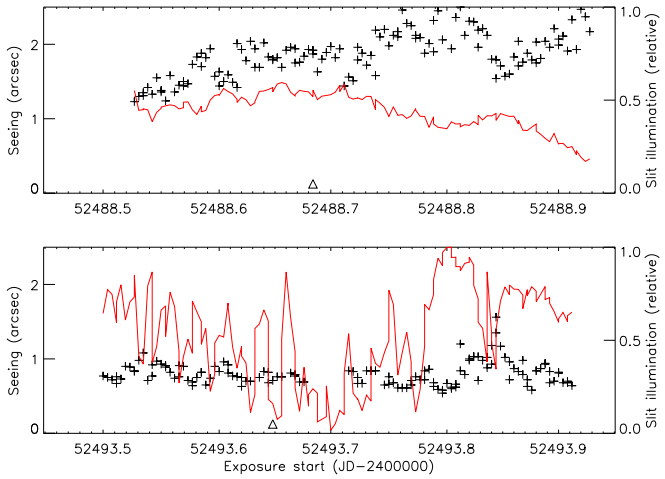

Figure 7.2: Observing conditions for the August 2002 spectra of HD197890, each panel shows one observing night. The seeing values (+) were measured by the VLT seeing monitor, the slit illuminations (continuous curve) are the values of the UVES red arm exposure meter, normalized to the overall maximum. The triangles mark the upper culminations of HD197890.

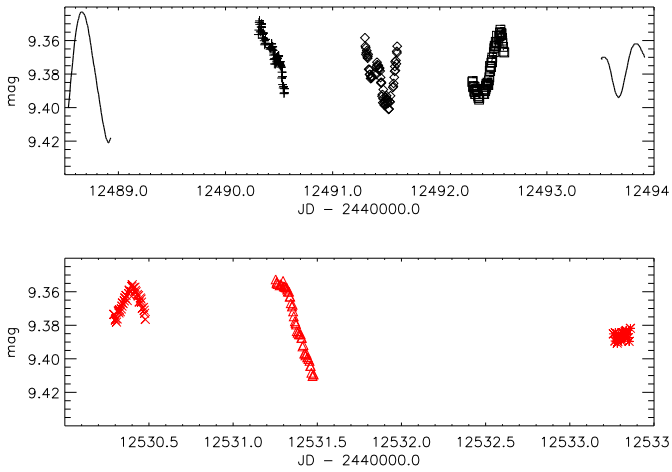

Figure 7.3: Lightcurves of all observations of HD197890 during August and September 2002 (upper and lower panel respectively). The discrete symbols represent photometric V-band observations, the same as in Fig. 7.7. The smooth graphs show lightcurves of CLDI reconstructions, here they only serve to indicate the time span covered by the DI input spectra. Note that CLDI lightcurves have not been used for the determination of the rotation period.

of view is clearly visible in the figure. However, only a few spectra were lost, and the telescope never had to shut down, although humidity several times came close to a critical level.

During the first night, the exposure times of HD197890 were kept constant at 200 s. Longer exposures, up to the limit of about 500 s set by the acceptable phase smearing, would have been advantageous to reduce loss of observation time by CCD-readout. However, they were not possible to avoid over-exposing the CCD. For the second night, the HD197890 exposure times were varied between 120s and 200s, according to the sky transmission, in order to avoid overexposure and to minimize CCD readout timeloss.

During each night, several reference stars were observed, they are summarized below. For the data analysis described here, only the observations of Gl472 were used. They supplied a template spectrum for the line profile extraction by sLSD. The HR9006 spectra, containing relatively few absorption lines, were used for consistency checks during the data reduction and for inspecting the strength of telluric lines.

Two usable spectra resulted from the March 2002 spectroscopy, intended as test exposures. They were useful for preparing the data analysis, but turned out to be insignificant for the final results. This is due to the significant spot-induced deformations of individual line profiles, which can only be properly interpreted as a part of a continuous time series.

Table 7.3: Spectroscopic comparison stars observed

Gl 433	Slowly rotating M1.5-template
Gl 472	Slowly rotating K1V-template
HD 119850	Slowly rotating M1.5 template
HD 136442	Slowly rotating K0V template
HD 155885	Slowly rotating K1V template
HD 171488	Fast rotating G0V
HD 192310	K0V-K2V variable star
HR 9006	(B3V) Flux calibration and telluric line template

Photometric observations

Photometric observation time was available parallel to the spectroscopic observation nights, including the nights in between. Unfortunately, weather conditions at the SAAO for 2002 August 1-8 permitted only observations of comparatively poor quality for August 3-5. Only after the (potential) uncertainties about the rotation period had become clear, some more photometric data were obtained at the SAAO during September 2002.

7.3 Lightcurves

Periodogram analysis

The "classical" periodogram is defined as the squared modulus of the discrete Fourier transform (Scargle, 1982, Eq. 3) which makes it a "power spectrum" for discretely (possibly unevenly) sampled data. The periodogram is a tool for analyzing time series with the aim of detecting periodic components of the data. It is commonly used in a "slightly modified" form due to Scargle (1982, Sec. 1 & appendix A), termed *Lomb-Scargle periodogram*[12] Scargle's modification makes the periodogram a well defined statistical estimator in the general case of an uneven sampling. If suitably normalized, the periodogram amplitudes can be translated into an estimate for the probability that the input data is (normally distributed) random noise.[13] The Lomb-Scargle periodogram, as a function of angular frequency, for the data values X_j sampled at the times t_j is defined as

$$P_X(\omega) = \frac{1}{2}\left\{ \frac{\left[\sum_j X_j \cos\omega(t_j-\tau)\right]^2}{\sum_j \cos^2\omega(t_j-\tau)} + \frac{\left[\sum_j X_j \sin\omega(t_j-\tau)\right]^2}{\sum_j \sin^2\omega(t_j-\tau)} \right\} \qquad (7.7)$$

(Scargle, 1982, Eqs. 10 or B1) with τ defined as

$$\tau = \frac{1}{2\omega}\tan^{-1}\left[\frac{\sum_j \sin 2\omega t_j}{\sum_j \cos 2\omega t_j}\right] \qquad (7.8)$$

However, for the applications below, the periodogram has not been used as a statistical estimator and the significance levels should be taken as quite arbitrary. The reason is that the null hypothesis of this statistical estimation, namely that the data consists purely of random noise, is quite irrelevant for these applications (possibly excepting the case of Figure 7.9): The analyzed lightcurves are certainly (quasi) periodic, the question is if they contain a stable dominating period and the value of that period.

Instead, the periodogram is used below as a "harmonic least-squares analysis". It is shown in Scargle (1982, appendix C) that *the maximum periodogram peak coincides with the frequency which minimizes the least-squares deviation when fitting a sine of that frequency*, but of arbitrary amplitude and phase to the input data. This property of the Lomb-Scargle periodogram is the main reason for choosing the denominator terms in Equation 7.7 (apart from ensuring the time-translation invariance, see Scargle, 1982, appendix B).

The "least-squares-sine-fit" interpretation of the periodogram is useful to keep in mind when interpreting periodograms of unevenly sampled data: If a suitable sine "happens" to fit the sampled intervals of the input data, possibly due to *aperiodic* variations, it leads to a pronounced peak in the periodogram. It must be checked in such cases of uneven sampling whether the resulting period-folded input signal "makes sense".

7.3.1 Photometry August-September 2002

An overview of the observations of HD197890 in August/September 2002 is given in Figure 7.3. The longest interval sampled every night spans August 3-5, a periodogram of these data is shown in Figure 7.5. The alias structure is caused by the roughly 24h-periodic sampling window.[14] Of the three strongest peaks, only the highest amplitude peak (P≈0.44 days) yields an unscattered period-folded lightcurve, shown in Figure 7.7.

The lightcurve of the August/September 2002 observations exhibits intrinsic variations on timescales of a few rotations. This reduces the precision of period determination, already limited because of the short nightly-sampled intervals. It also makes an error estimation of the determined period difficult. An attempt to estimate the maximum "acceptable" period deviations, only using the August 3-5 observations and *assuming a periodic lightcurve during that time span* is illustrated in Figure 7.4. For the shown tentative upper and lower period limits, the deviations between lightcurve intervals of different rotations clearly exceed the estimated photometric error. The resulting rotation period estimate is $P = 0.44\,^{+0.04}_{-0.03}$.[15]

[12] Citing Scargle (1982, p. 838): "The term *slightly modified* is used because the actual values are typically not changed much [compared to the "classical" periodogram], even though the form is significantly changed."

[13] More precisely (following the terminology of Press et al., 1992, which is equivalent to the treatment in appendix A of Scargle, 1982) the probability $P(>z)$ that any of the periodogram peaks exceeds a value of z, in the case of normally distributed random input data, is approximately

$$P(>z) \approx M \cdot e^{-z} \quad .$$

For this probability estimate the periodogram must be *normalized* according to Press et al. (1992, Eq. 13.8.4), the required variance σ^2 can directly be computed from the deviations of the input data from their mean (Press et al., 1992, p. 580, procedure "`avevar`"). M is an estimate of the number of "independent" frequency components in the data; M is of the order of the number of sampled data data points for "quite evenly" spaced samplings, cf. Press et al. (1992) for details.

[14] The "secondary bump" right of each strong peak in the periodogram is caused by a "6/5-resonance" ($5 \cdot 0.44 = 6 \cdot 0.3\overline{6} = 2.2$), i.e. an ambiguity in matching the lightcurve parts which are sampled about two days apart.

[15] Gray (1992, p. 384) gives an "estimation prescription" for the error of rotation period determination: $\frac{\Delta_n P}{P} \approx \frac{2.5}{n} \cdot \Delta_1\phi$. Here $\Delta_n P$ is the period error from an observation covering n rotation periods, $\Delta_1\phi$ is the phase(shift) uncertainty for a single rotation lightcurve.

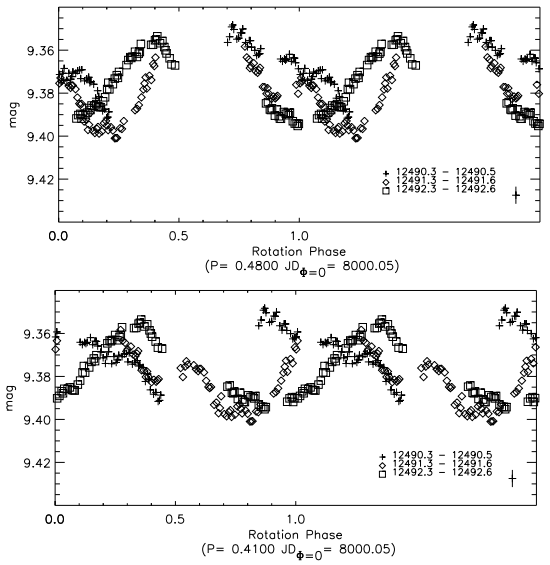

Figure 7.4: August 2002 lightcurves of HD197890, folded with the upper and lower error bounds of the estimated rotation period $P = 0.44^{+0.04}_{-0.03}$ days. Folded with these periods, given below each panel, the deviations between lightcurves of different rotations clearly exceed the photometric error, indicated by the error bar in the lower right corners.

The September 2002 observations are consistent with this error range; the most conspicuous interval (JD 2440000+12531) indicates significant spot reconfigurations during the unobserved time span between the August 2002 and September 2002 observations. However, the September 2002 observations do not supply new information to the period determination, even if a stable rotation period and phase over this time span are assumed. Only two rotations are covered during consecutive nights and the gap between the August and September observations corresponds to a difference of the order of 90 rotations. The uncertainty of the precise number of rotations filling this gap gives rise to the closely spaced peaks in the periodogram of the combined August and September data (Figure 7.6).

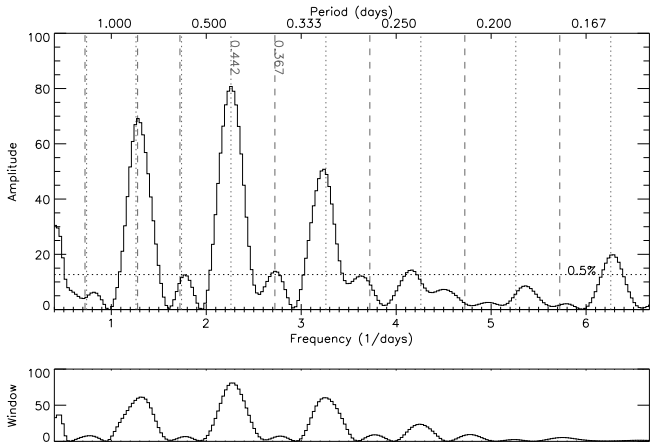

Figure 7.5: Periodogram of the August 2002 photometric data of HD197890 (upper panel). The window function, i.e. the response of the periodogram to a simple periodic signal (here a sine of period 0.44 days) is shown below. Aliases, due to a 24-hour periodic observation window, of the two selected periods are marked by dotted and dashed vertical lines. The amplitude corresponding to a "false alarm" probability of 0.5% (i.e. to a significance level of 99.5%) is marked by the horizontal dotted line, it is not further used in the analysis.

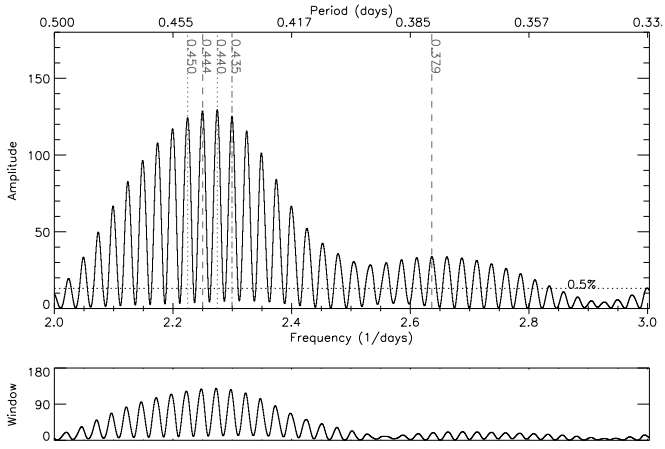

Figure 7.6: Same as Fig. 7.5, but for the combined August and September 2002 photometric data of HD197890. No aliases are marked, they lie outside the shown period range.

The August 3-5 observations cover 6 rotations, so the above prescription would require a phase determination with a precision of $\Delta_1\phi \lesssim 0.15$ to achieve a relative period error of $\frac{\Delta_n P}{P} = \frac{0.03}{0.44}$. This is reasonable for the available lightcurve (Fig. 7.7).

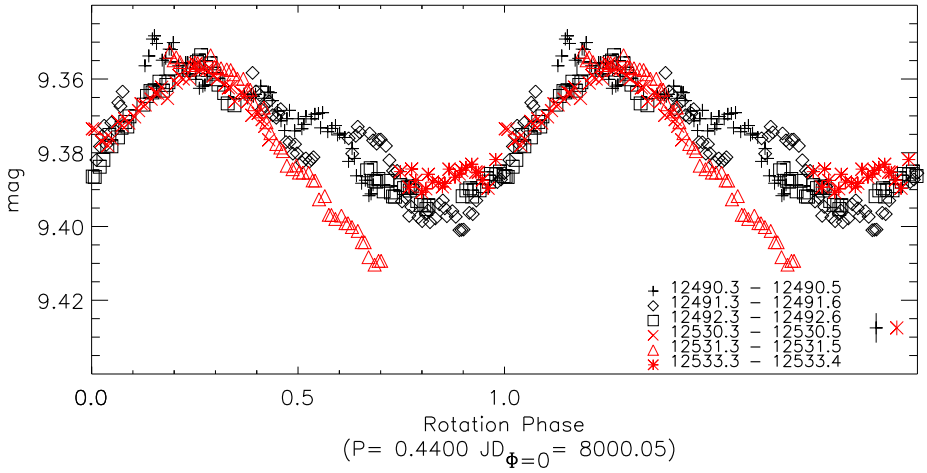

Figure 7.7: Lightcurves from photometric V-band observations of HD197890 during August and September 2002. The error bars right of the symbol legend show estimated errors of the photometry (left error bar for the first three symbols, right error bar for the remaining three). The data are shown as a function of rotation phase, folded with a period of $P = 0.440$ days, determined from the August photometry alone, *assuming a periodic lightcurve during that time span* (see text). Note that at the 0.001 day level, the folding period could be chosen, with very similar results, as any of the peak-positions near the main maximum in the periodogram of Fig. 7.6, one example is shown in Fig. 7.24. Dates given are JD-2440000.

7.3.2 Lightcurves 1990-1996

Most observations of HD197890 by the HIPPARCOS astrometry satellite are far too sparsely sampled for studying rotational modulation, given the limited spot lifetimes. Only two stretches of observations, each covering about 3 days quite continously, yield useful information about its rotation period. They are termed the 1990 and 1993 HIP-lightcurves in the following and shown in Figure 7.8. Three short sampling intervals have been added to the 1990 HIP-lightcurve; they suggest a remarkable stability of the lightcurve during the (discontinuously) covered time span of about three months.

The HIPPARCOS (HIP) lightcurves shown here are broadband photometry results of the main detector of the HIPPARCOS satellite, calibrated in H_p-magnitudes. The V_T- and B_T-lightcurves, observed by the "star-tracker" instrument on board HIPPARCOS (measured in the filter system of the Tycho-catalogue) exhibit too large measurement errors (typically ± 0.2 mag) for the construction of a reliable lightcurve of HD197890.

The conversion of H_p into V_J-magnitudes (Johnson-V) depends sensitively on the colour index of the object.[16] The colour index of HD197890 varies significantly with rotation phase, due to the varying spot filling factor of the visible hemisphere. Consequently, no correction has been attempted and the HIP-lightcurves can only be used for the purpose of period determination and qualitative comparison with the V_J-lightcurves.

However, the available two HIP-lightcurves of appropriately continuous sampling (Figure 7.8) are of particular interest because their sampling is not subjected to the 24-hour periodicity of single-site terrestrial observations; this leads to a different structure of aliasing periods (see the discussion of "sampling resonances" below). More importantly, the two lightcurves are remarkably different in character: The 1990 HIP-lightcurve (upper panel of Figure 7.8) clearly shows periodic variations with a period of 0.380 days, with remarkably small variations during the available sampling, covering a time span of 90 days. In contrast, the HIP-lightcurve of 1993 (lower panel of the same figure) shows smaller, but clearly significant brightness variations without any stable period. This suggests spot pattern reconfigurations during the short total sampling interval of 3 days, covering about 7 rotations. The lack of a stable period is confirmed by the periodogram of the data shown in Figure 7.9. None of

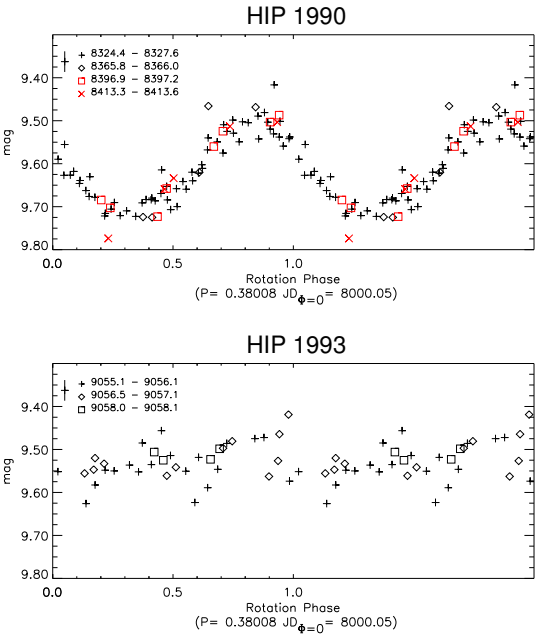

Figure 7.8: Lightcurves of HD197890 from the HIPPARCOS archive, given in units of H_p-magnitudes (dates are given in the annotation as JD-2440000). This figure shows all HIPPARCOS observations "usefully sampled" for the study of rotational modulation. The upper (1990 data) and lower panel (1993 data) are remarkable examples of qualitatively different lightcurves of HD197890, showing a well-defined period and the absence of a stable period, respectively. The lightcurves are folded with the periods given in days below each plot, these periods belong to the strongest peaks of the corresponding periodograms. The photometric errors are indicated by the error bars in the upper left corner of each panel.

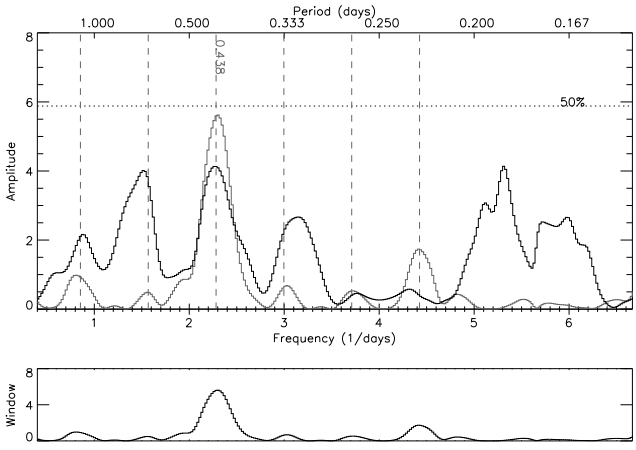

Figure 7.9: Periodogram of the HIP-lightcurve of 1993 (lower panel of Fig. 7.8). In spite of the short total sampling interval of 3 days, no significant period is present. The largest period peak and its sampling period aliases are marked by dashed lines. The window function (the response to a sine of period 0.438 days) is shown in the lower panel and as the gray curve in the upper panel.

[16] The conversion is given as a function of $(V-I)$ in ESA SP-1200 (1997, p. 59). The measurements of $(V-I)$ of HD197890, available from the September 2002 photometry, exhibit too large errors for the construction of a lightcurve. However, their mean value of 1.113 ± 0.006 is consistent with a K0V classification (Cox, 2000, Ch.15.3.1). This results in a correction of $V_J \approx H_p - 0.14$.

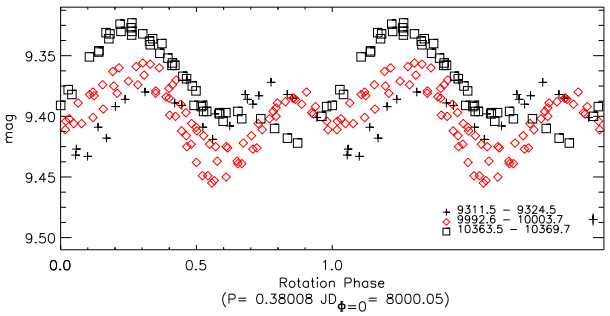

Figure 7.10: Lightcurves from photometric V-band observations of HD197890 observed by G. Cutispoto in 1993 (+), 1995 (◇) and 1996 (□), each covering 6 to 10 nights. Dates given are JD-2440000. The error bar right of the symbol legend indicates the measurement error. The lightcurves are folded with a period of P=0.38008 days; this folding period has been slightly tuned for plotting purposes only, reducing the scatter between the three datasets.

the high periodogram peaks yields a reasonable period-folded lightcurve (in accord with their low significance below 50%).

The photometric data of Anders et al. (1993), observed in August/September 1991, do not allow a reliable determination of a rotation period, consequently they have not been used here. However, it is worth noting that their reported peak-to-peak amplitude of 0.2 mag in the V-band is the largest yet observed for HD197890.[17]

Of the three lightcurves observed at ESO in 1993, 1995 and 1996 (Figure 7.10), only the latter two are sampled densely enough for a reliable period determination. Their periodograms are shown in Figures 7.11 and 7.12. For both, the dominating period is 0.380 days; Cutispoto et al. (1997) give a value of P=0.380 $\pm$ 0.004 days, based on the 1996 data alone.

The strong secondary peaks in the 1996 periodogram (P=0.434 days and aliases) are mentioned by Cutispoto et al., but not further analysed. Comparison with the window function shown in Figure 7.11 shows, that these secondary peaks are very closely reproduced by the response to a sinusoidal signal of period 0.380 days. They are an artefact of the sampling window, caused by a "7/8-resonance" ($7 \cdot 0.434 = 8 \cdot 0.380 = 3.04$). This means that sampling a signal of dominating period 0.380 days (or 0.434 days) at three day intervals yields little information on which of the periods is true. The seven nights of the 1996 photometry were observed with a pattern "ooxooxo" (o=observed, x=missing), which makes three days the time interval between 3 pairs of nights (compared to two night-pairs with no night in between and two night-pairs with one night in between). This causes the strong 0.434 day "secondary" peak in the periodogram.

[17]The complete data of the HIPPARCOS/Tycho-photometry of HD197890 contains spuriously sampled brightness increases of up to two magnitudes, presumably attributable to flares.

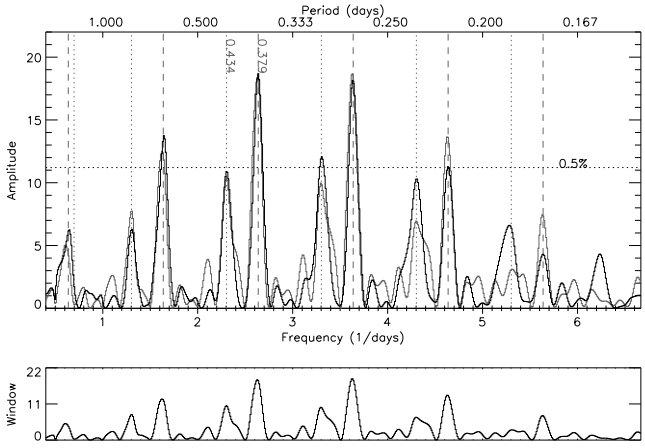

Figure 7.11: Periodogram of the October 1996 V-band photometry of HD197890 (upper panel, black), see Fig. 7.5 for annotations. The data used is the same as that used for Fig. 1 of Cutispoto et al. (1997). The window function (lower panel, and the gray graph in the upper) is chosen as the response to a sine of the strongest period, namely 0.380 days. Note how closely the periodogram resembles this simple window function, including the secondary peaks; this indicates that the strong secondary period (0.43 days) and its aliases are caused by the pattern of observed and lost nights (see text).

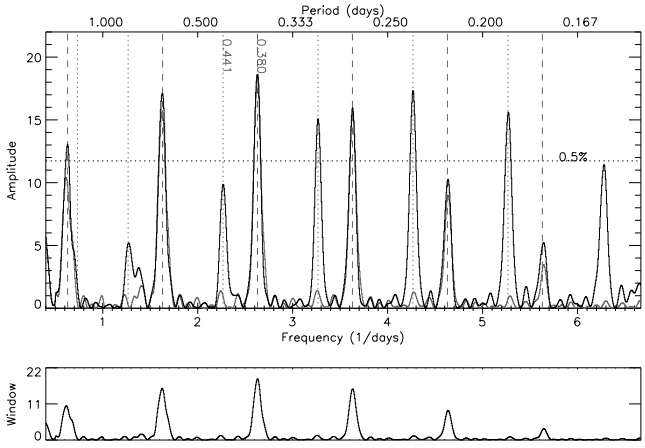

Figure 7.12: Same as Fig. 7.11, but for the October 1995 photometric data of HD197890. Here, the window function does not reproduce the secondary period peaks (0.44 days and aliases); the reason for this is unclear (see text).

The ESO 1995 lightcurve (spanning 11 days) exhibits significant scatter when folded with the 0.380 days period. Here, due to the different sampling, the response to a sinusoidal signal of a period of 0.380 days causes a considerably weaker peak at 0.44 days (and its aliases) than the peak of the observed data (Figure 7.12).

Actually, the larger scatter of the 1995 lightcurve, compared to its 1996 counterpart, shows that the 0.380 day-periodic component is superimposed by a secondary component. However, this secondary component need not be periodic to cause secondary peaks in the periodogram.

7.3.3 Summary

The preceeding sections describe an analysis of all densely sampled (V-band and broad-band) photometric time series of HD197890 available to us; this includes the two published datasets (Anders et al., 1993 and Cutispoto et al., 1997). This analysis reveals two characteristics of HD197890's lightcurves:

(a) The published rotation period of P=0.380±0.004 days (Cutispoto et al., 1997) is clearly dominant in several datasets and stable on timescales exceeding 3-6 days (apparently more than three months for the HIPPARCOS time series of 1990).

(b) Several datasets show significant deviations from a stable periodic lightcurve on timescales of a few days (less than 3 days in the case of the HIPPARCOS time series of 1993).

Item (a) strongly indicates that a period of approximately 0.38 days is the true rotation period of HD197890. In the presence of strong surface differential rotation several modulation periods could be observed (induced by spots at different latitudes); however, this possibility is not supported by the apparently quite precisely recurrent value of about 0.380 days for several observation periods. In analogy to the Sun a continuous range of spot latitudes should be expected, leading to a continuous distribution of rotation periods bounded by a lower and upper limit.

Item (b) strongly indicates intermediate-scale variations of the surface features of HD197890 on timescales of a few days during some epochs. However, the only lightcurve suggesting a *periodic* modulation with a period not consistent with the value of 0.380±0.004 days is given by the August 2002 data, yielding a period of $0.44^{+0.04}_{-0.03}$ days (Figure 7.4).

The only way to make the August 2002 lightcurve comply with a rotation period of about 0.38 days is the assumption of significant reconfigurations of surface features on HD197890 during the time span between two consecutive lightcurve intervals (i.e. during about 24 hours in this case).

Such fast large- or intermediate-scale changes of the spot pattern could explain the unperiodic lightcurve resulting from the August 2002 photometry when folded with the 0.380 days period, shown in Figure 7.39.

7.4 Line profile extraction (sLSD)

The line profiles (rotational broadening functions, RBFs) used as input of CLDI were extracted by spectrum deconvolution using sLSD (selective least squares deconvolution, described in Chapter 6).

Two separate wavelength ranges were selected for the application of sLSD with the aim of extracting two RBF time series based on independent input information; these two ranges are

- The "6120 Å"-range: 6117-6127 Å
  Shown in Figure 6.7
  Template spectrum: Gl 472 (observed).

- The "6400 Å"-range: 6389-6440 Å
  Shown in Figure 6.1
  Template: PHOENIX 5200 K (synthetic).[18]

Individual characteristics of the two regions are discussed in Section 6.5. While the "6120 Å" region represents the application of line profile deconvolution to a narrow spectral range, dominated by a single line (Ca I λ6122), the "6400 Å" leads to a profile averaging several pronounced lines. Both wavelength ranges were adjusted to reduce the influence of strong lines in their vicinity on the extracted profiles.

While the Gl 472 template spectrum allows quite good fits in the "6120 Å" region, no suitable synthetic PHOENIX spectrum could be constructed: No set of atmospheric parameters managed to produce a proper ratio of the dominating Ca I and the Ti I line depths, controlling the shape of the resulting blend.

Both templates, the Gl 472 and the PHOENIX 5200 K, were comparably successful in producing good fits to the spectrum in the "6400 Å" region.

The choice of the two named wavelength regions is to some degree arbitrary. Several other regions well suitable for DI could definitely be found in the wide wavelength range of the available spectra of HD197890. However, in the context of this work, other spectral ranges have only been studied sporadically, mostly during the fruitless quest for spectral signatures of a hypothetic secondary companion of HD197890 (Section 7.1.1).

However, the study of other wavelength regions will be of significant interest for future work, see Section 7.9.1.

[18]The model used was a PHOENIX "NextGen" (Hauschildt et al., 1999) with an effective temperature of 5200 K, $\log\ g$=4.5 and a metallicity reduced by -0.5 dex compared to solar metallicity.

7.5 Doppler imaging

The Doppler images presented and discussed in this section were constructed from the August 2002 observations of HD197890. They represent the final of several "generations" of images. The major advances in this genealogy were made by an improved reduction of the raw spectra (Section 8.1), increasing experience with the adjustment of parameters of CLDI (Section 5.5) and improvements of the sLSD line profile extraction. While the large-scale features of the solutions have persisted through all reconstructions, the reliability of the images could be extended to increasingly smaller image features.

The purpose of refining the Doppler imaging reconstructions was to produce a *consistent* set of images, *optimizing their resolution* and gaining *information about their reliability*. The final goal was the production of *two* images, one for each observation night covering quite precisely one rotation, allowing the reliable identification of features common to both of them.

As discussed below, all four goals could be reached because of the extraordinary phase sampling and quality of the August 2002 spectral time series. However, the last goal turned out to be the most difficult because of the unexpectedly fast intrinsic evolution of spot patterns on HD197890. It was only reached near the end of the described analysis after finally accepting that this fast spot evolution leads to a markedly unperiodic lightcurve during the observed time span of August 2-7.

As a consequence, the following discussion of image consistency, reliability and resolution is mainly carried out for the images adopting the (in retrospect) presumably incorrect rotation period $P_{\rm alt}$ (Table 7.4). This is justifiable because of the limited influence of the period difference between P_0 and $P_{\rm alt}$ on the reconstructions, affecting the compared images in the same way. See Section 5.5.6 for a general discussion of Doppler imaging errors resulting from incorrectly adopted rotation periods.

7.5.1 Images and consistency

The "final" images

Two wavelength regions were selected for the extraction of line profiles of HD197890 (Section 7.4), the resulting images are termed "6120 Å" and "6400 Å" images in the following. The reconstruction parameters summarized in Table 7.4 have been used for the CLDI reconstructions of this chapter, unless noted otherwise. Adopting a correct rotation period for the reconstructions has been a major issue during the analysis. The choice was made difficult by partly contradicting results of the photometry of HD197890 at different epochs (Section 7.3.3), an appar-

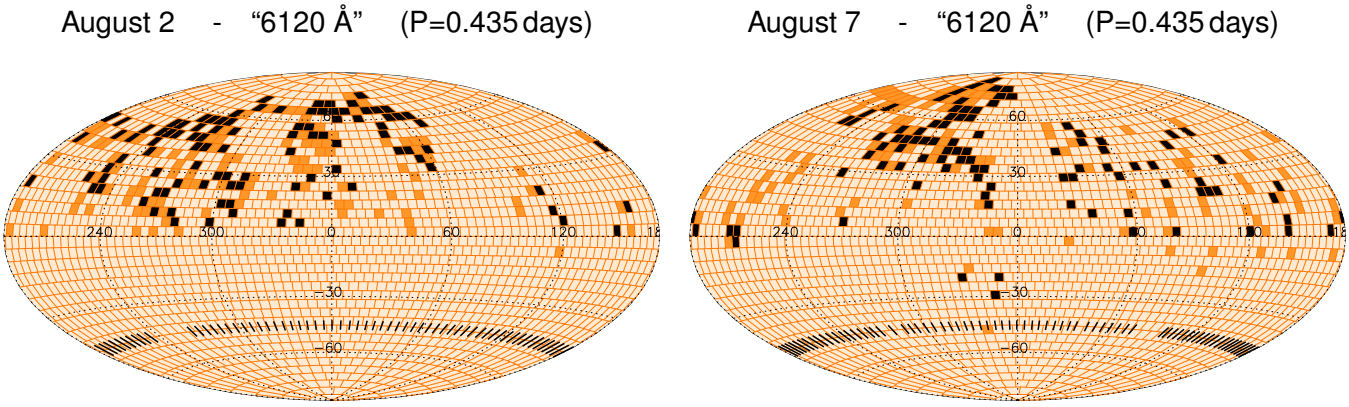

Figure 7.13: CLDI images of HD197890, reconstructed with an adopted rotation period of 0.435 days from line profiles extracted in the “6120 Å” wavelength region (Fig. 6.10). The reconstruction parameters are summarized in Table 7.4. Subobserver longitudes of observed phases are marked by short lines. A rotation phase $\phi = 0$ corresponds to a subobserver longitude of $\varphi = 0° \hat{=} 360°$; rotation proceeds with *decreasing* subobserver longitude. Given the adopted rotation period, about 11.5 stellar rotations have passed between the two images.

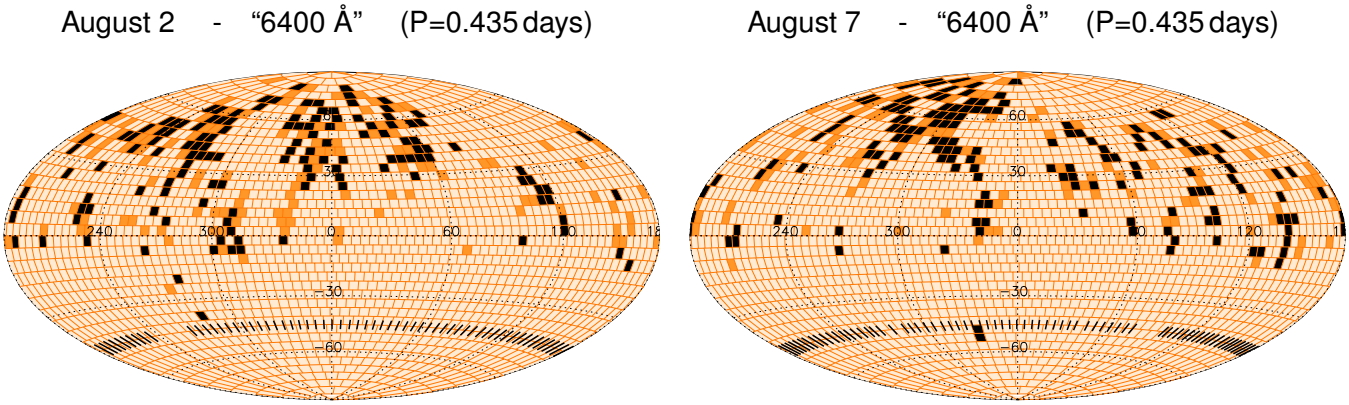

Figure 7.14: Same as Fig. 7.13, but for line profiles from the “6400 Å” wavelength region (Fig. 6.11). These maps, together with those of Fig. 7.13 are used for the image consistency analysis of Section 7.5.1.

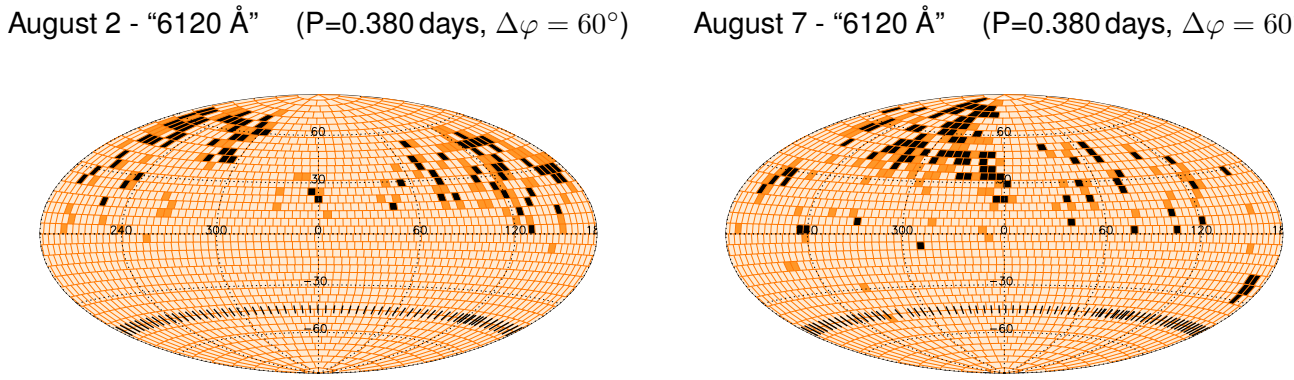

Figure 7.15: Example influence of the rotation period used for the CLDI reconstruction: Same as Fig. 7.13, but for a reconstruction period of 0.380 days. The coordinate systems of both maps here have been rotated by 60° (i.e. a phase $\phi = 0$ corresponds to a subobserver longitude of $\varphi = 60°$). This rotation is motivated by the phase shift introduced by the different periods, the rotation angle is arbitrarily chosen to facilitate comparisons with the 0.435 day-period maps.

Table 7.4: Parameters adopted for the construction of the "main" Doppler images of HD197890. Two different rotation periods have been tried out, they are noted for the corresponding images. $\delta_{\mathtt{FF}}$ indicates the filling factor increment per CLDI step (Section 5.3), ϵ represents the linear limb darkening coefficient. The spot continuum flux is given relative to an undisturbed photospheric continuum flux of one. Note that the given margins designate the deviations between parameters adopted for different reconstructions, they are no proper error estimates.

Rotation period	P_0=0.380 days
	$P_{\rm alt}$=0.435 days
Inclination	70°
Spot continuum flux	0.5
CLDI backprojection	RM×TSA
CLDI $\delta_{\mathtt{FF}}$	0.5
$v \sin i$	134±2 km s^{-1}
ϵ	0.9±0.1 ("6120 Å")
	0.7±0.1 ("6400 Å")

ently satisfactory solution of the "two-period-puzzle" is described in Section 7.8.3. The determination of the inclination is discussed in Section 7.5.2.

The limb-darkening and $v \sin i$ values given in Table 7.4 have been determined by fitting analytical rotation profiles to average RBFs (rotational broadening functions) of HD197890 (Section 6.4). It should be noted, that the errors of the fit parameters are presumably larger than the margins given in the table. This is mostly due to the significant asymmetries of the average RBFs, introducing considerable uncertainties into the fit.[19]

In agreement with the synthetic CLDI reconstruction results described in Section 5.5.1, different CLDI backprojection algorithms (namely $\mathtt{RM}_{0.5}$- or RM×TSA-backprojections, described in Section 5.2) show little influence on the reconstructions of HD197890. Because of the *veto scheme* implemented in the RM×TSA-backprojections, they have been constantly used for the "final" images. They are the most "conservative" reconstructions CLDI can offer, in the sense that they usually produce solutions with a minimum total filling factor compared to other backprojections.

Consistency

The term "consistency" of different Doppler images of the same object, reconstructed for the same observation time span, is used here to describe the following aspects:

(a) appropriately fitting migrating deformations of the input line profiles, (b) consistency with the available photometric lightcurves (c) correspondence of images from line profiles of different wavelength ranges and (d) stability of the images against selecting different data subsets.

While (a) is a most natural requirement, for poor input data showing few well-defined features it is hard to verify (cf. e.g. Fig. 2 of Barnes et al., 2001). Inspection of Figures 6.10 and 6.11 shows that it is met here with the exception of very few profiles. As discussed in Section 6.5, these exceptions are partly caused by deficiencies of the line profile deconvolution. In addition they could also be due to fast changes of HD197890's spot patterns.

Item (b) is discussed in Section 7.8. As outlined there, no photometry *strictly* parallel to the input spectra of the Doppler images exists. Since spot-reconfigurations on timescales of very few rotations cannot be ruled out for HD197890, actually they are inferred from the combined results of this chapter, requirement (b) cannot be truly checked.

Also (c) is a natural requirement, occasionally examined for published Doppler images (e.g. Stout-Batalha & Vogt, 1999; Rice & Strassmeier, 2001).[20] Inspecting the corresponding maps of Figures 7.13 and 7.14 reveals a substantial amount of correspondences. In comparison to e.g. the results of Rice & Strassmeier (2001), our results appear well presentable, even if the the poorer SNR and phase sampling of the cited work are kept in mind.

Finally, requirement (d) is a straightforward test[21] if the phase sampling of the observations is dense enough to allow it. Its application to the images presented here, together with requirement (c) is discussed some more below, used for judging the reliability and resolution of the images. The results may be compared to Barnes et al. (1998, Figures 7,9 and 11), or Rice & Strassmeier (2001, Figures 6 and 7); again our results appear well presentable.

Reliability and resolution

The criteria (c) and (d) of the above list describe the "self-consistency" of the presented Doppler images. They allow some estimation of their reliability ("Which image features are presumably real, which are artefacts?") and resolution ("Is this image feature correctly positioned, how precisely has its shape been reconstructed?") of the im-

[19] Analyzing the profiles with the Fourier based line profile analysis method of Reiners et al. (described in Section 3.2), yields $v \sin i \approx 131 \pm 2$ km s^{-1}. However, since this method is also affected with problems of profile asymmetry, the error may well be larger.

[20] Stout-Batalha & Vogt (1999) perform a very extensive and partly quantitative comparison of images of 15 different spectral lines.

[21] Another simple "sanity check" is swapping the line profiles of adjacent phases. If well-defined structures are present in the line profiles, this should considerably affect the convergence of the DI. For the data discussed here, CLDI stops converging after relatively few reconstruction steps for such a swapped time-series.

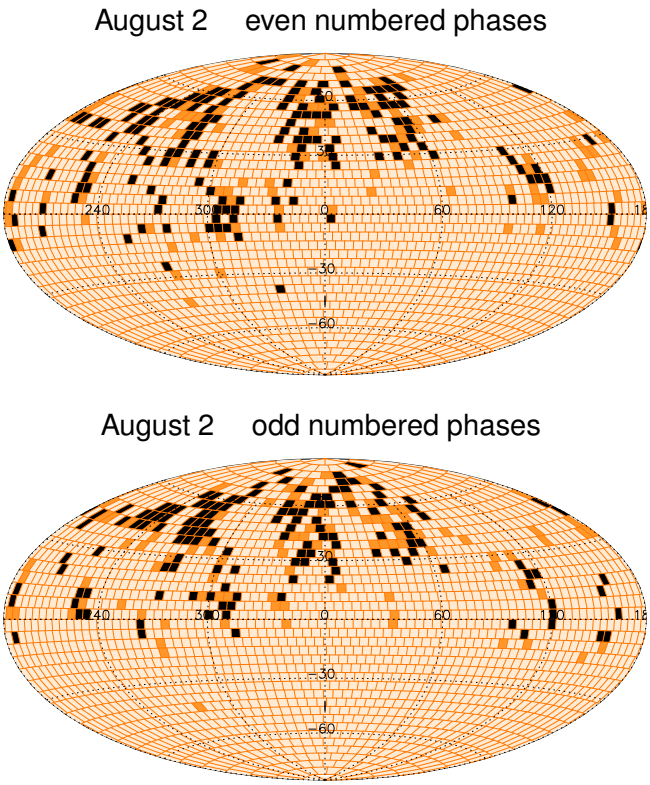

Figure 7.16: CLDI images of HD197890 from two independent datasets covering the same rotation, observed on August 2. Both panels show reconstructions based on line profiles extracted in the "6400 Å" wavelength region, adopting a period of 0.435 days. The complete times series of profiles (Fig. 6.11) has been split into the even-numbered (upper panel) and odd-numbered phases (lower panel).

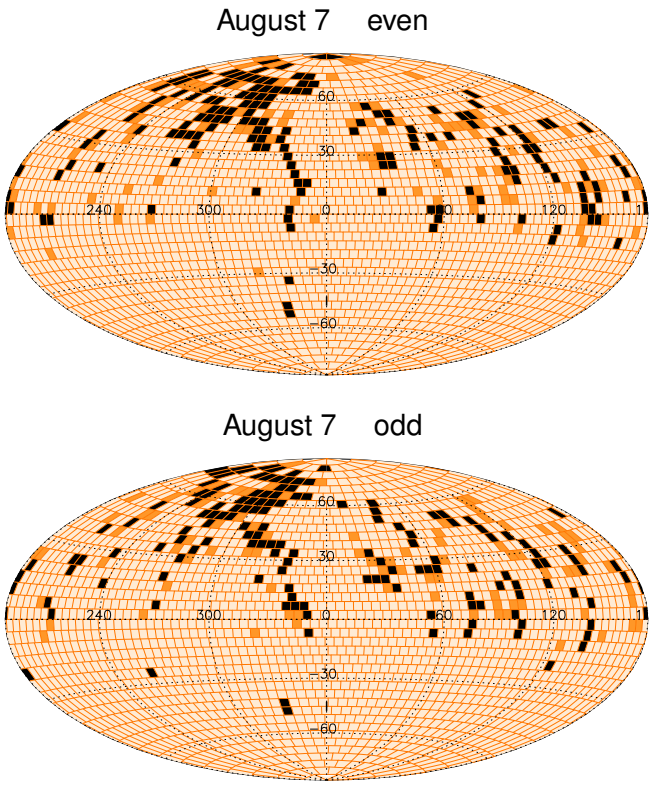

Figure 7.17: Same as Fig. 7.16, for the August 7 observations of HD197890.

ages. A discussion of these aspects on a general basis can be found in Sections 4.2 and 5.5.4.

Obviously, image reliability and resolution are closely related: Both describe the resolution, concentrating on larger and smaller scales, respectively. However, apart from corresponding to the "human" way of judging the quality of an image, they describe different characteristics of the DI-reconstruction. The reliability reflects the *stability* of discerning "true" (i.e. migrating properly with rotation) from spurious deformations of the line profile time series. The resolution describes, to what extent these "true" deformations are reconstructed into position information on the surface. Because CLDI (as Maximum-entropy DI) does not offer an "error map" as a side product of the reconstruction, its image resolutions cannot be *strictly* quantified.

Comparing "data-subset" images

Comparing the images belonging to the same rotation and the same wavelength region, but reconstructed from different subsets of the available line profiles (Figures 7.16, 7.17 and 7.14), justifies the following statements:
(i) "Spot groups" containing more than 3-4 surface elements are reliably reconstructed in the corresponding images. (ii) The positions of spotted surface elements inside these groups differs by typically 1-2 surface-grid positions; for low latitudes ($\lesssim 25^\circ$), the latitude uncertainty is larger.

Actually, (i) and (ii) are only poorly satisfied for the "spread-out" spot regions of the August 7 images (longitudes $0^\circ \lesssim \varphi \lesssim 180^\circ$). These regions put high demands on the reconstruction, because of the complex and weak line profile deformations associated with them. As a consequence they may benefit significantly from the denser phase sampling of the whole time series compared to the "odd" and "even" subsets. In addition, they are presumably most affected by reconstruction period uncertainties. As discussed below in Section 7.8.3 they are more coherently reconstructed adopting a period of 0.380 days (Figure 7.33, longitudes $300^\circ \lesssim \varphi \lesssim 120^\circ$ in the August 7 maps). In fact that is an indication of the correctness of the latter rotation period.

Given the size of the surface elements,[22] (i) and (ii) translate into a resolution of about 10 degrees on the surface, not including the named regions close to the equa-

[22] $4.5^\circ \times 4.5^\circ$ at the equator, increasing in longitude towards the poles, e.g. about $8^\circ \times 4.5^\circ$ at $\pm 60^\circ$ latitude

tor, where the latitude of the features is less well known. In accord with reconstructions of synthetic data (Section 5.5.4), the resolution is lower for apparently non-coherent surface structures.

Comparing "different-wavelength" images

The correspondence of images belonging to the same rotation but constructed from different wavelength regions (Figures 7.13 and 7.14), is poorer than the correspondence of different "data-subset" maps discussed above. This is no surprise since the errors of the line profile extraction/modelling enter in addition to the CLDI reconstruction uncertainties.

However, there is a close correspondence between the different-wavelength images of the same rotation. Slightly relaxed versions of the statements (i) and (ii) above hold, again not including the "spread-out" spot regions in the August 7 images.

The procedure illustrated in Figure 7.18 substantiates the surface resolution estimate of about 10° for the presented Doppler images of HD197890: The cross-correlation maxima for each latitude (see Section 7.6) are widely scattered when correlating unsmoothed Doppler maps of the same rotation, but reconstructed from different wavelength ranges. These maxima concentrate in a narrow band (inside $\pm 10°$ longitude shift), when the same maps are smoothed by a boxcar of about $10° \times 10°$extension to simulate a blurring due to the tentative "true" resolution of the images.

Another indication of the "improved correlation" of the smoothed Doppler images comes from the image congruence measure $\mathcal{C}$ (Equation 5.15). It increases considerably from 0.47 for the unsmoothed images correlated in the upper panel of Figure 7.18, to 0.78 for their smoothed counterparts correlated in the lower panel.[23]

Absence of a polar spot

In contrast to the case of many other apparently single ultrafast rotating solar-like stars, the Doppler images of HD197890 do not show a polar spot. This agrees with the Doppler images of HD197890 by Barnes et al. (2001).[24]

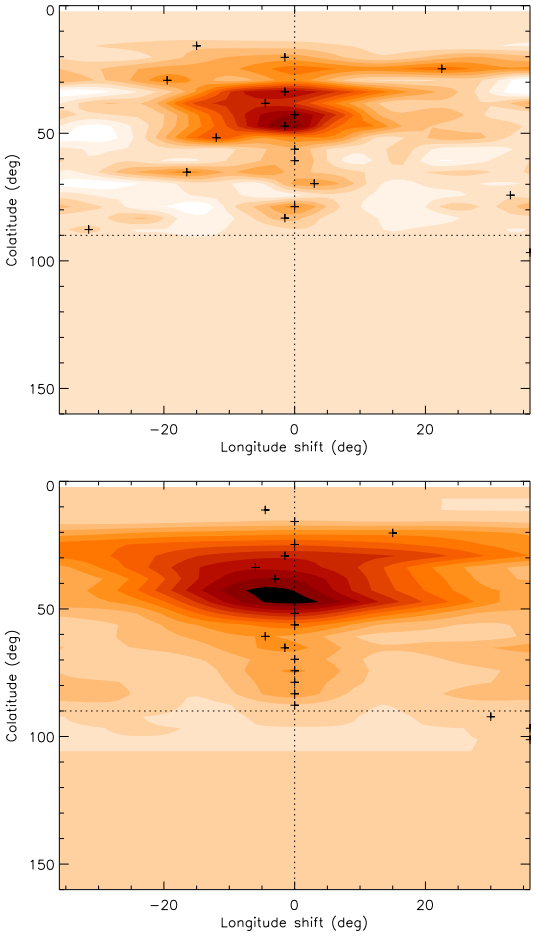

Figure 7.18: Cross-correlation of different-wavelength Doppler images of *the same rotation* (August 2, "6120 Å" and "6400 Å" images for P=0.435 days). The panels show the cross-correlation function of the unsmoothed images (upper panel) and the images smoothed by a boxcar extending 13.5° in latitude and 9° in longitude (lower panel), approximately simulating the tentative surface resolution of the compared Doppler images. The maximum of the cross-correlation function for each latitude is marked by a plus. Note how these cross-correlation maxima concentrate around 0° for the smoothed case, indicating a substantial congruence of the maps when taking the above tentative resolution into account. See Sec. 7.6 for details of the cross-correlation procedure.

[23] As a numerical example for comparison, $\mathcal{C}$ increases much less when comparing the "6120 Å" images of August 2 and 7, i.e. "truly different" images: From 0.34 (unsmoothed) to 0.41 (smoothed).

[24] Examples of apparently single ultrafast rotating solar-like stars with prominent polar spots found in their Doppler images are:
HII 686 (K4V, P=0.40 days, Stout-Batalha & Vogt, 1999)
HII 3163 (K0V, P=0.42 days, Stout-Batalha & Vogt, 1999)
AB Dor (K0V, P=0.51 days, Donati et al., 1999)
PZ Tel (K0V, P=0.94 days, Barnes et al., 2000)
It is worth noticing that the Doppler images of AB Dor by Kürster et al. (1994), reconstructed using the "old" CLDI, do not show a polar spot, in contrast to all other published Doppler images of AB Dor (Hussain,

Since a rotationally symmetric polar spot causes a *phase-independent* deformation of the line profiles, their detection (or proving their absence) by Doppler imaging puts higher demands on the line profile modelling than the case of migrating profile deformations. Consequently the presence or absence of polar spots in Doppler images has always been scrutinized and in many cases been a matter of debate (e.g. Bruls; Solanki & Schüssler, 1998; for some general remarks on polar spots in Doppler images, cf. Rice, 2002, Sec. 3.3).

The following items support the reality of a "missing" polar spot on HD197890 during the Doppler imaged time span:
(a) The extracted RBFs do not show a markedly "flat-bottomed" line profile, neither has such a "flat-bottomed" profile shape been corrected for during the RBF correction performed prior to CLDI (Section 6.4). (b) None of the Doppler images presented in this chapter show a polar spot, independent of reconstruction parameters and wavelength range. Actually, item (a) is the truly fundamental argument, while item (b) is practically a direct consequence of it.

7.5.2 Reconstruction parameter influence

The CLDI reconstruction parameters adopted for the "main" Doppler images of HD197890 are summarized in Table 7.4. All Doppler images shown in this chapter were constructed with these parameters, unless noted differently. Differently chosen $v \sin i$ and limb darkening coefficients ϵ lead to rotationally symmetric structures in the Doppler images (polar caps or spotted belts, see Section 5.5.6).

Adopting a lower spot continuum flux (i.e. a higher brightness contrast between spots and undisturbed photosphere) leads to decreased filling factors of the resulting Doppler images; increasing the spot continuum flux has the opposite effect.[25]

Inclination

Adopting an inclination for the Doppler imaging is commonly done by attempting reconstructions at different inclinations and selecting the one yielding the best line profile fits (Section 5.5.5).

Figures 7.20 and 7.21 show the line profile fit quality χ^2_{final} as a function of inclination for different datasets of HD197890 and for differently adopted rotation periods.

Since the discussion of Section 7.8.3 strongly suggests the 0.380 days period to be correct for HD197890, the χ^2_{final}-curves of Figure 7.20 should be considered for the inclination determination.[26] Actually, the minima of three of these curves agree quite well on an inclination value to adopt, even if they are poorly pronounced, namely between 60° and 70°.

The deviation of the August 2 "6120 Å" χ^2_{final}-curve from this behaviour is puzzling. It may be related to one peculiarity of the corresponding profile time series: It contains two phase ranges with outstandingly ill-fitted migrating deformations (irrespective of the adopted period), found close to phases 0.1 and 0.8 in Figure 6.12. Although the reason for these ill-fitted ranges is unclear, they introduce an offset in χ^2_{final} which may (by accident) depend on the adopted inclination and lead to a shift of the minimum of χ^2_{final}.

An inclination of 70° was finally adopted for the DI reconstructions of HD197890 presented here. This choice deviates from the value of 55° determined by Barnes et al. (2001, Fig. 1), however the deviation is small, considering the influence on the resulting Doppler images: Varying the inclination of the reconstruction star e.g. by 20° from the adopted best value has rather little influence on the resulting images. An example for this is shown in Figure 7.19. Actually a stronger influence can hardly be expected, given the weak "contrast" of line profile fit quality resulting from varying the inclination (only about 5% of the best achieved χ^2_{final} in the discussed cases). This illustrates once more that the inclination is only approximately determined by the line profile time series alone.

The χ^2_{final}-contrasts for the observed input data are lower than those shown by CLDI reconstructions of synthetic data (e.g. about 20% for the datasets with a SNR of 100 in Figure 5.36). This is at least partly caused by the already named offset of χ^2_{final} due to some line profiles of the time series which are constantly ill-fitted by CLDI, irrespective of inclination (another example are phases 0.787-0.860 in Figure 6.11, including instability-jitter of

2002, Sec. 4.1). This presumably reflects true changes of AB Dor's surface appearance; it is most certainly not related to the use of CLDI: Any DI algorithm is able to reconstruct "flat-bottom line cores" into cool polar spots. Instead, details of the line profile synthesis and its adopted parameters decide whether a line profile is regarded as "flat-bottomed".

[25] In agreement with the results of Kürster et al. (1994, Sec. 4.4.2) a large range of brightness contrasts can be adopted without significantly influencing the quality of the CLDI line profile fits. Kürster et al. give a possible range of spot-photosphere flux ratios between 0.3 and 0.75 for their images of AB Dor. In the context of this thesis the adopted contrast ratio of 0.5 is an arbitrarily chosen intermediate value, see Section 7.9.1 for possibilities of properly determining this value.

[26] The 0.435 days period χ^2_{final}-curves (Figure 7.21) show more pronounced and better agreeing minima than their 0.380 days period counterparts. Assuming the (approximate) correctness of the latter period this is surprising, no compelling reason could be found for this behaviour.

sLSD at phase 0.860).[27]

Summing up, the August 2002 DI-reconstructions combined with Barnes et al.'s measurements agree on an intermediate inclination for HD197890 of about $60\pm10°$. As discussed in Section 7.1, the observed projected rotational velocity together with the "small" radius estimated from evolutionary models are in favour of a large inclination in the given range.

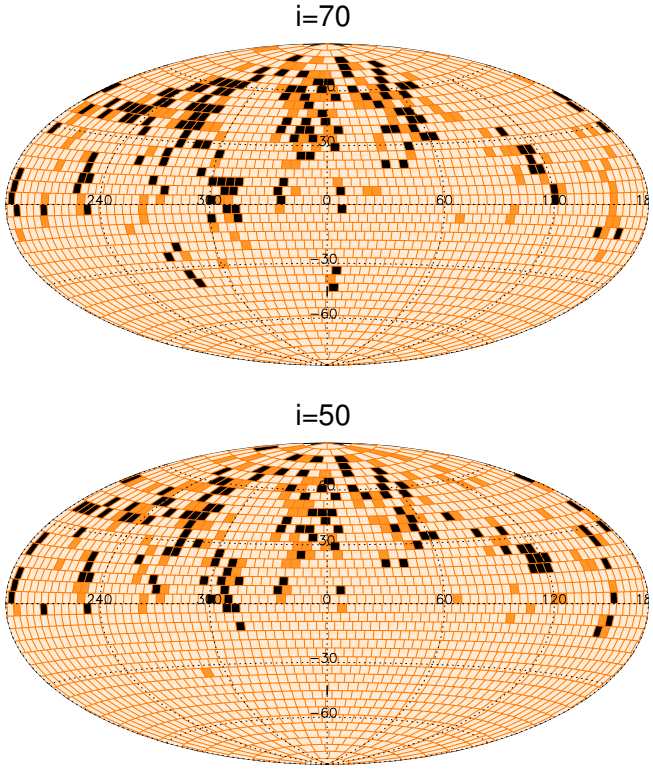

Figure 7.19: Varying the inclination of the reconstruction star (given above each plot) for CLDI $\mathtt{RM}_{0.5}$ reconstructions. Both maps show reconstructions from the August 7 "6400 Å" data, adopting a period of 0.435 days. The lower inclination of $i = 50°$ is too small in the light of the results of Sec. 7.1. Note, however, that this difference in inclination of 20 degrees has a rather limited influence on the spot pattern of the resulting Doppler images.

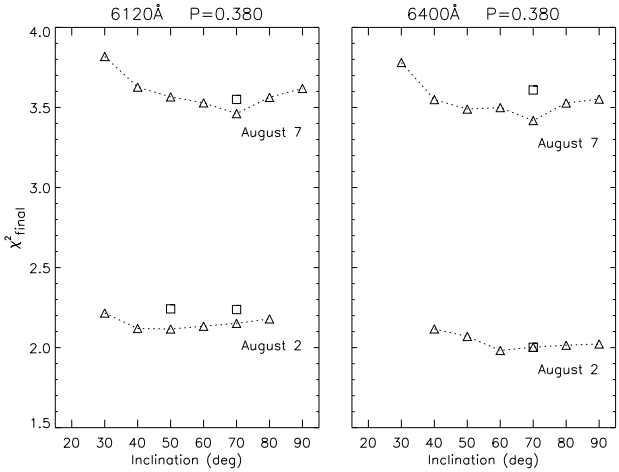

Figure 7.20: Quality of CLDI line profile fits $\chi^2_{\rm final}$ for different datasets of HD197890 as a function of the adopted inclination of the reconstruction star. The wavelength range and adopted reconstruction period (in days) is given above each plot, the observation date corresponding to each graph is annotated. Triangles indicate CLDI-$\mathtt{RM}_{0.5}$ reconstructions, actually used for the inclination determination. Squares indicate some corresponding CLDI-$\mathtt{RM}\times\mathtt{TSA}$ reconstructions plotted for comparison.

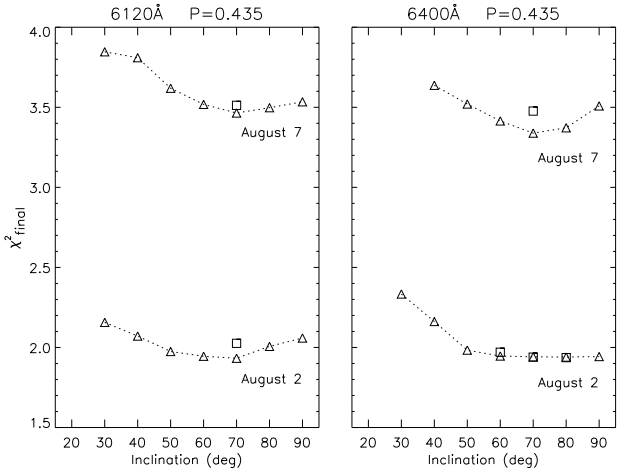

Figure 7.21: Companion to Fig. 7.20, but for an adopted rotation period of 0.435 days.

[27] Several of those ill-fitted phase intervals appear close to (and inside) the phase-overlap ranges of the start and end of each August 2002 night. This suggests that the inclination determination based on DI line profile fit quality may be hampered by intrinsic evolution of the spot pattern during one rotation. However, as discussed in Section 7.8.3 this issue remains presently unsettled.

Rotation period

As discussed in Section 5.5.6, adopting different rotation periods for the DI reconstruction may have a pronounced influence on the resulting Doppler images. As also discussed there, the effects of an incorrectly adopted period are primarily a "regular" transformation in longitude and latitude, if (a) only line profiles of the same stellar rotation are used for a single DI and (b) the period deviation is sufficiently small to avoid intrinsic inconsistencies of the profile time series. An example of such a (mostly) "regular" transformation can be seen by comparing the maps of Figure 7.15 to those of Figure 7.13.

As a result, different Doppler images meeting the above requirements (a) and (b) can be compared with meaningful results, if reconstructed for the same adopted rotation period (even if this has substantial uncertainties). The reason is that the distortions due to a potentially wrong rotation period affect both images in the same way.

Requirement (a) is obviously met by the presented August 2002 images of HD197890. The line profile fit quality of the DI-reconstructions does not significantly depend on which of the two considered rotation periods is adopted (see Figures 7.20 and 7.21). This indicates that the presented images also fulfil requirement (b), because intrinsic inconsistencies of the profile time series would reduce the profile fit quality.

7.6 Surface comparison by cross-correlation

Assuming that small-scale spot patterns are sufficiently long-lived, surface differential rotation simply shears the large-scale pattern formed by the spots. In that case, given two maps of the spot pattern at different times, a simple procedure can be applied to measure the shear as a function of latitude: Cross-correlating corresponding "constant-latitude slices" (Donati & Collier Cameron) of the two images. This technique has been successfully applied to the ultrafast rotator AB Dor (Donati & Collier Cameron, 1997a)

The algorithm used here, referred to as "surface cross-correlation", is described in the following. It consists of three steps: (i) Mapping each surface on a rectangular grid, (ii) optionally smoothing these rectangular maps and (iii) measuring the congruence of corresponding iso-latitude slices in these maps as a function of relative shift.

A sample application of steps (i) and (ii) can be seen in the upper map of Figure 7.22. Although step (i) is not strictly necessary, it facilitates the subsequent steps, because the longitude resolution of the resulting rectangular grid is independent of latitude, which is not the case for the surface discretization used by CLDI (Section 5.4.1). The resulting maps are sometimes called Pseudo-Mercator projections.[28] For the Pseudo-Mercator maps used in the following, the latitude resolution was chosen to be the same as the latitude intervals of the original surface discretization (4.5°). The spot pattern at each latitude is described by a vector, called iso-latitude vector here.

The necessity for step (ii) arises if the latitude resolution of the Pseudo-Mercator map significantly exceeds the latitude resolution of the original CLDI reconstruction. In that case, surface features are (quite) randomly distributed over neighbouring iso-latitude vectors, since the CLDI images are not smoothed themselves by any regularization. Since step (iii) only correlates iso-latitude vectors at *exactly* equal latitudes, this random latitude-smearing reduces the cross-correlation contrast; a smoothing during step (ii) improves that contrast. The effect of such a smoothing can be seen in Figure 7.18.

The smoothing kernel chosen here is a boxcar extending 13.5° in latitude and 9° in longitude, which roughly corresponds to the surface resolution of the CLDI images (Section 7.5.1). Actually, the effect of smoothing in longitude on the correlation results is very small, as long as the smoothing kernel does not get larger than the "typical"

[28] A "proper" Mercator projection is a projection of the sphere onto a cylinder. In that case, equal latitude intervals are not equidistant on the map.

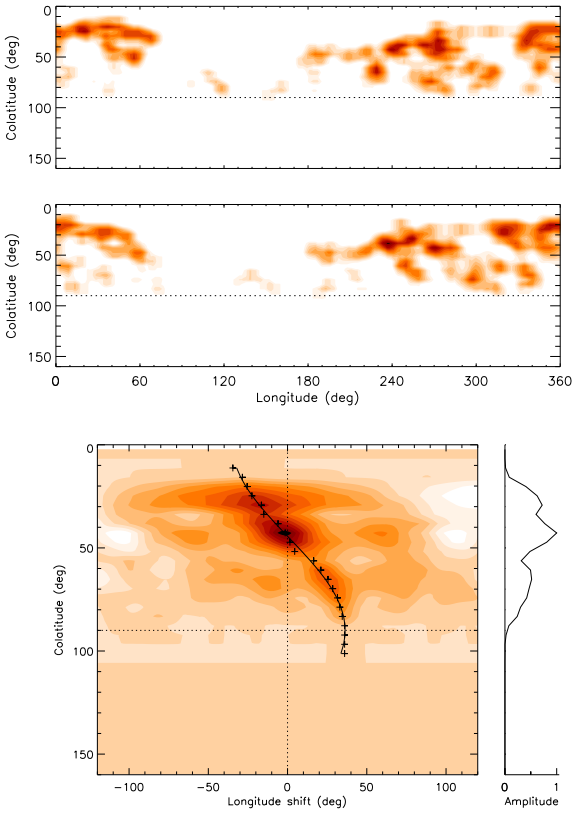

Figure 7.22: Artificially sheared spot pattern and cross-correlation plot: The upper Pseudo-Mercator map shows the August 2 "6120 Å" image of HD197890 (adopting P=0.435 days); it is the same image as the corresponding map of Fig. 7.13, but smoothed with a boxcar (9° longitude × 13.5° latitude) to approximately mimic the estimated resolution. This upper map has been sheared according to a $\cos^2(\theta)$ differential rotation law to produce the lower map. The amplitude of the longitude shear is 72° (equator relative to pole), its direction and strength result from a solar-like (α=0.2, faster rotation at the equator) differential rotation during one equatorial rotation. The cross-correlation function of the two maps is shown below, the maximum for each latitude is marked by a plus. A $\cos^2(\theta)$ function has been fitted to these maxima, it is represented by the smooth graph and measures the actual shear with only about one degree error.

longitude extension of the spots; this is due to the averaging already included in the (discrete) correlation integral. However, for visual inspection of the Pseudo-Mercator maps the smoothing in longitude is helpful, because the eye is not distracted by small-scale pixel structure.

Step (iii) computes the actual correlation. Correlation integrals, closely related to convolutions, are used e.g. in time-series analysis (Press et al., 1992)

$$\mathtt{Corr}(g,h) = \int_{-\infty}^{\infty} g(t+\tau)\, h(\tau)\, d\tau$$

If h is a replica of g, but delayed by a time interval Δt, the correlation $\mathtt{Corr}(g,h)$ yields the autocorrelation function of g, shifted in time by Δt. In practice it means that $\mathtt{Corr}(g,h)$ has a well-defined maximum at $t = \Delta t$, to the degree that different parts of g are distinguishable.

The situation of two identical spot patterns at a given latitude, shifted by an angle $\Delta\varphi$ is completely analogous. The only difference is that the above integral only extends from 0° to 360° in longitude, because of the rotational symmetry.[29] It is useful to keep the role of the autocorrelation in mind: The surface correlation can only yield results to the extent the surfaces show well-defined characteristics.

Although not strictly an *auto*correlation function, the lower panel of Figure 7.18 is well-suited to judge the maximum attainable resolution of the cross-correlation for the given maps of HD197890: In principle, it also to some degree incorporates reconstruction uncertainties due to different wavelength intervals.

In practice (as confirmed by tests) it is very similar to the true autocorrelation functions. Its main characteristics are the maximum amplitude at mid-latitudes, falling off towards pole and equator. This is caused by the concentration of well-defined spots at these latitudes. The increasing longitude extension of the autocorrelation maxima towards the pole is due to the corresponding decrease of resolution of the input Doppler images.

7.7 Computation and interpretation of lightcurves from Doppler images

The DI-lightcurves are computed from the visibilities and spot-filling-factors of the surface elements at each phase, the limb-darkening (which has little influence on the qualitative behaviour of the lightcurve) and the continuum flux difference (contrast) between the spotted and undisturbed surface.[30]

As a result, (a) the offset of the DI-lightcurves is undetermined and (b) they are not corrected for any standard magnitude system (e.g. Johnson-V). To measure the true brightness contrasts on the stellar surface, additional information would be needed, e.g. from multi-colour photometry. Such an analysis has not been performed in the context of this thesis.

For better comparison with the photometrically observed lightcurves, the DI-lightcurves are shifted by an arbitrary constant offset of 9.32 magnitudes. No effort has been made to "tune" the reconstruction parameters in order to adjust the amplitude of the DI-lightcurves.

Comparing DI-lightcurves to photometry

An extensive sample of DI-lightcurves and (quasi) simultaneous photometry can be found in Vogt et al. (1999). Their apparently successful procedure to make their Doppler images and photometric lightcurves agree consists of "thresholding" the raw images (i.e. successively removing mostly low-latitude spots of low contrast from the continuous spot temperature images) until their DI-lightcurve shows an improved agreement with the photometry. In some cases this produces quite massively modified reconstructions (e.g. their Figs. 29-34). In singular cases (e.g. their Figs. 39-42) they additionally introduce a "hot spot", i.e. a surface region warmer than the surrounding photosphere.

Many of Vogt et al.'s observations also "suffer" from not strictly simultaneous photometry and the questions of surface feature lifetime they bring about (a remarkable example of apparent surface reconfiguration on their object HR1099 during two months is shown in their Figure 56).

However, the DI-lightcurve uncertainties and their remedies by Vogt et al. do not seem directly analogous to the case of HD197890 in this work. The major difference is that their Doppler images are based on much sparser phase sampling. This leads to latitude uncertainties of the DI reconstruction and results in a spreading

[29] Given two N-element iso-latitude vectors $\mathbf{a}$ and $\mathbf{b}$ from the surfaces to be compared, sampled at a longitude resolution $\Delta\varphi$, the cross-correlation as a function of latitude shift $s \cdot \Delta\varphi$ can be calculated from

$$\mathtt{Corr}(\mathbf{a},\mathbf{b})(s) = \sum_{j=1}^{N} \mathbf{a}_j \cdot \mathbf{b}_{((j+s)\, mod\, N)}$$

Here, the index of $\mathbf{b}$ accomplishes the "cyclic permutation" of its elements by s positions.

[30] The brightness m (in magnitudes) at a given phase is computed from

$$m - m_0 = -2.5 \cdot \log_{10} \sum_j vis_j \cdot (\sigma_j \cdot \mathcal{F}_{\mathsf{spot}} + (1-\sigma_j) \cdot \mathcal{F}_{\mathsf{nospot}})$$

where the sum extends over all visible surface elements. For each each surface element, the visibility measure includes limb darkening and σ represents the spot-filling factor of each element. The reference brightness m_0 is chosen such that $m = 0$ corresponds to a completely unspotted surface.

of surface features in latitude, as well as their concentration on longitudes corresponding to the observed rotation phases ("phase ghosting", cf. also Stout-Batalha & Vogt, 1999, Secs. 4.3-4.4).[31]

Summing up, a rotationally modulated lightcurve reacts sensitively to features misplaced *in longitude*. As discussed above, sparse phase sampling leads to longitude (and latitude) uncertainties of Doppler images, including spots systematically concentrated on subobserver longitudes. These reconstruction uncertainties may significantly distort the resulting DI-lightcurve.

Given the dense phase sampling of the presented Doppler images of HD197890, these reconstruction uncertainties should be small (and have been shown to be). Consequently the qualitative behaviour of the resulting DI-lightcurves should be quite reliable.

[31] This phase ghosting is possibly related to their maximum entropy DI code making use of the response matrix for the image reconstruction (Section 4.3.1). At least the CLDI "backprojection" using the transpose of the response matrix does concentrate spots on the subobserver longitudes of observed phases, as can be inferred from the discussion of Section 5.2.1.

7.8 Observed spot evolution on Speedy Mic

The following sections discuss different "rotation scenarios" for HD197890 based on the August 2002 observations. These scenarios result from adopting the different rotation periods P_0=0.380 days and $P_{\rm alt}$=0.435 days given in Table 7.4. The discussions of Sections 7.8.1 and 7.8.2 are based on adopting $P_{\rm alt}$, tentatively inferred from the August 2002 photometry. Finally, Section 7.8.3 combines the results of the preceding discussions and outlines the construction of a "most convincing" rotation scenario for HD197890.

7.8.1 Lightcurve comparison for P=0.435 days

Figure 7.23 shows the lightcurves computed from the Doppler images of Figures 7.13 and 7.14. For comparing the lightcurves to the corresponding Doppler images, keep in mind that rotation takes place with *decreasing* sub-observer latitude, with the longitude 0° passing below the observer at zero phase.

The DI-lightcurves belonging to the August 2 spectra (JD 2440000+12488) agree quite well between the two wavelength regions. On the other hand, the August 7 DI-lightcurves of the two wavelength regions (JD 2440000+12493) show much less qualitative agreement. Looking at the "6120 Å" and "6400 Å" images of August 7 (right panels of Figures 7.13 and 7.14), this disagreement is surprising at first, because *qualitatively* the maps agree quite well. Closer inspection shows that the disagreement of the lightcurves is mainly caused by the "spread-out" spotted regions of the images (longitudes $0° \lesssim \varphi \lesssim 180°$, corresponding to the phase range $0.5 \lesssim \phi \lesssim 1$). These "spread-out" regions exhibit higher spot filling factors in the "6400 Å" images, compared to the "6120 Å" images.

A "second" comparison of the August 7 DI-lightcurves of the "6120 Å" and "6400 Å" Doppler images does reveal similarities: The local brightness maxima at about phase 0.5 (closer to 0.4 in the "6400 Å" DI-lightcurve) and 0.9 (due to the "spot gap" around 0° longitude, common to both August 7 images), as well as the corresponding brightness minima. However, the amplitudes of those features are different for the two August 7 DI-lightcurves.

As Figure 7.24 shows, the *qualitative* behaviour of the "6120 Å" DI-lightcurves is similar to observed changes of HD197890's lightcurve when folded with the period $P_{\rm alt}$.

In the context of the discussion of individual properties of the two wavelength regions (Section 6.5), it would

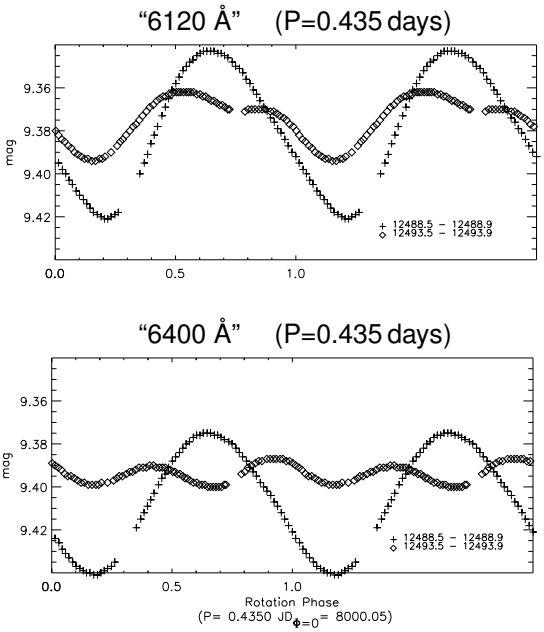

Figure 7.23: Lightcurves computed from CLDI reconstructions of two different wavelength regions, adopting a rotation period of 0.435 days. Different symbols represent the August 2 (+) and August 7 (◇) reconstructions. The lightcurves are computed from the surfaces shown in Figs. 7.13 and 7.14, respectively. The annotation dates are JD-2440000.

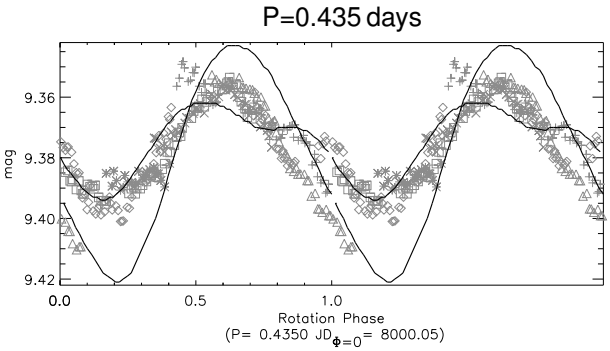

Figure 7.24: Comparison of observed lightcurves and lightcurves of CLDI reconstructions. The observed data are the same as in Fig. 7.7, using the same symbols; note the slightly different folding period. The CLDI reconstruction lightcurves are represented by the continuous curves, they are the same as in the "6120 Å" panel of Fig. 7.23.

be unexpected if the "6120 Å" region were much more reliable concerning the lightcurve. Unfortunately, the available August 2002 photometry does not allow to settle this question. The photometric lightcurve of HD197890 strongly suggests significant changes on timescales of a few rotations and *strictly simultaneous* photometry to the presented Doppler images is not available.[32]

7.8.2 Spot evolution adopting P=0.435 days

Already a short glance at Figures 7.13 and 7.14, comparing the August 2 and August 7 images, reveals substantial differences of the spots patterns. The discussions of the preceding sections strongly suggest, that the images are reliable down to a scale of about $10^\circ \times 10^\circ$on the surface. That means, that massive reconfigurations of spots must have taken place on HD197890 during the roughly 12 stellar rotations having passed between the images.

Although this is an interesting result in itself, it severely limits the chances of observing signatures of differential rotation shear by comparing the images. However, an attempt is made in the following.

The Pseudo-Mercator maps of the "main" August 2002 Doppler images of HD197890 are shown in Figure 7.25. Showing the same images as Figures 7.13 and 7.14, they confirm the above mentioned substantial reconfigurations of spots. All images show concentrations of spots around $\varphi \approx 300^\circ$ longitude. However, this main spot group exhibits massive differences between the August 2 and August 7 images: Apparently, the longitude extension is reduced and the quite well-defined unspotted gap of the August 2 images, around $\varphi \approx 320^\circ$, can no longer be identified in their August 7 counterparts.

Subjectively, maybe the most tempting "common" feature for identification is the "S"-shaped feature (with the lowest S-part missing) appearing most distinct in the "6400 Å" August 7 image, centered at a longitude of $\varphi \approx 320^\circ$. A similar feature appears in the August 2 images, centered at $\varphi \approx 290^\circ$. Unfortunately, no other distinct features support this simple shift of about 30° in longitude between the August 2 and August 7 images.[33]

[32] As Figure 7.2 illustrates, the "lightcurve" of the spectrograph exposure meter is not helpful in this context. While for stable photometric observing conditions it may have contributed some information, for the given data it is clearly dominated by seeing and transmission variations.
At least for the time span of the August 2 observations it does show that no strong flare has occurred on HD197890.

[33] Assuming a rigid rotation of the spot pattern, such a relatively small shift in longitude could be caused by a slightly wrong rotation period adopted for the reconstruction.

Table 7.5: Shear function parameters φ_s and φ_0, determined from the "6120 Å" cross-correlation function of the P=0.435 days DI reconstructions (Fig. 7.26). The resulting differential rotation parameters are calculated below, the corresponding results for the "6400 Å" correlation function differ by less than 2% from the values given here. The symbols are defined in the text.

φ_s	332	deg
φ_0	34	deg
$\Delta\Omega$	66	deg/day
$\Omega^{(corr)}$	834	deg/day
$\Omega_\mathsf{eq}^{(corr)}$	867	deg/day
α	0.08 ± 0.02	
P_eq	0.42	days
P_pole	0.45	days

Differential rotation and cross-correlation

A *simulated case* of differential rotation shear is shown in Figure 7.22. The correlation function for this synthetic example is simply a sheared version of the autocorrelation function discussed above. Obviously, this is a highly idealized case: In the real case, intrinsic changes of the spot pattern, DI reconstruction artefacts and limited resolution will cause deviations. In addition, as outlined in Section 2.2.2, a differential rotation law substantially differing from the (close to solar) $\cos^2(\theta)$-law should be kept in mind as a possibility.

The cross-correlation functions comparing the August 2 and August 7 images of HD197890 for a period of P_alt are shown in Figure 7.26. The shearing-functions fitted to the correlation maxima at each colatitude θ are defined as

$$\Delta\varphi(\theta) = \varphi_\mathsf{s} \cdot \left(\frac{1}{2} - \cos^2(\theta)\right) + \varphi_0 \qquad (7.9)$$

where φ_s describes the shear amplitude of the equator, relative to the poles, φ_0 a "rigid" turn. A positive φ_s means that the equator rotates faster than the poles. The term "$\frac{1}{2}$" causes the $\pm 45^\circ$-latitudes to be unaffected by the shear.[34]

The shear parameters fitted to the shown cross-correlation functions are $\varphi_\mathsf{s} = 332^\circ$, $\varphi_0 = 34^\circ$ ("6120 Å") and $\varphi_\mathsf{s} = 342^\circ$, $\varphi_0 = 57^\circ$ ("6400 Å").

[34] This convention means that the rotation period adopted for the DI-reconstructions is *not* the equatorial rotation period, but the period at the latitudes $\pm 45^\circ$.
This definition is motivated by (a) mid-latitudes being systematically more reliable in Doppler images, compared to equatorial latitudes and (b) their usually dominating influence on the lightcurve for high or intermediate stellar inclinations.

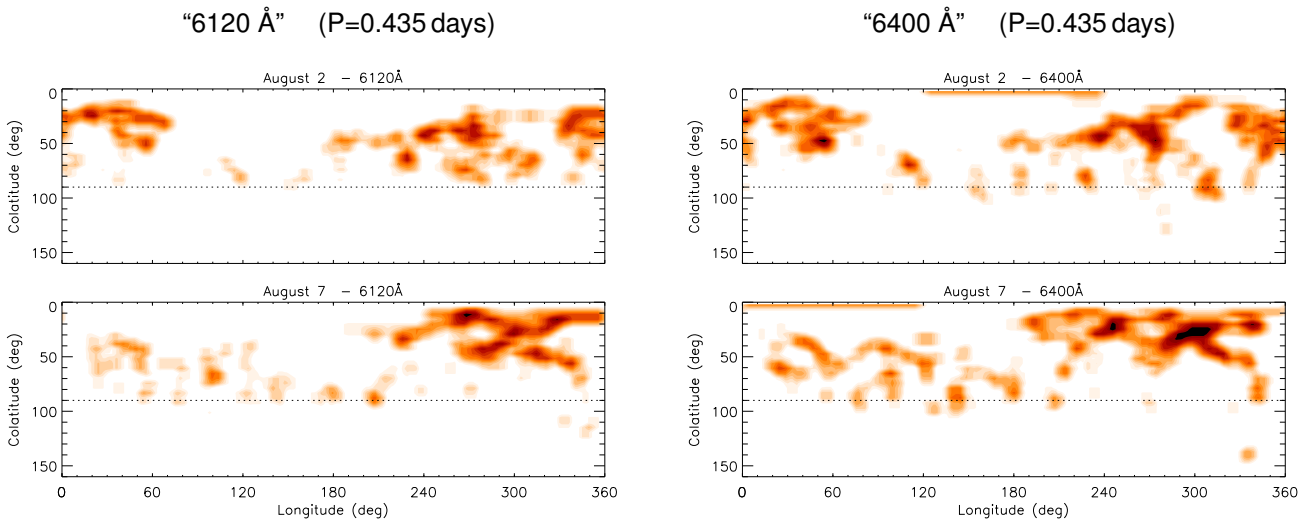

Figure 7.25: Spot pattern evolution on HD197890 during about 11.5 rotations, adopting a rotation period of 0.435 days: Pseudo-Mercator projections of the August 2 and August 7 Doppler images reconstructed from the given wavelength ranges. The images are the same as in Figs.7.13 and 7.14, smoothed with a boxcar (9° longitude x 13.5° latitude) to approximately mimic the estimated resolution of the reconstructions.

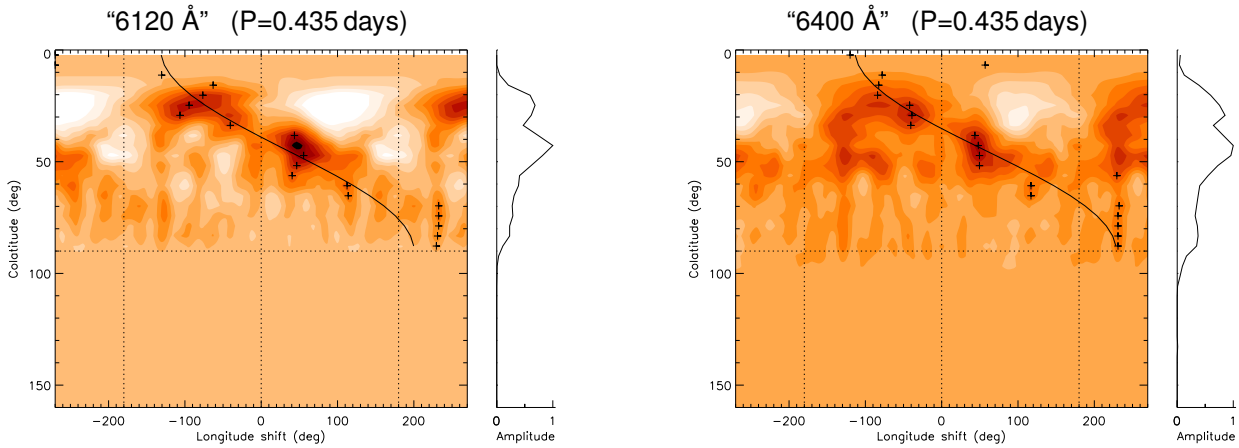

Figure 7.26: Cross-correlation of corresponding latitudes, comparing the August 2 and August 7 maps of Fig. 7.25. The maximum correlation at each latitude is marked by a plus; the smooth graphs are $\Delta\varphi(\theta)$-shear-laws (Eq. 7.9) fitted to these maxima, modelling a shear by differential rotation, (see text for details).

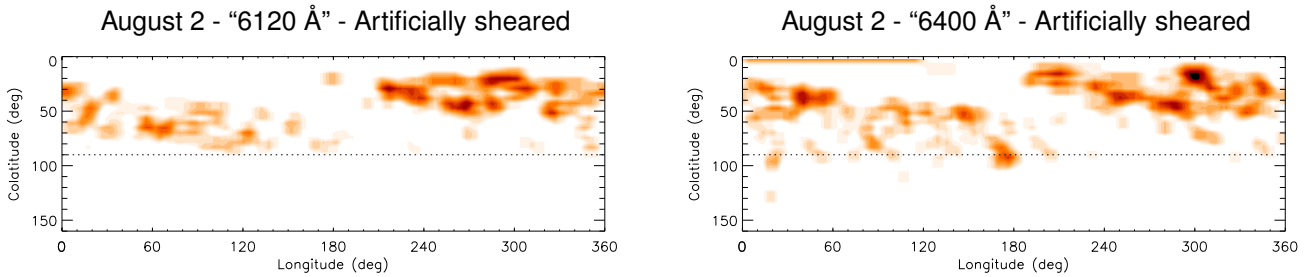

Figure 7.27: Artificially sheared August 2 Doppler images from Fig. 7.25. The maps have been sheared (and shifted in longitude), according to the shearing-laws fitted to the cross-correlation functions, shown in Fig. 7.26. If these shearing-laws were strictly correct and the only spot pattern evolution mechanism, these artificially transformed maps would be identical to the August 7 maps. Although this is not the case, the large-scale appearance of the maps is similar.

As Figure 7.27 illustrates, the fitted shear functions do reflect a conceivable large-scale transformation of the compared images; it shows the August 2 images artificially sheared by the fitted functions $\Delta\varphi(\theta)$. If these shearing-laws were strictly correct and no other evolution processes present, these artificially transformed maps would be identical to the August 7 maps. Actually, the large-scale spot distributions of the maps are quite similar, while the small- and medium-scale structures differ completely. However, even in the ideal case of a completely known shearing law, such differences would be present due to intrinsic spot evolution, keeping in mind that about 12 rotations lie between the images.

A calculation of the differential rotation parameters resulting from the fitted shear functions is carried out in Table 7.5. The equator-pole difference in angular velocity is calculated from $\Delta\Omega = \frac{\varphi_s}{\Delta t}$, where Δt is the average time interval between the observation of the two compared images.[35]

The angular velocity $\bar{\Omega} = 360^\circ/0.435\,\mathrm{days}$ $= 828\,\mathrm{deg/day}$ used for the DI reconstructions has been corrected for this calculation, according to the measured longitude shift between the compared images:

$$\Omega^{(corr)} = \bar{\Omega} + \frac{\varphi_0}{\Delta\, t}$$

Here, this correction amounts to about 1%; it has been carried out for the sake of completeness only.

Since the used shear Function 7.9 leaves the latitudes $\pm 45^\circ$ unchanged, $\bar{\Omega}^{(corr)}$ represents the angular velocity at these latitudes. The equatorial angular velocity can be computed from

$$\Omega_{\mathsf{eq}}^{(corr)} = \Omega^{(corr)} + \frac{\Delta\Omega}{2}$$

Finally, the differential rotation parameter α (Definition 2.6) is computed from

$$\alpha = \frac{\Delta\Omega}{\Omega_{\mathsf{eq}}^{(corr)}}$$

The main error sources entering the preceding calculation are the uncertainty in the measured φ_s and the error caused by adopting a constant "average" $\Delta\, t$.

A precise error estimation of φ_s is difficult, it could at best be estimated from a Monte-Carlo simulation trying to incorporate the DI reconstruction uncertainties. Such an attempt has not been made here; to be truly significant, such a simulation should set out with generating artificially "disturbed" (by noise, possibly e.g. by tentative reduction errors or sLSD template spectrum deficiencies). Only in this way the presumably relevant errors introduced by the line profile deconvolution *and* by CLDI could be taken into account.

Instead, the uncertainty in φ_s is estimated to be about $\pm 60^\circ$. This rather large uncertainty results from the ill-defined shear near the pole and the equator, as well as from the extended mid-latitude maxima of the cross-correlation function. This results in an uncertainty in $\Delta\Omega$ of roughly $\frac{60^\circ}{360^\circ} \approx 20\%$.

The error introduced by the average $\Delta\, t$ has been estimated above to result in about 5% error in the determined angular velocities. Together with the error in $\Delta\Omega$, this leads to the given error estimate of α.

7.8.3 Solving the "two-period-puzzle"

As discussed in Section 7.3, assuming nearly rigid rotation, the rotation period determined from the August 2002 photometry ($P_{\mathrm{alt}} = 0.44^{+0.04}_{-0.03}$ days) is not compatible with the rotation period of $P_0 = 0.380 \pm 0.004$ days, observed for HD197890 at other epochs. This situation is referred to as the "two-period-puzzle" here.

Three different tentative solutions to this puzzle are discussed in the following:

- **(i)** Differential rotation strong enough to yield both rotation periods P_0 and P_{alt} at different latitudes of the surface at the same time.
- **(ii)** Moderate differential rotation of the strength estimated in Section 7.8.2, qualitatively yielding the observed August 2002 lightcurve.
- **(iii)** Approximately rigid rotation accompanied by a substantial intermediate-scale reconfiguration of spots during the 5 days observation time span of August 2002.

The discussion of scenarios (i) and (ii) is based on the results of Section 7.8.2. It is assumed that the intermediate-scale spot patterns "survive" the massive large-scale shear effected by the differential rotation during the 5 days observation time span of August 2002. This assumption is necessary for the surface cross-correlation to yield significant results.

Scenarios (i) and (ii) are in a way attractive to solve the two-period puzzle. While (ii) could be supported by the August 2002 Doppler images, scenario (i) can be excluded, as shown below. As also discussed below, *both* scenarios are not in accord with the August 2002 photometry.

This situation leaves scenario (iii) as the most consistent solution. However, it comes at the price of assuming

[35] Actually $\Delta\, t$ is different for different longitudes of the compared Doppler maps. The reason is that $\Delta\, t$, strictly speaking, is the time interval between the observation of the line profile deformations leading to the spots at the compared longitude.
However, a constant Δt =5.0 days has been used for the following calculations, this introduces an error below half a rotation period here, i.e. a relative error below about $\frac{0.2\ \mathrm{days}}{5\ \mathrm{days}} = 5\%$.

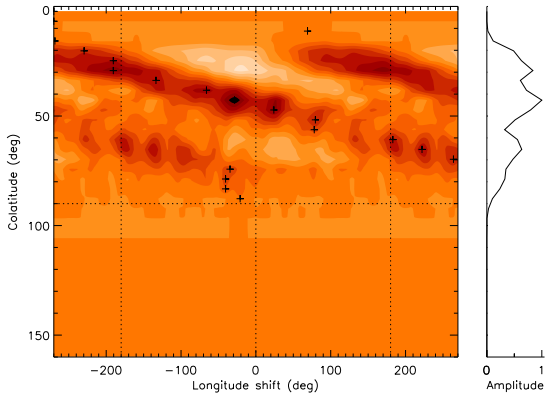

Figure 7.28: Simulated example of the equator nearly twice lapping the pole: Cross-correlation function comparing the "6120 Å" August 2 Doppler image and a copy of it, artificially sheared with an amplitude of $\varphi_s = 690°$, using the shear function of Equation 7.9.

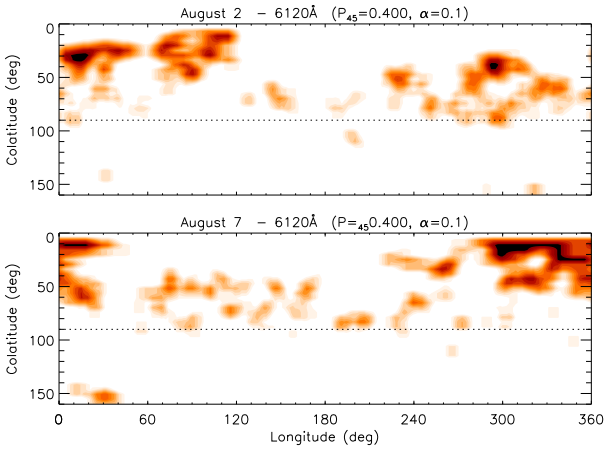

Figure 7.29: Same as Fig. 7.25, but adopting a moderately strong solar-like differential rotation (α=0.1) for the CLDI reconstruction. The adopted mid-latitude rotation period at latitudes of $\pm 45°$ is P_{45}=0.400 days, resulting in an equatorial and polar rotation period of 0.38 days and 0.42 days, respectively.

a markedly unperiodic lightcurve for HD197890 during the observed time span covering 2002 August 2-7.

(i) Strong differential rotation

Although compatible with a moderately strong differential rotation of $\alpha = 0.08 \pm 0.02$, the Doppler images do not support a differential rotation permitting the simultaneous presence of both rotation periods. This is demonstrated below.

Simultaneously producing both rotation periods would require a differential rotation with $\alpha \gtrsim \frac{0.06}{0.44} \approx 0.15$, corresponding to an equator-pole difference in angular velocity of

$$\begin{aligned} \Delta\Omega &= \alpha \cdot \Omega_{\mathsf{eq}} \approx 0.15 \cdot 850 \text{ deg/day} \\ &\approx 130 \text{ deg/day} \end{aligned}$$

At such a strong differential rotation, the equator would "safely" lap the regions close to the poles during the 5 days interval between the Doppler images of August 2002. However, the cross-correlation functions discussed above do not show any signatures of such a lapping, which would "twist" the surface pattern in a characteristic way. A simulated case of surface twisting by the equator nearly twice lapping the polar regions is shown in Figure 7.28; clearly that surface cross-correlation pattern bears no resemblance to the observed cross-correlation (Figure 7.26).

(ii) Moderate differential rotation

The following scenario is intended as a very simple realization of the tentative differential rotation of $\alpha = 0.08 \pm 0.02$ determined above, assuming the complete absence of other spot pattern evolution. It should be kept in mind that the latter simplification would presumably be at best a rough approximation to reality.

Figure 7.29 shows two Doppler images of HD197890, reconstructed with the same parameters as the other reconstructions of this chapter (Table 7.4), but adopting a differential rotation with $\alpha = 0.1$. This is chosen at the upper end of the above error range of α to increase the effect of differential rotation on the simulation.[36]
The adopted differential rotation law is

$$\Delta\Omega(\theta) = \Omega_{45} + \alpha \cdot \left(\frac{1}{2} - \cos^2(\theta)\right) \quad , \qquad (7.10)$$

describing the angular velocity Ω as a function of colatitude θ. This definition corresponds to the shear function defined in Equation 7.9, here Ω_{45} represents the angular velocity at colatitudes 45° and 135° (corresponding to the latitudes $\pm 45°$).
The adopted period for the reconstructions is

$$P_{45} = \frac{2\pi}{\Omega_{45}} = 0.40 \text{ days}$$

which yields P_{eq}=0.38 days and P_{pole}=0.42 days for the equator and "polar" rotation period, respectively.

Comparing the differential rotation CLDI reconstructions of Figure 7.29 with their rigid rotation counterparts in Figure 7.25 shows that the influence of the adopted differential rotation on the images is is limited, although easily visible (keeping in mind the longitude shifts between

[36] As outlined in Section 5.5.6, CLDI currently only takes the surface shear due to differential rotation into account, without modelling the influence on the overall line profile shape. As also outlined there, this has presumably only a small influence on the reconstruction at a "moderate" differential rotation with $\alpha \lesssim 0.1$.

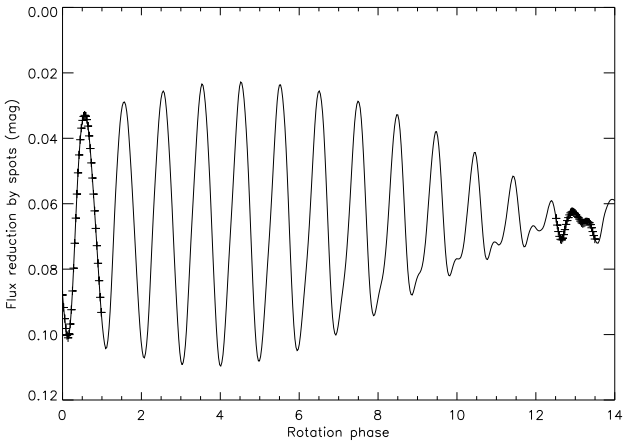

Figure 7.30: Simulated lightcurve spanning the whole 2002 August observation time span, the August 2 and August 7 observation intervals are marked by plusses. The lightcurve was computed from the August 2 surface of Fig. 7.29 differentially rotating with an α of 0.1 and a mid-latitude rotation period of P_{45}=0.40 days.

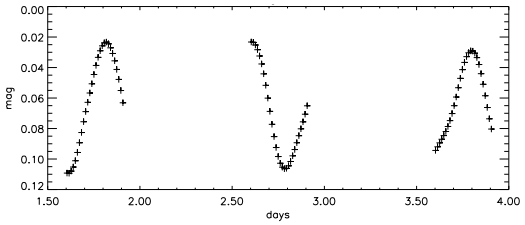

Figure 7.31: Lightcurve subintervals sampled from the artificial lightcurve of Fig. 7.30. The shown sampling simulates three consecutive observing nights of 8 hours duration each, approximately corresponding to the 2002 August 3-5 photometric observations. The covered timespan extends from approximately rotation phase four to ten in Fig. 7.30.

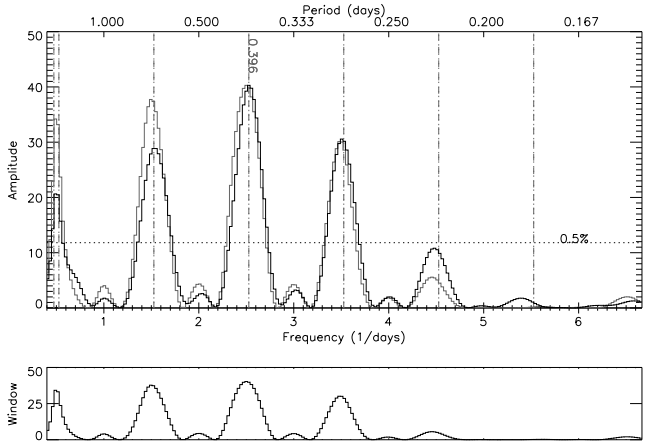

Figure 7.32: Periodogram (black curve) of the sampled simulated lightcurve of Fig. 7.31. Aliases due to the one day-periodic observation window are marked by dashed lines. The period of the maximum peak is annotated. The lower panel and the gray curve show the response to a sine of period 0.400 days.

the compared maps due to the resulting different rotation phase conventions). These relatively small changes are in accord with what is expected from the discussion of Section 5.5.6. As a result, the surface cross-correlation function comparing both images of Figure 7.29 looks pretty much the same as those of Figure 7.26 and is not shown here.

An unfolded lightcurve for this tentative differential rotation scenario is shown in Figure 7.30. It was calculated by continuously rotating the August 2 image of Figure 7.29 according to the surface rotation law of Equation 7.10, adopting α=0.1 and $\Omega_{45} = \frac{2\pi}{0.40 \text{ days}}$. It shows beats indicating that the lightcurve is dominated by two spot groups moving at different angular velocities and contributing to it with comparable amplitudes.

At first glance such beats could be in accord with the qualitative lightcurve behaviour shown by the DI-lightcurves of Figure 7.24 . However, a closer inspection shows that this is not the case: As Figure 7.3 shows, the *observed* night-to-night variations of the lightcurve amplitude during the 3 consecutive August 2002 nights are small (August 3-5, JD 2440000+ 12490.3 to 12492.6).[37]

Assuming, for the moment, the scenario of Figure 7.30 to be true, it suggests that the 3 consecutive August 2002 nights are located somewhere in the slowly varying portion of the unfolded lightcurve, surrounded by the spectroscopic observation nights of August 2 and August 7. This situation is tentatively realized by the sampling intervals shown in Figure 7.31.

The lightcurve intervals sampled in Figure 7.31 are dominated by a weakly modulated sine (the sampled maxima in the figure are located at about 1.8, 2.6 and 3.8 days and agree well with a period of 0.4 days). This is confirmed by the periodogram of Figure 7.32 which is clearly dominated by a peak close to 0.4 days and its 1-day observation window aliases.

The important point is that the lightcurve sampling of Figure 7.31 *does not at all mimic a larger rotation period* than the adopted mid-latitude period of P_{45}=0.40 days. However, such a mimicry would be needed to make the adopted scenario comply with the actual August 3-5 photometry and its periodogram (Figure 7.5) showing a peak at 0.44 days.

While to some degree arbitrary, this scenario seems to rule out that the spot pattern evolution observed by the *combined photometric and DI observations* is primarily effected by a moderately strong differential rotation with a strength of the order of $\alpha \approx 0.1$.[38] It is noted in pass-

[37] However, only 3 lightcurve extrema are completely sampled during August 3-5. Consequently, larger amplitude variations cannot be strictly ruled out.

[38] This remains valid for significant deviations from the $\cos^2$-rotation law of Equation 7.10, as long as the rotation law is "regular"

ing that this is an additional argument against the above scenario (i).

Summing up, the rotation parameters of scenario (ii) could qualitatively explain the observed large-scale spot evolution on HD197890 between the two Doppler images of August 2 and August 7. This is illustrated by Figure 7.27, assuming that the intermediate-scale spots survive the massive large-scale shearing. However, the lightcurve generated by such a scenario is not supported by the photometric observations of August 3-5.

(iii) First part: Approximately rigid rotation

Putting the August 3-5 photometry aside for a moment, we are left with two informations about the rotation period of HD197890 (Section 7.3.3): The only stable observed rotation period of HD197890 is P_0=0.380 days; however, there are time spans at least several days long when the lightcurve is not periodic, suggesting substantial changes of the surface spot pattern during these time spans.

Figures 7.33 and 7.34 offer "another" look at the CLDI reconstructions for a rotation period P_0 (the "6120 Å" images have already been shown on a rotated surface coordinate system in Figure 7.15). Comparing the August 2 and August 7 images, several spot groups appear to be recognizable in all images:

- A_0 A large irregularily shaped spotted area extending from about 120° to 240° in longitude and from about 30° up to above 60° in latitude.
- A_1 A smaller spot (group) centered slightly below 30° latitude and at about 290° longitude
- B An extended area sparsely covered with spots, centered close to 0° longitude and 30° latitude; its shape is reminiscent of a "λ"
- $\tilde{\mathsf{C}}_0$ A spot group extending from about 50° to 120° in longitude and from close to the equator to about 60° in latitude. In the August 2 images this group is far more pronounced, showing a separation in two distinct, apparently quite coherent groups.
- $\tilde{\mathsf{C}}_\mathsf{s}$ The small coherent southern spot only visible in the August 7 images at about 110° longitude and -25° latitude. It may be mirrored to the northern hemisphere in the August 2 images, appearing there as part of group $\tilde{\mathsf{C}}_0$.

Using the above terminology, the following evolution of the spot pattern appears to have taken place during the about $\frac{5}{0.380} = 13.2$ rotations lying between the August 2 and August 7 images: Group A_0 undergoes rather weak changes but is shifted in longitude by roughly 30°. Equivalently A_0 could be said to stay in place and fade at lower longitudes while growing at its high longitude side. Group A_1 appears to stay in place, getting connected to A_0. Group B remains largely unchanged, preserving its λ-shape and growing a weak "annex" to the north west at about 320° longitude and 45° latitude. Finally, most of group $\tilde{\mathsf{C}}_0$ disappears with possibly one component reappearing in the spot $\tilde{\mathsf{C}}_\mathsf{s}$.[39]

Summing up, the Doppler images reconstructed for the period P_0 show several features at a wide range of latitudes which appear to be recognizable at similar surface positions after about 13 rotations.[40]

For the following it needs to be kept in mind that for the convention adopted here, rotation takes place with *decreasing* sub-observer latitude, with the longitude 0° passing below the observer at zero phase. The apparent shift of group A_0 towards increasing longitudes (i.e. earlier rotation phases), combined with the near disappearance of group $\tilde{\mathsf{C}}_0$ at lower longitudes (i.e. later rotation phases) leads to a "darkening" at earlier phases and a "brightening" at later ones. As a result, the lightcurve minimum should be shifted to earlier phases when going from August 2 to August 7; this is indeed the case as shown in Figures 7.37 and 7.38.

in the sense that mid-latitudes rotate at some intermediate angular velocity between the equatorial and polar values. Given the two rotation periods of about 0.38 days and 0.44 days to be "explained" (assuming the reality of both), such a rotation law would lead to an intermediate rotation period of roughly 0.4 days, irrespective of its detailed characteristics. Since mid-latitudes dominate the lightcurve behaviour for the spot distributions of HD197890 shown by the August 2002 Doppler images, also the dominating period of the resulting lightcurve should be close to 0.4 days.

A few tentative anti-solar differential rotation cases (i.e. "slow equator") of moderate $\alpha \approx$-0.1 to -0.2 have also been tried. However, they lead to very poor convergence of CLDI, indicating that a $\cos^2$-rotation law (Equation 7.10) with significantly negative $\alpha \lesssim$-0.1 is not compatible with the observed line profile time series.

[39] The southern spot $\tilde{\mathsf{C}}_\mathsf{s}$ is intriguing, its "mirroring" to different hemispheres is particularly suggested by the pseudo-Mercator maps of Fig. 7.25. Whether it is really located on the southern hemisphere and only successfully reconstructed there in the August 7 images because of its isolation seems doubtful, but cannot be excluded. It is associated with the bump (sharply defined in the August 7 "6400 Å" time series of Fig. 6.13) passing the profile center at about phase $1 - \frac{110^\circ}{360^\circ} \approx 0.7$; its migrating counterparts can be seen clearly in about 12 profiles from phase 0.629 to 0.767.

In principle, the `RM×TSA` backprojections of CLDI, which are used here and make use of visibility information, can extract information about a spot's hemisphere from the profile time series.

Actually, this has not been the case for the synthetic tests described in Section 5.5, see especially Fig. 5.25. However, the phase sampling density of the August 7 time series of HD197890 (72 profiles) is more than twice the density of the best synthetic test cases (32 profiles). In addition, the spot $\tilde{\mathsf{C}}_\mathsf{s}$ is apparently very small which should augment its "hemispherical information" in the time series because of a well-defined visibility as a function of phase.

However, resolving this issue would need specific synthetic tests which have not been performed.

[40] At least subjectively, the amount of recognizable features is larger than for the 0.435 days-period reconstructions, where the only "striking" similarity is the "S"-shaped feature discussed in Section 7.8.2.

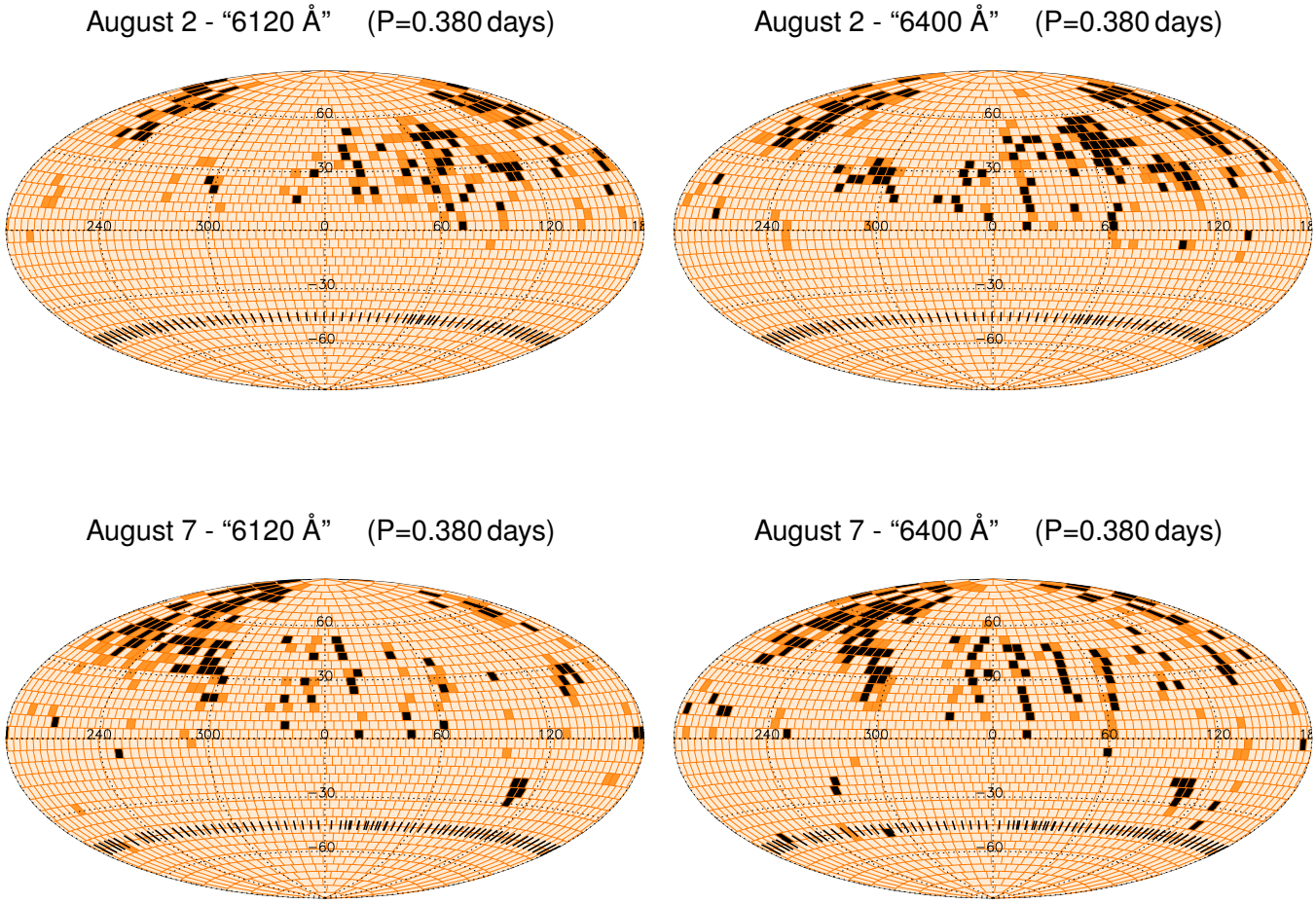

Figure 7.33: CLDI images of HD197890, reconstructed with an adopted rotation period of 0.380 days from line profiles extracted in the wavelength region given above each map (Figs. 6.12 and 6.13). The reconstruction parameters are summarized in Table 7.4. Subobserver longitudes of observed phases are marked by short lines. A rotation phase $\phi = 0$ corresponds to a subobserver longitude of $\varphi = 0° \hat{=} 360°$; rotation proceeds with *decreasing* subobserver longitude. Given the adopted rotation period, about 13 stellar rotations have passed between the two images. Companion to Figs. 7.13 and 7.14; it is **important** to note the differently arranged maps compared to those figures.

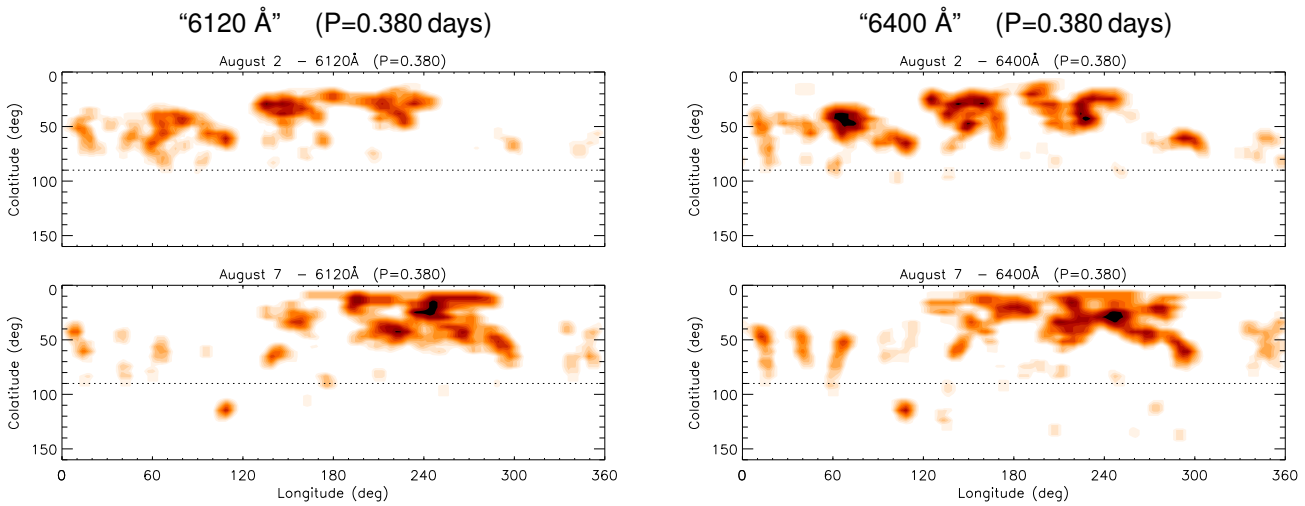

Figure 7.34: Spot pattern evolution on HD197890 during about 13 rotations, adopting a rotation period of 0.380 days: Pseudo-Mercator projections of the August 2 and August 7 Doppler images reconstructed from the given wavelength ranges. The images are the same as in Fig.7.33, smoothed with a boxcar (9° longitude × 13.5° latitude) to approximately mimic the estimated resolution of the reconstructions.

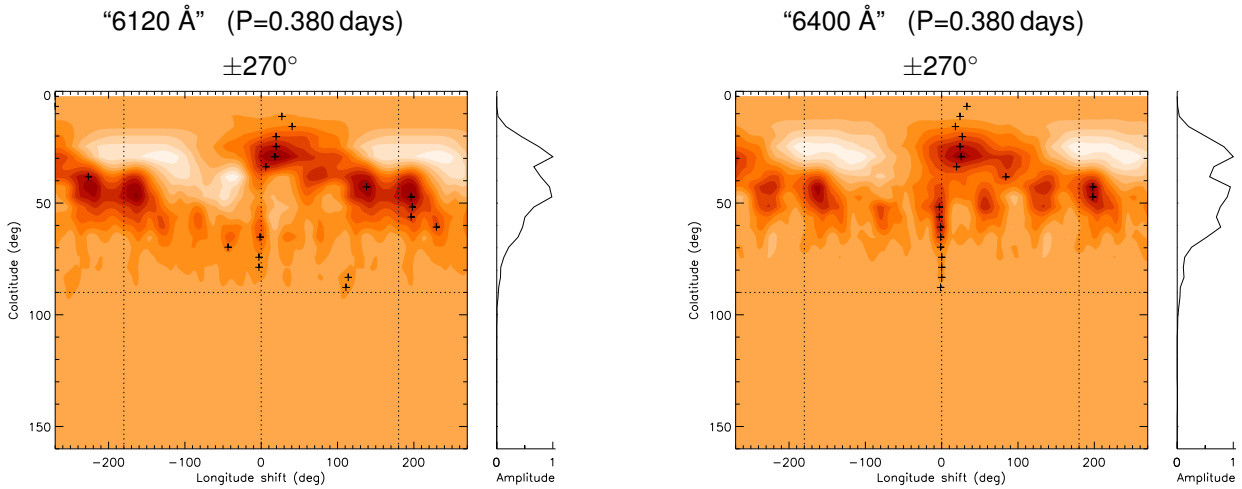

Figure 7.35: Cross-correlation of corresponding latitudes, comparing the August 2 and August 7 maps of Fig. 7.34. The maximum correlation at each latitude is marked by a plus.

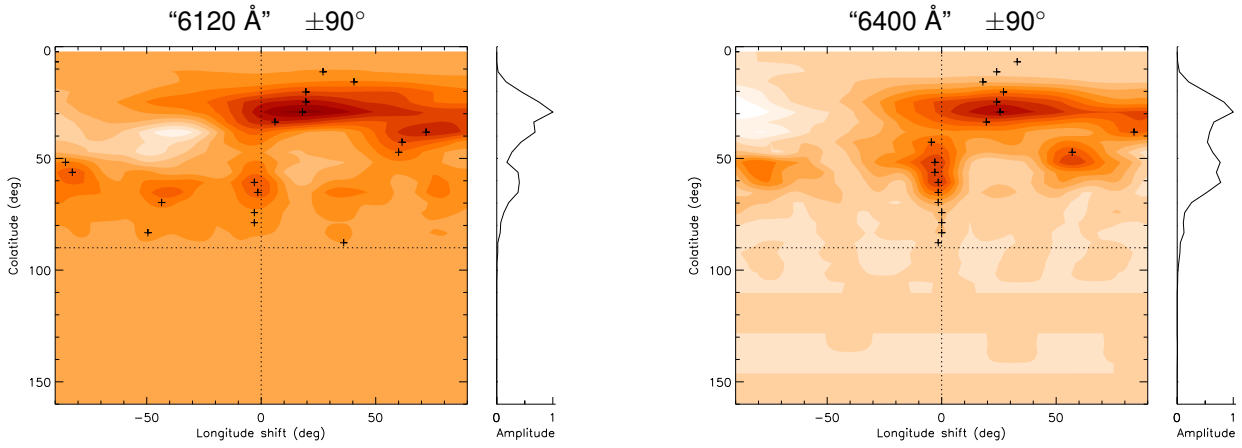

Figure 7.36: "Zoomed" view of Fig. 7.35 showing the cross correlation on a narrower angular range.

The DI-lightcurves of the two wavelength ranges agree much better than in the case of the reconstructions adopting the period $P_{\rm alt}$=0.435 days (Figure 7.23). This is a clue in favour of the correctness of the reconstruction period P_0.

As mentioned in Section 7.8.1, the "spread-out" weakly spotted regions of the August 7 images (named group B here) are difficult to reconstruct for DI. As also discussed there they significantly influence the resulting DI-lightcurve. While these reconstruction difficulties generally arise in Doppler images for irregularly shaped parts of the spot pattern (Section 5.5.4), an additional problem about group B arises for the August 7 images: It is located close to the *"phase overlap region"* of sub-observer longitudes assigned to phases observed at the start and the end of the August 7 night (these overlap regions are marked by the dense phase-ticks around 30° longitude in the August 7 maps of Figure 7.33).

In the light of the discussion of this section, the period $P_{\rm alt}$ is presumably wrong. In addition to the named general reconstruction difficulties, this phase overlap region is presumably poorly reconstructed adopting $P_{\rm alt}$ because of slight intrinsic inconsistencies of the line profile time series when phased with a wrong period (Section 5.5.6). This poor reconstruction would be accompanied by a reduced reliability of the resulting Doppler images which could be the reason for the poor agreement between the "6120 Å" and "6400 Å" DI-lightcurves of August 7 for the period $P_{\rm alt}$.

On the other hand, for the P_0-reconstructions (assuming the correctness of the period) the overlap region would be more reliably reconstructed due to the same reasons, leading to a better agreement of the "6120 Å" and "6400 Å" DI-lightcurves of August 7.

The remaining disagreement between the two DI-lightcurves, i.e. the "unnaturally" flat maximum of the "6400 Å" DI-lightcurve, may be caused by the mentioned general reconstruction difficulties for irregularily shaped spot groups. It could also be caused by intrinsic changes of the spot pattern between the start and the end of the observed rotation, again leading to reconstruction uncertainties in the overlap region.

(iii) Second part: Estimating the differential rotation strength

The intermediate to high latitude spot group A_0 is apparently shifted to larger longitudes (i.e. against the direction of rotation) by about 30°, while features closer to the equator (including group A_1) roughly seem to keep stationary. Already this "visual" inspection of the Doppler images of HD197890 leads to a *preliminary* estimate of the differential rotation strength during the about 13.2 rotations between them

$$|\alpha| \lesssim \left|\frac{-30^\circ}{13.2\cdot 360^\circ}\right| = 0.006 \qquad (7.11)$$
$$\left(\alpha \approx \frac{-30^\circ}{13.2\cdot 360^\circ} = -0.006\right)$$

Here Equation 2.9 was generalized to the given number of rotations and the minus sign indicates the anti-solar direction of the surface shear. Obviously, the lower "version" of Equation 7.11, stating anti-solar differential rotation, is more restrictive. Its validity depends on the interpretation of the behaviour of the spot group A_0: If it is considered as due to intrinsic spot evolution, only the upper "version" of Equation 7.11 applies; if its behaviour is attributed to differential rotation, both versions hold true. In both cases the upper limit estimate of Equation 7.11 characterizes the order of magnitude of the shear angles on which the large scale spot patterns appear to be stationary during the observed time span.

It should be noted that Equation 7.11 is mostly based on the features A_0 and A_1. The behaviour of the other named features B and $\tilde{\mathsf{C}}_0$ is much less clear with respect to differential rotation, they rather suggest (although not unambiguously) a rigid rotation up to about 60° latitude.

The estimate of Equation 7.11 is confirmed by the cross-correlation maps shown in Figures 7.35 and 7.36; they indicate an "anti-solar" shear of $\Delta\varphi = -20\pm 10^\circ$ of the polar regions compared to the equator. The given error range of $\pm 10^\circ$ is not strictly determined: While for the "6400 Å" images the correlation maxima show a smaller scatter up to a colatitude of 50°, the error of the shear estimate is dominated by regions closer to the pole. There the longitude scatter is of the order of 10° which leads to the above estimate.
Using the above pole to equator longitude shear $\Delta\varphi$ estimated from the surface cross-correlation leads to

$$|\alpha| < \left|\frac{-20\pm 10^\circ}{13.2\cdot 360^\circ}\right| = 0.004 \pm 0.002 \qquad (7.12)$$

It seems appropriate to define the meaning of the values in Equation 7.12 clearly: The given upper limit of $|\alpha|$ characterizes the approximate maximum equator-pole surface shear compatible with the surface cross-correlation; this value quantitatively describes the large-scale spot evolution. The error given for this upper limit describes how precisely this shear can be determined from the available Doppler images. It is estimated from the scatter of the cross-correlation function and quantifies the typical extension of the small-scale spot evolution as well as the resolution of the Doppler images.

Fitting a known rotation law to the cross-correlation maxima would allow a more precise determination of α.

However, a $\cos^2$-law is certainly not suggested by the distribution of the maxima; lacking any other a priori rotation law, such a fit is not attempted.

Whether the behaviour of the spot group A_0 can be attributed to differential rotation cannot be decided on the basis of the observations of HD197890. If such an assumption is made, Equation 7.12 can be written more restrictive as

$$\Big(\alpha = -0.004 \pm 0.002 \Big) \qquad (7.13)$$

In summary the estimate of Equation 7.12, stating a rigid rotation of HD197890 or a differential rotation weak compared to the Sun, is quite reliable, since it is founded on all spot patterns apparently recognizable for both the August 2 and the August 7 images.

On the other hand, the estimate of Equation 7.13, stating a weak anti-solar differential rotation, should be considered with some care. Its "weakness" is that it is dominated by the behaviour of the spot group A_0. All other features named above apparently "co-rotate" with the equator with the period P_0, they do not show pronounced signs of a slower rotation towards the poles. If the evolution of A_0 were of intrinsic nature instead of dominated by differential rotation, no token of differential rotation would remain in the Doppler images.

(iii) Third part: Spot lifetimes and lightcurves

In the light of the preceeding discussion the Doppler images of scenario (iii), based on an adopted approximately rigid rotation $P_0 = 0.380 \pm 0.004$ days, are more "trustworthy" than the reconstructions of the other rotation scenarios (i) and (ii). Given the Doppler images alone, this judgement is based on the better correspondence of spot patterns between the two observed rotations and on the better agreement of DI-lightcurves computed from Doppler images based on different wavelength ranges (Figures 7.37 and 7.38).

Adding the information of the photometry of HD197890, the superiority of scenario (iii) is potentially challenged by some aspects, while it is strengthened by others. The adoption of the rotation period P_0 for the DI reconstruction is a straightforward choice (and in that sense the best), because P_0 has been observed recurrently and is the only period that has been observed to be stable on time scales of weeks, with less certainty even on time scales of months.

Checking scenario (iii) against the August 2002 photometry is hampered by the fact that no strictly simultaneous photometry to the derived Doppler images is available. As a consequence, the quite

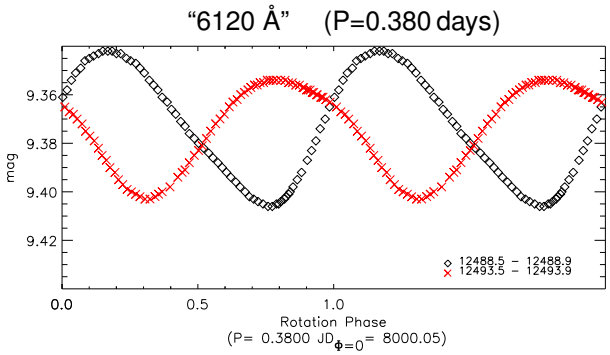

Figure 7.37: Lightcurves computed from CLDI reconstructions of the "6120 Å" region, adopting a rotation period of 0.380 days. The symbols represent the August 2 (◇) and August 7 (×) reconstructions, respectively. The lightcurves are computed from the corresponding surfaces shown in Fig. 7.33. The annotation dates are JD-2440000.

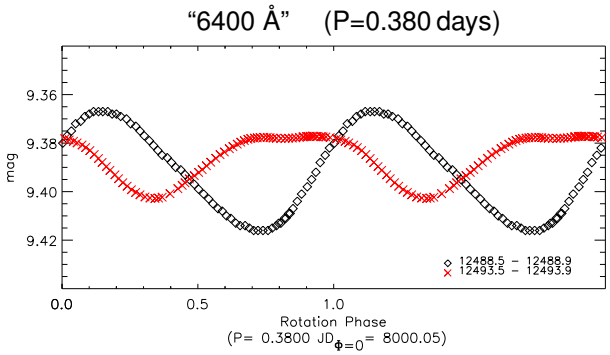

Figure 7.38: Companion to Fig. 7.37, but for lightcurves computed from CLDI reconstructions of the "6400 Å" region.

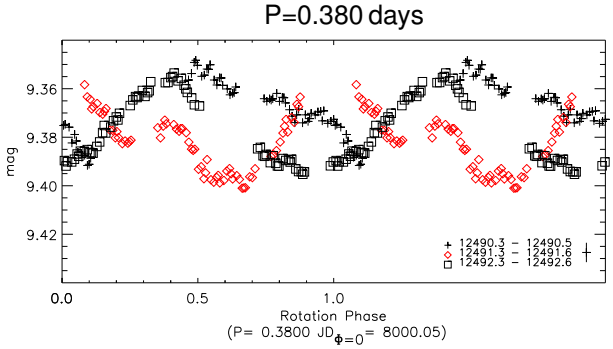

Figure 7.39: Lightcurve of HD197890 (2002 August 3-5), folded with a period of 0.380 days. Note that this folding period does not merge any portion of the data observed during different nights into a unique lightcurve. The symbols and annotations are the same as in Figure 7.7: + = August 3, ◇ = August 4 and □ = August 5.

well-agreeing DI-lightcurves of scenario (iii) cannot be compared to simultaneous photometric counterparts.

First of all, the appearance of the strongest peak at the period $P_{\rm alt}$ in the periodogram (Figure 7.5) is easily explained assuming the correctness of scenario (iii) and the resulting *unperiodic lightcurve* of Figure 7.39. The August 3 lightcurve interval approximately merges into a smooth curve with the August 5 interval, albeit with a considerable deviation between about phases 0.5 and 1.0. On the other hand, both intervals are completely out of phase with the August 4 interval observed in between. That means that the lightcurve parts observed at three day intervals roughly match, leading to the "7/8-resonance" of the period determination discussed in Section 7.3.2; this yields an alias peak close to $8/7 \cdot 0.380 = 0.434$ days. Additionally the "main" period peak at P_0, which would be strongest in the absence of spot reconfigurations, is suppressed because lightcurve intervals from consecutive nights are largely out of phase.

Accepting the unperiodic lightcurve of Figure 7.39 has far reaching consequences for the spot lifetimes implied by scenario (iii): The DI-lightcurves alone (Figures 7.37 and 7.38) could be explained by a gradual evolution of the spot groups A_0 and $\tilde{\mathsf{C}}_0$ during the 13.2 rotations taking place between them. Assuming that the center of group A_0 is slowly shifted while group $\tilde{\mathsf{C}}_0$ continuously fades away, such a gradual evolution would cause a monotonic shift of the lightcurve minimum from about phase 0.75 to 0.3 between August 2 and August 7. However, such a monotonic phase shift is not seen in the photometric lightcurve observed during that time span. Instead, as described above, during August 3-5 the lightcurve minimum appears to "flip" from very roughly 0.3 over 0.6 to 0.9. *This indicates a much faster evolution of the spot pattern than implied by the Doppler images alone*. Actually for scenario (iii) the August 3-5 lightcurve implies that spot reconfigurations of similar extent as those seen between the August 2 and August 7 Doppler images take place during the 1 day/$P_0 \approx 2.6$ rotations lying between each consecutive photometric observation night.

Naturally, such pronounced spot evolution during about two rotations suggests that some reconfiguration has taken place during *each* observed rotation, too. In principle, such fast changes of the spot pattern should lead to mismatches between the observed and reconstructed line profile time series, because the latter is synthesized from the DI solution surface which (in the absence of strong differential rotation) does not change during rotation. However, looking for such mismatches may be futile. Depending on its latitude, the line profile deformation of a particular spot group passes through the "core" of the profile during about 0.2 rotations.[41] This is still considerably shorter than the above 2.6 rotations, so given the limited resolution of the individual line profile deformations, a tentative change of their shape during their passage through the line profile would not lead to significant mismatches between the observed and reconstructed line profiles.

Consequently, the best opportunity to detect signs of spot reconfigurations during one rotation are the phase overlap regions between the start and the end of each spectral observation night (they are marked by horizontally hatched regions in Figures 6.12 and 6.13). Unfortunately, the behaviour of the profile deformations in the phase overlap regions does not offer unambiguous clues on this issue. The most pronounced mismatch of observed and reconstructed line profiles is found in the overlap region of the "6120 Å" time series of August 2 (discernible between about phases 0.77 to 0.88). However, this mismatch is hardly visible in the corresponding "6400 Å" profiles; consequently its cause is unclear.[42]

The mismatches in the overlap regions of the August 7 time series are less pronounced than their August 2 counterparts. While the August 7 overlap regions do show a qualitative agreement between the two wavelength regions, their mismatches with the CLDI reconstruction profiles are not more pronounced than mismatches found elsewhere in the time series. As a consequence they cannot be interpreted as unambiguous signs of a spot reconfiguration during the observed rotation.

However, the potential futility of the above inspection has already been mentioned. Unless very pronounced spot reconfigurations take place nearly instantaneously during the continuously sampled part of the time series (or during one rotation for the phase overlap region), the complex spot patterns of H197890's Doppler images could certainly be "adjusted" to cover up the line profile changes, in the sense that the profile mismatch would be evenly distributed as weak deviations over a wide range of phases.

[41] As an example take the line profile bump passing the center of the profile at about phase 0.95 in the P_0 August 2 time series (Figs. 6.12 and 6.13). This bump is associated with the the narrow spot group located at about 20° longitude in the corresponding Doppler images (Fig. 7.33). Its migration through the profile can easily be followed from phase 0.85 to phase 0.03, i.e. during 0.18 rotations.

[42] Possibly it is caused by deficiencies of the line profile extraction as suggested by the profiles at phases 0.806 and 0.840 in "6120 Å" time series. They appear to lag behind the "bump migration speed" indicated by the profiles of the surrounding phases.

7.9 Discussion

The two observed low-noise spectral time series (2002 August 2 and 7) each sample about one rotation period of HD197890 with a high and practically homogeneous phase sampling density. The spectral time series have been analyzed with the aim of constructing one Doppler image for each observed rotation and estimating the reliability of the images. The reliability and resolution of the images was estimated by comparing reconstructions from two separate wavelength ranges and from different independent subsets of the phase sampling. In this way the resolution of the Doppler images was shown to be about 10×10 degrees on the stellar surface, not including latitudes close to the poles and the equator (Section 7.5.1). However, potential southern features are mirrored to the northern hemisphere.

Based on the discussion of Section 6.5, in case of conflict, the "6400 Å" Doppler images should be more trustworthy than their "6120 Å" counterparts, presumably showing a higher resolution. However, since no third set of images from a different wavelength range has been produced, their increased "credibility" has not been further quantified.

The Doppler imaging reconstructions have been performed twice, based on two differently adopted rotation periods. The first set of images was reconstructed based on the rotation period $P_{\rm alt} = 0.44^{+0.04}_{-0.03}$ days; this period was determined from the 2002 August 3-5 photometry, assuming an approximately periodic and stable lightcurve during that time span. For the first set of reconstructions a rigid rotation with a period of 0.435 days was adopted; this contradicts the period of $P_0 = 0.380 \pm 0.004$ days, reliably observed for HD197890 at several other epochs. This contradiction could not be removed by tentatively adopting different scenarios of strong differential rotation which could have explained considerably different rotation periods on the surface of HD197890.

The second set of images was reconstructed adopting a rigid rotation with the period P_0. Compared to the "$P_{\rm alt}$-reconstructions" these "P_0-reconstructions" yield a closer correspondence of spot patterns consistently recognized in both the August 2 and the August 7 Doppler images. In addition, the lightcurves computed from the P_0-reconstructions agree much better than their $P_{\rm alt}$-counterparts when reconstructions based on different wavelength regions are compared. This is an additional clue of a more reliable and successful reconstruction based on the period P_0.

Summing up, the Doppler images of HD197890 based on a rigid rotation with a period P_0 should be considered the correct reconstructions based on the observed spectral time series. Their resolution has been determined to be about 10×10 degrees on the stellar surface.

None of the Doppler images shows indications of a polar spot on HD197890, this is in accord with the observations of Barnes et al. (2001).

Differential rotation on Speedy Mic?

A tentative "moderately strong solar-like" differential rotation scenario for HD197890 (i.e. with a faster rotating equator and of comparable relative strength as the Sun) has been studied in the preceeding sections as one possibility. Such a scenario is to some degree suggested by the complex behaviour of the August 2002 photometric lightcurve and appears as a possible interpretation of the cross-correlation maps of the August 2002 Doppler images (Figure 7.26 for the $P_{\rm alt}$-reconstructions, however the P_0-reconstructions show a similar strucure).

However, such a "moderately strong solar-like" differential rotation could not be substantiated by the August 2002 observations:

- Although supported by the *large scale* structure of the Doppler images (see e.g. Figure 7.27), the correspondance of images reconstructed adopting a rigid rotation with a period P_0 is much more convincing on large *and intermediate* image scales.
- It does not explain the August 2002 photometric lightcurve without additionally assuming a massive intrinsic evolution of the spot pattern.

Instead, a "weak, potentially anti-solar" differential rotation (i.e. much weaker than on the Sun in terms of $|\alpha|$ and with a slower rotating equator in terms of the angular velocity) with a period P_0 has been found to be the most convincing scenario based on the August 2002 Doppler images.

The resulting Doppler images have been constructed adopting a rigid rotation with a period of P_0. Their comparison by cross-correlation yields an estimated upper limit of the differential rotation strength as $|\alpha| < 0.004 \pm 0.002$ (about 2% of the solar value of 0.2). This estimate is deduced from the spot evolution during the about 13 rotations between the two Doppler images; it corresponds to a surface shear below $0.004 \cdot 360^\circ = 1.4^\circ$ during each rotation and justifies a Doppler imaging reconstruction adopting rigid rotation. This estimated upper limit of α is based on the evolution of several well-defined spot groups and can be considered reliable.

The evidence for *anti-solar* differential rotation is dominated by the evolution of the largest spot group present on HD197890's surface during the observations. If the behaviour of this group is tentatively attributed to differential rotation, a value of $\alpha = -0.004 \pm 0.002$ is estimated. Because the spot pattern changes are clearly dominated by intrinsic evolution of the spots, with the

weak differential rotation at most a side effect, the validity of this "anti-solar estimate" cannot be verified any further on the basis of the available two Doppler images.

The derived upper limit of α agrees well with estimate of $\alpha \lesssim 0.0064$ determined for HD197890 by Barnes et al. (2001), based on the comparison of two Doppler images observed 2-3 nights apart in 1998.[43]

It should be kept in mind that the given analyis of surface differential rotation of HD197890 is based on the evolution of its photospheric spots. It is still unclear to what degree these spots follow the bulk motion of the surrounding plasma on highly active stars. A significant decoupling of these two motions has been proposed e.g. for the case of RS CVn stars (Vogt et al., 1999); it is suggested by recent measurements of surface differential rotation on ultrafast rotators, simultaneously observing the behaviour of magnetic features and dark photospheric regions (Donati et al., 2003).

However, the deduced weak differential rotation of HD197890 is in accord with observational results of other fast rotating stars (Section 2.2.3) which show a pronounced general trend of a decreasing value of α with deceasing rotation period for otherwise similar objects.

As discussed in Section 2.2.2, the theoretical modelling results for the differential rotation of highly active fast rotating stars are not yet fully conclusive. Convection zone models based on mean-field hydrodynamics presently assume a "simple" structure of the meridional flows; they predict a *solar-like* (fast-equator) differential rotation, irrespective of the stellar rotation period P, with α strongly decreasing with P. The models of (Kitchatinov & Rüdiger, 1999, Fig. 1) only extend down to 1 day rotation period due to numerical limitations; interpolating their modelling results down to the rotation period of HD197890 yields an "expected" surface differential rotation of $\alpha \approx +0.0015$ (see Figure 7.40).

Three-dimensional hydrodynamic simulations do not yet advance into the regime of ultrafast rotating stars. However, their results for the (comparatively slowly rotating) Sun suggest that some assumptions of the mean-field approach may not be strictly valid. Among the debated assumptions are the "simple" single-cell meridional flows, and the reality of large-scale "self-organized" patterns of deep convective cells. None of the present models incorporates the potential influence of large-scale magnetic structures inside the convection zone; however, such structures may massively influence the large-scale flows, including differential rotation.

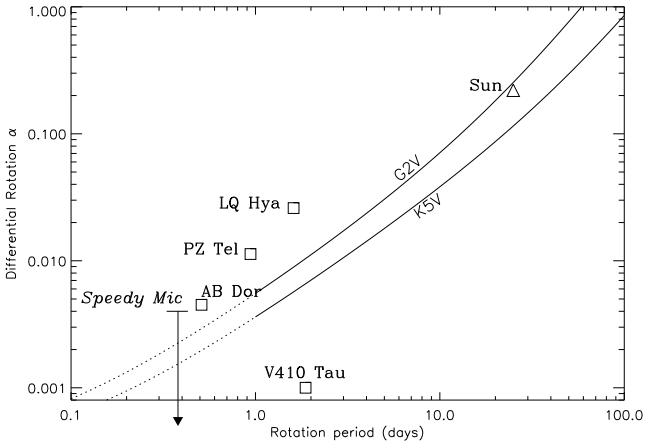

Figure 7.40: Theory and measurements of differential rotation of (apparently) single dwarf stars. The curves are adapted from Kitchatinov & Rüdiger (1999) and extrapolated below a period of one day (see Figure 2.14). Squares mark measurements based on comparisons of Doppler images (or related methods). The upper limit of $|\alpha| = 0.004 \pm 0.002$ determined for HD197890 (Speedy Mic) in this work is rendered by the arrow's top. The arrowhead drawn outside the plot signifies the less reliable indication of an *anti-solar* differential rotation (i.e. a potentially negative value of α). Companion to Fig. 2.16, see its caption for additional details.

Observed spot lifetimes on Speedy Mic

The spot pattern on HD197890 has changed substantially during the about 13 rotations between the two available Doppler images of 2002 August 2 and 7. However, many spot groups on small and intermediate scales survived these reconfigurations.

The available photometric lightcurve (August 3-5) contains only disk-integrated information about the spot pattern; even though it was observed on three consecutive nights, it contains unobserved gaps each lasting about 1.5 rotations due to the short rotation period of HD197890. However, the lightcurve indicates that spot reconfigurations comparable to those seen in the Doppler images have occured on time scales as short as about two rotations.

The inferred fast changes of some of HD197890's spots during the August 2002 observations on the one hand, and the snapshot-like information of the Doppler images (as well as the lightcurves) on the other, make definite statements about the spot lifetimes difficult. However, several observations can be made:

[43] Barnes et al. (2001) give a lower limit of 59 days for the time it takes the pole of HD197890 to lap the equator. For the period P_0 this translates into 155 rotations and correspondingly into a pole-equator shear upper limit of $\frac{360^\circ}{155} = 2.2^\circ$ for each rotation. This in turn results in a upper limit of $\alpha < \frac{360^\circ}{2.2^\circ} = 0.0064$.
In spite of the good agreement with our value this estimate of Barnes et al. should be considered as approximate, it is given without an error estimate. The value is based on the comparison of a narrow range of longitudes (90° wide) of two Doppler images reconstructed from rather unevenly phase sampled profile time series.

(a) Several spot groups of irregular shape, typically extending 10-20° on the surface, located from equatorial up to about 60° latitudes, reappear remarkably well-preserved after 13 rotations.

(b) One quite coherent spot group of about 30°×30° surface extension has largely vanished after 13 rotations.

(c) The only large spot group, quite coherent but of irregular shape, extends more than 100° in longitude and about 50° in latitude. It reappears after 13 rotations with a comparable surface extension but significantly shifted and transformed on scales of about 30°.

It should be kept in mind that all named spot groups found in the Doppler images may comprise groups truly located on both stellar hemispheres, incorrectly reconstructed only on the northern hemisphere by Doppler imaging.

As mentioned above, the photometric lightcurve indicates that changes of comparable extension to (b) and (c) have *repeatedly* taken place on timescales of about two rotations. However, the discontinuous sampling of the lightcurve and its merely disk-integrated information do not allow to further constrain these changes.

Other densely sampled photometric lightcurves of HD197890 have been observed from 1990 to 1996. Some of them show epochs of apparent spot pattern stability on time scales of weeks, possibly months, while other lightcurves indicate intermediate scale reconfigurations of spots on time scales of days.

The 1998 Doppler images of Barnes et al. (2001) do not allow conclusive statements about spot lifetimes on HD197890. Comparing e.g. their July 10&11 image to their July 13&14 image reveals few similarities. However, due to the somewhat poor quality of their input spectra (cf. their Figure 2 for the "noise-reduced" line profiles obtained by spectrum deconvolution) and the irregular phase sampling the reliability of their images must be considered low on all but the largest image scales.

Presently, no theoretical lifetime estimates for starspots exist. Observational results on starspot lifetimes are sparse, implying typical lifetimes of weeks or months for intermediate-scale and large-scale spots on fast-rotating stars (see Section 2.1.2). Compared to these values, the deduced lifetimes of *some* intermediate-scale spots on HD197890 are small. However, most of the spot groups on HD197890 do survive the 13 rotations between our Doppler images with recognizable shapes down to about 20° on the surface; this includes many characteristics of the large-scale spot pattern.[44]

[44]The Ca II K line core emission also observed with the 2002 August 2 and 7 spectra (although based on a preliminary data reduction and analysis, see Section 8.3) shows a more stable behaviour as a function of rotation phase than the photospheric brightness variations deduced from the Doppler images (Fig. 8.9).
If the Ca K core emission, a tracer of chromospheric activity, is also taken as an indicator of large-scale magnetic structures on HD197890, its relative stability implies the corresponding stability of those magnetic structures during the observed time span.

7.9.1 Outlook

The line profiles (rotational broadening functions) used as input for the presented Doppler images have been determined by a deconvolution of the observed spectra on two wavelength ranges about 10 Å and 50 Å wide, respectively. The spectrum deconvolution was performed using "selective least squares deconvolution" (sLSD). The use of spectrum deconvolution to generate input line profiles for Doppler imaging has been introduced by Donati et al. (1997b, coining the term "least squares deconvolution", LSD) and is still extensively applied by them. However, their applications concentrate on reducing the noise of the input line profiles by averaging the profile information of many spectral lines, applying the deconvolution to spectral ranges of typically 1000 Å width or more. While the (random) noise level of the resulting profiles is reduced by using such wide spectral ranges as input, it is not clear to what degree the line profile shape information is truly augmented at the same time. Individual characteristics of a part of the spectral lines (including undetected deficits of the template spectra for specific lines) certainly put a limit to the profile shape information that can be extracted on increasingly wider spectral ranges. This question is not systematically studied in the published results of Donati et al.. The "narrow-range" applications of sLSD in this work are a step in the direction of such studies. However, as a first step they focused on the construction of independent and consistent Doppler images, not on the systematic limitations of (s)LSD.

Such a study would have to include an extensive comparison of line profiles extracted from several narrow wavelength ranges to those extracted from very wide ranges. Only in this way the "true" limitations of spectrum deconvolution could be reliably established.

The issue of spot temperature contrasts to the quiet photosphere has not been treated in this work. The extraction of ("high-quality") time series of line profiles from a set of spectral regions, each containing only a few lines or one (quasi) isolated line, would open up another interesting option: If the spectral lines thus selected were chosen with markedly different temperature sensitivities, they could in principle be used to obtain information on the spot temperature contrasts by *simultaneously* fitting their line profiles in a common Doppler imaging reconstruction. Such a reconstruction could explicitly take the individual line characteristics into account. While this idea is

not particularity original (Piskunov, 1990, cf. e.g.), it has not been carried out extensively (e.g. Rice & Strassmeier, 2001) much due to computational limitations and the high noise level of most observations for individual lines.

The Doppler imaging algorithm CLDI developed and used during this work is presently not equipped with facilities for fitting several lines simultaneously, some prospects of their implementation are discussed in Section 5.6.3. As also discussed there, concerning the computational resources needed, CLDI should be able to perform such a simultaneous fitting of several line profiles.

The spectrum deconvolution method sLSD used in conjunction with CLDI is specifically adapted to operating in narrow wavelength ranges. Actually, these ranges do not have to be connected. So sLSD could be used to extract line profiles from ranges carefully selected to contain dominating spectral lines of similar temperature sensitivity. Possibly in this way "average" line profiles with a pretty well defined temperature sensitivity could be extracted. This would be a chance to overcome the above mentioned noise limitations.

This is an outlook. While the above items are certainly feasible, their success remains to be explored. The excellent quality of the available August 2002 VLT/UVES spectra makes them very well suited for such a study, unfortunately they lack simultaneous multicolour photometry and do not contain the TiO bands, e.g. at 7055 Å and 8860 Å which would be useful for starspot temperature diagnostics.

The behaviour of spectral lines sensitive to chromospheric activity, especially the Ca II H&K line core emission, has only been preliminarily studied in the context of this work (see Section 8.3). This preliminary analysis indicates that other spectral lines especially sensitive to chromospheric activity (e.g. the Ca I λ6122 line used for Doppler imaging here, cf. Bruls; Solanki & Schüssler, 1998, Tab. 1) show deformations correlated with the simultaneously observed Ca K line core emission. However, a thorough reduction of the spectra and a more careful analysis will be necessary to safely confirm these correlations. This analysis may allow to approximately localize some chromospheric emission sources on HD197890; these localized chromospheric structures could possibly be correlated with features of the photospheric spot pattern seen in the Doppler images.

Chapter 8

Appendix

8.1 Reduction of low-noise spectra

The potential pitfalls and individual problems of the reduction of echelle spectra are numerous. They depend on detailed instrumental characteristics and the envisaged use of the resultant data. This section concentrates on those reduction problems which are crucial to the line profile information later required for Doppler imaging. The focus of this section is rather on practical than on fundamental aspects; the figures are "control plots" produced during the spectral reduction, only sparingly processed for the presentation.

The following contains some information about the used spectrograph UVES, including technical details relevant for the spectral reduction. However, many of the problems discussed here are in a similar way valid for any echelle spectrograph.[1]

A spectrograph records the stellar spectrum as a two-dimensional image, nowadays on one or more CCDs. These "raw spectrum images" must be converted into one-dimensional spectra, containing a *linear* function of the observed flux at each wavelength. This process is intended to purge the data of instrumental effects and to get rid of information irrelevant for further processing. The amount of data is diminished considerably during this process, hence the name "data reduction" (or spectra reduction). The data reduction in the context of this work was performed in the IRAF environment.

Besides the usual aim of keeping the noise level low and minimizing systematic errors, the primary goal of the reduction performed here was stability. The number of stellar spectra taken during the 2002 August 2 and 7 observations exceeds 300, their wavelength range spans more than 3000 Å each (with several hundred Ångströms potentially intended to be used for Doppler imaging in the context of this work). During the two observing nights the observing conditions varied considerably, resulting in a varying point spread function of the star on the spectrograph slit and exposure levels varying by nearly a factor of ten for the main target star. The extraction must be trusted to some extent to react in a stable way to these changes since a close inspection of each spectrum in the whole relevant wavelength range is not feasible. In fact it would be partly meaningless since *small* changes in the spectrum are intrinsic to spectra of fast rotating active stars and could hardly be discerned from small reduction errors.

Some of the reduction steps described below can easily introduce spectral "artefacts", i.e. structures in the resultant spectra that are not present in the real stellar spectrum. Since Doppler imaging (DI) uses the information contained in typically small *variations* of line profiles, especially *time dependent artefacts* will mislead the imaging reconstruction and must be avoided, i.e. kept below the low noise level of the spectra.

8.1.1 The spectrograph UVES

The spectral observations were performed at the VLT (Very Large Telescope) of the ESO using the spectrograph UVES (Ultraviolet and visual Echelle spectrograph) mounted at the Nasmyth focus of the second VLT unit telescope "Kueyen".

UVES actually contains two independent spectrographs: The "blue arm" (wavelength range inside 3000-5000 Å) and the "red arm" (wavelength range inside 4200-11000 Å). The two arms have an identical optical layout but are optimized for the respective spectral ranges. UVES was used in the *dichroic mode*, i.e. the light entering the spectrograph is split up into two beams by a dichroic prism, feeding the two arms simultaneously. The ranges thus covered were 3260 Å$< \lambda <$ 4450 Å and 4760 Å$< \lambda <$ 6840 Å for the blue and red arm, respectively. This permits at the same time the observation of the ranges above 6000 Å, well suited for DI, and of the Ca II H&K lines below 4000 Å, useful as activity indi-

[1] In spite of the overall very good quality of the UVES documentation (although some information is easily overlooked on the numerous web-pages), some aspects discussed here are not found in detail there. The reason is that the UVES documentation concentrates on the reduction of "poorly" exposed spectra typical of faint objects, while the problems described here focus on the opposite: Well-exposed spectra.

cators. Unfortunately the TiO bands e.g. at 7055 Å and 8860 Å, which are useful for (starspot) temperature diagnostics, could not be covered simultaneously.

The spectrum in the red arm is contained in the echelle orders 92 to 132, each covering a wavelength interval of 80 Å to 110 Å, their width increasing from blue to red. Adjacent orders overlap by about 40 Å, however for the high signal-to-noise-ratio (SNR) aimed at, the finally usable overlap diminished to typically 10-15 Å. This is due to an imperfect flatfielding near the order edges (see below).

The red arm spectrum is recorded by a mosaic of two CCDs (2048x4096 pixels each), mounted with a gap of about 1mm, see Figure 8.5. As visible in the same figure, this gap causes a loss of parts of one echelle order, about 50 Å around 5800 Å for the UVES setup used. Unfortunately the wavelength range primarily intended for the DI ($\lambda \gtrsim$6000 Å) is recorded by the most problematic of the three CCDs used, the "MIT/LL W7C2", this is further discussed below. The CCDs were read out in a 2x2 binning mode, i.e. squares of 4 CCD pixels were summed up into one "data pixel". This was done to reduce the data amount and avoid unnecessary oversampling at the chosen spectral resolution In the following the terms CCD pixel, CCD row and CCD column refer to those "data pixels", unless noted otherwise.

The spectrograph slit width was chosen to correspond to 1" on the sky, offering a spectral resolution of $\lambda/\Delta\lambda$ of about 40 000. This resolution is completely adequate for the intended Doppler imaging (Section 7.2.1), a narrower slit would have led to unnecessary light loss in the case of poor seeing. The use of an image slicer was not possible for the dichroic mode at low object elevations (which were inavoidable for the performed observations).

In each UVES arm a small part of the beam is directed towards a photomultiplier acting as a realtime exposure meter. This part of the beam does not contribute to the spectrum because it would otherwise fall onto a small ungrooved gap present on each echelle grating which cannot be manufactured as one continuous segment due to their huge dimensions (84cmx21cm). Apart from monitoring information during observation, the averaged signal and scatter of this exposure meter is helpful for analyzing the quality of the spectra during later data reduction. For stable observing conditions this exposure meter can be used to detect strong variations of the object brightness (e.g. by stellar flares).

8.1.2 Spectra extraction and order merging

The pre-processing of the CCD images (bias treatment and trimming) and the scattered light treatment are not outlined here, the masking of bad pixels and the removal of cosmic particle hits on the CCD was performed at a later step.

Echelle order Extraction

The extraction converts the two-dimensional image of each echelle order into a one dimensional data vector. To this end, the order maximum is traced by a smooth curve, in case of UVES a fourth order polynomial of low curvature is appropriate. The data values perpendicular to this curve are called the *order profile*, they are formed by the one dimensional image of the star along the spectrograph slit. For the seeing variations encountered, about 0.7" to 2.5", the width (FWHM) of the order profile varied from about 2 to 7 data pixels.

Figure 8.1 shows the profile of one order, for the same exposure, as recorded 10 CCD pixel rows apart. On the top panel the profile maximum falls quite directly onto a data pixel, on the lower panel it nearly falls onto the gap between two data pixels. This shift of the profile maximum is caused by the inclination of the orders relative to the CCD columns. In the case of UVES the shift is repeated nearly periodically as a function of the CCD rows since the curvature of the orders is low.

The extraction estimates the integral of the profile for each data row by numerical integration. In the simplest case, called *"average extraction"*, an aperture of constant width to the right and left of the profile is defined (in Figure 8.1 assume it to extend from column 220 to 230) The data values of all columns inside the aperture are summed up for each row, the data pixels at the edges are weighted by their fractional width contained inside the aperture. For the chosen example, this procedure systematically overestimates the profile integral for the left panel case and quite correctly estimates it in the right panel, causing the extraction ripple shown in Figure 8.2. In the case of UVES the orders have an inclination of about 3° relative to the CCD columns, resulting in a ripple period of about 20 CCD rows.[2] For a typical dispersion of the chosen instrument setup (0.05 Å per data pixel), this translates into a period of 1 Å as a function of wavelength. Consequently the ripples are easily mistaken as features of the rotationally broadened line profiles (with a typical width of the order of $\frac{2\cdot 100\ \mathrm{km\,s^{-1}}}{c}\cdot 6000$ Å$\approx$ 4 Å at 6000 Å for ultrafast rotating stars), so they have to be avoided.

For the example of extraction ripple discussed above, the problem could easily be solved by choosing a wider aperture. However, adjusting the aperture width for the worst seeing encountered and using this "maximum" width aperture for all exposures is not a good strategy,

[2] For (the idealized case of) a constant inclination of precisely 3° the ripple period should be about 19 pixels, because it would take 19 CCD rows to cross one CCD column ($\tan(3°) \approx \frac{1}{19}$).

because for good seeing only a fraction of the extracted aperture would contain relevant data. In this way noise and defects due to bad pixels would be introduced unnecessarily into the spectrum.

Several disadvantages of "average extraction" can be overcome by a scheme called *"optimum extraction"* (Horne, 1986) which also incorporates a detection and rejection of bad pixels. While optimum extraction focusses on minimizing the noise of the extracted spectrum, its primary merit here is its built-in adaption of the extraction aperture.

For optimum extraction, a model of the expected flux in each pixel and its expected variance (i.e. noise) is constructed. Weighting a pixel proportional to its expected flux P_i and inversely proportional to its expected variance V_i yields an estimator of minimum variance for the flux at each wavelength (Marsh, 1989). For the limit of high flux, i.e. pure photon noise ($V_i \propto P_i$), this yields uniform weights just like average extraction. However, the weights differ for low fluxes when background noise becomes relevant. The expected flux is modelled by fitting the order profile with a set of functions varying smoothly along the dispersion direction. The variance is usually estimated from a two-component noise model consisting of photon noise and the readout noise of the CCD. By rejecting pixels deviating more than an appropriately chosen threshold, bad pixels can effectively be removed during the extraction process.

Following Horne (1986), the order profiles were fitted by polynomials along the CCD rows (i.e. *approximately* perpendicular to the dispersion direction) which is appropriate because of the low inclination of the spectrum orders relative to the CCD columns. *This provided the required stable adaption of the aperture width to the varying width of the order profiles.* The polynomial fit is more flexible than e.g. fitting the aperture profile by Gaussians as performed by the standard UVES pipeline reduction. The Gaussian fit becomes worse for high exposure levels, especially combined with a narrow order profile caused by good seeing values. As a result some of the standard pipeline reduced spectra show an extraction ripple similar to the effect described above.

Flatfield correction

After extraction the preliminary spectrum actually is a collection of spectra: For each echelle order, the extracted CCD counts are given as a function of the CCD pixel row. These counts are still markedly nonlinear functions of the object flux, distorted by (at least) two factors: the (constant) blaze function of the gratings and the (possibly time-dependent) sensitivity variations of the CCD.[3]

These distortions can be corrected by "flatfielding", i.e. dividing the spectra by a so-called flatfield exposure, created from spectra of a continuous light source. Several such exposures are combined in order to reduce their noise (which is introduced into the result spectra).

The flatfielding can be done before the extraction by dividing the two-dimensional raw spectra pixel by pixel. This is the best option to remove the sensitivity variations of the CCD. However it is not feasible in conjunction with optimum extraction, because the true fluxes are required for a correct variance model. Consequently the flatfielding was done after extraction, also extracting flatfield spectra.

Figure 8.5 shows a typical extracted flatfield order for the MIT-CCD of the UVES red arm (i.e. the CCD recording the spectrum above about 5800 Å for the used setup). While the large-scale behaviour clearly shows the modulation by the blaze function of the echelle grating, the small-scale variations are slightly unusual, they reveal strong (up to ca. 15%) variations of the CCD sensitivity. These variations are one dimensional cuts through the "brickwall pattern" visible in Figures 8.3 and 8.4.[4]

This brickwall pattern is apparently very stable (according to the UVES documentation; no significant variations could be detected for the available flatfields). However, it exhibits occasional large variations over length scales of very few CCD pixels. Consequently, if the flatfielding is performed after the extraction of the orders, care must be taken to extract the flatfield orders with *exactly* the same apertures as those of each individual stellar specrum (i.e. for the optimum extraction, its order definitions must be seperately stored for this step). Only in this way the extracted flatfield orders can appropriately correct for the small-scale sensitivity variations of the CCD actually affecting the stellar spectrum. Due to varying seeing and different positioning of the object on the spectrograph slit, there are considerable variations of the position and width of the extraction apertures.

[3] Some aspects of the blaze function are discussed in Chapter 3 of Gray (1992, especially Figs. 3.11 and 3.12),notice the details depending on the polarization of the incident light.
The CCD sensitivity is often referred to by different terms depending on the considered length scale: pixel-to-pixel variations (slightly misleading named "fixed pattern noise"), medium-scale variations (Photon-Response-Non-Uniformity, PRNU) and large-scale variations (sometimes ambiguously termed sensitivity gradients).

[4] This "brickwall pattern" of some CCD types is a spatial variation of their quantum efficiency caused by "laser annealing" during their manufacturing. It should not be confused with CCD "fringing" which is caused by multiple reflection inside the CCD substrate at large wavelengths (due to the increasing transparency of silicon as a function of wavelength).

Merging of echelle orders

The process of combining the echelle orders into a single spectrum is called merging. To combine the overlapping wavelength regions of the adjacent orders, this has to be done after wavelength calibration of the spectra. In the absence of wavelength calibration and flatfielding errors merging would simply mean averaging these overlapping regions, thereby increasing their SNR (lower compared to the order centers because of the blaze function of each order).

However, in the presence of these errors, the spectra can get distorted inside or at the edges of the overlap regions. Since these distortions of the final spectrum in general cannot be discerned from real spectral features (or are simply "forgotten" at later stages of the analysis), the safest way is to use the unmerged spectra whenever possible. Actually, the flatfielding problems described above were detected by carefully comparing these overlap regions.

Since the final spectra were intended to be used on wavelength ranges wider than or not coinciding with the individual echelle orders, merging the spectra was inavoidable. While the flat field correction was found to be successful on small and intermediate scales, *large-scale* deviations (on typical scales of 100 pixels) of up to about 5% between overlapping orders remained.[5] For the present reduction this was corrected for by multiplying each order by a linear function of wavelength (independent of time and order number) and trimming each overlap region to a width of about 20 Å. An example of a overlap region between two adjacent echelle orders (corrected by the mentioned linear function) is shown in Figure 8.6, demonstrating the successful flatfield correction.

[5] This is a "known effect" for UVES (S. Hubrig, priv. comm.), however its reasons are unclear. Somehow the differing illumination (scattered light?, polarization inside the spectrograph?) for the observation of a star or exposure by a flatfield lamp apparently influence the blaze-function. This leads to a large-scale "deficiency" of the flatfield correction. Presumably a correction determined from a standard star observation would be the best way to resolve this problem.

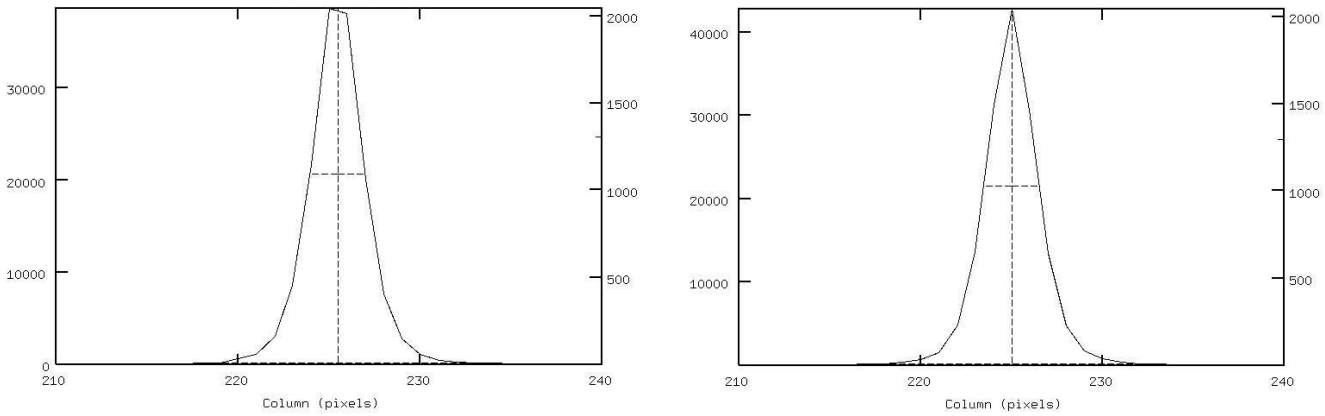

Figure 8.1: Two echelle order profiles from a UVES red-arm spectrum of HD197890 observed at a seeing of about 1.5". Each panel shows the values of the CCD pixels in a part of one CCD row shown as a function of CCD columns. Note that the continuous graph is slightly misleading because the shown data are discretely sampled by the CCD. The left hand y-axis of each panel is annotated in ADC (analog-digital converter) counts, the right hand y-axis and tick mark indicate the shown CCD row (1305 and 1295 in the left and right panel, respectively). Due to a flaw of the graphics hardcopy of the IRAF routine (`apedit` from `noao.twodspec`) the extraction aperture is not marked. It extends from about columns 222.5 to 228.5 in the left panel and from about 222.0 to 228.0 in the right panel. Note that this narrow aperture cuts off a considerable portion of the profile wings, it was defined for better seeing conditions. Here it is used to illustrate the effect of "extraction ripple" shown in Fig. 8.2, resulting from a poorly adapted aperture and the inclination of the echelle orders relative to the CCD rows.

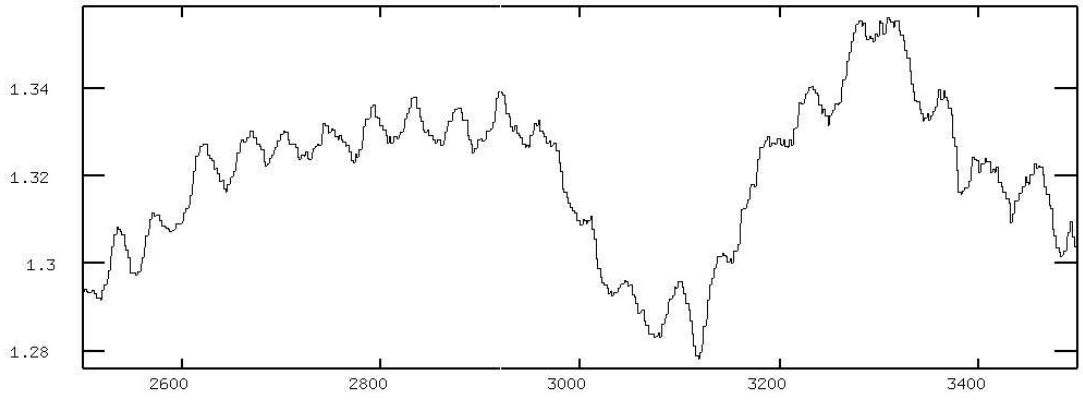

Figure 8.2: A prounounced example of "extraction ripple" caused by an inadequate definition of echelle order extraction apertures. The curve shows a part of one flatfielded order extracted from the same spectrum and apertures illustrated in Figure 8.1. The curve shows the relative flux as a function of "raw" (unbinned) CCD rows. Note the quite regular structure of the ripple with an amplitude below 1% of the spectrum flux in this example.

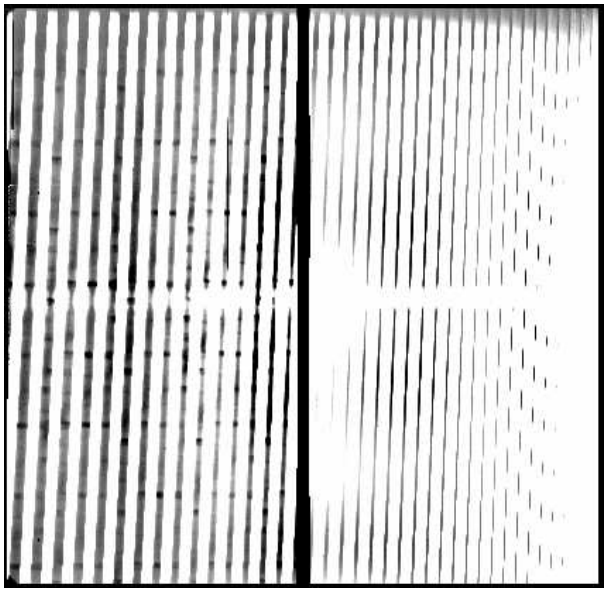

Figure 8.3: Flatfield exposure of the red arm of UVES, showing parts of the "brickwall pattern" (more clearly visible in Fig. 8.4). The CCD rows run vertically, the columns horizontally; the wavelength increases to the left and to the bottom. This image has been severely processed to pronounce the brickwall pattern: First, the blaze of the echelle and cross-disperser gratings has been removed by dividing the image by a smoothly varying two-dimensional polynomial. Second, the gray scale only renders a small dynamic range of the CCD pixel values which causes only a part of each echelle order to be rendered dark, so their true width is not visible here. However, the two CCDs recording the spectrum ("MIT" chip left, "EEV" chip right) and the about 1 mm gap between them (rendered black since it contains zero values, artificially inserted into the image) are clearly visible. The spectral order crossing this gap is incompletely recorded by the CCDs and causes a gap of about 50 Å in the red arm spectra.

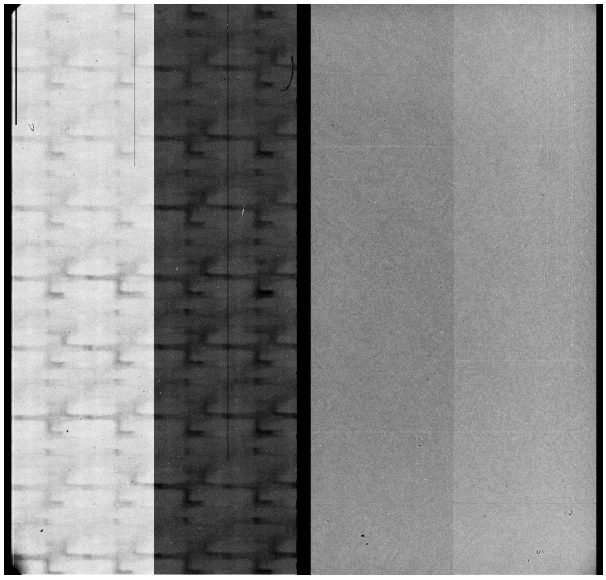

Figure 8.4: "Technical flatfield" of the UVES red arm CCDs (from the UVES webpages "UVES Scientific CCD System" (ESO)), showing the complete brickwall pattern on the left CCD ("MIT" chip). The brickwalls are regions of reduced sensitivity of the CCD pixels rendered dark here. For this image the CCDs were removed from the spectrograph and exposed with monochromatic light of a wavelength of 6500 Å. The rendering of each CCD divided into a brighter and darker half does not reflect different sensitivities.

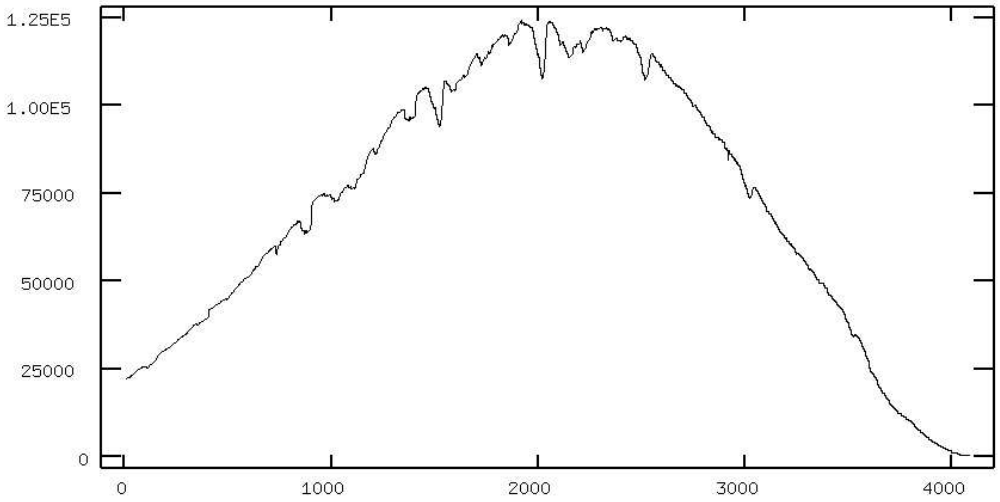

Figure 8.5: Extracted echelle order from a flatfield exposure of the "MIT" CCD of the UVES red arm. The curve shows integrated ADC (analog-digital converter) counts as a function of "raw" (unbinned) CCD rows. The blaze of the echelle grating is visible the large-scale shape of the curve. The small-scale dips are caused by CCD sensitivity variations due to the brickwall pattern shown in Fig 8.4.

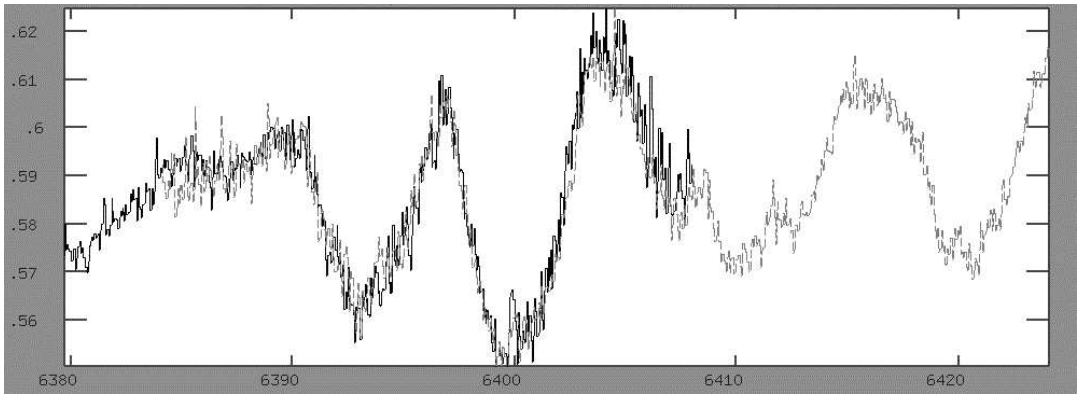

Figure 8.6: Example of two overlapping echelle orders in a UVES red arm spectrum of HD197890, showing the observed flux (in arbitrary units) as a function of wavelength (Å). The overlapping wavelength region has been truncated to about 20 Å for merging of the orders into a continuous spectrum. The good consistency between the two orders in the overlapping region illustrates the success of the flatfielding and the additional linear ramp correction that has been applied (see text).

8.2 August 2002 spectra of Speedy Mic

Tables 8.1 and 8.2 give an overview of the spectra of HD197890 observed during the two VLT/UVES observation nights in August 2002. They were used as input data for the Doppler imaging described in Chapter 7.

All spectra, except for the very last (JD 2400000+52 493.915) are sums of two adjacently observed "raw" spectra (the exposure time of individual spectra was limited in order to avoid overexposure); only two such raw spectra were discarded (between JD 2400000+52 493.691 and JD 2400000+52 493.712) because of their exceptionally poor quality due to low sky transmission (with an SNR below 100). Apart from these two spectra an uninterrupted phase sampling of HD197890 could be achieved during both observation nights.

The signal-to-noise (SNR) values are defined for a binwidth of about 0.083 Å. However, they should be considered as rough estimates, because they have merely been estimated from a 3 Å-wide spectral region (6425.5 Å − 6427 Å) which is practically free of features in the spectrum of HD197890.

The spectrum of Gl 472 (K1V, m_V=7.1) which was used as a template for the spectrum deconvolution by sLSD were observed on August 2 at JD 2400000+52 488.515 with a total exposure time of 60 s, resulting in an SNR exceeding 300.

The χ^2 values of Table 8.1 measure the quality of the spectrum fit achieved by the spectrum deconvolution using sLSD ("selective least squares deconvolution", see Chapter 6). They deviate substantially from unity for the "6400 Å" wavelength region; this does not indicate a poor line profile extraction (possibly excepting "outliers" like JD 2400000+52 488.667), but is instead largely due to constantly imperfectly fitted wavelength intervals caused by small template spectrum deficiencies (see Figure 6.1).

Table 8.1: Overview of spectra of HD197890 observed on 2002 August 2. Dates given are JD$^\diamond$=JD-2400000. The SNR values are estimated on a narrow wavelength range near 6400 Å for a spectral binwidth of 0.083 Å. The χ^2 values measure the quality of the spectrum fit achieved by the line profile extraction (using "selective least squares deconvolution", sLSD) in the given wavelength ranges (see Sec. 7.4). The line profiles ("rotational broadening functions", RBFs) extracted by sLSD were used as input for the Doppler images of HD197890 presented in this work.

JD$^\diamond$	Exposure time [s]	SNR	"6120 Å" χ^2	"6400 Å" χ^2	JD$^\diamond$	Exposure time [s]	SNR	"6120 Å" χ^2	"6400 Å" χ^2
52 488.533	500	393	0.7	4.8	52 488.738	400	423	1.4	5.1
52 488.541	400	352	1.0	3.9	52 488.744	400	406	0.7	4.4
52 488.547	400	418	1.2	5.3	52 488.750	400	488	1.5	7.3
52 488.553	400	406	1.1	5.1	52 488.757	400	396	1.2	4.5
52 488.559	400	443	1.2	5.8	52 488.763	400	419	1.3	4.8
52 488.566	400	400	1.3	4.8	52 488.769	400	530	1.7	8.9
52 488.573	400	458	1.8	6.4	52 488.776	400	436	1.3	6.0
52 488.579	400	384	0.9	4.6	52 488.782	400	509	2.1	7.6
52 488.585	400	415	1.6	5.4	52 488.788	400	386	1.3	4.3
52 488.591	400	337	0.8	3.3	52 488.795	400	444	2.1	6.3
52 488.598	400	570	2.7	10.5	52 488.801	400	430	1.7	6.1
52 488.604	400	394	1.0	4.4	52 488.808	400	426	1.4	5.5
52 488.611	400	434	0.9	6.0	52 488.815	400	346	1.0	3.7
52 488.617	400	405	0.7	5.1	52 488.821	400	404	1.6	5.2
52 488.623	400	338	0.7	3.6	52 488.828	400	399	1.0	4.7
52 488.629	400	461	1.6	6.1	52 488.834	400	417	1.3	5.7
52 488.636	400	408	1.4	5.0	52 488.840	400	400	1.0	4.7
52 488.642	400	434	0.7	5.2	52 488.846	400	398	1.4	5.0
52 488.648	400	438	0.8	5.8	52 488.853	400	507	2.0	8.0
52 488.654	400	442	1.2	5.7	52 488.859	400	348	1.0	4.0
52 488.661	400	469	1.2	6.1	52 488.865	400	330	0.8	3.3
52 488.667	400	674	2.2	12.8	52 488.872	400	367	1.4	4.3
52 488.674	400	480	1.2	6.8	52 488.878	400	445	2.3	6.8
52 488.680	400	373	0.6	3.9	52 488.884	400	399	1.7	5.4
52 488.686	400	527	1.7	7.6	52 488.891	400	354	1.1	4.3
52 488.692	400	556	1.6	9.3	52 488.898	400	311	0.9	3.3
52 488.700	400	500	1.2	7.8	52 488.904	400	309	1.3	3.5
52 488.706	400	437	1.0	5.6	52 488.910	400	415	2.7	7.2
52 488.713	400	415	1.2	4.8	52 488.916	400	295	1.4	3.3
52 488.719	400	395	0.9	4.5	52 488.923	400	270	1.2	3.4
52 488.725	400	456	1.6	6.0	52 488.929	400	225	1.0	2.8
52 488.732	400	495	1.5	7.2					

Table 8.2: Companion to Tab. 8.1 for the spectra of HD197890 observed on 2002 August 7.

JD$^{\diamond}$	Exposure time	SNR	"6120 Å" χ^2	"6400 Å" χ^2	JD$^{\diamond}$	Exposure time	SNR	"6120 Å" χ^2	"6400 Å" χ^2
52 493.507	400	293	0.5	2.8	52 493.735	350	287	1.4	4.3
52 493.514	400	303	0.7	3.0	52 493.741	350	336	1.4	4.7
52 493.520	400	402	1.1	5.5	52 493.746	350	442	3.0	7.4
52 493.526	400	383	1.1	4.5	52 493.752	350	359	1.2	4.4
52 493.533	400	456	1.5	6.1	52 493.758	350	371	0.8	4.2
52 493.539	375	445	1.7	7.2	52 493.765	350	423	1.7	7.5
52 493.545	375	346	1.1	3.9	52 493.771	350	459	1.5	7.8
52 493.555	350	312	0.9	3.0	52 493.777	350	100	0.2	0.4
52 493.560	350	342	1.3	3.8	52 493.784	350	274	0.9	2.9
52 493.566	350	401	1.0	5.2	52 493.789	350	440	1.5	5.8
52 493.571	350	314	1.2	3.9	52 493.795	325	362	0.8	4.2
52 493.578	350	316	0.8	3.7	52 493.800	260	374	0.7	4.6
52 493.583	350	387	1.3	5.0	52 493.805	250	418	1.3	5.9
52 493.589	350	370	1.3	4.2	52 493.810	240	438	1.4	6.0
52 493.595	350	369	1.2	4.8	52 493.814	240	311	0.7	3.1
52 493.601	350	328	1.5	4.4	52 493.819	240	360	0.8	4.5
52 493.606	350	444	1.5	6.3	52 493.823	240	431	1.5	5.9
52 493.612	350	457	1.4	6.7	52 493.827	240	320	0.6	3.5
52 493.617	350	531	2.2	9.5	52 493.832	240	330	1.0	3.5
52 493.624	350	387	1.4	5.3	52 493.837	240	324	1.2	3.8
52 493.629	350	443	2.1	6.9	52 493.842	240	274	1.1	3.1
52 493.635	350	236	1.3	2.7	52 493.845	240	378	1.7	5.0
52 493.641	350	377	1.0	4.7	52 493.850	240	368	1.2	5.4
52 493.647	350	434	1.3	6.4	52 493.856	350	365	0.8	4.2
52 493.653	350	339	2.3	6.2	52 493.862	350	329	0.5	3.7
52 493.659	350	197	2.0	2.8	52 493.867	280	362	0.8	4.9
52 493.666	350	399	1.3	4.8	52 493.872	280	447	1.4	6.7
52 493.673	350	364	1.9	4.3	52 493.877	280	330	0.7	3.6
52 493.680	350	329	2.1	4.8	52 493.882	280	379	0.9	4.9
52 493.685	350	261	1.9	3.4	52 493.887	280	379	1.1	4.9
52 493.691	350	269	1.4	6.0	52 493.892	280	339	0.9	4.1
52 493.701	350	239	1.8	3.2	52 493.897	280	342	0.8	4.1
52 493.712	350	212	1.7	3.3	52 493.902	280	284	0.6	2.6
52 493.717	350	333	2.3	4.7	52 493.907	280	329	1.0	3.4
52 493.722	350	424	1.9	7.6	52 493.912	280	286	0.8	3.0
52 493.728	350	253	1.6	3.1	52 493.915	140	221	0.8	2.3

8.3 Ca H&K observations of Speedy Mic

The core emission of the Ca II H&K lines (3968.49 Å and 3933.68 Å) could be observed in the 2002 August 2 and 7 spectra due to the use of the "dichroic" mode of the spectrograph UVES (Section 8.1.1).

Because of their strength and the ionization of the atomic species, these lines are formed in high layers of the stellar atmosphere. They react sensitively to the temperature in these layers (i.e. to chromospheric activity in case of the Sun, cf. e.g. Foukal, 1990, Fig. 9.9). As a consequence they are widely used as (also quantitative) indicators of chromospheric activity on the Sun as well as on other stars (Foukal, 1990, Sec. 9, Schrijver & Zwaan, 2000, Secs. 2.3.4 & 9.3).

The behaviour of the Ca K core emission has been studied preliminarily in the context of this work. Figure 8.7 shows a portion of one August 2 spectrum of HD197890 around the Ca H&K lines. Due to HD197890's fast rotation the characteristic broad wings of the two lines are severely deformed by blending of lines in their flanks. Figure 8.8 shows a time series of Ca K line cores arbitrarily selected from the August 2 spectra. As e.g. the spectrum at phase 0.95 clearly shows, some of the spectra suffer from severe data reduction deficits. These are vivid examples of "extraction ripple" discussed in Section 8.1.2, caused by an imperfect extraction of orders from the echelle spectra.[6] Such deficits were produced by the "standard UVES pipeline reduction" only intended for quick inspection of the spectra. Due to similar data reduction deficiencies, the spectral ranges above 4800 Å, recorded by the "red arm" of the spectrograph UVES, including those intende for Doppler imaging, have been reduced anew as part of this work (see Section 8.1). Since the Ca H&K lines were recorded by the "blue arm" of UVES these spectra have not been newly reduced yet. As a consequence, their preliminary analysis is based on the rather deficient spectra resulting from the "standard UVES pipeline reduction".

In the following only the Ca K line is considered because it is less severely affected than Ca H by blending with other lines in the spectrum of HD197890. Since the extraction ripple is of quite constant amplitude over

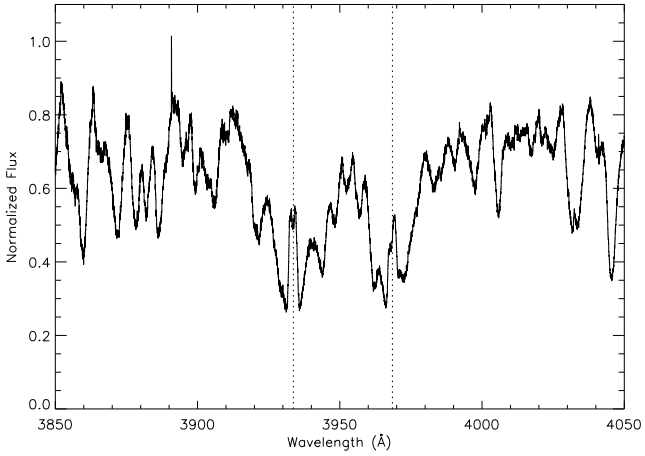

Figure 8.7: Sample spectrum showing the region around the Ca II H&K lines of HD197890 observed on 2002 August 2, dotted lines mark their central wavelengths. The spike at 3890 Å is due to a bad CCD pixel, illustrating the preliminary reduction status of the spectrum (see text).

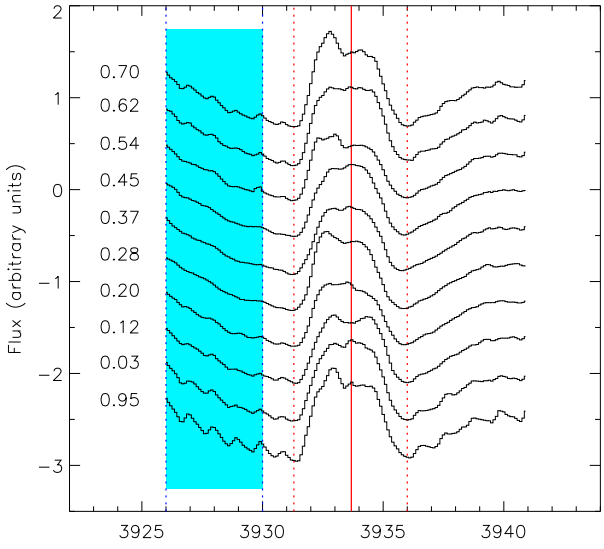

Figure 8.8: Time series of Ca K emission cores of HD197890 observed during one night on 2002 August 2, the rotation phase (same as in Fig. 8.9) is given left of each (shifted) spectrum. The shown spectra are only a coarsely sampled subset of the available time series. The "ripple" clearly visible in some of the spectra is due to a preliminary reduction of the spectra (see text). The spectra are ordered ascending with the time of their observation, spectra near the beginning and end of the night were observed at low elevations and have been omitted because of increasing ripple amplitude (see text).

[6] In the case of the "standard UVES pipeline reduced" blue arm spectra this ripple is presumably enhanced for observations at low elevations, because the object was positioned on the spectrograph slit according to the aquisition image of the UVES red arm. Because the slit was aligned vertically, the atmospheric dispersion causes a shift of the stellar image along the slit and results in an elevation dependent shift of the spectral orders on the blue arm CCD which is apparently not corrected by a proper recentering of the apertures used for order extraction.

the range of the Ca K line (and nearly absent in several phase intervals), the pronounced variations of the line core shape can safely be considered as real, albeit slightly distorted by the ripple. However, their detailed analysis will require a proper reduction of the spectra. The core shape variations evolve continuously as a function of phase (which is not clearly visible at the coarse phase resolution of Figure 8.8). The total width of the Ca K emission core (measured from the left to the right flux minima) is about 4.5 Å, this has been noted by Bromage et al. (1992) as "by far the broadest [of their stellar sample]" (without further discussion).[7]

The typical width of the Ca K emission core for solar plages is about 1Å (e.g. Foukal, 1990, Fig. 9.9). According to the "Wilson-Bappu effect" (Schrijver & Zwaan, 2000, Sec. 9.3.1) the "intrinsic" width of the Ca K correlates strongly with the absolute visual magnitude but depends only weakly on other stellar parameters.[8] So for the rough estimate performed here, the intrinsic width of the Ca K emission core of HD197890 can be estimated to be about 1 Å.

The rotational line width (induced by features distributed over the whole stellar disk) for HD197890 at this wavelength is about

$$\Delta\lambda \approx \frac{2 \cdot 134 \text{ km s}^{-1}}{c} \cdot 4000 \text{ A} = 3.6 \text{ A} \quad ,$$

using the value of $v \sin i$ from Table 7.4. So the observed total Ca K core width is close to that of a convolution of a "solar-plage-like" core profile with the given rotational broadening.[9] This suggests that (part of) the Ca K core emission regions are distributed over large portions of HD197890's surface.

However, the variable narrower spectral features in the Ca K core visible in Figure 8.8, with a width of the order of 1 Å, suggest that also localized emission regions of smaller surface extension exist.

[7] Bromage et al. (1992) give a value of 240±40 km/s ($\hat{=}$ 3.2±0.5 Å) for the FWHM of the Ca K emission core, based on low-resolution spectra (about 1 Å at 4000 Å). This is in accord with the above *total* width of 4.5 Å.

[8] The *empirical* relation for the width W_0 (in km/s) of the Ca K core by Lutz & Pagel (1982) reads

$$\log W_0 = -0.22 \log g + 1.65 \log T_{\text{eff}} + 0.10[\text{Fe/H}] - 3.69 \quad ,$$

so it depends most strongly on the effective temperature T_{eff} and less pronounced on the surface gravity g and metallicity [Fe/H]. The $\log T_{\text{eff}}$ of HD197890 deviates by about 0.1 from the solar value, so for the present estimation the intrinsic width of the Ca K emission core can be taken as the solar value.

[9] Since the emission regions of the line core are located in the upper atmospheric regions and are optically thin they show a rotational broadening more like a boxcar than the close to elliptical broadening profile of photospheric features which is due to projection and limb-darkening effects.

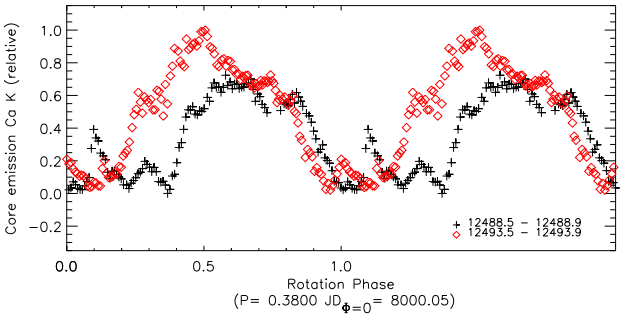

Figure 8.9: Time series of Ca K core emission measures observed on 2002 August 2 (+) and August 7 (◇). The folding period and the phase zero point are the same as those adopted for Figures 7.37 to 7.39, indicating the strong rotational modulation of the Ca K core emission. The emission measure is defined in the text, it is arbitrarily scaled here. Dates given in the annotation are JD-2440000.

For the present analysis a measure of the Ca K core emission has been defined in rough analogy to the Mt. Wilson Ca II-S-index as illustrated in Figure 8.8: The *Ca K core emission measure* used here is defined as the ratio of the flux integral of the core (between the dotted lines in Figure 8.8) and the flux integral of a region outside the core (the shade region in the same figure).

This core emission measure as a function of phase is shown in Figure 8.9 for the 2002 August 2 and 7 spectra of HD197890. Although the only preliminary reduction of the spectra should be kept in mind, this integral emission measure is presumably not very sensitive to the mentioned extraction ripple. Note that the scaling between 0 and 1 is completely arbitrary. As a comparison with Figure 8.8 shows, a core emission of zero does not mean a vanishing emission core, but an emission at the "basal" or "low" level of the observation interval.[10]

The curves of Figure 8.9 are interesting in several respects. They exhibit a pronounced dichotomy between one "high" emission and one "low" emission time span during each rotation. This apparently rotational modulation seems to show a correlated behaviour to the photospheric brightness variations deduced from the Doppler images ("DI-lightcurves", Figs. 7.37 and 7.38): For the August 2 observations the center phase of the high emis-

[10] The "raw" (i.e. not scaled to the interval [0,1]) values of the core emission measure range between 1.30 and 1.50, i.e. they show a rotationally modulated peak-to-peak variation of about 20%.
This can be compared to the rotationally modulated variations of the Mt. Wilson S index for the Sun (Hempelmann & Donahue, 1997, Figs. 1&2) which amount to typically about 10% peak-to-peak of the average level (which varies strongly with the activity cycle). However, without further analysis this comparison is of little significance, because the S index is based on a "historic" instrumental definition and is not at all a suitable measure for ultrafast rotators (Vaughan et al., 1978; Noyes et al., 1984).

sion time span (lasting from about phase 0.4 to 1.0, i.e. a center at phase 0.7) is close to the brightness minimum of the DI-lightcurves. Just as the DI-lightcurve minimum, this center phase of emission changes to a lower value (although by a different amount) when going to the August 7 observations.

While the shapes of the broad high emission maxima in Figure 8.9 show similarities between the August 2 and August 7 data, namely the rising and falling edges with a small dip near their top, there are also significant differences concerning the total width and a narrow top peak.[11]

It is tempting to try and localize the surface region(s) responsible for the high core emission. As suggested by the quite steep rise and decay of the high emission the emitting surface region, being above the photosphere proper and optically thin, attain their full intensity for the observer very soon after appearing on the visible disk. Because of the large inclination of HD197890 (about 70°, see Section 7.5.2) any such emission region of small surface extension should be visible about 0.5 rotations, only weakly dependent on latitude. Given this simplifying assumption, such a feature should reach the subobserver longitude 0.25 rotations after its appearance on (and analogously 0.25 rotations before its disappearance from) the visible disk, which would allow to localize it in longitude.

The August 2 high emission lasts, as mentioned, from about phase 0.4 to 1.0. With the above argument the emission region should be found between the longitudes

$$360^\circ \cdot \big(1 - (1.0 - 0.25)\big) \approx 90^\circ$$

from the phase of its disappearance and

$$360^\circ \cdot \big(1 - (0.4 + 0.25)\big) \approx 125^\circ$$

from the phase of appearance. Here it has been used that rotation takes place with decreasing subobserver longitude, starting at phase zero at a longitude of $0^\circ \cong 360^\circ$. In the same way, with the August 7 high emission lasting from about phase 0.2 to 0.9, the emission region should be found between longitudes of 125°and 200°. Inspecting these longitude ranges in the corresponding Doppler images (e.g. in Figure 7.34) does not reveal obvious correlations with the intermediate-scale photospheric spot pattern.

The preceeding discussion has attempted an interpretation of the apparently rotationally modulated behaviour of the Ca K core emission. Given the above visibility arguments (i.e. any sufficiently long-lived emission region should contribute to the disk-integrated emission for about 0.5 rotations), the variations of the core emission on time scales much shorter than half a rotation should be produced by transient emission regions. Again, the following discussion is preliminary in nature, last but not least because of the merely preliminary reduction of the spectral range containing the Ca K line.

There are several prominent short-term peaks with a "lifetime" of about 0.1 rotations. For the August 2 data (JD...+12488) these peaks are located at about phases 0.1, 0.3, 0.45 and 0.85; for the August 7 data (JD...+12483) their positions are close to phases 0.0, 0.3, 0.5 and 0.75. Interestingly there seems to be a correlation with deformations in the "6120 Å" wavelength range line profiles (rotational broadening functions) which are ill-fitted by the Doppler imaging reconstruction (Figure 6.12).[12] At the present state of the analysis, this correlation is definitely not conclusive. However, a poor fit by the Doppler imaging reconstruction would be the expected signature of profile deformations which are short-lived compared to their passage over the stellar disk.

It is especially interesting, that the corresponding phase ranges of the "6400 Å" line profiles show (mostly) no similar signatures. Assuming the reality of the tentatively proposed transient chromospheric emission regions "disturbing" the profile extracted from the "6120 Å" wavelength region, this may have a simple explanation: Bruls; Solanki & Schüssler (1998, cf. their Tab. 1) model the sensitivity of several spectral lines to (tentatively modelled) chromospheric activity. The three lines found most sensitive in their study (because of a large formation height and large strength) are Fe I λ5497, Ca I λ6122 and Fe I λ6430. The Fe I λ6430 line is part of the "6400 Å" region, but it is merely one of about 6 strong line (groups) in this region. As a result, the sensitive reaction of the Fe I λ6430 line would be "washed out" in the line profiles extracted in the "6400 Å" region due to averaging with its other lines. On the other hand, the "6120 Å" is completely dominated by the Ca I λ6122 line; this suggests, that a line profile extracted in that region should react sensitively to chromospheric activity.

[11] In the light of the mentioned differences it seems daring to identify the apparent shift of the high emission maximum to lower rotation phases between August 2 and 7 with a faster rotation. Although this is an attractive idea, because such faster rotation (compared to the "dominating" photospheric rotation period) could be caused by differential rotation. Alternatively (possibly related), it could be associated with a faster rotation of magnetic features compared to photospheric features.

[12] For the August 2 line profiles (rotational broadening functions, RBFs) the given phases are close to the (to different degree) poorly fitted phase ranges around phase 0.100 0.303 and 0.850; for phases about 0.435 no prominently poor fit is apparent.
For the August 7 line profiles this applies to phases 0.012, 0.287 and 0.754; here no prominently poor fit is apparent for phases about 0.486.

Summary

As stated in the introduction, the analysis of the Ca K line core emission in this section is yet preliminary. However, if confirmed by a more comprehensive treatment, the above results have a substantial bearing on the interpretation of some line profile deformations observed for HD197890. Especially, they may help to interpret some phase intervals constantly ill-fitted by the Doppler imaging reconstructions of HD197890 presented in this work; this could lead to Doppler images of improved reliability.

In addition, a proper reduction of the UVES blue arm spectra would be necessary to obtain Ca H&K spectra free of reduction artefacts, truly rendering the core emission profiles. These profiles may allow to approximately localize some transient chromospheric emission sources on HD197890's surface which possibly could be related to the photospheric spots seen in the Doppler images.

8.4 Comparison of CLDI and Maximum entropy reconstructions

This Section compares an exemplary reconstruction by CLDI, the Doppler imaging algorithm developed as part of this work, to a maximum entropy Doppler image. The used maximum entropy algorithm is called MAXENT, it is the implementation of Vogt et al. (1987), also described in Hatzes et al. (1989) and has been kindly supplied by A. Hatzes. MAXENT uses the "general purpose" maximum entropy optimization routine MEMSYS developed by Skilling (1984), shortly described in Section 4.3.1.

An exemplary maximum entropy Doppler image compared to a reconstruction of the "old" CLDI is shown by Kürster et al. (1994, Sec. 4.5), but not discussed in detail. Kürster et al. also used a maximum entropy Doppler imaging implementation based on MEMSYS which they do not further specify.

The CLDI and MAXENT reconstructions of this Section use the same input data, namely line profiles extracted by spectrum deconvolution in the "6120 Å" wavelength region (Section 7.4) of the 2002 August 2 spectra of HD197890.[13]

The reconstructions use the same adopted stellar parameters as those of Table 7.4 with a rotation period of 0.435 days. In the course of the analysis of Chapter 7 this period turned out to be presumably wrong. However, as outlined there, the influence of the differently adopted periods on the individual images of HD197890 is small so that the following discussion is valid independently of it.

The local line profiles used by CLDI for the undisturbed photosphere were translated into a limb angle-dependent lookup table used by MAXENT, adopting the same linear limb-darkening law.

The imaged surface parameter

Different from CLDI, MAXENT uses a "linearized temperature" $\tilde{T}$ as the reconstructed surface parameter.[14] However, the zero point and dynamic range of this temperature $\tilde{T}$ can be arbitrarily chosen for the MAXENT reconstruction. As a result, it can be transformed into a local spot filling factor $\tilde{\sigma}$ by applying

$$\tilde{\sigma} = \frac{T_{\max} - \tilde{T}}{T_{\max} - T_{\min}} \quad .$$

This results in a value of $\tilde{\sigma} = 1$ representing a "completely" spotted surface element emitting no flux and $\tilde{\sigma} = 0$ representing the undisturbed photosphere.

By choosing a spot-flux of zero CLDI could be set up such that the spot filling factor σ of its reconstructions had precisely the same meaning as $\tilde{\sigma}$. However, to facilitate the comparison with results of Chapter 7, the spot-photosphere contrast used there for the CLDI reconstructions, namely 0.5, has been maintained here.

In summary, the "measures of spottedness" of the MAXENT and CLDI reconstructions shown in this Section have the same physical interpretation, but they differ in the range of spot flux they represent. The CLDI reconstruction is restricted to a flux in the interval [0.5, 1] for each surface element (in units of the undisturbed photospheric flux). A value of $\sigma = 1$ for CLDI's local filling factor results in a flux of 0.5 of the corresponding surface element; for the MAXENT reconstruction, the same flux is emitted by a surface element with a value of $\tilde{\sigma} = 0.5$. In contrast to the CLDI image, each surface element of the MAXENT image can adopt any flux between zero (corresponding to $\tilde{\sigma} = 1$) and unity (corresponding to $\tilde{\sigma} = 0$).

The MAXENT Doppler image

The MAXENT Doppler image reconstructed from the input data described above is shown in Figure 8.12. The frequency of its local filling factor values $\tilde{\sigma}$ is shown in Figure 8.10. It is interesting to note that the most frequent values of $\tilde{\sigma}$ (apart from the (nearly) zero flux of the undisturbed photosphere) are close to 0.5, while "very dark" spots with $\tilde{\sigma} \gtrsim 0.6$ are relatively rare.[15] As dis-

[13] The input line profiles of this section (rotational broadening functions, RBFs, see Sec. 6.1) were extracted using sLSD ("selective least squares deconvolution"). The profiles were extracted from the "final" reduced spectra of HD197890 (Sec. 8.1), but using an earlier version (and slightly different settings) of sLSD than that used for the reconstructions of Section 7.5.
The profiles used in this section are shown in Fig. 8.16. They can be compared to their counterparts of Sec. 7.5, shown in Fig. 6.10, keeping in mind that the phase sampling resolutions differ by a factor of two.
A denser phase sampling resolution could not be chosen for MAXENT here (without modifications of the program), because its response matrix-based line profile synthesis ran into memory requirement problems.

[14] Actually this "linearized temperature" $\tilde{T}$ is a mixing parameter of local line profiles very similar to CLDI's local spot filling factor (defined in Eq. 5.9). MAXENT uses a preset minimum temperature $T_{\min}$ and a maximum $T_{\max}$ as input parameters of the reconstruction. The undisturbed photospheric local line profiles of MAXENT's lookup table are multiplied by

$$\frac{\tilde{T} - T_{\min}}{T_{\max} - T_{\min}}$$

according to the value of $\tilde{T}$ for each surface element during the disk integration. This results in an undisturbed photospheric local line profiles for $\tilde{T} = T_{\max}$ and in a zero profile (emission of no flux) for $\tilde{T} = T_{\min}$.
In summary, MAXENT's surface parameter $\tilde{T}$ controls the linear mixing of the adopted undisturbed photospheric line profile and a *zero profile* analogous to the mixing procedure of CLDI (Eq. 5.9). The difference to CLDI is that CLDI's adopted spot local line profile can be chosen as non-zero.

[15] This is related to the "constant solution trend" discussed as a property of the maximum entropy regularization in Section 4.3.1.

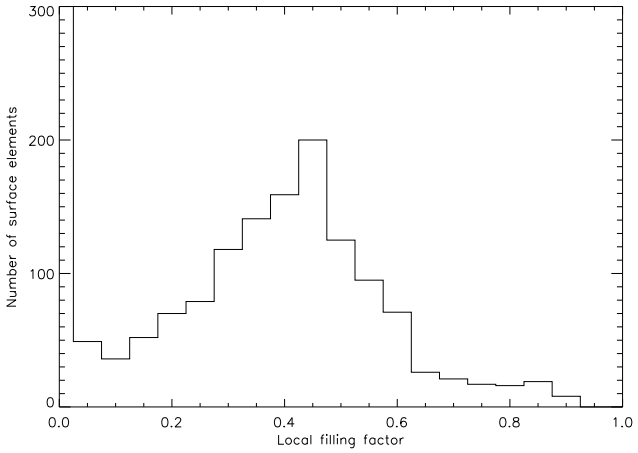

Figure 8.10: Histogram of local spot filling factors $\tilde{\sigma}$ of the surface elements of the MAXENT reconstruction shown in Fig. 8.14. The number of surface elements in the $\tilde{\sigma} \approx 0$-bin exceeds 700, it represents the "undisturbed photospheric" (or "unspotted") surface elements and is not visible at this scale. Note that the non zero local filling factors concentrate around intermediate values, leading to an "intermediate-contrast" Doppler image by MAXENT; this is a consequence of the maximum entropy regularisation, the MAXENT reconstruction used here allows all values with $0 \leq \tilde{\sigma} \leq 1$.

cussed above, these surface elements of the MAXENT image with $\tilde{\sigma} = 0.5$ correspond exactly to the "black" spots with $\sigma = 1$ in the CLDI images. This facilitates the comparison of both reconstructions.

Before coming to the comparison of the MAXENT image with its CLDI companion, a small correction is applied to the former: Comparing MAXENT's fits to the input line profiles to those by CLDI (Figures 8.16 and 8.17) it is immediately apparent that MAXENT's fits are superior. This is not surprising as such, considering the different nature of the methods.

However, it is worth noting that this superiority is not restricted to the profile deformations "migrating" with rotation phase. Instead, the MAXENT reconstruction also yields an "overall" closer fit extending far into the flanks of the line profiles. However, these outer flanks should not be significantly influenced by the spot pattern. How does MAXENT nevertheless manage to fit them so closely?

The reason is that MAXENT was "allowed" an additional freedom which was kept from CLDI: MAXENT has the option of automatically scaling each input line profile such that its equivalent width equals that of its reconstructed counterpart. This option has been enabled for the presented application of MAXENT, so that MAXENT performs such a scaling before each iteration. Such a scaling was not done by CLDI for the reconstructions presented in this work.[16]

Figure 8.13 illustrates how MAXENT efficiently makes use of that freedom to fit the average shape of the input line profiles closely: It shows the "Doppler image" reconstructed from an approximately undisturbed input profile (more precisely, it is the MAXENT "image" of a time-independent series of profiles in which all profiles are set to the average profile computed from the "true" input time series of Figure 8.16). Taking the average profile of the input time series as a proxy of the undisturbed line profile of HD197890, this means that MAXENT fits this undisturbed profile by reconstructing the (symmetrically) "disturbed" surface of Figure 8.13, instead of an unspotted surface as would be the case for a immaculately adopted line profile parameters.

The reason for this is slightly subtle: The automatic scaling of the line profiles adjusts their equivalent width by multiplying the deviations from the surrounding continuum with a common factor for the whole profile. MAXENT cannot "optimize" the parameters controlling the overall line profile shape, they are fixed as input parameters to the reconstruction. The applies to the adopted $v\,sini$ and the limb darkening which is defined by the lookup table of local line profiles supplied to MAXENT. As a result, MAXENT performs an optimization of the overall profile shape by adding a "weak" rotationally symmetric "background" structure to the reconstruction surface; additionally this "background" includes a weak pole to equator gradient with an amplitude of about $\Delta\tilde{\sigma} \approx 0.05$ (it is not visible in Figure 8.13, being outside the narrow range rendered by its gray scale).

As "seen" by CLDI, the situation is different. It is not enabled to scale its input line profiles; due to its discrete-contrast-step solution, it could not very well perform a "weak" symmetric correction of its solution surface as MAXENT does. However, just like MAXENT it has to make do with the line profile parameters supplied to it (especially the limb darkening parameter and $v\,sini$). Since it does not vary the depth of its input profiles by scaling them, these parameters are also a proper compromise (as determined by a fit with a synthetic rotation profile, described in Section 6.4). However, it is not as successful as the more flexible adaption of MAXENT.[17]

[16] As an alternative, it is suggested in the "manual" of MAXENT to switch off that automatic scaling. In this case, MAXENT can be stopped after a few iterations and the scaling of each profile can be carried out manually (this procedure has the advantage of higher transparency). However, the auto-scaling was found to work fine for the presented applications of MAXENT; it avoids the tedious manual scaling of the considerable number of input profiles of the time series.

[17] A few comments concerning the profile "symmetrization" described in Section 6.5 are in order here. First, this symmetrization is a tentative correction motivated by the practical demands that CLDI

Actually, a more flexible adaption to the average input profile, based on a MAXENT "correction image", may also be an interesting option for preparing the input profiles of CLDI.[18] In principle such a correction could be due to physical line profile features (e.g. a significant pole-equator temperature gradient).

The Doppler image of Figure 8.12 is the "physically correct" MAXENT reconstruction of the input profile time series in the sense that the rendered gray shades have a one-to-one correspondence to the local spot filling factors. However, the rotationally symmetric "background image" shown in Figure 8.13 is presumably due to deficiencies of the adopted line profile modelling parameters (and/or deficiencies of the line profile extraction by sLSD in the "6120 Å" region).

For the purpose of comparison to the CLDI image this background has been subtracted from the map of Figure 8.12, yielding the image shown in Figure 8.14. The thus processed image uses a slightly different gray scale which has no precise assignment to local filling factors; it has the advantage of rendering spots with higher contrast.

Comparison of image features

Comparing the corresponding maps of Figures 8.14 and 8.15 shows that all image features of the CLDI reconstruction down to scales of about 2×2 surface elements (corresponding to $9^\circ\times9^\circ$ on the surface near the equator) have corresponding features in the MAXENT reconstruction. However, there are a few features in the MAXENT image which have no (or no pronounced) counterpart in the CLDI image. This applies to several weaker equatorial features of the MAXENT image which form a "broken equatorial band"; it also applies to the weak feature at high latitudes found close to the subobserver longitude in the MAXENT map for ϕ=0.6.

Apart from the mentioned weak features, the MAXENT image is "a blurred version" of the CLDI image. As discussed in the following, this blurring is fully in accord with the information contained in the input line profiles. Correspondingly, the disconnected "super-resolved" features of the CLDI reconstruction are a result of the discrete solution algorithm; their reality cannot be proved on the basis of the input data.

Comparison of line profile fits

As mentioned above, it is directly obvious that the MAXENT fits to the input line profiles are closer than those by CLDI (Figures 8.16 and 8.17). This is confirmed by the corresponding achieved values of χ^2=0.81 for MAXENT compared to χ^2=2.30 for CLDI. Nevertheless, CLDI grasps all subjectively apparent migrating deformations of the line profiles and reconstructs structures fitting them (leading to an image well-comparable to that of MAXENT); this is a success of CLDI's backprojection approach.
In fact, two aspects of the superior line profile fit by MAXENT can be discerned:
(a) A better fit to the overall line profile shape, including the outer line flanks. (b) A closer fit to the shape of migrating profile deformations.

Aspect (a) has already been discussed above and is due to MAXENT's greater flexibility in adapting to slight deficiencies of the line profile modelling or extraction. Aspect (b) demonstrates how "elegantly" MAXENT adjusts the intricate weak image structures to achieve a close fit to the details of individual profile deformations. As an example, consider the small dip passing the profile center at about phase 0.743. The profile "bumps" right and left of it are associated with the quite weak group of spots around the subobserver longitude in the ϕ=0.6 MAXENT map. Only the near-equator left part of that spot group has a companion in the CLDI image. Correspondingly, CLDI's profile fits are less close than MAXENT's at the surrounding phases, most pronounced at phases 0.623 to 0.682.

Due to its discrete-step solution CLDI is not able to create structures quite as intricate. However, certainly a "sparse irregular group" of a few spotted surface elements could be found that would produce a much closer fit than the solution constructed by CLDI. However, the "deformation signature" of such a sparse spot group is not registered by CLDI's backprojections.

makes on its input profiles, it is not motivated by any physical assumptions. Actually, the preceding discussion shows that it is merely a compromise.
Second, as can be seen in Figure 6.5, this correction is much weaker for the "6400 Å" wavelength range than for the "6120 Å" region used for the presented application of MAXENT.

[18] Such a (continuous) "correction image" could be constructed prior to the CLDI reconstruction from an average line profile using MAXENT. During the CLDI iteration it could be added as a fixed offset image to the reconstruction (instead of a homogeneous unspotted surface).

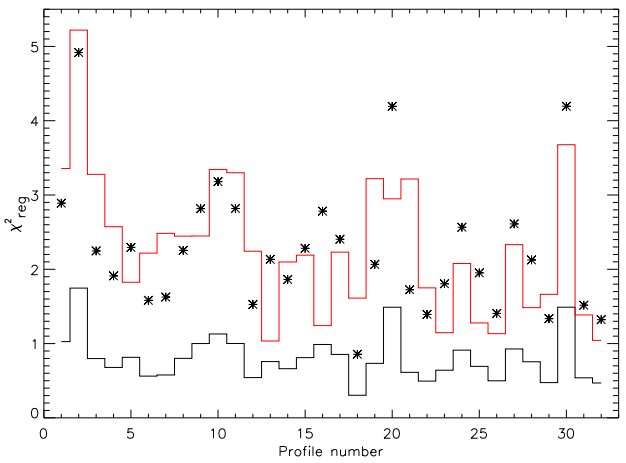

Figure 8.11: Regularized χ^2 values, characterizing the profile fit quality for each rotation phase as achieved by the MAXENT (black steps) and the CLDI reconstructions (red/gray steps) of this Section. For better comparison to the CLDI-χ^2-values , the stars also show the MAXENT values, multiplied by a common factor to adjust both curves to the same mean. See text for details.

A tentative view: The *conservative* CLDI

Another interesting phase interval is formed by the nearly overlapping phases of the beginning and end of the observing night.[19] As illustrated by Figure 8.11, the fit quality of CLDI apparently decreases when approaching those (nearly) overlapping phases *at the beginning* of the observation night; this is directly apparent from a visual inspection of the CLDI profile fits. This behaviour is completely untypical of CLDI, for synthetic input profiles of constant noise level it yields a constant fit quality as a function of phase, superimposed with a homogeneously distributed scatter.[20]

In the light of the results of Chapter 7 the rotation period of 0.435 days adopted here is presumably wrong. However, this is not the (main) reason for the misfit in the phase overlap region of the "6120 Å" region. As can be seen in Figure 6.12 the misfit remains equally pronounced when adopting the presumably correct period of 0.380 days. As discussed in Section 7.8.3, another straightforward explanation for the misfit between the phase overlapping profiles would be a significant spot evolution during one rotation. However, this is not significantly confirmed by the profile time series extracted from the "6400 Å" region which do not show a pronounced misfit in the phase overlap region. As discussed in Section 8.3 there is a possible correlation between poorly fitted phase intervals of the "6120 Å" profiles with the (preliminarily) determined Ca II H&K emission; however, these results are presently not conclusive.

Another possible reason which comes to mind is the decreasing SNR of the input spectra near the end of the observation night (see Table 8.1). However, this explanation is implausible for several reasons: (i) Such a decrease is not present at the beginning of the night (due to a higher elevation of HD197890). (ii) sLSD tends to react to excessive noise by "small-scale ripple" of its solutions (see Section 6.2, several examples are visible in Figure 6.9). Neither the input profiles of the reconstructions here, nor their fully "phase-resolved" counterparts of Figure 6.9 (which are based on input spectra of lower SNR) show such a ripple. Instead all of them show quite well-defined and agreeing profile deformations. This supports the reality of the profile deformations extracted by sLSD.

Although the reason is presently unclear, there is potentially something "weird" about the phase overlap interval of the August 2 "6120 Å" line profiles. Taking up the discussion of "conservative" solutions of CLDI (Section 5.6.2), CLDI's behaviour can also be described as conservative in this case: Instead of rendering an intricately modelled fine structure of the solution surface (which it presently could not even produce if it was desired) for the "weird" phase overlap interval, it simply stops converging. Actually, the resulting differences of the solution surfaces are not pronounced (as can be seen in the ϕ=0.35 maps of Figures 8.14 and 8.15 which show the affected regions close to the subsobserver meridian).

A note on the used χ^2-regularization

The following remarks complement those of Section 5.5 made in the context of synthetic input data for Doppler imaging.

The χ^2-values of this section (as those of Chapter 7) are regularized assuming an SNR of approximately 100 (relative to the continuum flux normalized to unity). This means that a rms noise amplitude of $\sigma_{\rm noise} \approx 0.01$ has been adopted (Equation 5.12).[21] At first glance this does

[19] Adopting a period of 0.435 days results in a gap of 0.1 rotations; using a period of 0.380 days, this would turn into a true overlap of about 0.03 rotations, see e.g. Figure 6.12. However, a phase gap of 0.1 corresponds to a rotation of "only" 0.1·360°=36°. As a result there are considerable surface regions commonly visible at the beginning and end of the observing night and the corresponding phases are simply referred to as the phase overlap (interval), irrespective of the precise value of the adopted period.

[20] CLDI shows this increase of χ^2 towards the beginning of the night in the same way when adopting the 0.380 days rotation period. Corresponding reconstructions have not been performed using MAXENT.

[21] More precisely, for calculating the χ^2 characterizing the "closeness-of-fit" of the reconstructed line profiles to their (observed) input counterparts, Eq. 5.13 was used. The noise amplitude estimate

not seem to comply with the much higher SNR of the input spectra of typically about 500 (see Table 8.1, keeping in mind that the spectra deconvolved for the line profiles of this section are sums of adjacent pairs of that list), corresponding to a noise amplitude of $\sigma_{\rm noise}$=0.002. However, although slightly arbitrary, the adopted SNR of 100 is an appropriate estimate for the noise-level of the *rotational broadening functions* (RBFs) considered here. Their typical depth (of nearly 0.65 as can be seen in Figure 8.16) is about five times larger than the typical depth of the rotationally broadened Ca I λ6122 line (about 0.13, see Figure 6.7) dominating the "6120 Å" region. These different depths are due to the chosen approximate normalization of the RBFs to unit area below the continuum (using normalized radial velocity units).

The resulting scaling factor of five for a moderately strong spectral line like Ca I λ6122 is equally "applied" to the noise amplitude $\sigma_{\rm noise}$, explaining the different values of the SNR above.[22]

Summary

Excluding a few weakly pronounced surface features it is appropriate to say that the MAXENT image is a blurred version of the CLDI image. This blurring is fully in accord with the information contained in the input line profiles because MAXENT fits them significantly better than CLDI. However, all features reconstructed by CLDI, down to scales of about 10×10 degrees on the surface, are confirmed by the MAXENT reconstruction for the presented example.

The discussed issue of an improved fit by MAXENT to the overall (average) line profile shape sheds an interesting light on the limitations of the line profile extraction by sLSD (especially on narrow wavelength ranges) and the subsequent modelling of these profiles by CLDI. This includes limitations of the adaption procedure for the average line profile described in Section 6.4; it is proposed that this adaption procedure may be improved by employing a MAXENT fit to the average line profile, prior to the CLDI reconstruction.

There appear to be two ways to overcome the line remaining "small-scale" inferiority of the CLDI line profile fits compared to their MAXENT counterparts. Both require an explicit optimization, thereby in a way leaving the framework of the current CLDI.

If a discrete-contrast-step solution is desired (although its reality cannot be proved on the basis of the observed line profiles) a discrete optimization scheme would need to be implemented (see Section 5.6.3 for some aspects of such an implementation).[23]

If the CLDI reconstruction is to be "polished" with the aim of improving the small-scale line profile fits, it is proposed here to give up the discrete-contrast-step restriction and construct a continuous solution "very similar" to the initial CLDI reconstruction. This could be easily implemented by using the CLDI solution (appropriately smoothed to mimic its approximate resolution) as the "default map" for the MAXENT reconstruction.[24] This procedure could preserve "conservative" features of the CLDI solution and possibly "encourage" stronger contrasts in the solution compared to a "pure" MAXENT reconstruction. It would limit the influence of the maximum entropy regularization to the small image scales. To what extent the thus continously "polished" CLDI solutions would be different from pure MAXENT reconstructions remains to be tested; for cases of sparse phase sampling there could be significant differences.

$\sigma_{\rm noise}$ used for each spectrum was calculated by multiplying the reciprocal values of SNR estimates (see Eq. 5.12) of each input spectrum (analogous to those of Table 8.1) by a (slightly arbitrary) correction factor of five. This correction factor is motivated below.
This correction and the resulting regularization of χ^2 must be considered as approximations, because they do not take all sources of noise (errors) affecting the line profiles into account. As an example imperfections of the profile extraction of sLSD are not included; although they are somehow quantified by χ^2 values of the sLSD fit, as in Table 8.1, they do not result in random deviations, let alone normally distributed ones. As a consequence, they cannot be consistently incorporated into a χ^2 regularization.

[22] Describing the errors of the RBFs (rotational broadening functions), resulting from spectrum deconvolution, by a signal-to-*noise*-ratio is mathematically not satisfactory and should be considered as a rough description. The reason is that the errors of the RBFs are not normally distributed random deviations (e.g. due to the regularization included in sLSD) but seem to be more appropriately described as "solution instabilities". A systematic study of the errors of spectrum deconvolution has not been carried out as a part of this work (and presently not by other authors for their implementations of spectrum deconvolution). As a consequence, the RBFs are assigned (somewhat arbitrary) SNR values here for comparison purposes; the preliminary nature of this description should be kept in mind.

[23] Kürster (1991) presents the idea of "CLEANing the MAXENT" solution for improving the profile fits of CLDI (i.e. in some way using MAXENT reconstructions as backprojections of CLDI). This procedure is certainly conceivable, but it seems slightly cumbersome. It would leave CLDI in control of the reconstruction process, thereby keeping up a solution assembly instead of an explicit optimization. While the advantages of that seem unclear, in addition it would give up the conceptual independence of CLDI and MAXENT.

[24] This option of a non-constant "default map" has been omitted in Section 4.3.1, discussing fundamental aspects of maximum entropy DI. Actually the denominators of the sum in Equation 4.10 can be modified to incorporate such a default map (Narayan & Nityananda, 1986, Eq. 10 and Sec. 3.2). If such a non-constant default map is used, the "constant solution trend" of maximum entropy DI, discussed in Section 4.3.1, is turned into a trend towards that default map.

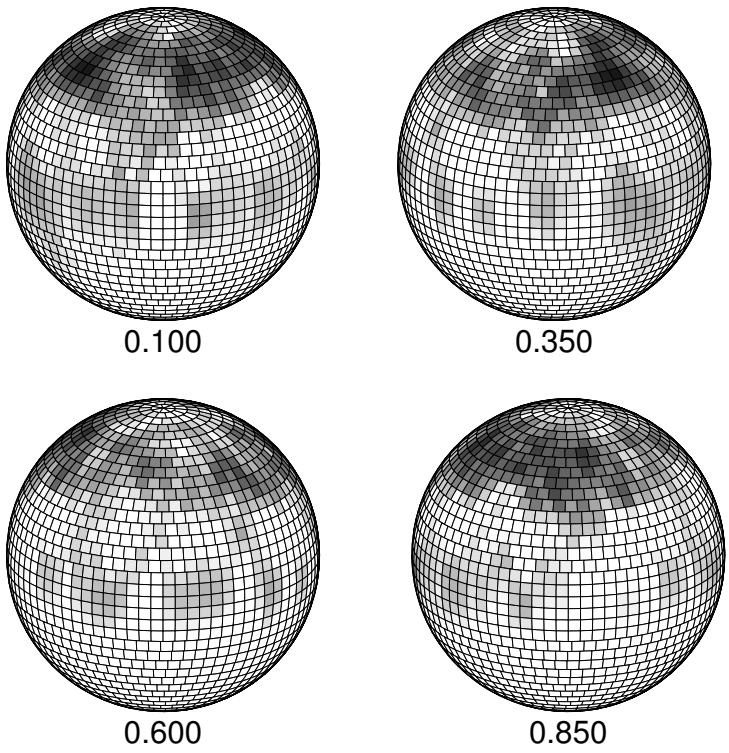

Figure 8.12: Maximum entropy Doppler image of HD197890 reconstructed by MAXENT from a time series of 32 evenly phase sampled line profiles (2002 August 2, adopting a rotation period of P=0.435 days, shown in Fig. 8.16). Further reconstruction parameters are listed in Tab. 7.4. White regions represent the undisturbed photosphere ($\tilde{\sigma}$=0), darker shades represent larger local spot filling factors $0 < \tilde{\sigma} \leq 1$ (see also Fig. 8.10). The surface is shown at four equidistant rotation phases, annotated below each map.

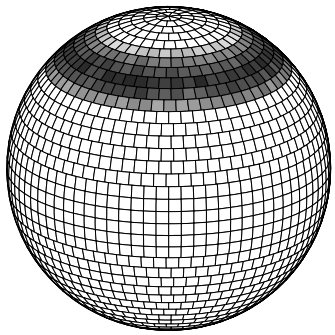

Figure 8.13: Correction surface computed by MAXENT from the average line profile of the input time series used for reconstructing the map of Fig. 8.12 (see text for details). **Note** that the gray scale used here is significantly different from the other maps shown in this Section; it has been adapted to render only a narrow range of surface values. The dark ring of this map is also weakly visible in Fig. 8.12, it contains local filling factors of $\tilde{\sigma} \lesssim 0.2$.

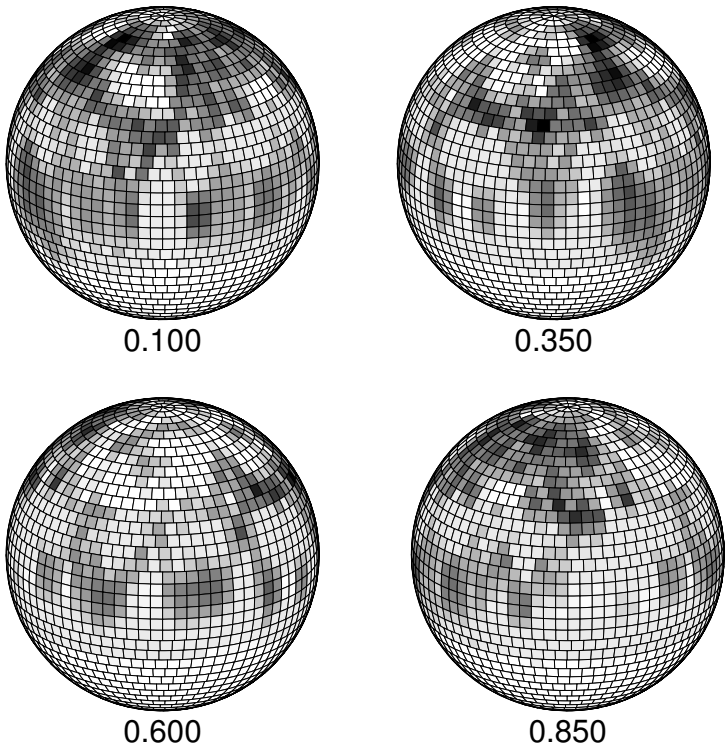

Figure 8.14: Maximum entropy Doppler image of HD197890: The maps show the same surface as in Fig. 8.12, but after subtraction of the correction surface of Fig. 8.13. White regions represent the undisturbed photosphere ($\tilde{\sigma}$=0), darker shades represent larger local spot filling factors $0< \tilde{\sigma} \leq 1$. However, a strictly unambiguous assignment of gray shades to values of the local filling factor is lost due the applied correction. The shown rotation phases are annotated below each map.

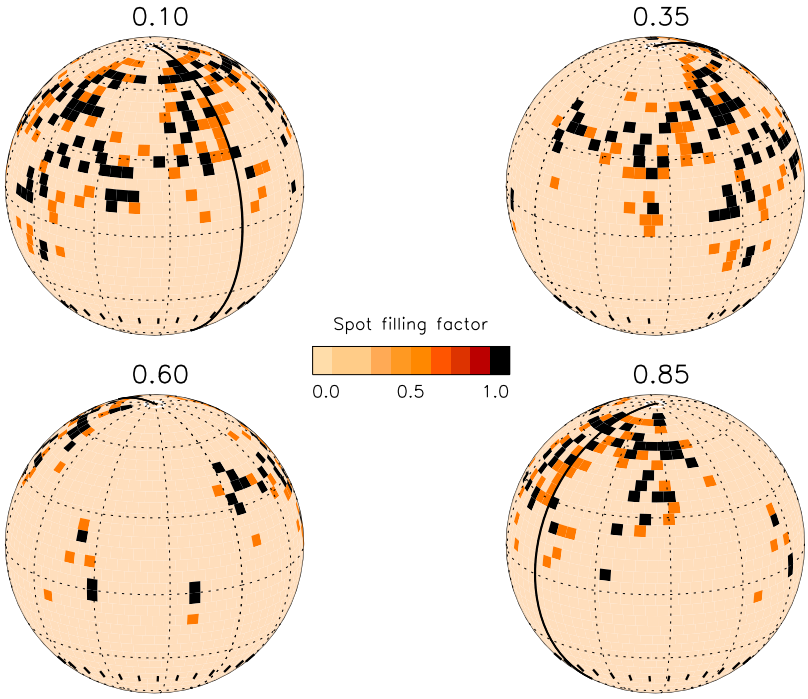

Figure 8.15: CLDI reconstruction of the same input data as the MAXENT reconstruction of Fig. 8.14. Darker colours correspond to larger local spot filling factors σ. See text for a precise definitions of σ, compared to the measure $\tilde{\sigma}$ defined for MAXENT and used in Fig. 8.14.

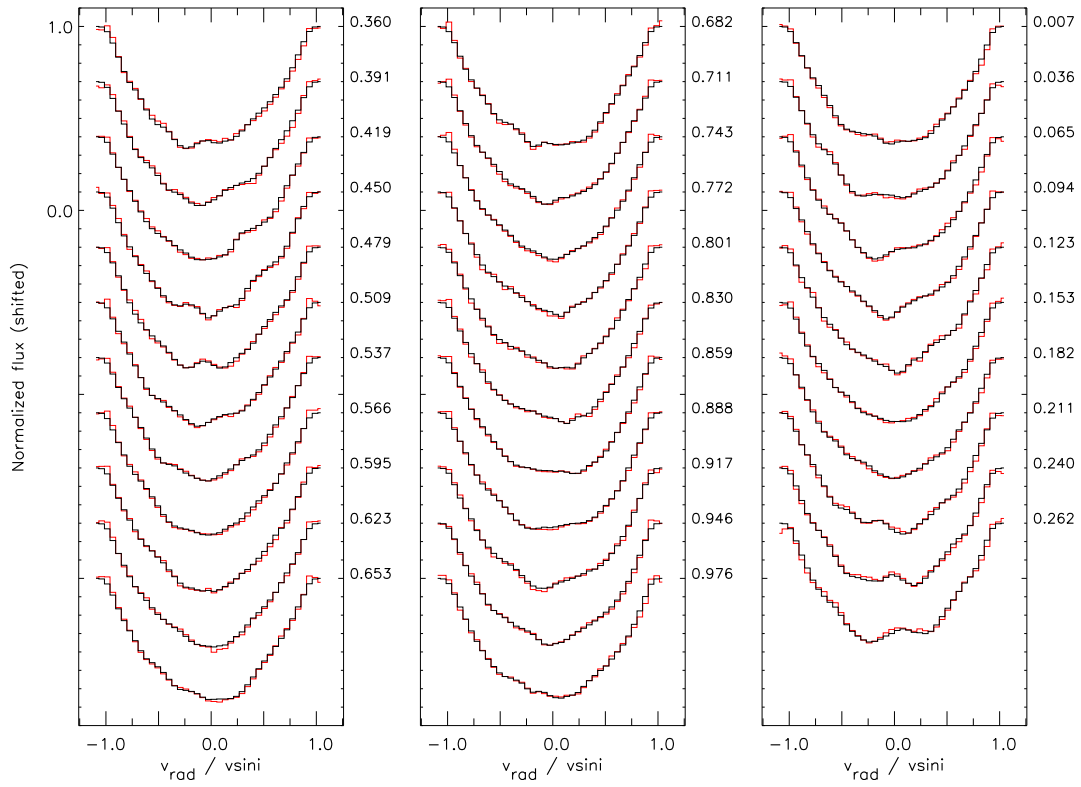

Figure 8.16: Input time series of line profiles (red/gray) used for the MAXENT reconstruction shown in Figs. 8.12 and 8.14. The black line profiles are the fits by MAXENT to the input profiles. The rotation phase of observation is annotated right of each profile continuum (adopting a rotation period of P=0.435 days and a phase zero point at $\mathrm{JD}_{\phi=0} = 2448000.05$). The profiles can be compared to those of Fig. 6.10; note that the phase sampling resolution differs by a factor of two from that figure.

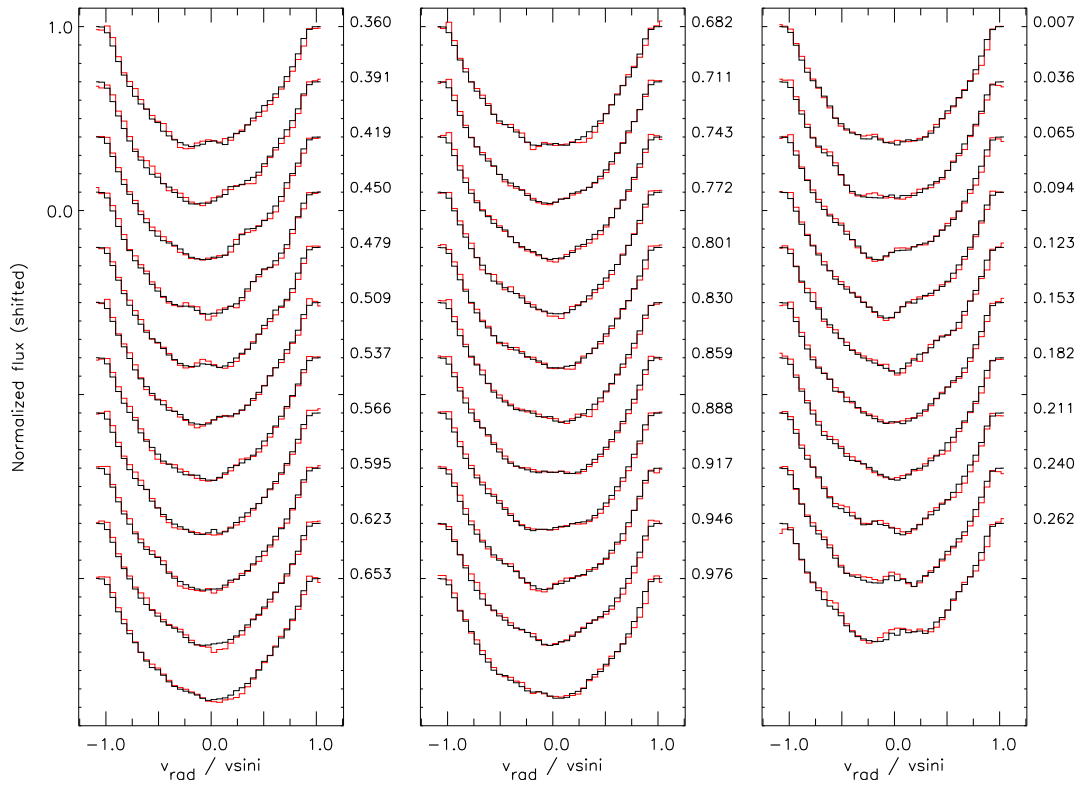

Figure 8.17: Companion to Fig. 8.16, showing the same input line profiles in red/gray, but fits by CLDI (black) computed from the reconstruction shown in Fig. 8.15.

8.5 The "spot" package

The purpose of this Section is to give a short overview of the current implementation of the Doppler imaging algorithm CLDI (CLEAN-like Doppler imaging).

CLDI and the programs for preparing its input, as well as those for interpreting the output have been realized in the programming language of the data analysis package IDL (copyright by Research Systems Inc.). The IDL programming language offers control structures and data types similar to other programming languages.[25] IDL has been chosen for the realization of CLDI because of its extensive and well-documented library of routines for numerical analysis and graphics output. In addition, IDL offers quite presentable debugging facilities.

Table 8.3 contains a list of the programs related to performing Doppler imaging by CLDI, these programs are referred to as the "`spot`-package" in the following.

A few technical remarks

The programs of the `spot`-package (file extension ".pro") are primarily controlled by parameter files (file extension ".par") which contain assignments to variables used in the corresponding program, written in IDL syntax.[26] The parameter files may, do and should contain extensive comments.

The `spot`-package makes use of strictly defined complex data types e.g. for stellar surfaces, line profile time series etc. These complex data types are usually sets of arrays and possibly additional scalar variables. They are not explicitly realized by any IDL structure (which turned out as unwieldy at an early stage), but instead by keeping to a strict scheme of naming the variables. The properties of these complex data types are defined in corresponding "comment-sections" of the subroutine libraries (Table 8.4); presently, the subroutines of the `spot`-package work strictly according to these definitions.[27]

[25] Concerning computational efficiency it is important to make full use of the programming structures which IDL offers for (arithmetic) manipulation of arrays.

[26] Unfortunately, IDL does not support constants (i.e. values protected against changes during runtime); to avoid trouble with "forgotten" changes of the input parameters somewhere "deep in the program", the `spot`-package programs make a rule of not changing them outside the parameter files (excepting a section directly at the beginning of each program which may e.g. be used to disable outdated parameter settings). However, it is the responsibility of the programmer to ensure that this rule is obeyed for future extensions.
Another potential trap when programming in IDL is that all parameters are passed by reference to functions and subroutines (procedures), without an optional check of their modification inside the routines. This means that there is no conceptual difference between input and output variables to those routines. To avoid trouble with unintentional side-effects, *all* output variables of the functions and procedures of the `spot`-package have been explicitly declared as such in the documentation of each subroutine.

[27] Spectra, line profiles, and surfaces are handled by the programs of the `spot`-package as fits-files (Hanisch et al, 2001); conversions to ascii files are provided e.g. for data exchange with other programs. This includes time series of line profiles for which an individual format (file extension ".AiO.fits", "all-in-one") has been defined; these files contain all profiles of a time series strung end-to-end and can e.g. quite comfortably be inspected (or even renormalized etc.) by IRAF procedures.
The input spectra for `spot_LSD` are binned "logarithmically", in wavelength i.e. the ratio of the center wavelength of two adjacent spectral bins is constant (this facilitates the treatment of Doppler shifts in spectra covering wider spectral ranges). Logarithmic binning is e.g. supported by the routines of IRAF's `onedspec` package (the routine `dispcor` can be used for conversion); see the documentation of the routine `init_spec` inside `spot_lipro` for details.
Each ".AiO.fits"-file is accompanied by an ascii-file (file extension ".AiO.obspars") containing information (observation time, SNR, etc.) for each profile of the time series.

Table 8.3: Overview of programs of the `spot`-package directly related to Doppler imaging.

Program	Description
`spot_lipro`	Generates synthetic line profile time series.
`spot_template`	Generates a spectrum from a list of spectral lines (e.g. compiled from the line database VALD).
`spec_plot`	Allows inspection and plotting of spectra. Creates "pretty" plots of line profile time series in conjunction with `spec_plot-stackAiO`. Can perform quantitative comparisons of line profile time series.
`spot_specTS`	Plots time series of line profiles, performs some analysis.
`spot_LSD`	Performs the sLSD spectrum deconvolution of a time series of spectra.
`spot_RBFdeblend`	Determines line profile parameters by fitting an analytic rotationally broadened line profile (used to determine reconstruction parameters for CLDI).
`spot_inspect`	Allows inspection of surfaces in conjunction with line profiles. Optionally performs a cross-correlation of surfaces. Performs conversions between different formats of line profile time series.
`spot_clean`	Performs the CLDI Doppler imaging.

Table 8.4: Overview of subroutine libraries of the `spot`-package.

Library	Description
`spot_stars`	Routines for handling stars and surfaces.
`spot_lips`	Routines for handling line profiles and spectra. Includes general purpose routines, especially file handling.
`spot_plots`	Routines for graphics output, supports CRT (screen), PS (postscript) and mpeg (movies).
`spot_widget`	Routines for GUI (graphical user interface) support.

References

Abney, W. De W. Capt., 1877, MNRAS, 37, 278
Acheson D.J., 1990, Elementary Fluid Dynamics, Clarendon Press, Oxford
Albregtsen F., Maltby P., 1978, Nature, 274, 41
Albregtsen F., Maltby P., 1981, SoPh, 71, 269
Anders G.J., Jeffries R.D., Kellet B.J., Coates D.W., 1993, MNRAS 265, 941
Babcock H.W., 1961, ApJ, 133, 572
Backus G.E., Gilbert F., Philosophical Transact. of the Royal Soc. of London, 1970, 266, 123
Baliunas et al., 1995, ApJ, 438, 269
Baraffe I., Chabrier G., Allard F., Hauschildt P., 2002, A&A, 382, 563
Barnes J.R., Collier Cameron, A., Unruh Y.C., Donati J.-F., Hussain G.A.J., 1998, MNRAS 299, 904
Barnes J.R., Collier Cameron, A., James D.J., Donati J.-F., 2000, MNRAS 314, 162
Barnes J.R., Collier Cameron, A., James D.J., Donati J.-F., 2001, MNRAS 324, 231
Beck J.G., Duvall Jr. T.L., Scherrer P.H., Hoeksema J.T, 1998, in: Structure and Dynamics of the Interior of the Sun and Sun-like stars, Procedings of the SOHO 6/GONG 98 workshop, p. 725
Beck J.G., 1999, Sol.Phys., 191, 47
Berdyugina S.V., Berdyugin A.V., Ilyin I., Tuominen I., 1998, A&A, 340, 437
Berdyugina S.V., 1998, A&A, 338, 97
Berdyugina S.V., 2002, AN, 323, 192
Biermann L., 1941, Vierteljahresschrift der Astron. Ges., 76, 194
Biermann L., 1948, ZA, 25, 135
Biermann L., 1951, ZA, 28, 304
Bouchy, Carrier, 2001, A&A, 374, L5-L8
Brandenburg A., 1991, in: The Sun and Cool stars, activity, magnetism, dynamos, eds. I. Tuominen, D. Moss, and G. Rüdiger, Springer Verlag, New York, p. 223
Braun D.C., Fan Y., 1998, ApJ, 508, L105
Brants J.J., Zwaan C., 1982, Sol.Phys., 80, 251
Bromage G.E., Jeffries R.D., Innis J.L., Matthews L., Anders G.J., Coates D.W., 1992, ASP Conf. Ser., Vol. 26, 80
Brown S.F., Donati J.-F., Rees D.E., Semel M., 1991, A&A, 250, 463
Bruls J.H.M.J., Solanki S.K., Schüssler M., 1998, A&A 336, 231
Brun A.S., Toomre J., 2002, ApJ, 570, 865
Caligari P., Moreno-Insertis F., Schüessler M., 1995, ApJ, 441, 886
Cameron A.C., 2000, Spot mapping in cool stars, Proceedings of Astro-Tomography: An International Workshop on Indirect Imaging, ed. H. Boffin, Danny Steeghs, Jan Guypers. Lecture Notes in Physics (2000), in press
Carrington R.C., 1858, MNRAS, 19, 1
Carrington R.C., 1859, MNRAS, 19, 81
Carrington R.C., 1863, Observations of the spots on the Sun, Williams & Norgate, London
Catalano S., Biazzo K., Frasca A., Marilli E., 2002, A&A, 394, 1009
Cattaneo F., Hughes D.W., 1988, Journal of Fluid Mechanics, 196, 323
Charbonneau P., 1995, ApJS, 101, 309
Charbonneau P., Christensen-Dalsgaard J., Henning R., Larsen R.M., Schou J., Thompson M.J., Tomczyk S., 1999, ApJ, 527, 445
Choi P.I., Herbst W., 1996, Astron.J., 111, 283
Cornwell T.J., 1983, in: Indirect Imaging. Measurement and Processing for Indirect Imaging. J.A. Roberts (ed.),

p. 291, Cambridge University Press, Cambridge
Cox A. (ed.), 2000, Allens Astrophysical Quantities, Springer, New York
Christensen-Dalsgaard J., Hansen P.C., Thompson M.J., 1993, MNRAS, 264, 541
Christensen-Dalsgaard J., 2002, Rev.Mod.Phys., 74, 1073
Christensen-Dalsgaard J., 2003, Ap&SS, 284, 277
Claret A., 2000, A&A, 359, 289
Collier Cameron A., 2000, Spot mapping in cool stars
Collier Cameron A., Donati J.F., Semel M., 2001, MNRAS, 330, 699
Cowling T.G., 1958, IAUS, 6, 105
Cutispoto G., Kürster M., Pagano I., Rodono M., 1997, Information Bulletin on Variable Stars, 4419, 1
Deutsch A.J., 1958, in IAU Symposium 6, Electromagnetic phenomena in cosmical physics, p. 209
Deutsch A.J., 1970, ApJ, 159, 985
Donahue R.A., Saar S.H., and Baliunas S.L., 1996, ApJ, 466, 384
Donati J.-F., Collier Cameron A., 1997, MNRAS, 291, 1
Donati J.-F., Semel M., Carter B.D., Rees D.E. Collier Cameron A., 1997, MNRAS, 291, 658
Donati J.-F., Collier Cameron A., Hussain G.A.J., Semel M., 1999, MNRAS, 302, 437
Donati J.-F., Collier Cameron A., Petit P., 2003, MNRAS, 345, 1187
Dunér N.C., 1890, AN, 124, 267
Dunér N.C., 1905, AN, 167, 167
Durney B.R., Spruit H.C., 1979, ApJ, 234, 1067
Durney B.R., de Young D.S., Roxburgh I.W., 1993, Sol.Phys., 145, 207
Durney B.R., 2000, ApJ, 528, 486
Duvall T.L., Kosovichev A.G., Scherrer P. et al., Bogart R.S., Bush R.I., de Forest C., Hoeksema T.J., Schou J., Saba J.L.R, Tarbell, T. D., 1997, Sol.Phys., 170, 63
Eaton N.L., Herbst W., Hillebrand L., 1995, Astron.J., 110, 1735
Eaton N.L., Henry G.W., Fekel F.C., 1995, ApJ, 462, 893
Eddington A.S., 1926, The internal constitution of the stars, Cambridge University Press
Edwards S., Strom S.E., Hartigan P.,Strom K.M., Hillebrand L.A., Herbst W.,Attridge J.,Merril K.M., Probst R., Gatley I., 1993, Astron.J., 106, 372
Emden R., 1907, Gaskugeln - Anwendungen der mechanischen Wärmetheorie, Teubner, Leipzig
Falk A., Wehlau W.H., 1974, ApJ, 192, 409
Foukal P., 1990, Solar Astrophysics, Wiley, New York
Giampapa M.S., 1990, Nature, 348, 488
Gilman P., 1979, IAU Symp.51, p. 19
Gilman P., 2000, Sol.Phys, 192, 27
Gilman P., Morrow A., Deluca, E., 1989, ApJ, 338, 528
Gizon L., Duvall Jr. T.L., Schou J., 2003, Nature, 421, 43
Goncharsky A.V., Stepanov V.V., Khokhlova V.L., Yagola A.G., 1982, Sov.Astron. 26(6), 690
Granzer T., 2002, AN, 323, 395
Gray D.F., 1977, ApJ, 211, 198
Gray D.F., 1988, Lectures on spectral-line analysis: F, G and K stars, The Publisher, Arva
Gray D.F., 1992, The observation and analysis of stellar photospheres, Cambridge Univ. Press, Cambridge
Gregory R.L., Heard P., 1979, Perception, 8, 365
Gull S.F., Skilling J., 1983, in: Indirect Imaging. Measurement and Processing for Indirect Imaging. J.A. Roberts (ed.), p. 267, Cambridge University Press, Cambridge
Gunn A.G., Mitrou C.K., Doyle J.G., 1998, MNRAS, 296, 150
Gustafsson B., Bell R.A., Eriksson K., Nordlund A., 1975, A&A, 42, 407
Haber D.A., Hindman B.W., Toomre J., Bogart R.S., Larsen R.M., Hill F., 2002, ApJ, 570, 855
Hale G.E., 1908, ApJ, 28, 315
Hall, D.S., 1991, in: The Sun and Cool stars, activity, magnetism, dynamos, eds. I. Tuominen, D. Moss, and G. Rüdiger, Springer Verlag, New York, p. 353
Hall, D.S., 1996 in: Strassmeier K.G., Linsky J.L. (eds.), 1996, IAUS 176, 217

Hanisch R. J., Farris A., Greisen E. W., Pence W. D., Schlesinger B. M., Teuben P. J., Thompson R. W., Warnock A. III, 2001, A&A, 376, 359
Hathawy D.H., 1996, ApJ, 460, 1027
Hatzes A.P., Penrod G.D., Vogt S.S., 1989, ApJ, 341, 456
Hatzes A.P., Vogt S.S., 1992 MNRAS, 258, 387
Hatzes A.P., 1990, MNRAS, 245, 56
Hatzes A.P., 1998, A&A, 330, 541
Hauck B., Mermilliod M., A&AS, 129, 431
Hauschildt P., Allard F., ApJ, 512, 377
Hempelmann A., Donahue R.A., 1997, A&A, 322, 835
Hendry , Mochnacki, 2000, ApJ, 531, 467
ESA SP-1200, 1997, The Hipparcos and Tycho Catalogues, Vol.1, Introduction and Guide to the Data
Högbom J.A., 1974, A&AS, 15, 417
Holland J.H., 1975, "Adaptation in natural and artificial systems. An introductory analysis with applications to biology, control and artificial intelligence", MIT Press, Ann Arbor (University of Michigan)
Horne K., 1986, PASP 98, 1220
Howard R., LaBonte B.J., 1980, ApJ, 228, L45
Howard R., 1984, ARA&A, 22, 131
Howard R., 1996, ARA&A, 34, 75
Hurlburt N.E., Matthews P.C., Rucklidge A.M., 2000, SoPh, 192, 109
Hurlburt N.E., Matthews P.C., Rucklidge A.M., 2000, MNRAS, 314, 793
Hussain G.A.J., 2002, AN, 323, 349
Javaraiah J., 2003, Sol.Phys., 212, 23
Jankov S., Foing B.H., 1992, A&A, 256, 533
Jankov S., Foing B.H., 1992, in: Proc. of the ESA workshop on solar physics and astrophysics at interferometric resolutions, p. 113
Jaynes E.T., 1957, Phys.Rev., 106, 620
Jaynes E.T., 1982, in: Proceedings of the IEEE, Vol.70, No.9, 939-952
Jeffries R.D., 1993, MNRAS 264, 106
Keppens R., MacGregor K.B., Charbonneau P., 1995, A&A, 294, 469
Kawaler S.D., 1987, Publ.Astron.Soc.Pac., 99, 1322
Kippenhahn R., Möllenhoff C., 1975, Elementare Plasmaphysik, Bibliographisches institut
Kippenhahn R., Weigert , 1990, Stellar structure and evolution, Springer Verlag, Berlin
Kirkpatrick S., Gelatt C.D., Vecchi M.P., 1983, Science, 220, 671
Kitchatinov L.L., and Rüdiger G., 1993, A&A, 276, 96
Kitchatinov L.L., and Rüdiger G., 1994, AN, 315, 157
Kitchatinov L.L., and Rüdiger G., 1995, A&A, 299, 446
Kitchatinov L.L., and Rüdiger G., 1999, A&A, 344, 911
Kochukhov O., Piskunov N.E., 2002, A&A, 381, 736
Komm R.W., Howard R.F., and Harvey J.W., 1993, Sol. Phys., 143, 19
Komm R.W., Howard R.F., and Harvey J.W., 1993, Sol. Phys., 147, 207
Korhonen H., Berdyugina S.V., Strassmeier K.G., Tuominen I., 2001, A& A, 379, L30
Kuhn J.R., Bush R.I., Scheick X., Scherrer P., 1998, Nature, 392, 155
Kupka F., Piskunov N., Ryabchikova T.A., Stempels H.C., Weiss W.W., 1999, A&AS, 138, 119
Küker M., Rüdiger G., Kitchatinov L.L., 1993, A&A, L1
Kürster M., 1992, Ph D thesis, LMU München, FRG; MPE report 236
Kürster M., 1993, A&A, 274, 851
Kürster M., Schmitt J.H.M.M., Cutispoto G., 1994, A&A, 289, 899
Larmor J., 1919, Engineering, 108, 461
Lucy L.B., 1967, Z.f.Astrophysik, 65, 89
Lucy L.B., 1994, Reviews in modern astronomy, vol. 7, 31
Lutz T.E., Pagel B.E.J., 1982, MNRAS, 199, 1101

Marsh T.R., 1989, PASP, 101, 1032
Martínez Pillet V., 2002, AN, 323, 342
Maeder A., Meynet G., 2000, Ann.Rev.Astron.Astrophys., 38, 143
Mayor M., 1980, A&A 87, L1
Mazumdar A., Antia H.M., 2001, A&A, 368, L8
Messina S., Guinan E.F., Lanza A.F., and Armbruster C., 1999, A&A, 347, 249
Mestel L., Stellar magnetism, Clarendon Press, Oxford
Meyer F., Schmidt H.U., Weiss N.O., Wilson P.R., 1974, MNRAS, 169, 35
Miesch M., 2000, Sol.Phys., 192, 59
Monnier J.D., 2003, Rep. Prog. Phys., 66, 789
Montes D., Lopez-Santiago J., Galvez M.C., Fernandez-Figueroa M.J., De Castro E., Cornide M., 2001, MNRAS, 328, 45
Moon T.T., 1984, MNRAS 211, 21
Moon T.T., Comm. Univ. London Obs., 78
Moore R., Rabin D.,1985, AR&A, 23, 239
Napiwotzki R., Schönberger D., Wenske V., 1993, A&A, 268, 653
Narayan R., Nityananda R., 1986, Ann.Rev.Astron.Astrophys. 24, 127
Newton H.W., and Nunn M.L., 1951, MNRAS, 111, 413
Noyes R.W., Hartmann L.W., Baliunas S.L., Duncan D.K., Vaughan A.H., 1984, ApJ, 279, 763
O'Neal D., Saar S.H., Neff J.E., 1996, ApJ, 463, 766
O'Neal D., Saar S.H., Neff J.E., 1998, ApJ, 501, L73
Olah K., Strassmeier K.G., Kovari Z., Guinan E.F., 2001, A&A, 372, 119
Parker E.N., 1955, ApJ, 122, 293
Parker E.N., 1955, ApJ, 121, 491
Parker E.N., 1970, ApJ, 162 ,665
Parker E.N., 1979, Cosmical Magnetic Fields, Clarendon Press, Oxford
Patten B.M., Simon T., 1996, APJS, 106, 489
Pedlosky J., 1987, Geophysical fluid dynamics (2nd ed.), Springer Verlag, New York
Peters C.H.F., 1859, MNRAS, 19, 173
Pham D.T., Karaboga D., 2000, Inteligent optimization techniques, Springer Verlag, New York
Pijpers F.P., Thompson M.J., 1992, A&A, 262, L33
Pinsonneault M., 1997, Ann.Rev.Astron.Astrophys., 35, 557
Piskunov N.E., 1985, Sov.Astron.Lett., 11(1), 18
Piskunov N.E., 1990, p. 309, in: The Sun and Cool Stars: activity, magnetism, dynamos, I. Tuominen, D. Moss, G. Rüdiger (ed.), IAU Coll. 130, Springer Verlag, Berlin
Piskunov N.E., Tuominen I., Vilhu O., 1990, A&A, 230, 363
Piskunov N.E., Wehlau W.H., 1990, A&A, 233, 497
Piskunov N.E., Kochukhov O., 2002, A&A, 381, 736
Pizzolato N., Ventura P., D'Antona F., et al., Maggio A., Micela G., Sciortino S., 2001, A&A, 373, 597
Press W.H., Flannery B.P., Teukolsky S.A., Vetterling W.T., Numerical recipes in C (2nd ed.), Cambridge Univ. Press
Proctor M.R.E., and Gilbert A.D., 1994, Lectures on Solar and Planetary Dynamos, Cambridge University Press
Pyper D.M., 1969, ApJS, 164, 18, 347
Reiners A., Schmitt J.H.M.M., Kürster M., 2001, A&A, 376, L13
Reiners A., 2002, Measurement of Differential Rotation in Line Profiles of Solar-like Stars, PhD thesis Hamburg
Reiners A., Schmitt J.H.M.M., 2002, A&A, 384, 155
Reiners A., Schmitt J.H.M.M., 2002, A&A, 388, 1120
Reiners A., Schmitt J.H.M.M., 2003, A&A, 398, 647
Reiners A., 2003, A&A, 408, 707
Rice J.B., Wehlau W.H., Khokhlova V.L., 1989, A&A, 208, 179
Rice J.B., Strassmeier K.G., 1996, A&A, 316, 164
Rice J.B., and Strassmeier K.G., 2000, A&AS, 147, 151
Rice J.B., and Strassmeier K.G., 2001, A&A, 377, 264

Rice J.B., 2002, AN, 323, 220
Richokainen A., Urpo S., Valtaoja E., 1998, A&A, 333, 741
Rüdiger G., 1977, AN, 298, 245
Rüdiger G., 1989, Stellar Rotation and Stellar Convection, Gordon and Breach science publ. / Akademie Verlag, Berlin
Rüdiger G., v. Rekowski B., Donahue R.A., Baliunas S., 1998, ApJ, 494, 691
Rüdiger G., Küker M., 2002, A&A, 308-312
Saar S.H., 1996, in: Uchida Y. (ed.), Magnetohydrodynamic Phenomena in the Solar Atmosphere - Prototypes of Stellar Magnetic Activity, Kluwer, p. 367
Saar S.H., Peterchef A., O'Neal D., Neff J.E., 2001, ASP Conf.Ser. 323, 1057
Scargle J.D., 1982, ApJ, 263, 835
Schüssler M., 1992, A&A, 264, L13
Schüssler M., 1995, Reviews in Modern Astronomy, 8, 11
Schüssler M., 2002, AN, 323, 377
Schwarz U.J., 1978, A&A, 65, 345
Siess L., Dufour E., Forestini M., 2000, A&A, 358, 593
Snodgrass H.B., Dailey S.B., 1996, Sol.Phys., 163, 21
Snodgrass H.B., 2000, Sol.Phys., 94, 13
Schatzmann E., Ann.Astrophys., 1962, 25, 18
Schou J., Antia H.M., Basu S., et al., 1998, ApJ, 505, 390
Schrijver C.J., and Zwaan C., 2000, Solar and Stellar Magnetic Activity, Cambridge University Press
Schrijver C.J., 2002 AN, 323, 157
Simon G.W., Weiss N.O., 1968, ZA, 69, 435
Skilling J., Bryan R.K., 1984, MNRAS 211, 111
Skumanitch A., 1972, ApJ, 171, 265
Soderblom D.R., Stauffer J.R., Hudon J.D., Jones B.F., 1993, ApJS, 85, 315
Soderblom D.R., Stauffer J.R., MacGregror K.B., Jones B.F., 1993, ApJ, 409, 624
Soderblom D.R., Jones B.F., Balachandran S., Stauffer J.R., Duncan D.K., Fedele S.B., Hudon J.D., 1993, ApJS, 85, 315
Solanki S.K., 2002, AN, 323, 165
Spörer F.W.G., 1861, AN, 55, 289
Spörer F.W.G., 1861, AN, 55, 379
Spruit H.C., 1981, Space Sci. Rev., 28, 435
Stix M., 2002, AN, 323, 179
Stix M., 2002, The Sun - An introduction (2nd ed.), Springer Verlag, Berlin
Stout-Batalha N.M., Vogt S.S., 1999, ApJS, 123, 251
Strassmeier K.G., Rice J.B., Wehlau W.H., Vogt S.S., Hatzes A.P., Tuominen I., Piskunov N.E., Hackman T., Poutanen M., 1991, A&A, 247, 130
Strassmeier K.G., Hall D.S., Henry G.W., 1994, A&A, 282, 535
Strassmeier K.G., 1997, Aktive Sterne, Springer Verlag, Berlin
Strassmeier K.G., 2002, AN, 323, 309
Strassmeier K.G., Pichler T., Weber M., Granzer T., 2003, A&A, 411, 595
Sturrock P.A., Scargle J.D., 2001, ApJ, 550, L101
Tassoul J,-L., 2000, Stellar rotation (2nd ed.), Cambridge University Press
Titterington D.M., 1985, A&A, 144, 381
Ulrich R.K., Bertello L., 1996, AJ, 465, L65
Unruh Y.C., Collier Cameron A., 1995, MNRAS, 273, 1
Unsöld A., Baschek B., 1988, Der Neue Kosmos (4. Aufl.) , Springer Verlag, Berlin
Vaughan A.H., Preston G.W., Wilson O.C., 1978, PASP, 90, 267
Vogel H.C., 1877, AN, 90, 71
Vogt S.S., 1981, ApJ, 250, 327
Vogt S.S., Penrod G.D., 1983, PASP 95, 565

Vogt S.S., Penrod G.D., A.P. Hatzes, 1987, ApJ, 321, 496
Vogt S.S., and Hatzes A.P., 1991, in: The Sun and Cool stars, activity, magnetism, dynamos, (eds.) I. Tuominen, D. Moss, and G. Rüdiger, Springer Verlag, New York, p. 297
Vogt S.S., Hatzes A.P., and Misch A.A., 1999, ApJSS, 121, 547
Walton S.R., Preminger D.A., Chapman G.A., 2003, SoPh, 213, 301
Weber M., Strassmeier K.G., 2001, A&A, 373, 974
Weischet W., 1977, Einführung in die allgemeine Klimatologie, Teubner, Stuttgard
Weiss N.O., 2002, AN, 323, 371
Wöhl H., 1983, in: Solar and Stellar Magnetic Fields: Origin and Coronal Effects, ed. J.O. Stenflo, IAU Symp. 102, Reidel Dordrecht, p. 155
Wöhl H., 2002, AN, 323, 329
Young J. S., Baldwin J. E., Boysen R. C., Haniff C. A., Lawson P. R., Mackay C. D., Pearson D., Rogers J., St.-Jacques D., Warner P. J., Wilson D.M.A., Wilson R.W., 2000, MNRAS 315, 635
Zhao J., Kosovichev G., Duvall Jr. T.L., 2001, ApJ, 557, 384
Zwaan C., 1969, Ann.Rev.Astron.Astrophys., 6, 135

Acknowledgements

This work, however humble, required some effort to carry out. I am indebted to a considerable number of people who have made it possible, who by advice and good company supported it. These people have made this work usually an aggreeable pastime as well as certainly a most instructive experience. I thank Prof. Jürgen Schmitt for making this thesis possible and for his exceptional support.
Although gratitude can be expressed in any language, I switch to german for a few paragraphs in the following.

> Wie erwähnt danke ich Prof. Jürgen Schmitt für das Thema und die Betreung, die Raum liess und doch immer Rat und Unterstützung bot wo sie benötigt wurden. Ich danke Jürgen darüber hinaus für viele anregende Diskussionen, gute Ideen und die gute Arbeitsatmosphäre die er in seiner Arbeitsgruppe zu schaffen versteht. Schade, dass Jürgen mit uns anderen wohl auf "sonnenartige" Bilder von Flecken auf sonnenartigen Sternen noch einige Instrumentengenerationen wird warten müssen. Dieses Ziel stellte und stellt einen wesentlichen Antrieb dieser Arbeit dar.
> Auch den übrigen Mitgliedern der Arbeitsgruppe gebührt Dank für gute Gesellschaft, lehrreiche Diskussionen sowie umfangreiche und gute Zusammenarbeit. Besondere Erwähnung verdienen dabei Alex(ander) Hempelmann, Rainer Wichmann, Marc Hempel, Jan-Uwe Ness, Ansgar Reiners und Birgit Fuhrmeister. Ansgar danke ich zudem für Jahre guter, unmittelbarer Schreibtischnachbarschaft und viele gemeinsame Malzkaffees; auch Marc war und ist immer für lehrreiche Diskussionen über Astronomie und anderes zu haben. Auch wenn es Kekse gibt.
> Meine Frau Andrea und meine Töchter Elisa und Amelie verdienen Dank der den Rahmen dieser "acknowledgements" sprengt; auch meiner Mutter, nebst Helmut, danke ich sehr für ihre Unterstützung.

I thank those people from the Hamburger Sternwarte who have not been explicitly mentioned above for their kind support and collaboration.

I owe thanks to several people who have assisted my work through their experience in numerous interesting discussions. Roughly in order of appearance they are: Martin Küster, Holger Lehmann, Dave Kilkenny, Artie P. Hatzes, Sacha Brun and Leonid Kitchatinov.

I thank Artie Hatzes for kindly supplying his maximum entropy Doppler imaging code MAXENT and quite some support with it. Had I decided to see this code in operation during earlier stages of this thesis, I would have been spared a considerable amount of "effort"; but presumably also quite some experience. I also thank Guiseppe Cutispoto for kindly supplying "his" photometric data of Speedy Mic as well as Sonja Isaacs for suggesting the connection with the SAAO which made the August 2002 photometry of Speedy Mic possible. If the South African weather had permitted more observation nights in August 2002, considerably more could have been learned from the photometry. Well, nobody is to blame for that ...

Last, in a different way, but not least I thank J.S. Bach for his music which has also been good company and provided inspiration during this work. I am nearly convinced (although not quite certain) that Mr. Bach would not have taken much interest in a work like this. However, it seems that efforts like the one at hand and his creations do, to a considerable part, serve a common purpose: To explore and illustrate the divine and strangely sublime creation man finds himself being part of.

I acknowledge financial support by the Deutsche Forschungsgemeinschaft under DFG - SCHM 1032/9-1.